Molecular Engineering Strategies for Morphology Control in Organic Semiconductors for Optoelectronics

THÈSE N^O 8520 (2018)

PRÉSENTÉE LE 30 AVRIL 2018
À LA FACULTÉ DES SCIENCES DE BASE
LABORATOIRE D'INGÉNIERIE MOLÉCULAIRE DES NANOMATÉRIAUX OPTOÉLECTRONIQUES
PROGRAMME DOCTORAL EN CHIMIE ET GÉNIE CHIMIQUE

ÉCOLE POLYTECHNIQUE FÉDÉRALE DE LAUSANNE

POUR L'OBTENTION DU GRADE DE DOCTEUR ÈS SCIENCES

PAR

Muhammad Aiman BIN RAHMANUDIN HAMDAN

acceptée sur proposition du jury:

Prof. U. A. Hagfeldt, président du jury
Prof. K. Sivula, directeur de thèse
Prof. B. Schroeder, rapporteur
Prof. G. Wantz, rapporteur
Dr S. M. Zakeeruddin, rapporteur

EPFL

ÉCOLE POLYTECHNIQUE
FÉDÉRALE DE LAUSANNE

Suisse
2018

Saya khaskan tesis ini untuk allahyarham atuk Hamdan yang tersayang

"I liked Science. I wasn't mathematically oriented, so I became an organic chemist."

Koji Nakanishi

Acknowledgements

I would first like to thank Professor Kevin Sivula for giving me the opportunity to conduct my doctoral research and to be a part of the team in LIMNO. I have learnt a lot from you – from the rough start and struggle at beginning and towards the successful end of my PhD. Your guidance and caring advice on the proper ways to do research and also about academic life will be something I will cherish and remember. Thank you for believing in me and I really appreciate the time you have taken in supporting my time at LIMNO.

I am deeply gratefully to all my colleagues at LIMNO who have helped me as without you none of this would been possible. I especially would like to thank Liang for being a friend and a partner in the lab, for always being there to discuss about research, coming out with new ideas and helping me with experiments. Furthermore, your support and constant motivation have helped me through the times when experiments fail and did not work. I could not have asked for a better Post-doc to guide me during my PhD, so thank you!

Xavier, we both went through the same struggles and we survived it! – from making devices and characterizing them to fun times inside and outside of the lab, the jamming sessions and drunk times on the roof of EPFL. The 4 years would not have been as fun if not for you, so thank you! To Xiaoyun, thank you being a good friend in the lab, your support and kindness and for always being there to provide a listening ear especially during the lowest points I had in lab. Emilie thank you being supportive and a good friend while you were here. To Florian, thank you for your willingness to help (especially listening to me giving my endless rapid-fire practice talks) and of course your advice and wisdom about academic life. I appreciate it and thank you! Junho for always being a fun guy to talk to both about science, snowboarding and kimchi making, and also thank you for helping with revising my thesis. Simon and Arvindh, thank you for bearing with me while I was supervising and making the both of you work extra hard during your master's thesis. The work that the both of you have done had significant impact towards my PhD Thesis, so I really appreciate your respective contributions. To Charles, thanks for going snowboarding on the weekends while I was finishing up my thesis and up until the day of my defence. I needed the break which helped a lot, and now that its over let's keep shredding the slopes! To Xavier da Costa and Barbara for helping with the printing and binding of my thesis on the day of submission, I was in a rush and slightly panicked so without you I would have not made it in time for the deadline. Thank you also to the rest of the LIMNO family both old and new: Nestor, Pauline, Melissa, Sebastien, Mathieu, Andrea, Xiaodi, Rebecca, Nukorn, Yong Peng.

Abstract

It is understood that the optoelectronic performance of organic electronic devices is determinant on the macroscopic solid state self-assembly of organic semiconductors (OSC), which is driven by the supramolecular π-π stacking interactions between the conjugated segments in its molecular structure. Molecular engineering approaches directly impacts the intrinsic self-assembling properties of the OSCs, but the flexibility of organic chemistry on modulating the backbone architecture of the π-conjugated system has led a vast library of OSCs with various functionalities, which fundamentally changes the electronic properties of the π-conjugated system. It is highlighted that introducing conjugation break spacers (flexible linkers) between the π-conjugated segments in the OSC, showed great promise in controlling supramolecular self-assembly without altering the semiconducting core of the OSC. Previous examples on controlling the morphology of the molecular OSC, DPP(TBFu)$_2$ using horizontal and vertical dimers, and a horizontal flexibly linked polymer analogues, have shown great promise in effecting the self-assembly behaviour and stabilizing the morphology of the parent (non-flexibly linked) DPP(TBFu)$_2$ molecule, when used as an additive.

In this thesis, an extension of this work is presented whereby the flexible linking approach is used to design and synthesize two molecular compatibilizers that consists of the donor component, DPP(TBFu)$_2$ that is linked with an aliphatic spacer to an acceptor component, based on a fullerene and perylenediimde small molecule OSC. In chapter 2, a comparison between the compatiblizer (CP) and an in-situ linker approach (ISL) was explored to elucidate the impact of stabilizing a multi-component bulk heterojunction (BHJ) morphology and its device performance for organic photovoltaics (OPVs). It was concluded that the CP approach shows the most promise in stabilizing the BHJ morphology for OPVs, which was then applied onto a highly crystalline BHJ system with a perylenediimde acceptor to demonstrate its versatility as described in chapter 3. Taking leverage from this demonstration, chapter 4 discusses how the CP approach is used to tune the phase-domain size of the BHJ that is processed from a homogeneous single-phase melt, to obtain a photoactive BHJ in an OPV device. This unique demonstration, ultimately opens up vast new possibilities for solvent free "green" processing of OPVs.

Lastly in Chapter 5, the approached used to address BHJ morphological stabilization is slightly different from that of previous chapters, where the (kinetic) stability of a binary donor-acceptor BHJ is addressed. In this chapter, a fully-conjugated block copolymer (BCP) consisting of donor–acceptor blocks is used to demonstrate its applicability for a single-component BHJ for OPVs. However, the main challenge for this approach is in the synthetic methodology, and to overcome this, a modular synthetic strategy using Heck coupling between two functionalized donor and accepting marcromonomers showed promise in obtaining a fully conjugated BCP for OPVs

Résumé

Il est aujourd'hui établi que la performance optoélectronique des cellules solaires organiques est déterminée par l'auto-assemblage macroscopique des semiconducteurs organiques à l'état solide (SCO), qui est causé par les interactions supramoléculaires – empilement π-π – entre les segments conjugués de sa structure moléculaire. Les approches d'ingénierie moléculaire ont un impact direct sur les propriétés d'auto-assemblage intrinsèques des SCO, mais les possibilités que la chimie organique offre concernant la modification de la chaine conjuguée centrale a conduit à l'existence d'une vaste bibliothèque de SCO aux fonctionnalités variées qui modifie la conjugaison de la chaine carbonée. Il est démontré que l'introduction de chaines alkyl qui interrompent la conjugaison entre les segments conjugués π dans les SCO (liens flexibles), est une méthode séduisante pour le contrôle de l'auto-assemblage supramoléculaire, sans que cela n'altère la chaine semi-conductrice du SCO. Des exemples précédents de contrôle de la morphologie du SCO moléculaire DPP(TBFu)$_2$, utilisant des dimères horizontaux et verticaux, ou des polymères analogues contenant des liens flexibles horizontaux, se sont avérés très efficaces pour favoriser l'auto-assemblage et stabiliser la morphologie de la molécule primaire DPP(TBFu)$_2$ (non reliés par des chaines flexibles) , lorsque la molécule dérivée est utilisé comme additif.

Dans cette thèse, une extension de ces précédentes recherches est détaillée, en utilisant l'approche consistant à ajouter des liaisons flexibles pour concevoir et synthétiser deux molécules compatibilisantes qui se compose chacune d'un segment donneur, DPP (TBFu)$_2$, relié par un espaceur aliphatique à un segment accepteur, basé sur un fullerène et sur une molécule organique semi-conductrice, le perylenediimide. Dans le chapitre 2, une comparaison entre l'approche avec molécules compatbilisantes (CP) et une approche de liaison in-situ (LIS) a été effectuée pour élucider le rôle de la méthode sur la stabilisation de l'héterojonction organique entre le donneur et l'accepteur (BHJ) ainsi que sur la performance des couches formées en tant que cellule photovoltaïque (OPV). Il est ainsi démontré que l'approche CP est la plus prometteuse pour stabiliser la morphologie de la BHJ pour les OPV, qui a ensuite été appliquée sur un autre système d'hétrérojonction organique, hautement cristallin, avec un accepteur de perylènediimde pour démontrer la polyvalence de la méthode, comme décrit au chapitre 3. A partir de cette démonstration, le chapitre 4 détaille comment l'approche CP est utilisée pour contrôler la taille du domaine des phases dans la BHJ obtenue à partir d'une phase fondue unique et homogène, afin d'obtenir une BHJ photoactive dans une cellule solaire. Cette démonstration unique ouvre en définitive de nouvelles possibilités pour une fabrication des OPV sans solvant, suivant les préceptes de la chimie verte.

Finalement, dans le chapitre 5, l'approche utilisée pour stabiliser la morphologie des BHJ est légèrement modifiée par rapport à celle employée dans les chapitres précédents, qui décrivaient des méthodes pour améliorer la stabilité (cinétique) des héteorjonctions donneur-accepteur binaires. Dans ce chapitre, un copolymère entièrement conjugué (BCP), constitué de blocs séquencés donneur-accepteur est utilisé pour démontrer son applicabilité pour une hétérojonction contenant un seul type de molécule pour les cellules solaires. Cependant, le principal défi de cette approche réside dans la méthodologie de la synthèse, et pour surmonter cette difficulté, une stratégie synthétique modulaire utilisant le couplage de Heck entre deux donneurs fonctionnalisés et acceptant des macromonomères s'est avérée encourageante pour obtenir un BCP entièrement conjugué pour les OPV.

Contents

List of Figures

Chapter 1 -Introduction

Chapter 2 - Morphology Stabilization Stratergies for Small Molecule Bulk Heterojunction Photovoltaics

Chapter 3 - Stabilizing the Bulk Heterojunction Morphology of a Small Molecule Organic Solar Cell based on a Perylenediimide Acceptor via a Compatibilization Approach

Chapter 4 - Melt Processing of Small Molecule Organic Photovoltaics via Bulk Heterojunction Compatibilization

Chapter 5 - Heck-Mizoroki Reaction of Functionalized Macromonomers for the Formation of Fully-Conjugated block-copolymers for Organic Photovoltaics

NMR spectrum of tri-BCP to indicate the proton assignments on tri-BCP of the aromatic region and the respective protons on the aliphatic chains of the donor and acceptor blocks where * indicates deuterated-chloroform solvent peak (See Appendix 5 Figure S4 for the full ^{1}H NMR Spectra), and c) The chemical structure of tri-BCP.

List of Tables

CHAPTER 1

Introduction

"Polymer synthesis in the 1950s was dominated by Karl Ziegler and Giulio Natta, whose discoveries of polymerization catalysts were of great importance for the development of the modem 'plastics' industry."

Alan J. Heeger

1.1 Importance of self-assembly and its effect on optoelectronic properties

Over the past decade, π-conjugated semiconductors have attracted significant attention from both academic and industrial laboratories due to a wealth of potential applications, from solution-processed thin-film electronics to the roll-to-roll fabrication of organic light-emitting-diodes,[1] thin film transistors,[2] photovoltaics (PV),[3] and bioelectronics.[4] This is largely due to innovation in synthetic methods and material design that have been extensively applied to manipulate molecular architecture of the π-conjugated system, leading to a vast library of small-molecule and polymer semiconductors with a variety of functionalities.[5] While tuning band-gap, electron affinity, and processability of these materials has been well developed, a discrepancy in understanding these fundamental properties with their solid-state morphology, and the resulting optoelectronic properties, remain to be fully addressed.[6]

Theoretical calculations based on density functional theory (DFT) do not typically consider the macroscopic thin-film morphological structure.[7] This is exemplified by the apparent disaccord between the maximum predicted charge carrier (hole) mobility, μ_h, using DFT and the experimentally measured, μ_h, in organic-thin-film-transistors (OTFTs). For instance, DFT predictions on prototypical thiophene-based semiconducting polymers such as poly(3-hexylthiophene), P3HT, and poly-2,5-bis[3-alkylthiophen-2-ylthiono(3,2-*b*)thiophene], PBTTT, give μ_h as high as 31 and 15 cm^2 V^{-1} s^{-1}, respectively, but OTFTs measurements give only up to 0.1 and 1.0 cm^2 V^{-1} s^{-1}.[8] This discrepancy suggests that substantial improvements in performance remain attainable. A key reason for this is that optoelectronic performance is largely dictated by the macroscopic thin film morphology of the π-conjugated semiconductor in the device, where upon deposition it self-assembles into complex hierarchal structures over various length scales.[9] These morphological intricacies result in a thin film that contain defect formation,[10] varying crystal structure/polymorphism,[11] domain orientation and grain boundaries,[12] or phase separation and domain crystallization in binary blends.[13] Taking into consideration that charge transport in π-conjugated semiconductors occur through fast intramolecular charge carrier migration along the π-conjugated backbone, and intermolecular hopping of charges

3

happen between conjugated segments in the π-stacking direction, attempts in predicting how charge transport is affected by the multifaceted π-π stacking self-assembly into macroscopic thin films has been particularly difficult.[14] Therefore, the need to engineer morphology control strategies to rationalize links between molecular structure, self-assembly, and function in π-conjugated semiconductors is crucial to further advance the field towards improving device performance,[15] and realizing potential unique functionalities for novel applications.[16]

1.2 Molecular engineering approaches
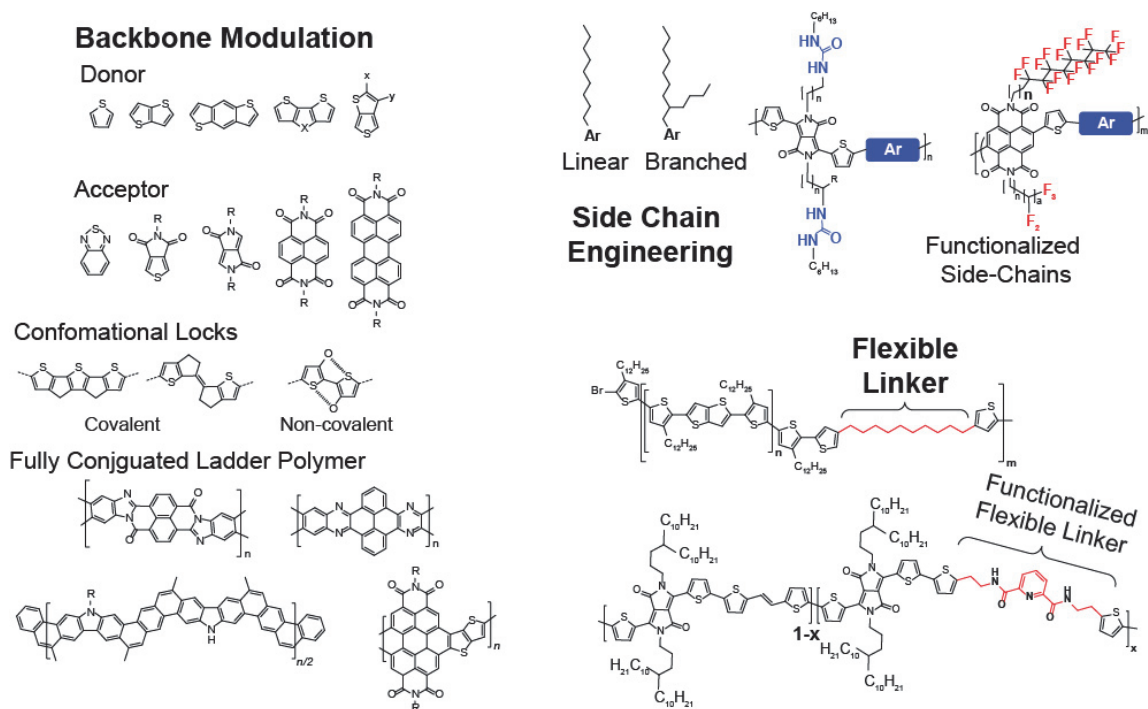
Figure 1. Molecular engineering approaches

Solution processing techniques using spin coating, meniscus-guided coating, and printing,[17] the use of processing additives such as nucleation promoters[18] and insulating polymers[19], and post-deposition treatment,[20] show a promising degree in controlling the thin film morphology. Unfortunately, these approaches are greatly influenced by extrinsic factors, *i.e.* type of substrate and solvent, evaporation rate, and processing technique, which demand an empirical approach that is non-universal towards arbitrary molecular architectures.[9] On the other hand, molecular engineering approaches directly impact the intrinsic self-assembling properties of the π-conjugated semiconductor (See Figure 1).[21] For

instance, modulating the π-conjugated backbone by introducing highly planar π-extended conjugated monomer units,[22] alternating donor and acceptor moieties,[23] restricting rotation between monomers through connecting neighbouring aromatic rings with covalent bonds, *i.e.* ladder-type polymers[24] or using non-covalent conformational locks,[25] have shown to enhance effective conjugation and π-π stacking interactions, which directly affect the *intra* and *inter* molecular charge transport respectively (See Figure 1.). Although in some cases, addition of planar co-monomer units result in a curved backbone structure that induces intermolecular steric hindrances.[26]

Secondly, the attachment of alkyl side-chains induces solubility, but at the same time depending on the size and structure, it can modulate π-π stacking of neighbouring conjugated segments (See Figure 1).[27] Linear alkyl chains minimize intermolecular steric hindrances leading to 1D co-stacking of the conjugated backbone, while branching distorts efficient stacking.[28] Interestingly, shifting the position of the branching point away from the conjugate core induces extremely short π-π stacking distances without comprising solubility[29]. In addition, inducing ordering by hydrogen bonding of urea containing groups,[30] or functionalizing side chains *via* fluorinated alkyl chains with strong self-organization,[31] have shown to drive a high degree of order between π-conjugated segments. However, despite the potential of side-chain engineering in affecting self-assembly, π-π stacking interactions still dominate the overall supramolecular assembly.[32]

1.3 Introduction of conjugation break spacers (flexible linkers) between π-conjugated segments
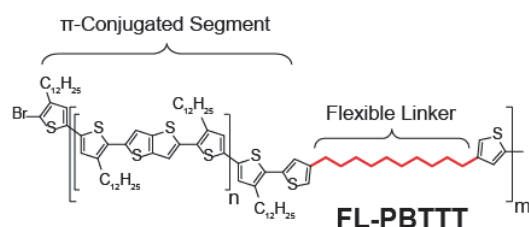
Scheme 1. Representative chemical structure a flexibly linked polymer FL-PBTTT to indicate the inclusion of conjugation break spacers (flexible linkers) between π-conjugated segments of a low molecular weight PBTTT polymer.

Another interesting method to control the supramolecular assembly without altering the semiconducting core is *via* covalent tethering of the π-conjugated segments with a flexible conjugation break spacer (See Scheme 1.).[33] Intuitively, the inclusion of flexible linkers (which are electrically insulating) could disrupt the effective conjugation across the π-conjugated backbone, and create high degrees of conformational freedom and disorder between the π-conjugated segments. Technically, this should negatively impact charge transport, but recent demonstrations highlighted below show otherwise. More importantly, the employment of these flexible linkers that break continuous backbone conjugation has recently shown promising effects by easing backbone rigidity to enhance processability, and offer unique self-assembly motifs for efficient device performance.[34]

1.3.1 Improving connectivity between π-conjugated segments for efficient charge transport
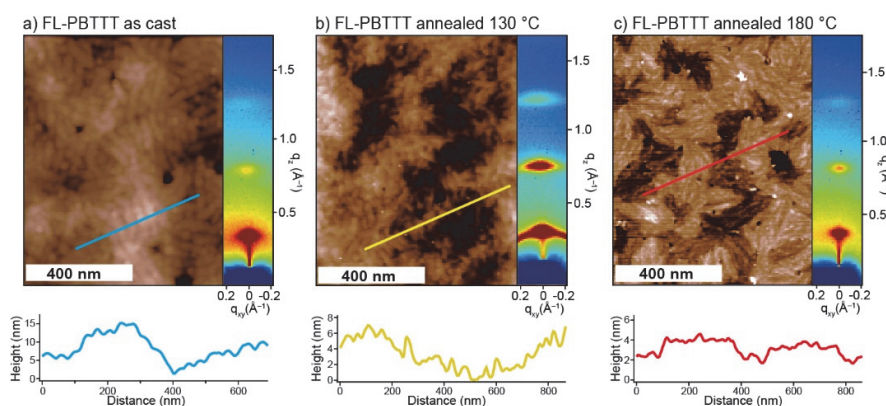
Figure 2. Tapping mode AFM topography of: a) FL-PBTTT as cast from o-dichlorobenzene 20 mg mL^{-1}, b) FL-PBTTT after annealing at 130°C, and c) after annealing at 180°C. The topographical profile along the indicated diagonal line in each case is shown below. The right side of each panel shows the 2D grazing –incidence x-ray diffraction plots of the same films with the vertical direction corresponding to the out-of-plane scatting vector, q_z, and the horizontal direction corresponding to q_{xy}. Red areas represent the highest scattering intensity while blue represent the lowest. Adapted from Ref. [34d] © The Royal Society of Chemistry 2014.

An example by Sivula and co-workers used the flexible linker approach to investigate the relationship between self-assembly and charge transport in PBTTT.[34d] Short low molecular weight PBTTT segments were ensembled into the flexibly-linked FL-PBTTT structure shown in Scheme 1 (with n = 10-12, m = 4-5). The FL-PBTTT was found to exhibit distinct thin-film morphologies (from rod-like fibrils, to terraces, see Figure 2) by just changing the processing condition and without changing the molecular weight or the length of the conjugated segments. In OTFTs, changing the film morphology gave rise to an

improvement of the charge carrier mobility from fibril-type (0.01 cm^2 V^{-1} s^{-1}) to terrace morphologies (0.04 cm^2 V^{-1} s^{-1}), while actually decreasing the overall crystallinity of the film (see 2D grazing-incidence X-ray diffraction plots in Figure 2). When compared to a fully-conjugated, high molecular weight PBTTT sample, the result suggest that the high μ_h of PBTTT is not solely due to improved intramolecular transport (thought to be caused by increasing the linearity of the chains[35]), but that the 2D charge-transport network afforded by the self-assembly significantly contributes to the observed high charge carrier mobility.

In contrast, it should be noted that recent high-performance polymers with increasingly sophisticated monomeric moieties such as napthelenediimides,[36] diketopyrollopyrole,[37] and carbazoles,[38] do not show long range crystalline order like P3HT and PBTTT but exhibit superior μ_h over 1cm^2 V^{-1} s^{-1}.[39] Despite their seemingly disordered morphology, these polymers do, however, exhibit solid-state aggregation consistent with improved intramolecular associations (indicative from resolvable vibronic progression near the absorption edge, and red shifting in their optical absorption spectra).[40] Thus, these recent results point to the conclusion that short-range ordering of the aggregates seems sufficient for efficient charge transport, so long as the aggregates are interconnected due to the nature of multiple trapping and release charge hopping mechanism between intermolecular and intramolecular charge transport of the aggregated domains.[41] Therefore, based on the discussion above, it may be said that the unifying requirement for efficient charge mobility is not to induce high crystallinity in the conjugated polymer film, but to improve the interconnectedness between aggregated domains, and reduce the amount of disorder within conjugated segments to facilitate intra- and intermolecular charge transport on the macroscopic level.
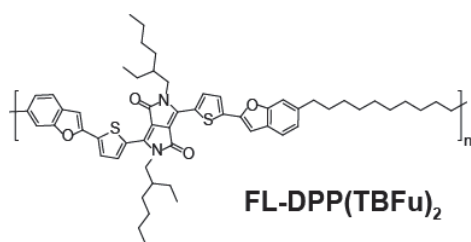
FL-DPP(TBFu)₂

Scheme 2. Chemical Structure of a flexibly polymer, FL-DPP(TBFu)$_2$, used to control the morphology of its parent small-molecule semiconductor, DPP(TBFu)$_2$.
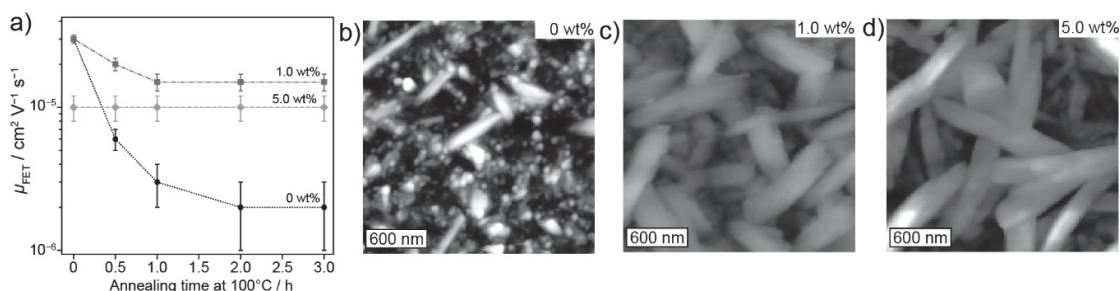
Figure 3. Thin film transistor performance and morphology of FL-DPP(TBFu)$_2$. Panel (a) shows the average extracted field effect mobility as a function of annealing time at 100°C for transistors of DPP(TBFu)$_2$ with added FL-DPP(TBFu)$_2$ at the wt% indicated. Atomic force micrographs (b-d) show the topology of the thin film transistor active layer after 3.0 hours at 100°C. Adapted from Ref. [33b] © 2015 WILEY-VCH Verlag GmbH & Co. KGaA.

The flexible linker strategy is very useful in this regard to improve connectivity in thin films of small molecule semiconductors. Indeed, while solution processesable small molecule semiconductors have purported advantages over polymer semiconductors, including synthetic simplicity and the ability to remove batch-to-batch variations,[42] they typically suffer from similar drawbacks to small low molecular weight conjugated polymers (i.e. a strong tendency to self-assemble into crystalline domains which results in film dewetting, unpredictable crystallite sizes, and grain boundaries) that confound the morphological control and charge transport in devices fabricated from these materials. The same authors applied the flexible linker concept with a common molecular semiconductor, 3,6-bis(5-(benzofuran-2-yl)thiophen-2-yl)-2,5-bis(2-ethylhexyl)-2,5-dihydropyrrolo[3,4-*c*]pyrrole-1,4-dione, and prepared the flexibly-linked version, FL-DPP(TBFu)$_2$ (See Scheme 2).[33b] OTFTs prepared with pure FL-DPP(TBFu)$_2$ showed no measureable μ_h in contrast to FL-PBTTT, likely due to a higher fraction of insulating alkyl groups. However, as-cast films of the FL-DPP(TBFu)$_2$ blended with the parent small molecule, DPP(TBFu)$_2$, gave interesting results when subjected to thermal stress (at 100°C) for an

extended period of time (See Figure 3a). The measured μ_h was found to decrease by an order of magnitude for the film of pure DPP(TBFu)$_2$ (0 wt %). However, a considerably smaller decrease is observed when 1 wt% of the FL-DPP(TBFu)$_2$ was added, and notably at 5 wt%, μ_h remained constant. The active layer morphology of these devices, after the extended thermal stress test, showed a drastic difference when adding the FL-DPP(TBFu)$_2$ (see Figure 3b-d). While the pure DPP(TBFu)$_2$ (0 wt%) device exhibited small circular domains (ca. 100-200 nm), and only a few long crystalline shards, the films containing 1 and 5 wt% of FL-DPP(TBFu)$_2$ exhibited large banded features of 200-500 nm in width and more than microns in length. These morphological observations, together with the transistor device thermal stability data show clearly that the FL-DPP(TBFu)$_2$ actively participates in the stabilization of the thin-film charge transport network. Given the polymeric structure of the FL-DPP(TBFu)$_2$, a plausible explanation for the observed behaviour suggests that the FL-DPP(TBFu)$_2$ was acting as a tie molecule to bridge adjacent crystal domains, effectively locking-in the active layer morphology.

1.3.2 Tuning processability and self-assembly motifs

Another notable aspect of the flexible linker strategy is the ability to tune the processabililty of the π-conjugated semiconductor (see chemical structure in Scheme 3). Bao and co-workers recently showed that the incorporation of non-conjugated flexible linkers into an isoindigo based semiconducting polymer coded Pil2T-X affected the processability of this material through modulating its viscoelastic properties.[34f] Rheometry and dynamic mechanical analysis revealed that solution viscosity is directly proportional to the content of non-conjugated linkers in the polymer backbone. The measured μ_h in OTFTs achieved unexpectedly high carrier mobilities despite having a non-fully conjugated polymer backbone. Notable, due to enhanced solubility, solution shearing (a method used to coat large-area substrates) of an all-polymer solar cell using Pil2T-X as donor polymer with a perylenediimide (PDI) polymer acceptor, achieved reasonable power conversion efficiency values of 3.7%.
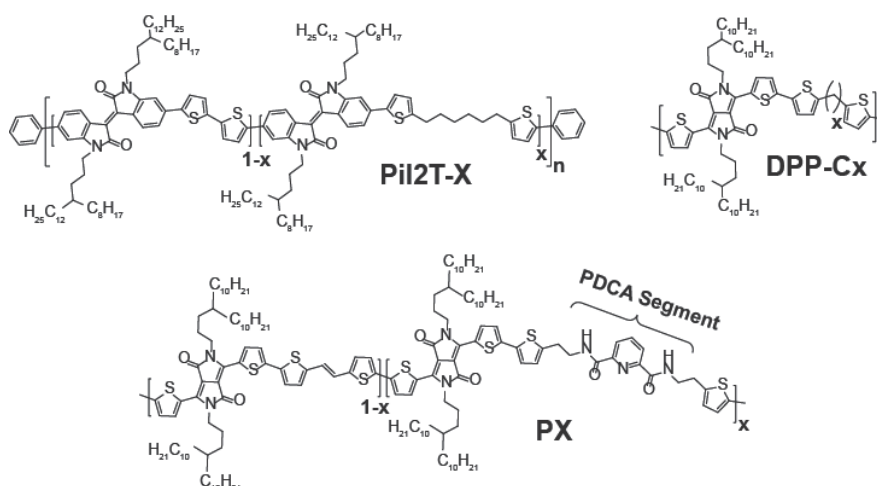
Scheme 3. Chemical Structures of flexibly linked polymers used to tune processability and induce unique self-asssembly motifs in polymer thin film devices; Pil2T-X – modulating viscoelastic properties, DPP-Cx – altering thermal transition for Melt Processing, and PX – inducing stretchable and self-healing properties.

Another example by Mei and co-workers demonstrated that the inclusion of flexible linkers into the conjugated backbone of diketopyrrolopyrole (DPP)-based semiconducting polymer coded DPP-CX (see chemical structure in Scheme 3) had a profound influence on its melting transition, and that blending of the polymer containing non-conjugated linkers, DPP-C5, as a matrix with its fully-conjugated counterpart, DPP-C0, which functions as a tie-chain, improves charge transport .[34g, 34h] The blend matrix was shown to impart strong intermolecular interactions between the components that stabilize its morphology, and permit melt processing of the polymers with excellent charge mobilities.[34i]

Furthermore, a unique functionalized FL-linker design concept presented by Bao and co-workers induced an intrinsic stretchability, and self-healing properties in OFETs based on a flexible DPP based conjugated polymer (see chemical structure PX in Scheme 3),.[34k] The chemical moiety, 2,3-pyridine dicarboxamide (PDCA) functionalized with alkyl spacers was introduced into the backbone of the DPP polymer as a flexible conjugation break spacer, which promoted dynamic non-covalent crosslinking in the polymer network due to the presence of moderate hydrogen-bonding between the amide groups. The authors proclaimed that the non-covalent crosslinking moieties undergo an energy dissipation mechanism though the breakage of hydrogen bonds when strain is applied, which preserves charge transport mobility and is able to recover it even after a hundred cycles at 100% applied strain.

1.3.3 Flexibly linking π-conjugated components in donor:acceptor bulk heterojunctions
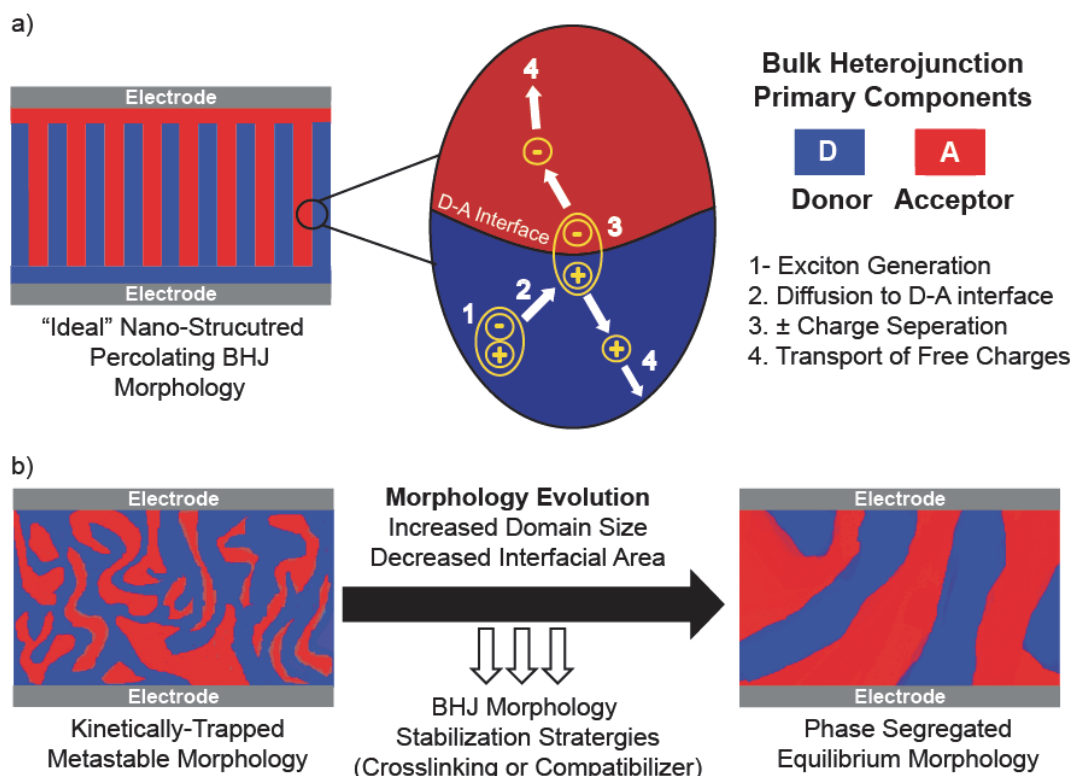
Figure 4. a) Schematic representation of an ideal bulk heterojunction active layer morphology and a basic description of the charge generation process: An exciton is first generated upon photon absorption either at the donor or/and acceptor (1). The Exciton is then required to diffuse to the donor-acceptor interface (2) to undergo charge separation of its tightly bound hole-electron pair (3), to generate free charges that will transport to their respective electrodes, where the holes will diffuse through the donor phase, and the electron in the acceptor phase (4); b) A schematic of a bulk heterojunction morphological evolution from an intimately mixed donor-acceptor kinetically-trapped metastable state towards a phase segregated thermodynamic equilibrium morphology with large domain sizes and lower interfacial area.

In the case for organic photovoltaics (OPV), an electron donating component (p-type conjugated small-molecule or polymer), and an electron accepting component (most often a small molecule n-type fullerene, but an n-type semiconducting polymer can also be used[43]) are blended together and cast into an active layer. Ideally the donor and acceptor must be intimately mixed on the length scale of tens of nanometres, which is the typical distance that a bound-electron hole pair (an exciton) can diffuse, to afford efficient free charge separation at the donor-acceptor interface (See Figure 4a). However the donor and acceptor components must also be sufficiently de-mixed to allow for the continuous transport of free charges generated at the donor:acceptor heterojunction to their

respective electrodes. Accordingly, the performance of an OPV is highly dependent on the morphology of this "bulk-heterojunction" (BHJ)[44] and, in order to gain appreciable control over the degree of phase segregation and the overall BHJ morphology, an understanding of both kinetic and thermodynamic factors of the self-assembly are required. [9, 13, 45]

Numerous strategies have been investigated to control the BHJ morphology such as the use of processing additives,[18, 46] and thermal,[47] or solvent annealing.[48] However, these approaches do not change the fundamental limitation of a multicomponent BHJ: the mixed components are kinetically trapped in a metastable morphology given that the thermodynamic equilibrium is that of phase separated domains with a minimum interfacial area, and thus minimal free charge generation (See Figure 4b).[49] While crosslinking[50] of the BHJ network triggered by an external stimuli (e.g. heat or light) of functional groups (e.g. oxetane, bromo, vinyl, or azide) incorporated on the solubilizing alkyl side chain,[51] or using small molecule additives,[50, 52] can effectively kinetically trap the morphology, this comes at the expense of a decrease in performance due to the introduction of charge trapping defects from the crosslinking reactions.[50a, 53]

The flexible linking approach is again useful in this regard, whereby phase segregation of the BHJ (especially under thermal stress) can be supressed without significant losses in device performance. McCulloch and co-workers synthesized a fullerene dumbbell dimer, (PCB)$_2$C$_2$ (see chemical structure in Scheme 4), by bridging the ester functional group on PCBM with an alkyl spacer, and used it as an additive in a BHJ blend of a polymer donor and fullerene acceptor[54]. The additive was able to improve device lifetimes efficiencies by 20% as compared to blends without the additive, which dramatically increased the BHJ morphological stability by inhibiting the formation of micron-scale crystallites of the fullerene acceptor under prolonged thermal annealing. Similarly, Sivula and co-workers also prepared two distinct dimer small molecules with a varied linker position relative to the orientation of the DPP(TBFu)$_2$ conjugated core (see chemical structure in Scheme 4).[55] The dimer with a "vertically" linked orientation, V-(DPP)$_2$, exhibited poor crystallinity in neat films, but improved the hole mobility in OFETs

by 10-fold, when used as an additive with the primary DPP(TBFu)$_2$ molecule. On the other hand, the dimer with a "horizontal" linking orientation, H-(DPP)$_2$, had no significant effect in charge carrier transport, but is found to induce BHJ thermal stability in DPP(TBFu)$_2$:PCBM blends in OPVs (See figure 5a). The device performance retained 90% of its initial conversion efficiency after 5 hours of thermal treatment, compared to a 45% retention for the devices without the dimer additive.
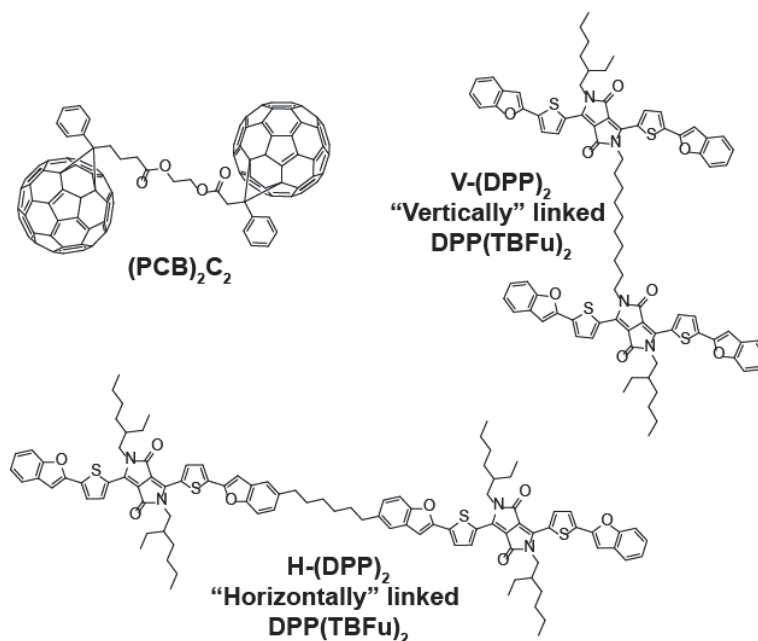
Scheme 4. Chemical Structures of flexibly linked small-molecule semiconductors: (PCB)$_2$C$_2$, and the "horizontally" and "vertically" linked DPP(TBFu)$_2$.

Thin film BHJ morphologies without H-(DPP)$_2$ revealed distinct aggregate formation as shown in figure 5b, while with 10wt% of H-(DPP) a relatively featureless thin film was observed in figure 5c. The polymeric version of H-(DPP)$_2$, FL-DPP(TBFu)$_2$ (See Scheme 2,) as previously mentioned in section 1.3.1, also demonstrated the ability to stabilize the BHJ network of DPP(TBFu)$_2$:PCBM.[56] Similarly, FL-DPP(TBFu)$_2$ was able to control the crystallization of the primary donor DPP(TBFu)$_2$, which is known to drive the phase segregation in the BHJ blend,[57] by preventing sever phase segregation under prolonged thermal annealing at 100°C. This can be observed in the morphological characterization of the BHJ blend films, where the topography and young modulus mapping via AFM showed similar intermixed BHJ morphology between as cast films and after 22 hours at 100°C with 1.5wt% of FL-DPP(TBFu)$_2$ (See

Figure 5d and e). On the other hand, with 0wt% the BHJ morphology indicated a homogenous morphology containing primarily of circular domains of DPP(TBFu)$_2$ (See figure 5f), suggesting a severe phase segregation of the components. This correlated well with preservation of device performance for the BHJ with FL-DPP(TBFu)$_2$ (See figure 5e). Despite the aforementioned approaches showing great promise in slowing down the kinetics of phase segregation by controlling the crystallization of the one of the components in a binary BHJ blend, the morphology is still fundamentally in a non-equilibrium metastable state.
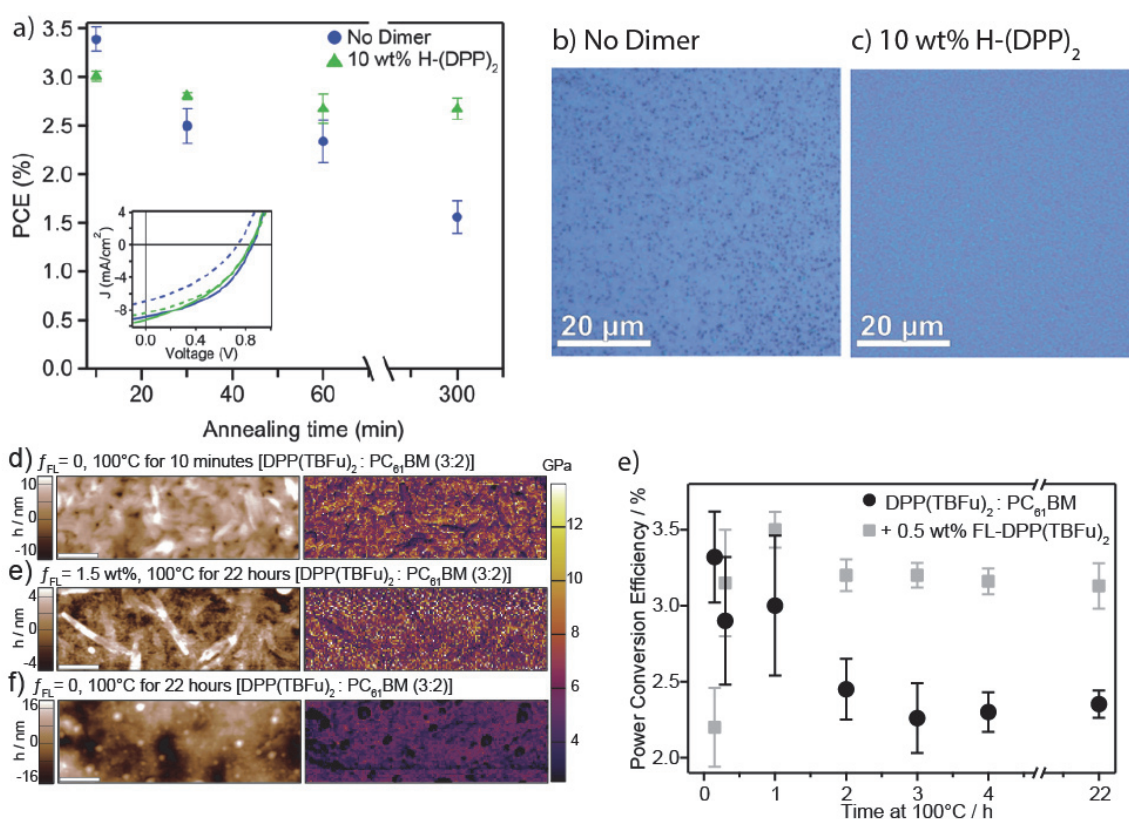
Figure 5. BHJ stability of DPP(TBFu)$_2$:PC$_{61}$BM devices with flexibly linked DPP(TBFu)$_2$ derivatives: H-(DPP)$_2$ and V-(DPP)$_2$; a) OPV power conversion efficiency as a function of the active layer annealing time at 100°C of BHJs with no dimer and with 10wt% of H-(DPP)$_2$ (The inset shows the J-V curves of the respective devices annealed for 10 min (solid-lines) and 5 h (broken lines) with (green) and without (blue) addition of 10wt% of H-(DPP)$_2$); Optical micrographs of BHJ with b) no dimer and with c) 10wt% of H-(DPP)$_2$ after thermal annealing. Figures are adapted from Ref.[55] © 2017 The Royal Society of Chemistry. BHJs with FL-DPP(TBFu)$_2$; d-f) BHJ topography (left panels) and Young's modulus mapping (right panels) of the corresponding area (The scale bars are 500nm), and PCE as a function of the active layer annealing time at 100°C of devices with 0wt% and 0.5wt% of FL-DPP(TBFu)$_2$. Figures are adapted from Ref. [33b] © 2015 WILEY-VCH Verlag GmbH & Co. KGaA.

1.4 Bulk heterojunctions using block-copolymers

An emerging strategy that has the potential to afford thermodynamically stable morphologies with ideal donor:acceptor phase separated nanostructures is the use of donor-*block*-acceptor copolymers as either compatibilizing additives,[58] or a single-component BHJ.[59] This prevalent interest stems from the nature of the self-assembling behaviour of traditional (non-semiconducting) commodity block copolymers (BCPs), where the incompatibility of the individual blocks drives morphological phase segregation to minimize surface energy, while the covalent linkage between the respective blocks prevents macroscopic separation, or it can compatibilize a binary blend by enhancing interfacial interaction between the components to control the degree of phase segregation[60]. Based on this behaviour, domain size can be tuned to the length scales for preferential exciton diffusion, while maintaining continuous pathways to enable charge extraction for efficient device performance.[61]

1.4.1 Compatibilizer Approach
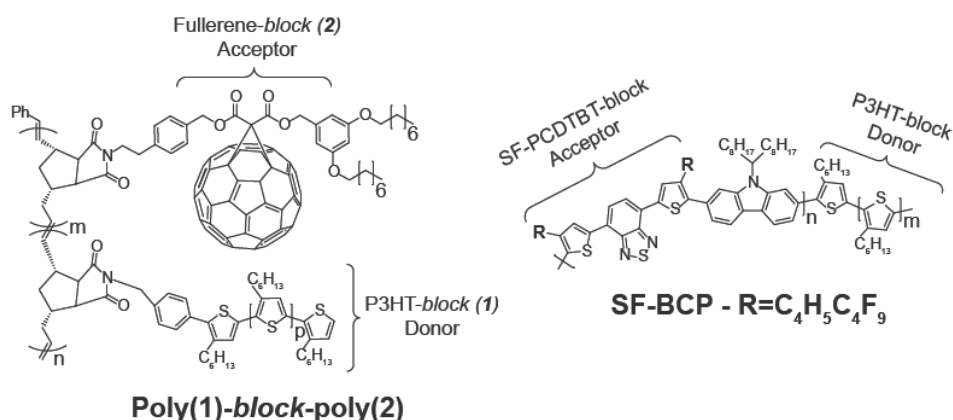
Scheme 5. Chemical structure of amphiphilic diblock copolymer compatibilizer, Poly(1)-*block*-poly(2) used in a BHJ blend of P3HT:PCBM OPVs, and fully-conjugated block copolymer containing fluorinated side-chains for melt-annealed compatibilized BHJ blends of all-polymer OPV of P3HT:PCDTBT.

Pioneering experiments by Frechet and co-workers in 2006 demonstrated the design and use of an amphiphilic diblock copolymer compatibilizer comprised of a P3HT donor block in one segment and fullerene pendants in the other segment for P3HT:PCBM based OPVs (See Chemical structure in Scheme 5).[62] As cast BHJ morphologies, with and without the compatibilizer exhibited similar characteristics, but upon thermal annealing, BHJ blends without the compatibilizer resulted in the

growth of aggregate formation that degraded device performance. In contrast, with suitable amounts of the compatibilizer in the BHJ blend, the interfacial energy between the donors and acceptor components was lowered, such that no detectable phase segregation and decrease in device performance was observed after annealing over a period of ten hours.

Recently, this concept was applied onto an all-polymer BHJ blend by Sommer and co-workers,[63] using a fully-conjugated BCP compatibilizer, coded SF-BCP, which is based on a P3HT donor block and an ambipolar semiconducting polymer, coded PCDTBT as an acceptor (See chemical structure in scheme 5). The authors revealed that efficient compatibilization during melt annealing is only feasible when the PCDTBT polymer is functionalized with fluorinated side chains in order to increase the Flory-Huggins interaction parameter between the donor and acceptor polymer components. This resulted in the control over phase segregation into thermodynamically stable donor-acceptor BHJ assembly, by modulating the amount of SF-BCP compatibilizer in the blend. Furthermore, the photovoltaic performance of compatibilized blends performed significantly better than pristine BHJ blends, which had large phase segregated domains non-ideal for device performance. Despite demonstrating the benefits of compatibilizing all-conjugated semicrystalline polymer blends for OPVs, it highlights a key drawback of semiconducting BCPs, where the lower degree of polymerization and similarities in its backbone architecture (restricted by limitation of its synthesis – discussed in the next section[64]), result in increased miscibility of individual blocks, which prevents preferential macrophase segregation for efficient device performance.[61a]

1.4.2 Single-component Active layer
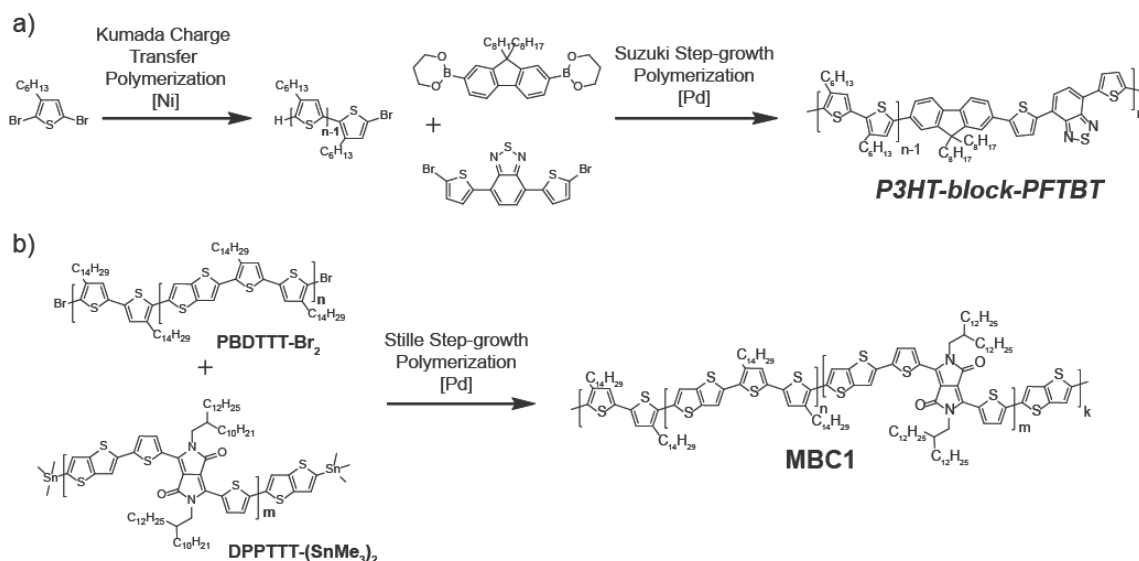
Scheme 6. Schematic of the synthetic routes used to obtain full-conjugated block copolymers: a) Two step approach using living charge transfer polymerization (CTP) of the P3HT homopolymer donor block, and a chain extension of the acceptor block using Suzuki step-growth polymerization to obtain P3HT-*block*-PFTBT, which obtained 3% PCE as shown by Gomez and co-workers;[61b] b) A di-functionalized macromonomer approach to obtain MBC1 as described by Sivula and co-workers.[65]

The use of semiconducting BCPs as a single-component BHJ for OPV was impressively demonstrated by Gomez and co-workers, using a P3HT-*block*-PFTBT (see structure in Scheme 6).[61b] Resonant soft X-ray scattering (RSOXS) allowed the authors to illustrate the phase segregation of the blocks at the ca. 10 nm length scale (Figure 6a), giving a reasonable approximation of an ideal BHJ (See Figure 4a). The champion OPV device prepared with the P3HT-*block*-PFTBT material gave a modest 3% overall solar power conversion efficiency (PCE) under 1 sun conditions (compared to over 10% demonstrated to date with optimized and separate donor and acceptor materials),[66] establishing the benchmark performance for semiconducting BCPs as a single-component solar cell that provides a clear pathway for enhancing efficiencies in fully conjugated block copolymers devices.

However, a limitation in the PCE of fully-conjugated BCPs for OPVs, is the use of high bandgap P3HT as a donor block, while current state-of-the-art binary donor-acceptor BHJ blends OPV, utilizes high efficiency low-band gap copolymers,[66-67] which rely on step-growth polycondensation that is unsuitable for the formation of BCPs, where it inevitably leads to a mixture of products composed

homo polymers, diblock and multi-block copolymers. Conversely, the synthesis of P3HT is able to afford well-defined, narrow molecular weight, and precise end-capping blocks through the use of quasi-living catalyst transfer polymerization (CTP) methods that are ideal for the formation of BCPs (See Scheme 6a for the example based on P3HT-*block*-PFTBT mentioned earlier).[64] The subsequent acceptor block is typically attached by a chain extension reaction using metal-mediated cross-coupling polymerization reactions such as Yamamoto,[68] Stille,[69] Suzuki,[70] or direct arylation polycondensation.[71] Nonetheless, significant developments in catalytic design have shown the induction of living chain-growth polymerization for electron deficient units.[72] or transforming step-growth to chain growth reactions.[73]

Despite the disadvantage of step-growth polymerization, recent reports have perused this method to obtain BCPs without P3HT,[74] by utilizing di-functionalized macromonomers to give multi-block copolymers. The clear advantage of this method is that each block can be prepared separately and purified before the final polymerization, but preparing pure functionalized macromonomers remains a major challenge. Recently, Sivula and co-workers used preparatory size exclusion chromatography to facilitate the preparation of pure macromonomers to synthesize an alternating multi-BCP with a di-brominated PBTTT blocks for the donor, and a di-stannylated DPP based polymer as the acceptor[65]. The polymer, coded MBC1 (see Scheme 6b) with n = 14, m = 5 and k = 6-8, demonstrated nanoscopic phase domain separation visualized by AFM (Figure 6b) that gave a domain spacing of about 50 nm (Figure 6c) consistent with the length of PBTTT used (40 nm). Reasonable charge transport across the active layer was observed with a μ_h of 0.08 cm^2 V^{-1} s^{-1} (compared to 9.0 × 10^{-3} cm^2 V^{-1} s^{-1} and 5.0 × 10^{-4} cm^2 V^{-1} s^{-1}, for the parent donor and acceptor macromonomers). Unfortunately, successful demonstration in OPV devices was not accomplished with MBC1, likely due to the less than ideal energetics of the donor:acceptor combination.
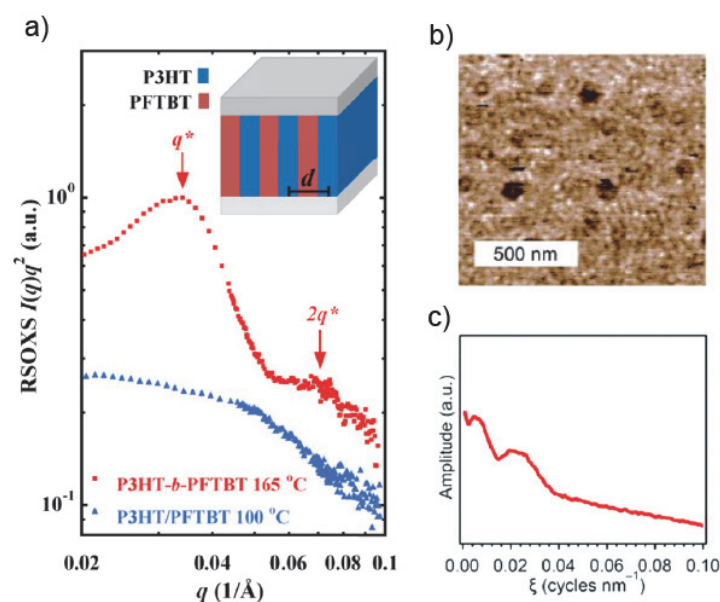
Figure 6. Fully-conjugated block copolymers used as single component BHJ for OPVs: (a) Comparison of the morphology in the active layers of optimized P3HT-b-PFTBT and P3HT/PFTBT photovoltaic devices using RSOXS. Scattering data are presented as a Kratky plot of I(q)q² vs q, where I(q) is the scattering intensity and q is the scattering vector. In optimized P3HT-b-PFTBT samples, a well-defined primary peak, q* (~0.035 Å⁻¹), and second-order reflection, 2q*, are identified. Schematic illustration of the lamellar morphology is shown in the inset with the average domain spacing indicated as *d*. This is taken from Ref. [61b] used with permission © 2013 American Chemical Society; (b) Characterization of the self-assembly of MBC1 showing the phase image from a tapping mode AFM image, and (c) shows the amplitude of the spatial frequency from the FFT of (b), which are adapted from Ref. [65] © The Royal Society of Chemistry 2017.

Nonetheless, the successful demonstration of an all-conjugated non-P3HT donor-acceptor block copolymer will open the door for further design of the next generation of semiconducting polymers with thermodynamically stable nano-scopic morphology and properties that are fully tunable by changing the block structure and length. Moreover, understanding how such polymeric structures self-assemble into stable equilibrium morphologies will address the problem of phase segregation as mentioned earlier, and allowing predictability in processing of such materials into thin films[75]. Furthermore, the further development of living polymerization methodologies to a wider range of monomeric units would also be crucial to obtain well-defined block-copolymers.[64, 72-73]

1.5 Objective of Thesis

So far this chapter has highlighted several key challenges that need to be addressed. Solution processing techniques have demonstrated great control over the self-assembly of these materials, but are still governed by extrinsic factors that rely on empirical approaches which are non-arbitrary to a specific molecular structure. A method that intrinsically affects the self-assembly of π-conjugated semiconductors is the molecular engineering of its chemical structure (see Figure 1): 1) backbone modulation of the monomeric units along the π-conjugation system, 2) side-chain engineering, which aids in processability into thin films and 3) flexible linker strategy that involves the introduction of conjugation break spaces between conjugated segments in the chemical structure.

Given that the chemical structure of the π-conjugated semiconductor directly impacts both the self-assembly and it fundamental optoelectronic properties, molecular engineering seems to be the most promising approach to address the aforementioned challenges. However, due to the vast library of semiconductors that have been synthesized, a general versatile strategy is needed to link morphology and device performance. Based on the various molecular engineering approaches, the flexible linker strategy has demonstrated control over supramolecular assembly without significantly altering the semiconducting core of the π-conjugated semiconductor. Therefore, this approach could be applied to a variety of well-established high performing semiconductors.

In this thesis, the objective is focused primarily on an extension of the flexible linker method that has been discussed earlier. Previously, our group pioneered the work based on this approach using prototypical polymer and small molecule semiconductors such as PBTTT and DPP(TBFu)$_2$ (See section 1.3.1 and 1.3.3). The results presented have shown that the flexible linker strategy is able to control morphology and stabilize the charge transporting network on these materials. However, the flexibly linked materials were designed to affect the self-assembly of a single conjugated component in active layer, either as an additive to its parent (non-flexibly linked) semiconductor, or as a semiconductor in itself. Herein this thesis the flexible linker method would be used to control the self-assembly of two

active components in a multi-comnponent BHJ blend, by linking the donor and acceptor π-conjugated components with an aliphatic spacer, and using it as a compatibilizing additive.

Chapter 2 will first elucidate an understanding of morphology stabilization strategies commonly applied to polymer BHJ systems onto small molecule BHJs. A novel in-situ linker with an azide active group and a molecular compatibilizer was synthesised, and used as an additive to stabilize the morphology of a prototypical small molecule BHJ based on DPP(TBFu)$_2$:PCBM, and reveal the effect on its photovoltaic device performance and BHJ thermal stability. Subsequently, in Chapter 3 the compatibilizer strategy will be reinforced on a challenging small molecule BHJ system that utilizes components that are highly crystalline, such as a non-fullerene acceptor, EP-PDI, and DPP(TBFu)$_2$ as a donor. After establishing the versatility of the compatbilizer strategy to stabilize small molecule BHJ systems under harsh thermal conditions, the approach is then applied onto a melt-processing of the BHJ in chapter 4, where insights into the prerequisites for solvent-free solid-state processing of small molecules binary BHJs are revealed. Finally chapter 5 presents a slightly different approach towards controlling the self-assembly of donor-acceptor BHJs is presented. As discussed in section 1.4, truly thermodynamically stable BHJ morphologies can be achieved using block copolymers, but current synthetic methodologies using quasi-living polymerization methods limit its usage to a wider range of monomeric units. This chapter will present a modular synthetic methodology using Heck coupling between di-functionalised macromonomers for the formation of a fully-conjugated block copolymer and its application in OPVs.

1.6 References

1.   Thejo Kalyani, N.; Dhoble, S. J., Organic light emitting diodes: Energy saving lighting technology—A review. *Renewable and Sustainable Energy Reviews* **2012,** *16* (5), 2696-2723.

2.   Sirringhaus, H., 25th Anniversary Article: Organic Field-Effect Transistors: The Path Beyond Amorphous Silicon. *Advanced Materials* **2014,** *26* (9), 1319-1335.

3.   Kang, H.; Kim, G.; Kim, J.; Kwon, S.; Kim, H.; Lee, K., Bulk-Heterojunction Organic Solar Cells: Five Core Technologies for Their Commercialization. *Advanced Materials* **2016,** *28* (36), 7821-7861.

4.   Someya, T.; Bao, Z.; Malliaras, G. G., The rise of plastic bioelectronics. *Nature* **2016,** *540* (7633), 379-385.

5.   (a) Morin, P.-O.; Bura, T.; Leclerc, M., Realizing the full potential of conjugated polymers: innovation in polymer synthesis. *Materials Horizons* **2015**; (b) Beaujuge, P. M.; Fréchet, J. M. J., Molecular Design and Ordering Effects in π-Functional Materials for Transistor and Solar Cell Applications. *Journal of the American Chemical Society* **2011,** *133* (50), 20009-20029.

6.   (a) Anthony, J. E., Organic electronics: Addressing challenges. *Nat Mater* **2014,** *13* (8), 773-775; (b) Street, R. A., Unraveling Charge Transport in Conjugated Polymers. *Science* **2013,** *341* (6150), 1072-1073.

7.   (a) Brédas, J. L.; Calbert, J. P.; da Silva Filho, D. A.; Cornil, J., Organic semiconductors: A theoretical characterization of the basic parameters governing charge transport. *Proceedings of the National Academy of Sciences* **2002,** *99* (9), 5804-5809; (b) Zhan, C.-G.; Nichols, J. A.; Dixon, D. A., Ionization Potential, Electron Affinity, Electronegativity, Hardness, and Electron Excitation Energy: Molecular Properties from Density Functional Theory Orbital Energies. *The Journal of Physical Chemistry A* **2003,** *107* (20), 4184-4195; (c) Oberhofer, H.; Reuter, K.; Blumberger, J., Charge Transport in Molecular Materials: An Assessment of Computational Methods. *Chemical Reviews* **2017,** *117* (15), 10319-10357.

8.   Northrup, J. E., Atomic and electronic structure of polymer organic semiconductors: P3HT, PQT, and PBTTT. *Physical Review B* **2007,** *76* (24), 245202.

9.   Hiszpanski, A. M.; Khlyabich, P. P.; Loo, Y.-L., Tuning kinetic competitions to traverse the rich structural space of organic semiconductor thin films. *MRS Communications* **2015,** *5* (3), 407-421.

10.   (a) Mikhnenko, O. V.; Kuik, M.; Lin, J.; van der Kaap, N.; Nguyen, T.-Q.; Blom, P. W. M., Trap-Limited Exciton Diffusion in Organic Semiconductors. *Advanced Materials* **2014,** *26* (12), 1912-1917; (b) Liscio, F.; Albonetti, C.; Broch, K.; Shehu, A.; Quiroga, S. D.; Ferlauto, L.; Frank, C.; Kowarik, S.; Nervo, R.; Gerlach, A.; Milita, S.; Schreiber, F.; Biscarini, F., Molecular Reorganization in Organic Field-Effect Transistors and Its Effect on Two-Dimensional Charge Transport Pathways. *ACS Nano* **2013,** *7* (2), 1257-1264.

11.   (a) Galindo, S.; Tamayo, A.; Leonardi, F.; Mas-Torrent, M., Control of Polymorphism and Morphology in Solution Sheared Organic Field-Effect Transistors. *Advanced Functional Materials* **2017,** *27* (25), 1700526-n/a; (b) Jones, A. O. F.; Chattopadhyay, B.; Geerts, Y. H.; Resel, R., Substrate-Induced

and Thin-Film Phases: Polymorphism of Organic Materials on Surfaces. *Advanced Functional Materials* **2016,** *26* (14), 2233-2255; (c) Diao, Y.; Lenn, K. M.; Lee, W.-Y.; Blood-Forsythe, M. A.; Xu, J.; Mao, Y.; Kim, Y.; Reinspach, J. A.; Park, S.; Aspuru-Guzik, A.; Xue, G.; Clancy, P.; Bao, Z.; Mannsfeld, S. C. B., Understanding Polymorphism in Organic Semiconductor Thin Films through Nanoconfinement. *Journal of the American Chemical Society* **2014,** *136* (49), 17046-17057.

12. (a) Rivnay, J.; Jimison, L. H.; Northrup, J. E.; Toney, M. F.; Noriega, R.; Lu, S.; Marks, T. J.; Facchetti, A.; Salleo, A., Large modulation of carrier transport by grain-boundary molecular packing and microstructure in organic thin films. *Nat Mater* **2009,** *8* (12), 952-958; (b) Proctor, C. M.; Kher, A. S.; Love, J. A.; Huang, Y.; Sharenko, A.; Bazan, G. C.; Nguyen, T.-Q., Understanding Charge Transport in Molecular Blend Films in Terms of Structural Order and Connectivity of Conductive Pathways. *Advanced Energy Materials* **2016,** *6* (9), 1502285-n/a.

13. Lee, S. S.; Muralidharan, S.; Woll, A. R.; Loth, M. A.; Li, Z.; Anthony, J. E.; Haataja, M.; Loo, Y.-L., Understanding Heterogeneous Nucleation in Binary, Solution-Processed, Organic Semiconductor Thin Films. *Chemistry of Materials* **2012,** *24* (15), 2920-2928.

14. (a) Price, S. L., Predicting crystal structures of organic compounds. *Chemical Society Reviews* **2014,** *43* (7), 2098-2111; (b) Huang, C.-F.; Wu, S.-L.; Huang, Y.-F.; Chen, Y.-C.; Chang, S.-T.; Wu, T.-Y.; Wu, K.-Y.; Chuang, W.-T.; Wang, C.-L., Packing Principles for Donor–Acceptor Oligomers from Analysis of Single Crystals. *Chemistry of Materials* **2016,** *28* (15), 5175-5190; (c) Do, K.; Ravva, M. K.; Wang, T.; Brédas, J.-L., Computational Methodologies for Developing Structure–Morphology–Performance Relationships in Organic Solar Cells: A Protocol Review. *Chemistry of Materials* **2016**.

15. Henson, Z. B.; Müllen, K.; Bazan, G. C., Design strategies for organic semiconductors beyond the molecular formula. *Nature Chemistry* **2012,** *4*, 699.

16. (a) Brandt, J. R.; Salerno, F.; Fuchter, M. J., The added value of small-molecule chirality in technological applications. *Nature Reviews Chemistry* **2017,** *1*, 0045; (b) Ke, C., A light-powered clockwork. *Nature Nanotechnology* **2017,** *12*, 504; (c) Dumur, F.; Gigmes, D.; Fouassier, J.-P.; Lalevée, J., Organic Electronics: An El Dorado in the Quest of New Photocatalysts for Polymerization Reactions. *Accounts of Chemical Research* **2016,** *49* (9), 1980-1989.

17. Diao, Y.; Shaw, L.; Bao, Z.; Mannsfeld, S. C. B., Morphology control strategies for solution-processed organic semiconductor thin films. *Energy & Environmental Science* **2014,** *7* (7), 2145-2159.

18. Treat, N. D.; Nekuda Malik, J. A.; Reid, O.; Yu, L.; Shuttle, C. G.; Rumbles, G.; Hawker, C. J.; Chabinyc, M. L.; Smith, P.; Stingelin, N., Microstructure formation in molecular and polymer semiconductors assisted by nucleation agents. *Nat Mater* **2013,** *12* (7), 628-633.

19. Scaccabarozzi, A. D.; Stingelin, N., Semiconducting:insulating polymer blends for optoelectronic applications-a review of recent advances. *Journal of Materials Chemistry A* **2014,** *2* (28), 10818-10824.

20. Hiszpanski, A. M.; Loo, Y.-L., Directing the film structure of organic semiconductors via post-deposition processing for transistor and solar cell applications. *Energy & Environmental Science* **2014,** *7* (2), 592-608.

21.   Tsao, H. N.; Mullen, K., Improving polymer transistor performance via morphology control. *Chemical Society Reviews* **2010,** *39* (7), 2372-2386.

22.   (a) Pisula, W.; Kastler, M.; Wasserfallen, D.; Mondeshki, M.; Piris, J.; Schnell, I.; Müllen, K., Relation between Supramolecular Order and Charge Carrier Mobility of Branched Alkyl Hexa-peri-hexabenzocoronenes. *Chemistry of Materials* **2006,** *18* (16), 3634-3640; (b) Zhang, L.; Rose, B. D.; Liu, Y.; Nahid, M. M.; Gann, E.; Ly, J.; Zhao, W.; Rosa, S. J.; Russell, T. P.; Facchetti, A.; McNeill, C. R.; Brédas, J.-L.; Briseno, A. L., Efficient Naphthalenediimide-Based Hole Semiconducting Polymer with Vinylene Linkers between Donor and Acceptor Units. *Chemistry of Materials* **2016**.

23.   Marszalek, T.; Li, M.; Pisula, W., Design directed self-assembly of donor-acceptor polymers. *Chemical Communications* **2016,** *52* (73), 10938-10947.

24.   Lee, J.; Kalin, A. J.; Yuan, T.; Al-Hashimi, M.; Fang, L., Fully conjugated ladder polymers. *Chemical Science* **2017,** *8* (4), 2503-2521.

25.   Huang, H.; Yang, L.; Facchetti, A.; Marks, T. J., Organic and Polymeric Semiconductors Enhanced by Noncovalent Conformational Locks. *Chemical Reviews* **2017,** *117* (15), 10291-10318.

26.   Lee, T.-H.; Wu, K.-Y.; Lin, T.-Y.; Wu, J.-S.; Wang, C.-L.; Hsu, C.-S., Role of the Comonomeric Units in Reaching Linear Backbone, High Solid-State Order and Charge Mobilities in Heptacyclic Arene-Based Alternating Copolymers. *Macromolecules* **2013,** *46* (19), 7687-7695.

27.   Mei, J.; Bao, Z., Side Chain Engineering in Solution-Processable Conjugated Polymers. *Chemistry of Materials* **2014,** *26* (1), 604-615.

28.   (a) Balakrishnan, K.; Datar, A.; Naddo, T.; Huang, J.; Oitker, R.; Yen, M.; Zhao, J.; Zang, L., Effect of Side-Chain Substituents on Self-Assembly of Perylene Diimide Molecules: Morphology Control. *Journal of the American Chemical Society* **2006,** *128* (22), 7390-7398; (b) Schroeder, B. C.; Kurosawa, T.; Fu, T.; Chiu, Y.-C.; Mun, J.; Wang, G.-J. N.; Gu, X.; Shaw, L.; Kneller, J. W. E.; Kreouzis, T.; Toney, M. F.; Bao, Z., Taming Charge Transport in Semiconducting Polymers with Branched Alkyl Side Chains. *Advanced Functional Materials* **2017,** *27* (34), 1701973-n/a.

29.   Kang, I.; Yun, H.-J.; Chung, D. S.; Kwon, S.-K.; Kim, Y.-H., Record High Hole Mobility in Polymer Semiconductors via Side-Chain Engineering. *Journal of the American Chemical Society* **2013,** *135* (40), 14896-14899.

30.   Yao, J.; Yu, C.; Liu, Z.; Luo, H.; Yang, Y.; Zhang, G.; Zhang, D., Significant Improvement of Semiconducting Performance of the Diketopyrrolopyrrole–Quaterthiophene Conjugated Polymer through Side-Chain Engineering via Hydrogen-Bonding. *Journal of the American Chemical Society* **2016,** *138* (1), 173-185.

31.   Kang, B.; Kim, R.; Lee, S. B.; Kwon, S.-K.; Kim, Y.-H.; Cho, K., Side-Chain-Induced Rigid Backbone Organization of Polymer Semiconductors through Semifluoroalkyl Side Chains. *Journal of the American Chemical Society* **2016,** *138* (11), 3679-3686.

32.   Tsao, H. N.; Cho, D. M.; Park, I.; Hansen, M. R.; Mavrinskiy, A.; Yoon, D. Y.; Graf, R.; Pisula, W.; Spiess, H. W.; Müllen, K., Ultrahigh Mobility in Polymer Field-Effect Transistors by Design. *Journal of the American Chemical Society* **2011,** *133* (8), 2605-2612.

33.   (a) Schroeder, B. C.; Li, Z.; Brady, M. A.; Faria, G. C.; Ashraf, R. S.; Takacs, C. J.; Cowart, J. S.; Duong, D. T.; Chiu, K. H.; Tan, C.-H.; Cabral, J. T.; Salleo, A.; Chabinyc, M. L.; Durrant, J. R.; McCulloch, I., Enhancing Fullerene-Based Solar Cell Lifetimes by Addition of a Fullerene Dumbbell. *Angewandte Chemie International Edition* **2014,** *53*, 12870-12875; (b) Gasperini, A.; Jeanbourquin, X. A.; Rahmanudin, A.; Yu, X.; Sivula, K., Enhancing the Thermal Stability of Solution-Processed Small-Molecule Semiconductor Thin Films Using a Flexible Linker Approach. *Advanced Materials* **2015,** *27* (37), 5541-5546; (c) Liang, Z.; Cormier, R. A.; Nardes, A. M.; Gregg, B. A., Developing perylene diimide based acceptor polymers for organic photovoltaics. *Synthetic Metals* **2011,** *161* (11–12), 1014-1021; (d) Xiang, X.; Shao, W.; Liang, L.; Chen, X.-Q.; Zhao, F.-G.; Lu, Z.; Wang, W.; Li, J.; Li, W.-S., Photovoltaic poly(rod-coil) polymers based on benzodithiophene-centred A-D-A type conjugated segments and dicarboxylate-linked alkyl non-conjugated segments. *RSC Advances* **2016,** *6* (28), 23300-23309.

34.   (a) Ding, L.; Li, H.-B.; Lei, T.; Ying, H.-Z.; Wang, R.-B.; Zhou, Y.; Su, Z.-M.; Pei, J., Alkylene-Chain Effect on Microwire Growth and Crystal Packing of π-Moieties. *Chemistry of Materials* **2012,** *24* (10), 1944-1949; (b) Zhu, X.; Traub, M. C.; Vanden Bout, D. A.; Plunkett, K. N., Well-Defined Alternating Copolymers of Oligo(phenylenevinylene)s and Flexible Chains. *Macromolecules* **2012,** *45*, 5051-5057; (c) Lin, X.; Hirono, M.; Seki, T.; Kurata, H.; Karatsu, T.; Kitamura, A.; Kuzuhara, D.; Yamada, H.; Ohba, T.; Saeki, A.; Seki, S.; Yagai, S., Covalent Modular Approach for Dimension-Controlled Self-Organization of Perylene Bisimide Dyes. *Chemistry – A European Journal* **2013,** *19*, 6561-6565; (d) Gasperini, A.; Bivaud, S.; Sivula, K., Controlling conjugated polymer morphology and charge carrier transport with a flexible-linker approach. *Chemical Science* **2014,** *5*, 4922-4927; (e) Shao, W.; Liang, L.; Xiang, X.; Li, H.-j.; Zhao, F.-g.; Li, W.-s., Changing to Poly(rod-coil) Polymers: a Promising Way for an Optoelectronic Compound to Improve Its Film Formation. *Chinese Journal of Chemistry* **2015,** *33*, 847-851; (f) Schroeder, B. C.; Chiu, Y.-C.; Gu, X.; Zhou, Y.; Xu, J.; Lopez, J.; Lu, C.; Toney, M. F.; Bao, Z., Non-Conjugated Flexible Linkers in Semiconducting Polymers: A Pathway to Improved Processability without Compromising Device Performance. *Advanced Electronic Materials* **2016,** *2* (7), 1600104-n/a; (g) Zhao, Y.; Zhao, X.; Zang, Y.; Di, C.-a.; Diao, Y.; Mei, J., Conjugation-Break Spacers in Semiconducting Polymers: Impact on Polymer Processability and Charge Transport Properties. *Macromolecules* **2015,** *48* (7), 2048-2053; (h) Zhao, X.; Zhao, Y.; Ge, Q.; Butrouna, K.; Diao, Y.; Graham, K. R.; Mei, J., Complementary Semiconducting Polymer Blends: The Influence of Conjugation-Break Spacer Length in Matrix Polymers. *Macromolecules* **2016,** *49* (7), 2601-2608; (i) Zhao, Y.; Zhao, X.; Roders, M.; Gumyusenge, A.; Ayzner, A. L.; Mei, J., Melt-Processing of Complementary Semiconducting Polymer Blends for High Performance Organic Transistors. *Advanced Materials* **2017,** *29* (6), 1605056-n/a; (j) Erdmann, T.; Fabiano, S.; Milián-Medina, B.; Hanifi, D.; Chen, Z.; Berggren, M.; Gierschner, J.; Salleo, A.; Kiriy, A.; Voit, B.; Facchetti, A., Naphthalenediimide Polymers with Finely Tuned In-Chain π-Conjugation: Electronic Structure, Film Microstructure, and Charge Transport Properties. *Advanced Materials* **2016,** *28* (41), 9169-9174; (k) Oh, J. Y.; Rondeau-Gagné, S.; Chiu, Y.-C.; Chortos, A.; Lissel, F.; Wang, G.-J. N.; Schroeder, B. C.; Kurosawa, T.; Lopez, J.; Katsumata, T.; Xu, J.; Zhu, C.; Gu, X.; Bae, W.-G.; Kim, Y.; Jin, L.; Chung, J. W.; Tok, J. B. H.; Bao, Z., Intrinsically stretchable and healable semiconducting polymer for organic transistors. *Nature* **2016,** *539*, 411.

35.   Zhang, X.; Bronstein, H.; Kronemeijer, A. J.; Smith, J.; Kim, Y.; Kline, R. J.; Richter, L. J.; Anthopoulos, T. D.; Sirringhaus, H.; Song, K.; Heeney, M.; Zhang, W.; McCulloch, I.; DeLongchamp, D. M., Molecular origin of high field-effect mobility in an indacenodithiophene–benzothiadiazole copolymer. *Nature Communications* **2013,** *4*, 2238.

36.   Sciascia, C.; Martino, N.; Schuettfort, T.; Watts, B.; Grancini, G.; Antognazza, M. R.; Zavelani-Rossi, M.; McNeill, C. R.; Caironi, M., Sub-Micrometer Charge Modulation Microscopy of a High Mobility Polymeric n-Channel Field-Effect Transistor. *Advanced Materials* **2011,** *23* (43), 5086-5090.

37.   Kronemeijer, A. J.; Gili, E.; Shahid, M.; Rivnay, J.; Salleo, A.; Heeney, M.; Sirringhaus, H., A Selenophene-Based Low-Bandgap Donor–Acceptor Polymer Leading to Fast Ambipolar Logic. *Advanced Materials* **2012,** *24* (12), 1558-1565.

38.   Beiley, Z. M.; Hoke, E. T.; Noriega, R.; Dacuña, J.; Burkhard, G. F.; Bartelt, J. A.; Salleo, A.; Toney, M. F.; McGehee, M. D., Morphology-Dependent Trap Formation in High Performance Polymer Bulk Heterojunction Solar Cells. *Advanced Energy Materials* **2011,** *1* (5), 954-962.

39.   Noriega, R.; Rivnay, J.; Vandewal, K.; Koch, F. P. V.; Stingelin, N.; Smith, P.; Toney, M. F.; Salleo, A., A general relationship between disorder, aggregation and charge transport in conjugated polymers. *Nat Mater* **2013,** *12* (11), 1038-1044.

40.   Steyrleuthner, R.; Schubert, M.; Howard, I.; Klaumünzer, B.; Schilling, K.; Chen, Z.; Saalfrank, P.; Laquai, F.; Facchetti, A.; Neher, D., Aggregation in a High-Mobility n-Type Low-Bandgap Copolymer with Implications on Semicrystalline Morphology. *Journal of the American Chemical Society* **2012,** *134* (44), 18303-18317.

41.   Pasveer, W. F.; Cottaar, J.; Tanase, C.; Coehoorn, R.; Bobbert, P. A.; Blom, P. W. M.; de Leeuw, D. M.; Michels, M. A. J., Unified Description of Charge-Carrier Mobilities in Disordered Semiconducting Polymers. *Physical Review Letters* **2005,** *94* (20), 206601.

42.   Collins, S. D.; Ran, N. A.; Heiber, M. C.; Nguyen, T.-Q., Small is Powerful: Recent Progress in Solution-Processed Small Molecule Solar Cells. *Advanced Energy Materials* **2017**, 1602242-n/a.

43.   Benten, H.; Mori, D.; Ohkita, H.; Ito, S., Recent research progress of polymer donor/polymer acceptor blend solar cells. *Journal of Materials Chemistry A* **2016,** *4* (15), 5340-5365.

44.   (a) Dimitrov, S. D.; Durrant, J. R., Materials Design Considerations for Charge Generation in Organic Solar Cells. *Chemistry of Materials* **2014,** *26* (1), 616-630; (b) Tamai, Y.; Ohkita, H.; Benten, H.; Ito, S., Exciton Diffusion in Conjugated Polymers: From Fundamental Understanding to Improvement in Photovoltaic Conversion Efficiency. *The Journal of Physical Chemistry Letters* **2015,** *6* (17), 3417-3428; (c) Brabec, C. J.; Heeney, M.; McCulloch, I.; Nelson, J., Influence of blend microstructure on bulk heterojunction organic photovoltaic performance. *Chemical Society Reviews* **2011,** *40* (3), 1185-1199.

45.   Structural Complexities in the Active Layers of Organic Electronics. *Annual Review of Chemical and Biomolecular Engineering* **2010,** *1* (1), 59-78.

46.   Lee, J. K.; Ma, W. L.; Brabec, C. J.; Yuen, J.; Moon, J. S.; Kim, J. Y.; Lee, K.; Bazan, G. C.; Heeger, A. J., Processing Additives for Improved Efficiency from Bulk Heterojunction Solar Cells. *Journal of the American Chemical Society* **2008,** *130* (11), 3619-3623.

47.   Verploegen, E.; Mondal, R.; Bettinger, C. J.; Sok, S.; Toney, M. F.; Bao, Z., Effects of Thermal Annealing Upon the Morphology of Polymer–Fullerene Blends. *Advanced Functional Materials* **2010,** *20* (20), 3519-3529.

48.   (a) Chen, H.; Hsiao, Y.-C.; Hu, B.; Dadmun, M., Tuning the Morphology and Performance of Low Bandgap Polymer:Fullerene Heterojunctions via Solvent Annealing in Selective Solvents. *Advanced Functional Materials* **2014,** *24* (32), 5129-5136; (b) Park, J. H.; Kim, J. S.; Lee, J. H.; Lee, W. H.; Cho, K., Effect of Annealing Solvent Solubility on the Performance of Poly(3-hexylthiophene)/Methanofullerene Solar Cells. *The Journal of Physical Chemistry C* **2009,** *113* (40), 17579-17584; (c) Pearson, A. J.; Wang, T.; Jones, R. A. L.; Lidzey, D. G.; Staniec, P. A.; Hopkinson, P. E.; Donald, A. M., Rationalizing Phase Transitions with Thermal Annealing Temperatures for P3HT:PCBM Organic Photovoltaic Devices. *Macromolecules* **2012,** *45* (3), 1499-1508.

49.   (a) Jørgensen, M.; Norrman, K.; Gevorgyan, S. A.; Tromholt, T.; Andreasen, B.; Krebs, F. C., Stability of Polymer Solar Cells. *Advanced Materials* **2012,** *24* (5), 580-612; (b) Fraga Domínguez, I.; Distler, A.; Lüer, L., Stability of Organic Solar Cells: The Influence of Nanostructured Carbon Materials. *Advanced Energy Materials* **2016**, 1601320-n/a.

50.   (a) Rumer, J. W.; McCulloch, I., Organic photovoltaics: Crosslinking for optimal morphology and stability. *Materials Today* **2015,** *18* (8), 425-435; (b) Wantz, G.; Derue, L.; Dautel, O.; Rivaton, A.; Hudhomme, P.; Dagron-Lartigau, C., Stabilizing polymer-based bulk heterojunction solar cells via crosslinking. *Polymer International* **2014,** *63* (8), 1346-1361.

51.   (a) Kim, H. J.; Han, A. R.; Cho, C.-H.; Kang, H.; Cho, H.-H.; Lee, M. Y.; Fréchet, J. M. J.; Oh, J. H.; Kim, B. J., Solvent-Resistant Organic Transistors and Thermally Stable Organic Photovoltaics Based on Cross-linkable Conjugated Polymers. *Chemistry of Materials* **2012,** *24* (1), 215-221; (b) Carle, J. E.; Andreasen, B.; Tromholt, T.; Madsen, M. V.; Norrman, K.; Jorgensen, M.; Krebs, F. C., Comparative studies of photochemical cross-linking methods for stabilizing the bulk hetero-junction morphology in polymer solar cells. *Journal of Materials Chemistry* **2012,** *22* (46), 24417-24423; (c) Cheng, Y.-J.; Hsieh, C.-H.; Li, P.-J.; Hsu, C.-S., Morphological Stabilization by In Situ Polymerization of Fullerene Derivatives Leading to Efficient, Thermally Stable Organic Photovoltaics. *Advanced Functional Materials* **2011,** *21* (9), 1723-1732; (d) Miyanishi, S.; Tajima, K.; Hashimoto, K., Morphological Stabilization of Polymer Photovoltaic Cells by Using Cross-Linkable Poly(3-(5-hexenyl)thiophene). *Macromolecules* **2009,** *42* (5), 1610-1618.

52.   Liu, B.; Png, R.-Q.; Zhao, L.-H.; Chua, L.-L.; Friend, R. H.; Ho, P. K. H., High internal quantum efficiency in fullerene solar cells based on crosslinked polymer donor networks. *Nat Commun* **2012,** *3*, 1321.

53.   (a) Madogni, V. I.; Kounouhéwa, B.; Akpo, A.; Agbomahéna, M.; Hounkpatin, S. A.; Awanou, C. N., Comparison of degradation mechanisms in organic photovoltaic devices upon exposure to a temperate and a subequatorial climate. *Chemical Physics Letters* **2015,** *640*, 201-214; (b) Heumueller, T.; Mateker, W. R.; Distler, A.; Fritze, U. F.; Cheacharoen, R.; Nguyen, W. H.; Biele, M.; Salvador, M.; von Delius, M.; Egelhaaf, H.-J.; McGehee, M. D.; Brabec, C. J., Morphological and electrical control of fullerene dimerization determines organic photovoltaic stability. *Energy & Environmental Science* **2016,** *9* (1), 247-256; (c) Fungura, F.; Lindemann, W. R.; Shinar, J.; Shinar, R., Carbon Dangling Bonds in Photodegraded Polymer:Fullerene Solar Cells. *Advanced Energy Materials* **2016**, 1601420-n/a.

54.   Schroeder, B. C.; Li, Z.; Brady, M. A.; Faria, G. C.; Ashraf, R. S.; Takacs, C. J.; Cowart, J. S.; Duong, D. T.; Chiu, K. H.; Tan, C.-H.; Cabral, J. T.; Salleo, A.; Chabinyc, M. L.; Durrant, J. R.; McCulloch, I., Enhancing Fullerene-Based Solar Cell Lifetimes by Addition of a Fullerene Dumbbell. *Angewandte Chemie International Edition* **2014,** *53* (47), 12870-12875.

55.   Jeanbourquin, X. A.; Rahmanudin, A.; Gasperini, A.; Ripaud, E.; Yu, X.; Johnson, M.; Guijarro, N.; Sivula, K., Engineering the self-assembly of diketopyrrolopyrrole-based molecular semiconductors via an aliphatic linker strategy. *Journal of Materials Chemistry A* **2017,** *5* (21), 10526-10536.

56.   Gasperini, A.; Jeanbourquin, X. A.; Rahmanudin, A.; Yu, X.; Sivula, K., Enhancing the Thermal Stability of Solution-Processed Small-Molecule Semiconductor Thin Films Using a Flexible Linker Approach. *Advanced Materials* **2015,** n/a-n/a.

57.   Sharenko, A.; Kuik, M.; Toney, M. F.; Nguyen, T.-Q., Crystallization-Induced Phase Separation in Solution-Processed Small Molecule Bulk Heterojunction Organic Solar Cells. *Advanced Functional Materials* **2014,** *24* (23), 3543-3550.

58.   Yuan, K.; Chen, L.; Chen, Y., Nanostructuring compatibilizers of block copolymers for organic photovoltaics. *Polymer International* **2014,** *63* (4), 593-606.

59.   (a) Darling, S. B., Block copolymers for photovoltaics. *Energy & Environmental Science* **2009,** *2* (12), 1266-1273; (b) Lee, Y.; Gomez, E. D., Challenges and Opportunities in the Development of Conjugated Block Copolymers for Photovoltaics. *Macromolecules* **2015,** *48* (20), 7385-7395.

60.   Kipp, D.; Verduzco, R.; Ganesan, V., Block copolymer compatibilizers for ternary blend polymer bulk heterojunction solar cells - an opportunity for computation aided molecular design. *Molecular Systems Design & Engineering* **2016.**

61.   (a) Lombeck, F.; Komber, H.; Sepe, A.; Friend, R. H.; Sommer, M., Enhancing Phase Separation and Photovoltaic Performance of All-Conjugated Donor–Acceptor Block Copolymers with Semifluorinated Alkyl Side Chains. *Macromolecules* **2015,** *48* (21), 7851-7860; (b) Guo, C.; Lin, Y.-H.; Witman, M. D.; Smith, K. A.; Wang, C.; Hexemer, A.; Strzalka, J.; Gomez, E. D.; Verduzco, R., Conjugated Block Copolymer Photovoltaics with near 3% Efficiency through Microphase Separation. *Nano Letters* **2013,** *13* (6), 2957-2963.

62.   Sivula, K.; Ball, Z. T.; Watanabe, N.; Fréchet, J. M. J., Amphiphilic Diblock Copolymer Compatibilizers and Their Effect on the Morphology and Performance of Polythiophene:Fullerene Solar Cells. *Advanced Materials* **2006,** *18* (2), 206-210.

63.   Lombeck, F.; Sepe, A.; Thomann, R.; Friend, R. H.; Sommer, M., Compatibilization of All-Conjugated Polymer Blends for Organic Photovoltaics. *ACS Nano* **2016,** *10* (8), 8087-8096.

64.   Wang, J.; Higashihara, T., Synthesis of all-conjugated donor-acceptor block copolymers and their application in all-polymer solar cells. *Polymer Chemistry* **2013,** *4* (22), 5518-5526.

65.   Gasperini, A.; Johnson, M.; Jeanbourquin, X.; Yao, L.; Rahmanudin, A.; Guijarro, N.; Sivula, K., Semiconducting alternating multi-block copolymers via a di-functionalized macromonomer approach. *Polymer Chemistry* **2017,** *8* (5), 824-827.

66.   Zhang, S.; Ye, L.; Hou, J., Breaking the 10% Efficiency Barrier in Organic Photovoltaics: Morphology and Device Optimization of Well-Known PBDTTT Polymers. *Advanced Energy Materials* **2016,** *6* (11), 1502529-n/a.

67.	Kang, H.; Lee, W.; Oh, J.; Kim, T.; Lee, C.; Kim, B. J., From Fullerene–Polymer to All-Polymer Solar Cells: The Importance of Molecular Packing, Orientation, and Morphology Control. *Accounts of Chemical Research* **2016,** *49* (11), 2424-2434.

68.	Nakabayashi, K.; Mori, H., All-Polymer Solar Cells Based on Fully Conjugated Block Copolymers Composed of Poly(3-hexylthiophene) and Poly(naphthalene bisimide) Segments. *Macromolecules* **2012,** *45* (24), 9618-9625.

69.	(a) Ku, S.-Y.; Brady, M. A.; Treat, N. D.; Cochran, J. E.; Robb, M. J.; Kramer, E. J.; Chabinyc, M. L.; Hawker, C. J., A Modular Strategy for Fully Conjugated Donor–Acceptor Block Copolymers. *Journal of the American Chemical Society* **2012,** *134* (38), 16040-16046; (b) Wang, S.; Yang, Q.; Tao, Y.; Guo, Y.; Yang, J.; Liu, Y.; Zhao, L.; Xie, Z.; Huang, W., Fully conjugated block copolymers for single-component solar cells: synthesis, purification, and characterization. *New Journal of Chemistry* **2016,** *40* (2), 1825-1833.

70.	Lee, Y.; Aplan, M. P.; Seibers, Z. D.; Kilbey, S. M.; Wang, Q.; Gomez, E. D., Tuning the synthesis of fully conjugated block copolymers to minimize architectural heterogeneity. *Journal of Materials Chemistry A* **2017**.

71.	Nübling, F.; Komber, H.; Sommer, M., All-Conjugated, All-Crystalline Donor–Acceptor Block Copolymers P3HT-b-PNDIT2 via Direct Arylation Polycondensation. *Macromolecules* **2017,** *50* (5), 1909-1918.

72.	(a) Grisorio, R.; Suranna, G. P., Intramolecular catalyst transfer polymerisation of conjugated monomers: from lessons learned to future challenges. *Polymer Chemistry* **2015,** *6* (45), 7781-7795; (b) Senkovskyy, V.; Tkachov, R.; Komber, H.; Sommer, M.; Heuken, M.; Voit, B.; Huck, W. T. S.; Kataev, V.; Petr, A.; Kiriy, A., Chain-Growth Polymerization of Unusual Anion-Radical Monomers Based on Naphthalene Diimide: A New Route to Well-Defined n-Type Conjugated Copolymers. *Journal of the American Chemical Society* **2011,** *133* (49), 19966-19970.

73.	Yokozawa, T.; Ohta, Y., Transformation of Step-Growth Polymerization into Living Chain-Growth Polymerization. *Chemical Reviews* **2016,** *116* (4), 1950-1968.

74.	(a) Mok, J. W.; Kipp, D.; Hasbun, L. R.; Dolocan, A.; Strzalka, J.; Ganesan, V.; Verduzco, R., Parallel bulk heterojunction photovoltaics based on all-conjugated block copolymer additives. *Journal of Materials Chemistry A* **2016,** *4* (38), 14804-14813; (b) Gao, D.; Gibson, G. L.; Hollinger, J.; Li, P.; Seferos, D. S., 'Blocky' donor-acceptor polymers containing selenophene, benzodithiophene and thienothiophene for improved molecular ordering. *Polymer Chemistry* **2015,** *6* (17), 3353-3360.

75.	(a) Kuei, B.; Gomez, E. D., Chain conformations and phase behavior of conjugated polymers. *Soft Matter* **2016**; (b) Kipp, D.; Mok, J.; Strzalka, J.; Darling, S. B.; Ganesan, V.; Verduzco, R., Rational Design of Thermally Stable, Bicontinuous Donor/Acceptor Morphologies with Conjugated Block Copolymer Additives. *ACS Macro Letters* **2015,** *4* (9), 867-871.

Chapter 2

Morphology Stabilization Strategies for Small-Molecule Bulk Heterojunction Photovoltaics

Abstract

The greater crystallinity of solution-processed small-molecule organic semiconductors, compared to their polymer counterparts renders the bulk heterojunction (BHJ) more susceptible to phase separation under thermal stress, decreasing device performance. Here we demonstrate and compare strategies to stabilize the donor:acceptor BHJ in DPP(TBFu)$_2$:PC$_{61}$BM solar cells using molecular additives designed to either afford compatiblization (CP) of the bulk heterojunction, or to in-situ link (ISL) the components using a functional azide group. Both additives were found to stop phase segregation of the BHJ under thermal stress. At 5 wt% loading the ISL additive prevented phase segregation, while altering the azide reaction mechanism by using UV-induced linking versus thermal induced linking was found to significantly affect the device performance. Including 5 wt% of the CP additive slowed phase segregation and devices retained 80 % of their optimum performance after 3000 min of thermal treatment at 110 °C (compared to 50% with the control). The CP additive at 10 wt% changed drastically the kinetics of phase segregation leading to devices with no decrease in performance over 3000 min thermal treatment. Thin film morphology characterization together with photoluminescence and impedance spectroscopy give further insight into the performance differences between the additives. These results reinforce the conclusion that the compatiblization method is the most promising strategy to engineer highly-efficient thermally-stable organic photovoltaics based on solution-processed small molecule semiconductors.

2.1 Introduction

The development of organic photovoltaics (OPV) using solution-processable molecular semiconductors has seen rapid progress in recent years[1] with solar power conversion efficiencies (PCE) now reaching 10%.[2] Small-molecule semiconductors, in particular, have recently received significant attention given their advantages over their polymeric counterparts including a reduction of preparation complexity, structural homogeneity, and potentially lower cost.[3] However, the stability of small molecule based OPVs still requires improvement for practical application.[4] While general OPV device degradation factors such as diffusion of electrode and buffer layers, reactions with oxygen and water, irradiation damage, and mechanical stress have been addressed extensively by engineering approaches,[5] a key remaining issue is the intrinsic morphological instability of the bulk heterojunction (BHJ) active layer—which is a metastable blend of disparate donor and acceptor species.[6] The relatively high crystallinity of small-molecule BHJs[3a, 6d, 7] drives donor-acceptor phase segregation, in some cases even at room temperature,[8] which reduces the interfacial area for free charge generation and thus lowers the device performance.[9]

In polymer-based BHJs three main approaches have been used to address morphological stability: 1) reducing crystallinity of one of the components via side-chain engineering,[10] 2) the in-situ cross-linking of polymer chains using functional groups (e.g. oxetane, bromo, vinyl, or azide) incorporated on the solubilizing alkyl side chains,[11] and 3) including an additive to reduce the phase segregation.[12] A common additive strategy is to covalently link the donor and acceptor components into a compatiblizer (e.g. a block co-polymer), which is included in the active layer during device fabrication.[13] Donor-acceptor block-copolymers can be envisioned as a single active component for truly thermodynamically stable polymer BHJs.[14]

Despite the interest in developing strategies for stabilization of polymer-based devices, few reports have addressed morphological stability in small-molecule BHJs even though this is reasonably a greater challenge, due to the relatively high crystallinity in small molecule semiconductors and the absence of

polymer entanglement, which leads to negligible mixing between the donor and acceptor.[15] Reducing the crystallinity of one of the components by side chain engineering,[16] or by including additives such as dimers[17] or polymers of linked small molecules[18] has shown some success in slowing the kinetics of phase segregation. However, the more effective cross-linking or compatibilization methods have not been carefully explored for small-molecule BHJ systems. Indeed, it is not clear if the in-situ linking of components in a "cross-linking" approach will be effective in a small molecule BHJ without polymer chains to be linked. Moreover, given the higher crystallinity of small molecule BHJs it is not clear if either approaches can be effective at preventing phase segregation under extended thermal stress without including a large fraction of linking/compatibilizing additives that may affect the electronic properties of the device. Herein, we examine these questions with a well-known small-molecule BHJ system[19] based on the donor coded DPP(TBFu)$_2$, and the acceptor PC$_{61}$BM, which is used to demonstrate and compare the effectiveness of these two distinct approaches to stabilize the BHJ and improve the device performance under accelerated thermal stress.

2.2 Synthesis and Characterization of Compatibilizing Additive and N$_3$-In Situ Linker

The structures of molecules used in this work are shown in Figure 1. The primary BHJ components DPP(TBFu)$_2$ (donor) and PC$_{61}$BM (acceptor) have previously been established as a common small-molecule system[19-20]. DPP(TBFu)$_2$ was synthesized according to an established procedure by Nguyen and co-workers, while PC$_{61}$BM was commercially purchased. To demonstrate the compatibilizer approach and the in-situ linking approach with the primary BHJ components, a linked version of the donor and acceptor unit was prepared and coded as the compatibilizing additive (CP), and an azide functionalized donor component additive, coded as N$_3$-ISL (See Figure1b and the appendix for full synthesis procedures and basic characterization of the N$_3$-ISL and CP compounds are given in the supporting information). The azide group is known to undergo either a thermal or photo-induced nitrene insertion reaction, which has previously been used to crosslink conjugated polymers.[11a] Briefly, the synthetic route begins with the alkylation of a mono alkylated DPP(Thiophene)$_2$ core 1 with a hexyl

36

chain containing a termini *n*-tert-butyloxycarbonyl group (2) to obtain 4a for the synthesis of CP and

1-azido-6-bromohexane (3) to obtain 4b for the synthesis of N_3-ISL. The thiophene groups flanking the

DPP core was then brominated using *N*-bromosuccinimide (NBS) to attach 2-benzofuranylboronic acid

(6) via standard suzuki-coupling reactions to obtain the precursor 6a for the final synthetic step for CP

and to obtain 6b with good yield of 76% for the azide functionalised DPP(TBFu)$_2$ N_3-ISL. Desterification

of PC$_{61}$BM to obtain [6,6]-phenyl-C$_{61}$-butyric acid (PC$_{61}$BA) was treated with HCl and acetic acid in

toluene and the deprotection of *n*-tert-butyloxycarbonyl on 6a was performed using trifluoracetic

acid in dichloromethane to a primary amine functionalized DPP(TBFu)$_2$. Finally, a mild room

temperature condensation reaction between this and PC$_{61}$BA using HATU and N,N-

diisopropylethylamine in a mixture of chloroform and DMF obtained CP at a reasonable yield of 56%.
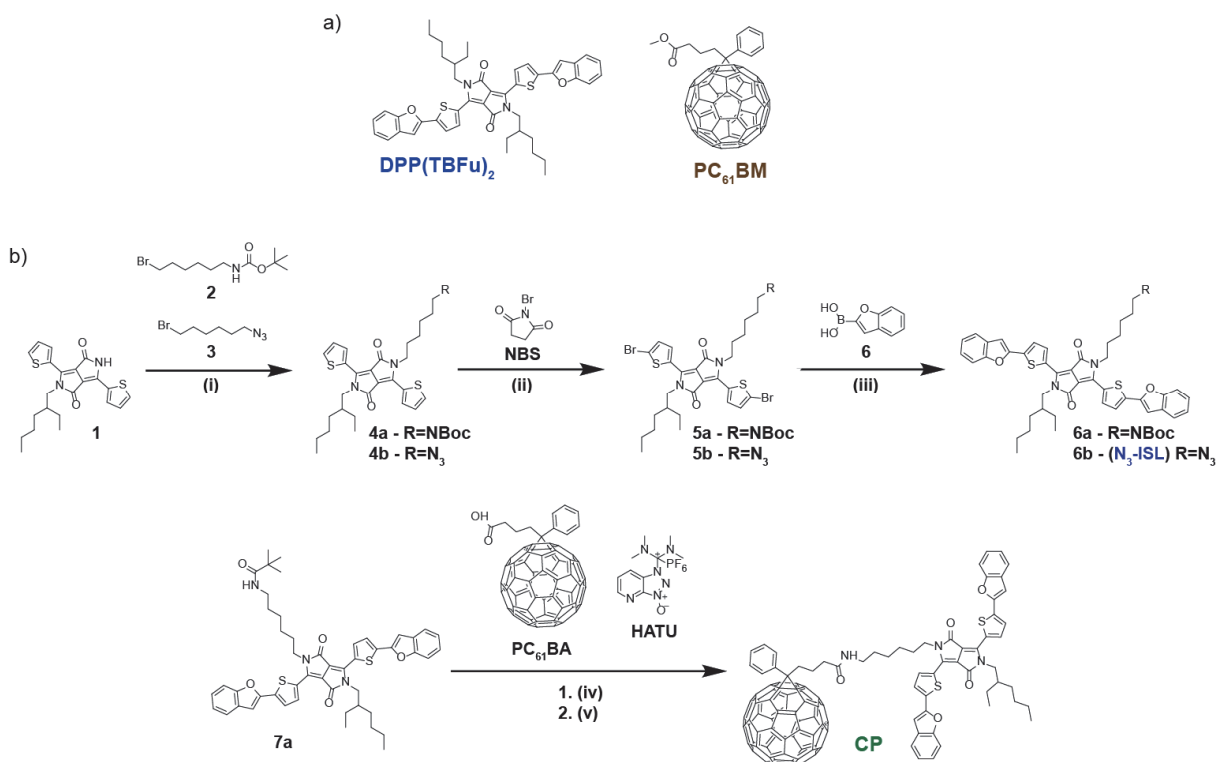
Figure 1. Molecular Structures of the active materials used in this work: a) Donor DPP(TBFu)$_2$ and Acceptor PC$_{61}$BM; b) Synthetic Route for N_3-ISL and CP: (i) 2 or 3(1.2eq) K_2CO_3 , DMF, 120°C,12hrs; (ii) NBS (2eq), Chloroform, 0°C in the dark; (iii) 6 (2.5eq)Pd$_2$(dba)$_3$(1.5%):tri-tert-butylphosphonium tetrafluoroborate (1:4), 2M H$_2$KPO$_4$, anhydrous Toluene, 90°C,12h; (iv) 7a (1eq), CF$_3$COOH (excess), CH$_2$Cl$_2$, R.T, 2h; (v) PC$_{61}$BA (0.4eq,)N,N-diisopropylethylamine (1.6eq), HATU (0.5eq), Chloroform/DMF, R.T, 3h.

The UV-vis absorption spectra of all four molecules from Figure 1 is shown in Figure S1, Supporting Information (SI). As expected, the spectrum of CP consists of the absorption of the DPP(TBFu)$_2$ and PC$_{61}$BM, while N$_3$-ISL does not differ significantly from the parent donor component suggesting that the optoelectronic properties of the conjugated core is not severely affected. However a slight difference in the shapes of the main absorption peak in spectra of the N$_3$-ISL and CP molecules when cast into thin films suggest that the solid state packing is slightly altered,[17] compared to the parent DPP(TBFu)$_2$. Indeed, differential scanning calorimetry (DSC) of CP showed no obvious phase transitions during its 1st and 2nd heating-cooling cycle (See Figure S2, SI), suggesting that the CP is not strongly crystalline in solid-state, in contrast to the primary components, which both exhibit melting transitions characteristic of a semi-crystalline morphology in the solid state. On the other hand, the DSC of N$_3$-ISL suggests that the terminal azide undergoes both photo and thermal activation of the nitrene insertion reaction. This is shown by the suppression of phase transitions in an UV-treated (254 nm illumination, exposure for 10 mins) sample of N$_3$-ISL, whereas non UV-treated N$_3$-ISL showed a series of exothermic and subsequent endothermic transitions peaks during its 1st heating cycle indicative of the thermal activation of the terminal azide[21] and upon cooling no obvious exotherms were observed.

2.3 In-Situ Linking Reaction

FT-IR spectroscopy also showed a reduction in the intensity of the azide stretch at approximately 2090 cm^{-1} as UV exposure time is increased (See Figure S3a, SI). Further analysis of the formation of photo- and thermal- reaction products upon addition of N$_3$-ISL to a blend of DPP(TBFu)$_2$ and PC$_{61}$BM was performed using Gel-Permeation-Chromatography (GPC) and mass spectroscopy (MALDI-TOF MS) (See SI, Figures S3-S5 for full details including experimental procedure and discussion). Briefly, GPC data indicate the presence high molecular weight species after UV and thermal treatments. Moreover, MALDI-TOF MS analysis (See Figures S4 SI) provide evidence of the unselective-nitrene insertion reaction towards both primary blend components by random photo- and thermally-linking the azide group onto the alkyl chains and conjugated backbone of the primary components used in the BHJ

matrix (See Figure S5 SI), along with the photo-dimerization of PC$_{61}$BM under UV illumination.[22] Overall these results confirm that the N$_3$-ISL can link with both primary BHJ components under UV or thermal treatment.

2.4 Photovoltaic Performance and Device Stability
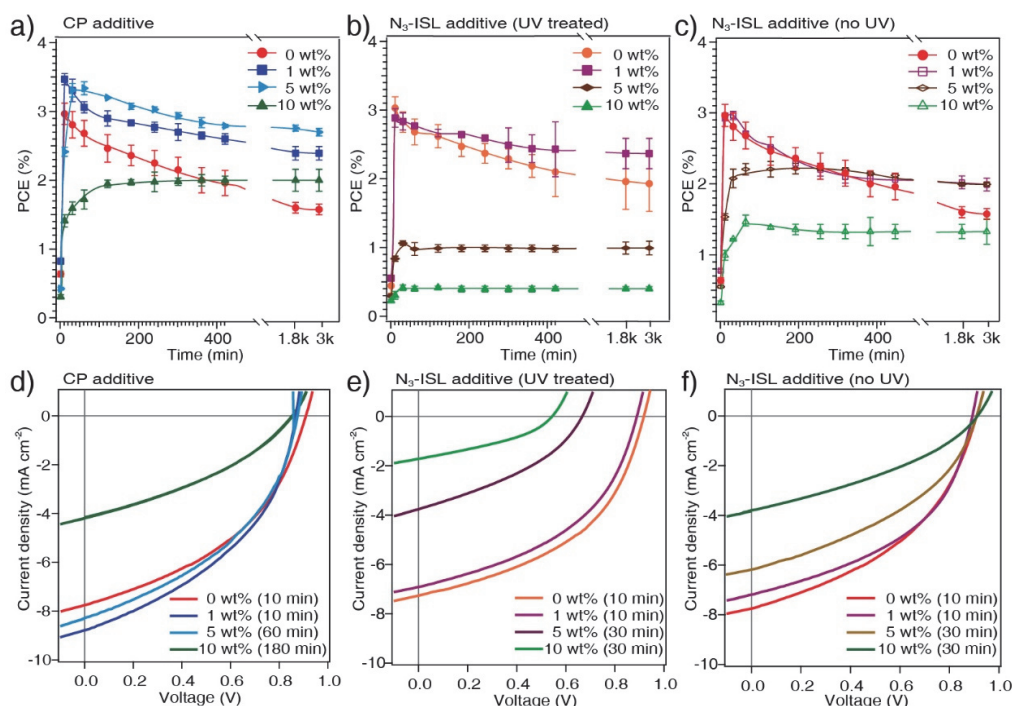
Figure 2. Photovoltaic device performance with respect to the thermal stress at 110°C. Panels (a-c) show the power conversion efficiency (PCE) of OPVs based on a 6:4 DPP(TBFu)$_2$:PC$_{61}$BM BHJ with (a) the CP additive (b) the N$_3$-ISL with 10 min UV treatment and (c) N$_3$-ISL without UV treatment. The loading of the additives are indicated in each case. Panels (d-f) show the J-V curves of devices with the BHJ blends using the respective additives at the specified annealing time (given in parentheses) to obtain its maximum PCE.

To test the performance of the additive molecules in their ability to stabilize the morphology of BHJs, standard ITO/PEDOT:PSS/BHJ/Al solar cell devices were prepared with a BHJ of DPP(TBFu)$_2$:PC$_{61}$BM at a ratio of 6:4 by weight, similar to previously reported conditions.[18-19] The loading of the CP and N$_3$-ISL additives in the BHJ matrix were varied (while maintaining the 6:4 ratio of donor:acceptor) and the effect of a UV pretreatment (10 min) to induce the in-situ linking reaction in as-cast BHJs with included N$_3$-ISL was also investigated in comparison to using thermal treatment only to induce linking. All as-cast devices (spun coat BHJ with top electrode deposited) were subject to thermal stress at 110°C over

a period of 3000 min (50 h) to drive the crystallization and phase segregation of the primary components, and the current density-voltage (J-V) characteristics were measured periodically under standard 1 sun illumination upon cooling the devices to 20°C. The power conversion efficiency (PCE) as a function of the thermal treatment time is shown in Figure 2a-c, with respect to the included additive (CP additive, N_3-ISL + UV treatment, and N_3-ISL no UV). The J-V curve at the time point corresponding to the highest PCE for each additive condition is shown in Figure 2d-f. Full device performance metrics are also included in the SI (Table S1).

The control device (0 wt% additive loading, red traces in Figure 2a,d) achieved its highest PCE of 3.0% after 10 minutes of thermal treatment. The observed performance increase from the as-cast state is expected due to the initial stages of crystallization, which results in an optimum degree of BHJ phase segregation, and has been previously reported under similar conditions.[18] Subsequent thermal treatment drives further phase separation [23] and reduces the performance of the device to 1.6% PCE after 3000 min (50 h). With respect to the compatibilizing linker, adding 1 wt% of CP to the BHJ slightly improved the best PCE to 3.5% (10 min thermal treatment) attributed to an increase in short circuit current density (J_{SC}) and fill factor (FF). A similar increase to 3.3% PCE was also observed at 5 wt% of CP loading, but interestingly a longer thermal treatment (60 min) was required to reach this maximum performance. Moreover, both the 1 and 5 wt% devices showed less decrease in performance over the testing period compared to the control device remaining at 2.4 and 2.7 % PCE, respectively after 3000 min. In contrast, increasing the CP loading to 10 wt% gave a significantly different device behavior. A gradual increase of the PCE was observed as a function of time under thermal stress, saturating at about 2% PCE after 180 min and remaining stable over the rest of the testing period. The lower optimum PCE stems from a significant reduction in J_{SC} and a reduction of the open circuit voltage (V_{OC}) compared to the control device, as seen on the J-V curve Figure 2d.

Regarding the N_3-ISL additive, firstly we established that a UV-treated control device (treated under UV without any added N_3-ISL, orange curves in Figure 2b,e) showed a maximum J_{SC} of 7.2 mA cm^{-2}

40

compared to 8.0 mAcm^{-2} for the control device without UV exposure, and only a slight change in PCE, suggesting that 10 min of UV exposure did not severely affect device performance (however we note that a 30 min UV treatment did decrease device performance substantially, see Figure S6 SI). While qualitatively similar behavior to the CP additive was observed when adding N$_3$-ISL to the BHJ, significant differences in the device performance with UV treatment (Figures 2b and e) and without (thermal linking only, Figures 2 c and f) are evident. With 1 wt% of the N$_3$-ISL additive, no significant change in the optimum device performance was seen regardless of the use of the UV or thermal linking treatment. The maximum PCE was about 3 % after 10 min at 110 °C and a decrease of device performance was observed as the thermal treatment time increased. Notably the 1 wt% devices do seemingly stabilize the BHJ. Indeed, the performance after 3000 min at 110 °C was higher in both cases (with and without UV) compared to the control devices. As the additive loading increased further, the device performance changed significantly. Similar to the CP additive, devices at 5 and 10 wt% N$_3$-ISL required a longer time at 110°C to reach the maximum PCE compared to the control devices. Moreover, at both 5 and 10 wt% of the N$_3$-ISL additive, a stable PCaE with respect to thermal treatment time was achieved after ca. 120 min (with or without UV treatment). However, a larger decrease in maximum device performance was observed when UV treatment was used, reaching a PCE of only 1 % (5 wt%) and 0.4 % (10 wt%), while a better maximum performance of 2.4 % (5 wt%) and 1.5 % (10 wt%) was recorded for non-UV cured devices. For the case of the UV treated devices, the lower performance was attributed to a decrease in the J$_{SC}$, FF, and V$_{OC}$ compared to control devices (Figure 2e), while interestingly, without UV treatment the difference was mainly due a decreased J$_{SC}$ only (Figure 2f). These results strongly suggest a different functioning of the N$_3$-ISL additive with or without the UV treatment, which will be discussed later. While it is clear that both the additives can improve the device stability under thermal stress, differences in the optimum additive loading and the maximum PCE obtained suggest dissimilarity in the evolution of the BHJ morphology with respect to the additive used. Analyzing the topography of the BHJ thin films by atomic force microscopy (AFM) was next performed to provide insight into morphological differences. **Figure 3** displays the

topography of the 6:4 donor:acceptor BHJs after thermal treatment at 110 °C for 3000 min (main images) compared to the as-cast state (image insets) for 0, 1, and 10wt% of the CP additive and 0, 1 and 10wt% of the N_3-ISL additive with a 10 min UV treatment applied before the thermal treatment.

2.5 Bulk Heterojunction Morphological Characterization

A relatively featureless morphology was observed in as-cast thin films across all additive loadings, but upon heating the BHJs at 110 °C for 3000 min clear differences were observed. Without additive and without UV treatment (Figure 3a), the morphology exhibited the expected haystack morphology with needle-like features corresponding to crystalline domains of the components.[18] It has been established that the driving force for phase segregation in this BHJ is the crystallization of DPP(TBFu)$_2$, which is reported to occur at temperatures as low as the cold crystallization temperature of approximately 70°C.[20a] The morphology of the BHJ with 1 wt% of the CP additive (Figure 3b) was significantly less rough than the control after the thermal treatment, but crystalline domains of a similar size as in the control can still be observed, suggesting a degree of phase segregation similar to the control, which is consistent with the evolution of the PCE seen at this condition. In contrast, at 10 wt% CP loading (Figure 3c) micron-sized needle-like features are completely suppressed after the thermal treatment. However, a slight coarsening of the grains from the as-cast condition can be seen, suggesting an increase in crystallinity during the 3000 min thermal treatment, consistent with the gradual increase in the PCE. With respect to the N_3-ISL additive we first note that the phase-segregated morphology containing needle-like features was also observed for the UV-treated BHJ without additive (Figure 3d) but with smaller-sized crystalline domains, suggesting that the UV treatment alone has an effect on the nucleation and growth of the crystalline domains. Upon loading N_3-ISL at even 1 wt% the formation of these needle-like domains was clearly suppressed. The resulting BHJ after thermal stress appeared with a larger roughness when using 1 wt% N_3-ISL (Figure 3e) compared to 10 wt% (Figure 3f), which suggests a different evolution of the phase separation consistent with the OPV results.
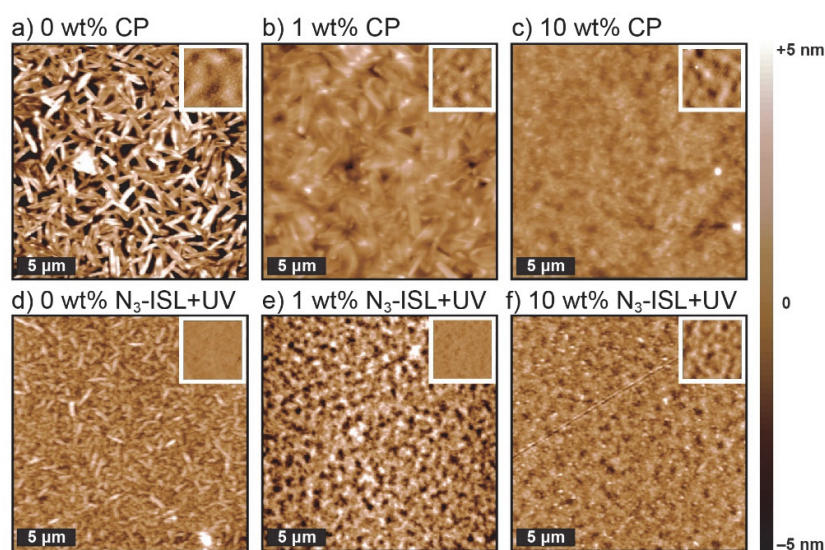
Figure 3. Thin Film topography by AFM of the 6:4 donor:acceptor blends after 3000 min at 110°C (main panels) and as spun-cast from Chloroform solutions (panel insets). a) with no additive b) with 1 wt% CP, c) with 10 wt% CP, d) with no additive but with 10 min UV treatment before thermal stress, e) with 1 wt% N_3-ISL + UV and f) with 10 wt% N_3-ISL with UV treatment.

The topography results together with the device performance suggest that the additives have an effect on the crystallinity of the BHJ. To confirm this, DSC was performed on 6:4 blends of DPP(TBFu)$_2$:PC$_{61}$BM with varying amounts of the additives. The first heating scan of the as-cast blends is shown in Figure 4a. While a melting transition of the crystalized DPP(TBFu)$_2$ in the BHJ is seen to onset at ca. 190°C, this transition was suppressed with the addition of 10 wt% of either additive, reducing the enthalpy of the transition by about half with N_3-ISL and by a factor of three with the CP additive (See Table S2, SI). Increasing the amount of the CP additive (to 50 wt%) led to an almost complete suppression of the melting transition, however about 20 % of the original melting enthalpy remained when 50 wt% of the N_3-ISL additive was used with a 10 min UV treatment. This suggests that the CP additive exhibits a qualitatively stronger ability to disrupt the crystallinity of the DPP(TBFu)$_2$ compared to the N_3-ISL additive, consistent with the rougher morphology observed after thermal stress with the N_3-ISL at 10 wt% loading compared to 10 wt% CP (as seen in Figure 2). However, the presence of large crystalline domains in the thermally stressed 1 wt% CP BHJ film morphology, but the absence of these domains in the 1 wt% N_3-ISL film suggests that while the CP may disrupt the π-πstacking of the DPP(TBFu)$_2$ to a greater degree, it does not prevent phase segregation as effectively as the N_3-ISL linker. This is

43

emphasized in the OPV results where 5 wt% of the CP has a less drastic effect on the evolution of the PCE compared to 5 wt% of N_3-ISL.

Despite the differences in the additive behavior, overall the DSC results suggest that crystallization of the BHJ components can be suppressed even under extreme thermal treatment, to further demonstrate this aspect, thin films were annealed at 240 °C (above the melting transition of DPP(TBFu)$_2$) and slowly cooled, in order to strongly drive phase segregation. Optical microscope images of the films are shown in Figure S7, SI. As expected, while the control film without additives crystallized with large (> 5μm) domains (slightly smaller, ~2 μm, for UV treated films without additive), the films with 10 wt% additives showed significantly smaller domains, mirroring the morphology of the films treated at 110 °C. This data show, that despite that the melting enthalpy remaining at 10 wt% additive loading, the thin film BHJ morphology can be stabilized even in under extreme conditions.

2.6 Optoelectronic effect on the BHJ Morphology

As it is important to better understand the optoelectronic differences between the two additives, photoluminescence (PL) spectroscopy was next performed on the BHJ films with varying the additive loading. Indeed, the PL intensity is known to be affected by the proximity/size of the donor and acceptor domains, where greater phase segregation leads to more PL emission from the donor upon its excitation. The PL spectra upon excitation at 532 nm show a main peak from the emission of DPP(TBFu)2 around 820 nm (see Figure S8, SI). The relative amount of emission compared to control BHJs without additives is summarized in Figure 4b as a function of the additive loading. While as-cast BHJs with added N_3-ISL only show a slight decline in the PL spectra, implying that the this additive does not alter significantly the as-cast BHJ morphology, the CP additive as a drastic effect on the PL of the as-cast BHJ film at just 1 wt% loading, giving only 35% of the emission compared to the control, consistent with the formation of a more mixed donor:acceptor BHJ after spin casting from solvent. After thermally treating the film at 110°C for 1 h, the 1 wt% CP BHJ increased in PL intensity to 50% (relative to the control) consistent with the phase segregation observed in the AFM topography. Higher

loadings of CP gave lower PL after annealing consistent with the suppression of phase separation. Interestingly, after annealing the BHJs with the N_3-ISL additive a greater relative drop in the PL is seen in the UV treated films compared to BHJs with N_3-ISL but without UV pre-treatment. This further indicates a different behaviour between the thermal linking and the UV linking approaches.
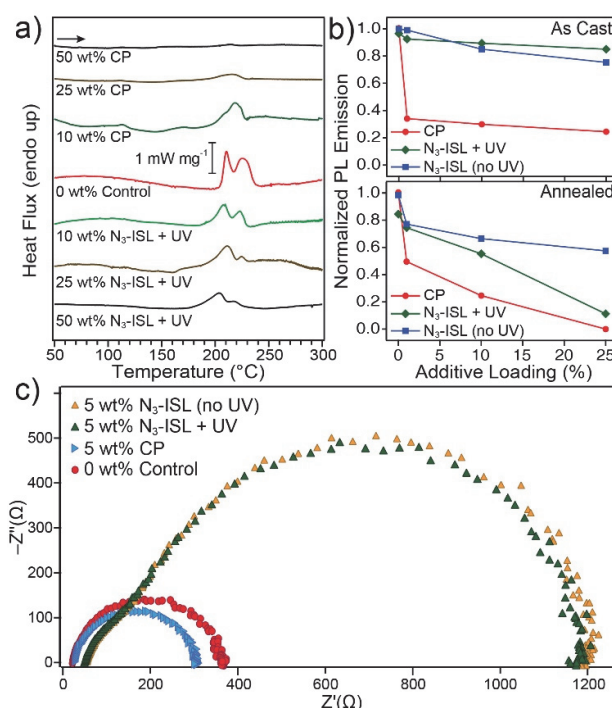
Figure 4. a) First DSC heating scans of drop cast BHJ films (6:4 donor:acceptor) with the respective additives. Blends with N_3-ISL were UV treated for 10 min. b.) Normalized (integrated) PL emission of as cast (top panel) and thermally annealed (bottom panel 110 °C, 1h) of 6:4 donor:acceptor blend thin-films is shown against additive loading. c) Nyquist plots of impedance spectra measured under 1 Sun illumination at open circuit conditions of thermally annealed (2 h, 110 °C) devices with respective additives and UV curing conditions.

For a final piece of data to compare the actions of the additives, we performed impedance spectroscopy (IS) on thermally treated (110°C, 2 h) devices, under illumination and at open circuit. Nyquist plots are shown in Figure 4c. The control device exhibited a single RC process, which has been previously ascribed to BHJ recombination under these conditions.[24] A device containing 5 wt% of CP (and which exhibited higher PCE compared to the control device) gave a similar behavior in IS, with a lower recombination resistance, consistent with a more intermixed phase (as compared to the reference device) where more free charges are generated.[24b] In stark contrast, the 5 wt% N_3-ISL device

that underwent UV pre-treatment exhibited an additional semicircle in the Nyquist plot at low frequency with a considerably higher associated resistivity. While this may be expected due to the poor PCE of this device compared to the control, notably we found that a device with 5 wt% N_3-ISL that did not undergo the UV treatment (and that had a similar PCE to the control device) exhibited a similarly large RC process as shown in Figure 4c. The presence of this large second semicircle can be attributed to trap state processes within the active layer,[25] which is reasonable given the confirmed presence (by MALDI-TOF MS, Figure S4) of randomly linked species formed by the reaction of the azide on N_3-ISL. However, the seemingly similar IS behaviour of the 5 wt% N_3-ISL devices with and without the UV treatment contrasts the very different behaviour that these two conditions give with respect to device PCE and the PL. A reasonable explanation for this difference is as follows: In both the thermal and UV linking approaches the azide linker reacts randomly forming linked BHJ components that retard phase segregation and in both cases introduce the presence of trapping states in the BHJ which reduce the device performance (Indeed we note that previous work on using random BHJ crosslinking methods on polymer-based OPVs have pointed out that the reactions may provoke the breaking of the conjugated polymer backbone, disrupt charge transport, and reduce performance).[11b, 11c, 21, 26] However since the UV activated linking clearly leads to a poorer performance the nature of the linking points or the linked species is reasonably somehow different. In fact careful analysis of the MALDI-TOF MS data between the UV linking and thermal linking approaches (Figure S4, SI), do suggest one clear difference: the presence of dimerized $PC_{61}BM$ (see structure Figure S5, SI) under UV treatment and not under thermal conditions. While breaking of the conjugated fullerene unit is known to cause the formation of traps[27] the presence of dimerized fullerene alone does not fully explain why the UV treatment suffers a poorer performance, as the control device (without N_3-ISL but with 10 min UV treatment) performed similar to the control device without UV. However, it has been suggested that UV excitation of azide derivatives results in an alternative, highly reactive reaction pathway of the nitrene insertion linking as compared to thermal activation (which has been characterized as more selective and milder).[21, 28] Thus we hypothesize that UV excitation causes the formation of important deep traps at

a faster rate in the presence of the N_3-ISL additive. These deep traps result in a lower device V_{OC} when using the UV treatment and thus the lower PCE. Moreover, we note further that at low loadings (1 wt%) of the N_3-ISL, when the linking reaction is not sufficient to prevent crystallization of the donor and acceptor phases in the BHJ, the few linked species could be excluded via crystallization to the grain boundaries or amorphous regions where they will have less of an effect on the charge transport through the pure phases. In contrast, when the N_3-ISL is at a sufficiently high concentration in the BHJ to arrest the phase segregation in the film (about 5 wt%) these charge trapping species cannot be excluded and the PL and device performance drops. Then the different nature of the linked species when including the UV treatment (perhaps more linking on the fullerene), compared to the thermal treatment leads to the drastic difference in performance.

2.6 Conclusion

In summary, two additives, a compatibilizer (CP) and an azide functionalized in-situ linker (N_3-ISL), were prepared to examine the possibility to stabilize BHJ OPVs prepared from solution-processed crystalline small molecules. The device results show that both additives have the ability to stop the phase segregation of the donor and acceptor in the BHJ when subject to thermal stress for an extended period. While the N_3-ISL additive required only 5 wt% loading to arrest phase segregation, altering the azide reaction mechanism by using UV-induced linking versus thermal induced linking gave significantly different performance attributed to a likely difference in reaction products, and UV treated devices performed poorer than thermally linked ones. However, the presence of the non-specific linked species in both cases led to increased BHJ charge trapping as shown by PL and IS spectroscopies, and reduced performance compared to the CP additive. Indeed, including 5 wt% of the CP additive retarded the BHJ phase segregation and led to the highest PCE of 2.8 % after 3000 min of thermal treatment at 110 °C. Moreover 10 wt% of the CP additive changed drastically the kinetics of phase segregation leading to devices that saturated in performance at 2 % after 120 min with no decrease for 3000 min (the length of our test). In this case the slower crystallization and phase segregation of the BHJ from

the as-cast state may also prove to be an advantage in offering the ability to avoid overshoot in the device annealing. Moreover, the observed control over phase segregation in the melt-annealed films with CP could potentially allow for melt processing of the BHJ, which is covered in chapter 4 of this thesis. Overall based on the results presented, employing the CP additives is a preferred strategy to stabilize the bulk heterojunction. Further efforts should be directed toward optimizing the CP strategy for other small-molecule systems to potentially enable solvent-free roll-to-roll processing of highly efficiency and stable OPVs.

2.7 Reference

1.   Mishra, A.; Bäuerle, P., Small Molecule Organic Semiconductors on the Move: Promises for Future Solar Energy Technology. *Angewandte Chemie International Edition* **2012,** *51* (9), 2020-2067.

2.   (a) Zhang, Q.; Kan, B.; Liu, F.; Long, G.; Wan, X.; Chen, X.; Zuo, Y.; Ni, W.; Zhang, H.; Li, M.; Hu, Z.; Huang, F.; Cao, Y.; Liang, Z.; Zhang, M.; Russell, T. P.; Chen, Y., Small-molecule solar cells with efficiency over 9%. *Nat. Photonics* **2015,** *9* (1), 35-41; (b) Kan, B.; Li, M.; Zhang, Q.; Liu, F.; Wan, X.; Wang, Y.; Ni, W.; Long, G.; Yang, X.; Feng, H.; Zuo, Y.; Zhang, M.; Huang, F.; Cao, Y.; Russell, T. P.; Chen, Y., A Series of Simple Oligomer-like Small Molecules Based on Oligothiophenes for Solution-Processed Solar Cells with High Efficiency. *Journal of the American Chemical Society* **2015,** *137* (11), 3886-3893; (c) Kan, B.; Zhang, Q.; Li, M.; Wan, X.; Ni, W.; Long, G.; Wang, Y.; Yang, X.; Feng, H.; Chen, Y., Solution-Processed Organic Solar Cells Based on Dialkylthiol-Substituted Benzodithiophene Unit with Efficiency near 10%. *J. Am. Chem. Soc.* **2014,** *136* (44), 15529-15532.

3.   (a) Collins, S. D.; Ran, N. A.; Heiber, M. C.; Nguyen, T.-Q., Small is Powerful: Recent Progress in Solution-Processed Small Molecule Solar Cells. *Advanced Energy Materials* **2017**, 1602242-n/a; (b) Osedach, T. P.; Andrew, T. L.; Bulovic, V., Effect of synthetic accessibility on the commercial viability of organic photovoltaics. *Energy & Environmental Science* **2013,** *6* (3), 711-718.

4.   Cheng, P.; Zhan, X., Stability of organic solar cells: challenges and strategies. *Chem. Soc. Rev.* **2016,** *45* (9), 2544-82.

5.   (a) Müller, C., On the Glass Transition of Polymer Semiconductors and Its Impact on Polymer Solar Cell Stability. *Chemistry of Materials* **2015,** *27* (8), 2740-2754; (b) Cheng, P.; Zhan, X., Versatile third components for efficient and stable organic solar cells. *Materials Horizons* **2015,** *2* (5), 462-485; (c) Savagatrup, S.; Printz, A. D.; O'Connor, T. F.; Zaretski, A. V.; Rodriquez, D.; Sawyer, E. J.; Rajan, K. M.; Acosta, R. I.; Root, S. E.; Lipomi, D. J., Mechanical degradation and stability of organic solar cells: molecular and microstructural determinants. *Energy & Environmental Science* **2015,** *8* (1), 55-80; (d) Scaccabarozzi, A. D.; Stingelin, N., Semiconducting:insulating polymer blends for optoelectronic applications-a review of recent advances. *Journal of Materials Chemistry A* **2014,** *2* (28), 10818-10824; (e) Jørgensen, M.; Norrman, K.; Gevorgyan, S. A.; Tromholt, T.; Andreasen, B.; Krebs, F. C., Stability of Polymer Solar Cells. *Advanced Materials* **2012,** *24* (5), 580-612.

6.   (a) Stingelin, N., On the phase behaviour of organic semiconductors. *Polymer International* **2012,** *61* (6), 866-873; (b) Moulé, A. J.; Meerholz, K., Morphology Control in Solution-Processed Bulk-Heterojunction Solar Cell Mixtures. *Advanced Functional Materials* **2009,** *19* (19), 3028-3036; (c) Peet, J.; Heeger, A. J.; Bazan, G. C., "Plastic" Solar Cells: Self-Assembly of Bulk Heterojunction Nanomaterials by Spontaneous Phase Separation. *Accounts of Chemical Research* **2009,** *42* (11), 1700-1708; (d) Collins, B. A.; Tumbleston, J. R.; Ade, H., Miscibility, Crystallinity, and Phase Development in P3HT/PCBM Solar Cells: Toward an Enlightened Understanding of Device Morphology and Stability. *J. Phys. Chem. Lett.* **2011,** *2* (24), 3135-3145.

7.   (a) Fraga Domínguez, I.; Distler, A.; Lüer, L., Stability of Organic Solar Cells: The Influence of Nanostructured Carbon Materials. *Advanced Energy Materials* **2016**, 1601320-n/a; (b) Cardinaletti, I.; Kesters, J.; Bertho, S.; Conings, B.; Piersimoni, F.; D'Haen, J.; Lutsen, L.; Nesladek, M.; Van Mele, B.; Van Assche, G.; Vandewal, K.; Salleo, A.; Vanderzande, D.; Maes, W.; Manca, J. V., Toward bulk heterojunction polymer solar cells with thermally stable active layer morphology. *PHOTOE* **2014,** *4* (1), 040997-040997.

8.   (a) Lee, W. H.; Lim, J. A.; Kim, D. H.; Cho, J. H.; Jang, Y.; Kim, Y. H.; Han, J. I.; Cho, K., Room-Temperature Self-Organizing Characteristics of Soluble Acene Field-Effect Transistors. *Advanced Functional Materials* **2008,** *18* (4), 560-565; (b) Keivanidis, P. E.; Laquai, F.; Howard, I. A.; Friend, R. H., Room-Temperature Phase Demixing in Bulk Heterojunction Layers of Solution-Processed Organic Photodetectors: the Effect of Active Layer Ageing on the Device Electro-optical Properties. *Advanced Functional Materials* **2011,** *21* (8), 1355-1363.

9.   (a) Schaffer, C. J.; Palumbiny, C. M.; Niedermeier, M. A.; Jendrzejewski, C.; Santoro, G.; Roth, S. V.; Müller-Buschbaum, P., A Direct Evidence of Morphological Degradation on a Nanometer Scale in Polymer Solar Cells. *Advanced Materials* **2013,** *25* (46), 6760-6764; (b) Dang, M. T.; Hirsch, L.; Wantz, G.; Wuest, J. D., Controlling the Morphology and Performance of Bulk Heterojunctions in Solar Cells. Lessons Learned from the Benchmark Poly(3-hexylthiophene):[6,6]-Phenyl-C61-butyric Acid Methyl Ester System. *Chemical Reviews* **2013,** *113* (5), 3734-3765; (c) Huang, Y.; Kramer, E. J.; Heeger, A. J.; Bazan, G. C., Bulk Heterojunction Solar Cells: Morphology and Performance Relationships. *Chemical Reviews* **2014,** *114* (14), 7006-7043.

10.   Li, Z.; Wu, F.; Lv, H.; Yang, D.; Chen, Z.; Zhao, X.; Yang, X., Side-Chain Engineering for Enhancing the Thermal Stability of Polymer Solar Cells. *Advanced Materials* **2015,** *27* (43), 6999-7003.

11.   (a) Carle, J. E.; Andreasen, B.; Tromholt, T.; Madsen, M. V.; Norrman, K.; Jorgensen, M.; Krebs, F. C., Comparative studies of photochemical cross-linking methods for stabilizing the bulk hetero-junction morphology in polymer solar cells. *J. Mater. Chem.* **2012,** *22* (46), 24417-24423; (b) Cheng, Y.-J.; Hsieh, C.-H.; Li, P.-J.; Hsu, C.-S., Morphological Stabilization by In Situ Polymerization of Fullerene Derivatives Leading to Efficient, Thermally Stable Organic Photovoltaics. *Advanced Functional Materials* **2011,** *21* (9), 1723-1732; (c) Rumer, J. W.; McCulloch, I., Organic photovoltaics: Crosslinking for optimal morphology and stability. *Materials Today* **2015,** *18* (8), 425-435; (d) Wantz, G.; Derue, L.; Dautel, O.; Rivaton, A.; Hudhomme, P.; Dagron-Lartigau, C., Stabilizing polymer-based bulk heterojunction solar cells via crosslinking. *Polymer International* **2014,** *63* (8), 1346-1361.

12.   (a) Schroeder, B. C.; Li, Z.; Brady, M. A.; Faria, G. C.; Ashraf, R. S.; Takacs, C. J.; Cowart, J. S.; Duong, D. T.; Chiu, K. H.; Tan, C.-H.; Cabral, J. T.; Salleo, A.; Chabinyc, M. L.; Durrant, J. R.; McCulloch, I., Enhancing Fullerene-Based Solar Cell Lifetimes by Addition of a Fullerene Dumbbell. *Angewandte Chemie International Edition* **2014,** *53* (47), 12870-12875; (b) Li, J.; Zhu, X.; Yuan, T.; Shen, J.; Liu, J.; Zhang, J.; Tu, G., Donor–Acceptor Interface Stabilizer Based on Fullerene Derivatives toward Efficient and Thermal Stable Organic Photovoltaics. *ACS Appl. Mater. Interfaces* **2017,** *9* (7), 6615-6623.

13.   (a) Yuan, K.; Chen, L.; Chen, Y., Nanostructuring compatibilizers of block copolymers for organic photovoltaics. *Polymer International* **2014,** *63* (4), 593-606; (b) Kipp, D.; Verduzco, R.; Ganesan, V., Block copolymer compatibilizers for ternary blend polymer bulk heterojunction solar cells - an opportunity for computation aided molecular design. *Mol. Syst. Des. Eng.* **2016,** *1* (4), 353-369; (c) Sivula, K.; Ball, Z. T.; Watanabe, N.; Fréchet, J. M. J., Amphiphilic Diblock Copolymer Compatibilizers and Their Effect on the Morphology and Performance of Polythiophene:Fullerene Solar Cells. *Advanced Materials* **2006,** *18* (2), 206-210; (d) Kim, J. B.; Allen, K.; Oh, S. J.; Lee, S.; Toney, M. F.; Kim, Y. S.; Kagan, C. R.; Nuckolls, C.; Loo, Y.-L., Small-Molecule Thiophene-C60 Dyads As Compatibilizers in Inverted Polymer Solar Cells. *Chemistry of Materials* **2010,** *22* (20), 5762-5773; (e) Lombeck, F.; Sepe, A.; Thomann, R.; Friend, R. H.; Sommer, M., Compatibilization of All-Conjugated Polymer Blends for Organic Photovoltaics. *ACS Nano* **2016,** *10* (8), 8087-8096; (f) Slota, J. E.; Elmalem, E.; Tu, G.; Watts, B.; Fang, J.; Oberhumer, P. M.; Friend, R. H.; Huck, W. T. S., Oligomeric Compatibilizers for Control of phase Separation in Conjugated Polymer Blend Films. *Macromolecules* **2012,** *45* (3), 1468-1475.

14.   (a) Guo, C.; Lin, Y.-H.; Witman, M. D.; Smith, K. A.; Wang, C.; Hexemer, A.; Strzalka, J.; Gomez, E. D.; Verduzco, R., Conjugated Block Copolymer Photovoltaics with near 3% Efficiency through Microphase Separation. *Nano Lett.* **2013,** *13* (6), 2957-2963; (b) Lee, Y.; Gomez, E. D., Challenges and Opportunities in the Development of Conjugated Block Copolymers for Photovoltaics. *Macromolecules* **2015,** *48* (20), 7385-7395; (c) Gasperini, A.; Johnson, M.; Jeanbourquin, X.; Yao, L.; Rahmanudin, A.; Guijarro, N.; Sivula, K., Semiconducting alternating multi-block copolymers via a di-functionalized macromonomer approach. *Polymer Chemistry* **2017,** *8* (5), 824-827; (d) Kipp, D.; Mok, J.; Strzalka, J.; Darling, S. B.; Ganesan, V.; Verduzco, R., Rational Design of Thermally Stable, Bicontinuous Donor/Acceptor Morphologies with Conjugated Block Copolymer Additives. *ACS Macro Letters* **2015,** *4* (9), 867-871.

15.   Oosterhout, S. D.; Savikhin, V.; Zhang, J.; Zhang, Y.; Burgers, M. A.; Marder, S. R.; Bazan, G. C.; Toney, M. F., Mixing Behavior in Small Molecule:Fullerene Organic Photovoltaics. *Chemistry of Materials* **2017,** *29* (7), 3062-3069.

16.   Min, J.; Cui, C.; Heumueller, T.; Fladischer, S.; Cheng, X.; Spiecker, E.; Li, Y.; Brabec, C. J., Side-Chain Engineering for Enhancing the Properties of Small Molecule Solar Cells: A Trade-off Beyond Efficiency. *Advanced Energy Materials* **2016,** *6* (14), 1600515-n/a.

17.   Jeanbourquin, X. A.; Rahmanudin, A.; Gasperini, A.; Ripaud, E.; Yu, X.; Johnson, M.; Guijarro, N.; Sivula, K., Engineering the self-assembly of diketopyrrolopyrrole-based molecular semiconductors via an aliphatic linker strategy. *Journal of Materials Chemistry A* **2017,** *5* (21), 10526-10536.

18.   Gasperini, A.; Jeanbourquin, X. A.; Rahmanudin, A.; Yu, X.; Sivula, K., Enhancing the Thermal Stability of Solution-Processed Small-Molecule Semiconductor Thin Films Using a Flexible Linker Approach. *Adv. Mater.* **2015,** *27* (37), 5541-5546.

19.   Walker, B.; Tamayo, A. B.; Dang, X.-D.; Zalar, P.; Seo, J. H.; Garcia, A.; Tantiwiwat, M.; Nguyen, T.-Q., Nanoscale Phase Separation and High Photovoltaic Efficiency in Solution-Processed, Small-Molecule Bulk Heterojunction Solar Cells. *Advanced Functional Materials* **2009,** *19* (19), 3063-3069.

20.   (a) Sharenko, A.; Kuik, M.; Toney, M. F.; Nguyen, T.-Q., Crystallization-Induced Phase Separation in Solution-Processed Small Molecule Bulk Heterojunction Organic Solar Cells. *Advanced Functional Materials* **2014,** *24* (23), 3543-3550; (b) Viterisi, A.; Gispert-Guirado, F.; Ryan, J. W.; Palomares, E., Formation of highly crystalline and texturized donor domains in DPP(TBFu)2:PC71BM SM-BHJ devices via solvent vapour annealing: implications for device function. *Journal of Materials Chemistry* **2012,** *22* (30), 15175-15182; (c) Fernandez, D.; Viterisi, A.; Ryan, J. W.; Gispert-Guirado, F.; Vidal, S.; Filippone, S.; Martin, N.; Palomares, E., Small molecule BHJ solar cells based on DPP(TBFu)2 and diphenylmethanofullerenes (DPM): linking morphology, transport, recombination and crystallinity. *Nanoscale* **2014,** *6* (11), 5871-8.

21.   Derue, L.; Dautel, O.; Tournebize, A.; Drees, M.; Pan, H.; Berthumeyrie, S.; Pavageau, B.; Cloutet, E.; Chambon, S.; Hirsch, L.; Rivaton, A.; Hudhomme, P.; Facchetti, A.; Wantz, G., Thermal Stabilisation of Polymer–Fullerene Bulk Heterojunction Morphology for Efficient Photovoltaic Solar Cells. *Advanced Materials* **2014,** *26* (33), 5831-5838.

22.   Dzwilewski, A.; Wågberg, T.; Edman, L., Photo-Induced and Resist-Free Imprint Patterning of Fullerene Materials for Use in Functional Electronics. *Journal of the American Chemical Society* **2009,** *131* (11), 4006-4011.

23.   (a) Dkhil, S. B.; Pfannmöller, M.; Saba, M. I.; Gaceur, M.; Heidari, H.; Videlot-Ackermann, C.; Margeat, O.; Guerrero, A.; Bisquert, J.; Garcia-Belmonte, G.; Mattoni, A.; Bals, S.; Ackermann, J., Toward High-Temperature Stability of PTB7-Based Bulk Heterojunction Solar Cells: Impact of Fullerene Size and Solvent Additive. *Advanced Energy Materials* **2016**, 1601486-n/a; (b) Tada, K., Thermally robust bulk heterojunction photocells based on PTB7:C70 composites. *Solar Energy Materials and Solar Cells* **2015,** *132*, 15-20; (c) Wu, C.-G.; Chiang, C.-H.; Han, H.-C., Manipulating the horizontal morphology and vertical distribution of the active layer in BHJ-PSC with a multi-functional solid organic additive. *Journal of Materials Chemistry A* **2014,** *2* (15), 5295-5303.

24.   (a) Leong, W. L.; Cowan, S. R.; Heeger, A. J., Differential Resistance Analysis of Charge Carrier Losses in Organic Bulk Heterojunction Solar Cells: Observing the Transition from Bimolecular to Trap-Assisted Recombination and Quantifying the Order of Recombination. *Advanced Energy Materials* **2011,** *1* (4), 517-522; (b) Credgington, D.; Durrant, J. R., Insights from Transient Optoelectronic Analyses on the Open-Circuit Voltage of Organic Solar Cells. *J. Phys. Chem. Lett.* **2012,** *3* (11), 1465-1478.

25.   Burtone, L.; Fischer, J.; Leo, K.; Riede, M., Trap states in ZnPc:C60 small-molecule organic solar cells. *Physical Review B* **2013,** *87* (4), 045432.

26.   (a) Nam, C.-Y.; Qin, Y.; Park, Y. S.; Hlaing, H.; Lu, X.; Ocko, B. M.; Black, C. T.; Grubbs, R. B., Photo-Cross-Linkable Azide-Functionalized Polythiophene for Thermally Stable Bulk Heterojunction Solar Cells. *Macromolecules* **2012,** *45* (5), 2338-2347; (b) Chen, L.; Li, X.; Chen, Y., Inter-crosslinking through both donor and acceptor with unsaturated bonds for highly efficient and stable organic solar cells. *Polymer Chemistry* **2013,** *4* (23), 5637-5644; (c) Miyanishi, S.; Tajima, K.; Hashimoto, K., Morphological Stabilization of Polymer Photovoltaic Cells by Using Cross-Linkable Poly(3-(5-hexenyl)thiophene). *Macromolecules* **2009,** *42* (5), 1610-1618.

27.   (a) Heumueller, T.; Mateker, W. R.; Distler, A.; Fritze, U. F.; Cheacharoen, R.; Nguyen, W. H.; Biele, M.; Salvador, M.; von Delius, M.; Egelhaaf, H.-J.; McGehee, M. D.; Brabec, C. J., Morphological and electrical control of fullerene dimerization determines organic photovoltaic stability. *Energy & Environmental Science* **2016,** *9* (1), 247-256; (b) Li, Z.; Wong, H. C.; Huang, Z.; Zhong, H.; Tan, C. H.; Tsoi, W. C.; Kim, J. S.; Durrant, J. R.; Cabral, J. T., Performance enhancement of fullerene-based solar cells by light processing. *Nat. Commun.* **2013,** *4*, 2227.

28.   Kahle, F.-J.; Saller, C.; Köhler, A.; Strohriegl, P., Crosslinked Semiconductor Polymers for Photovoltaic Applications. *Advanced Energy Materials*, 1700306-n/a.

CHAPTER 3

Stabilizing the Bulk Heterojunction Morphology of a Small Molecule Organic Solar Cell based on a Perylenediimide Acceptor *via* a Compatbilization Approach

Abstract

Here, we demonstrate the versatility of the compatibilization approach on a challenging highly crystalline small-molecule BHJ based on a diketopyrrolopyrrole based donor coded, DPP(TBFu)$_2$, with a perylenediimide acceptor coded, EP-PDI, and its molecular compatibilizer (MCP). It was found that MCP was able to slow down phase segregation of the BHJ under thermal stress (at 110°C for 480 min), while preserving device performance. After a slight initial decrease in performance over 70 min, the performance with 1 and 10wt% of MCP decreased by 43% and 7% respectively after thermal treatment at 110°C for 480 min. On the other hand, the BHJ without MCP reflected a significant decrease in PCE by 78%. BHJ morphology characterization *via* differential scanning calorimetry, grazing incidence X-ray diffraction, and photoluminescence emission, revealed insights into the relation between molecular order and phase segregation with respect to the device performance. Overall, the results demonstrate that the compatibilization approach is able to stabilize a highly crystalline small-molecule BHJ morphology and its resulting device performance. This reinforces the conclusion that this method is robust and versatile in engineering efficient and thermally stable BHJ organic solar cells.

3.1 Introduction

As demonstrated in the previous chapter, the compatibilization approach (CP) showed promise in engineering efficient and thermally stable OPVs for solution processed small–molecule BHJs based on a DPP(TBFu)$_2$:PC$_{61}$BM blend. In order to validate this concept further, this chapter will present the utilization of the CP approach on a challenging system with an acceptor molecule based on a perylenediimide (PDI) derivative known as EP-PDI. Generally, PDI based semiconductors are seen as candidates to replace fullerene acceptors mainly due to their photochemical stability, strong optical absorption, and low cost[1]. However, device performances have been limited due to its highly crystalline nature where it is prone to over crystallization upon solution processing from a BHJ blend[1], as well as a tendency to de-mix at room temperature[i]. Recent efforts to engineer its crystallinity by twisting its planar core has shown to suppress aggregation leading to improved device performance,[2] but such molecular systems still require multistep synthesis that potentially increases production cost akin to fullerene acceptors. Hence, the aim of this chapter is to demonstrate the versatility of the compatibilizer approach in stabilizing a highly crystalline BHJ system based on non-fullerene based acceptors.

3.2 Synthesis and the characterization of the Molecular Compatibilizer
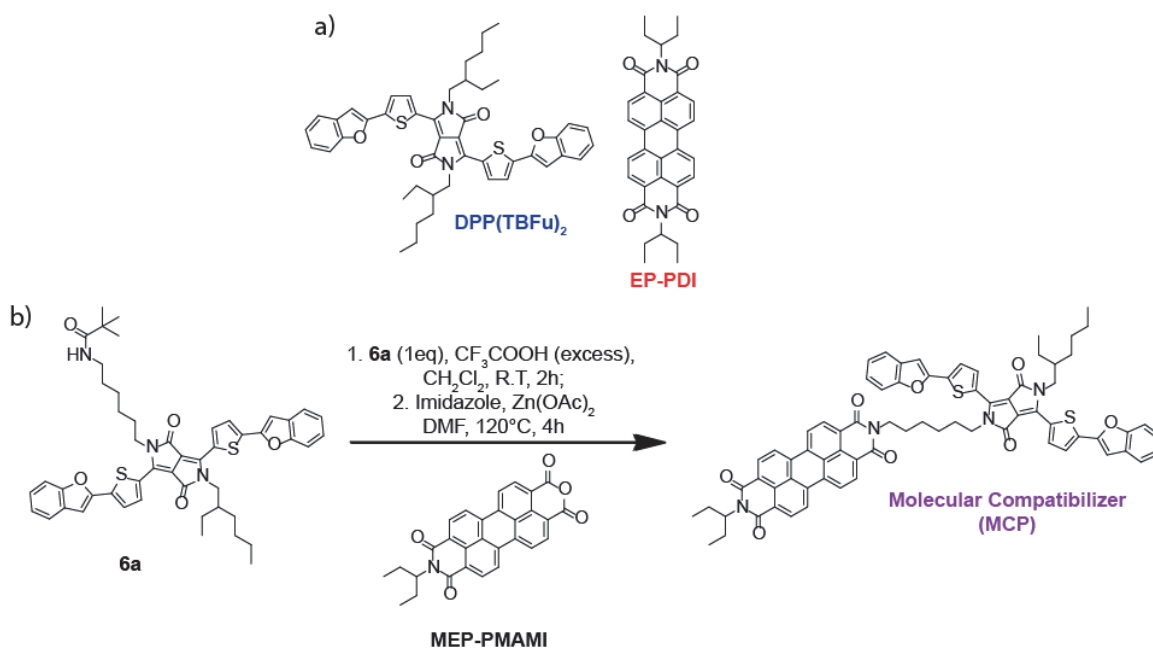
Figure 1. a) Primary small-molecule semiconductors used in this study with DPP(TBFu)₂ as donor and EP-PDI as acceptor; b) the synthetic route of the molecular compatibilizer.

In this study the primary BHJ components used is based on DPP(TBFu)$_2$ as a donor and EP-PDI as an acceptor (See Figure 1a). The molecular compatibilizer (MCP) was synthesized by first de-protecting the n-tert-butyloxycarbony group on 6a (See Chapter 2 Figure1b for synthetic route of 6a), to activate the terminal primary amine for a condensation reaction with the anhydride on MEP-PMAMI with Zn(OAc)$_2$, dissolved in a mixture of imidazole and DMF at 120°C (See Figure 1b). On the other hand, EP-PDI was selectively mono-dealkylated *via* a controlled hydrolysis reaction under basic conditions of KOH (85%) with *t*-BuOH in reflux over a period of 2 hours to obtain MEP-PMAMI. The chemical structures are fully characterized by ^{1}H NMR, ^{13}C NMR, and MALDI-TOFF MS (See Appendix 3 for supporting information (SI) on the full synthetic route and characterization of MCP). The ^{1}H NMR spectrum of the MCP in CDCl$_3$ solution shows sharp peaks in the aromatic region (See appendix 3 Figure S1a.). For instance, at the region between 8.45 -8.70 ppm, it shows four pairs of sharp doublets representing the eight protons on the perylene core moiety. This clearly indicates that the EP-PDI unit on the MCP is freely rotating in solution, and does not fold onto the DPP(TBFu)$_2$ unit at the flexible

aliphatic hexyl chain, suggesting that the MCP does not aggregate and remains sufficiently soluble in solution.[ii] As expected, the absorption spectra of the MCP in solution consists of the absorption of the DPP(TBFu)$_2$ and EP-DPI units, suggesting that the optoelectronic properties of the π-conjugated core is not severely affected (See appendix 3 Figure S1b.). Differential scanning calorimetry (DSC) of MCP did not reveal any obvious phase transition while no scattering peaks was seen in the X-ray Diffraction (XRD) of the thin films of MCP, indicating that it is not strongly crystalline in solid state (See appendix 3 Figure S1c and d).

3.3 The Effect of MCP on the BHJ Morphology

DSC was used to investigate the effect of MCP on the phase behavior of the BHJ (See Figure 2a and see appendix 3 table S1 for the endothermic enthalpy and temperature onset values). The first heating scan performed on a 1:1 blend (drop cast from chloroform) with 0wt% of MCP revealed two separate endothermic transitions attributed to the melting transition of crystalized DPP(TBFu)$_2$, at an onset of ca 212°C,[3] and a liquid phase mesophase transition of EP-PDI at ca 65°C.[4] As the amount of MCP increased to 1wt%, the endothermic transition of DPP(TBFu)$_2$ slightly increased while the enthalpy for EP-PDI showed a minor decrease, but as the amount of MCP increased to 10wt%, the endothermic enthalpy of DPP(TBFu)$_2$ and EP-PDI decreased by approximately 50% and 70%, respectively. This suggests a significant disruption of the molecular order with increasing MCP loading in the BHJ. To further support this claim, XRD scattering in the out-of-plane direction was characterized on spin coated thin films, consisting of the BHJ blends that were annealed at 110°C for 1 h (See Figure 2b). The XRD patterns revealed two clear scattering peaks at 2θ = 6.28° related to the (020) deflection of DPP(TBFu)$_2$, and at 2θ = 5.4° for the (200) deflection of EP-PDI[5] across all MCP loadings (as indexed from previous reports[6]). The intensity of the (020) peak increased slightly at 1wt% of MCP, but decreases after the addition of 10wt% of MCP. Conversely, the (200) peak for EP-PDI showed a gradual decrease in peak intensity with increasing MCP loading. This corresponds closely to the DSC results implying that the molecular ordering of DPP(TBFu)$_2$ in the BHJ improves perhaps slightly at 1wt% of

MCP, but decreases as the amount increases to 10wt%, while a gradual decrease in the ordering of EP-PDI follows closely with increase amounts of MCP.
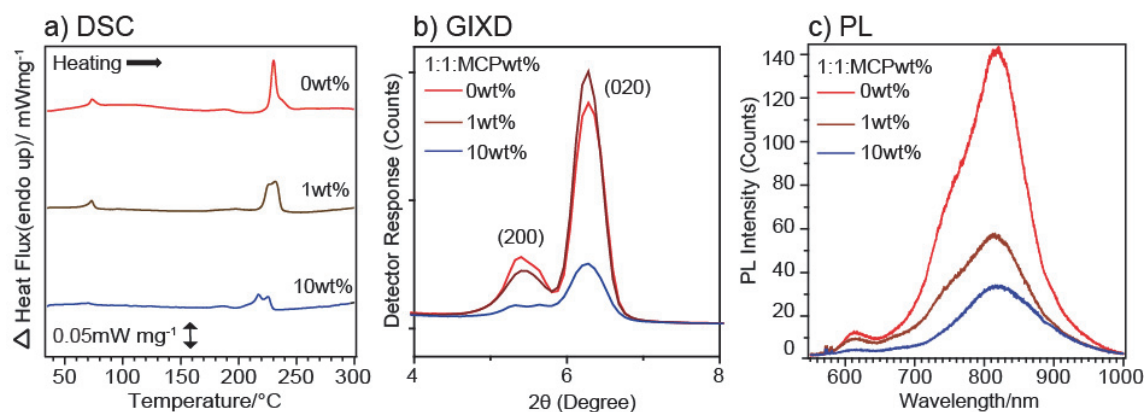
Figure 2. a) Differential scanning calorimetry of the 1st heating scan of the primary components and 1:1 blend with 1 and 10wt% of MCP at a scan rate of 10°C/min; Thin film characterization of the BHJ blend with 1 and 10wt% of MCP were annealed at 110°C for 1h: b) Grazing Incidence X-ray Diffraction in the out of plane direction; c) Photoluminescence Spectra after excitation at 532nm.

Photoluminescence (PL) emission spectra of annealed BHJ thin films were then acquired to assess the photogenerated exciton quenching (See Figure 2c and see appendix 3 Fig S2 for PL spectra of the individual components). Upon excitation of the BHJ films at 532nm, a prominent quenching of two peaks attributed to the PL emission of DPP(TBFu)$_2$ at 816nm and EP-PDI at 610nm with increasing amount of MCP was observed. The increase in quenching suggests that a higher probability of exciton separation occurs, as a result of enhancements in interfacial area between the donor-acceptor domains similarly observed in the CP system of DPP(TBFu)$_2$:PC$_{61}$BM discussed in chapter 2.[3b] Notably, it is interesting to note that at 1wt% of MCP, the DSC and GIXD data suggest that DPP(TBFu)$_2$ has a slightly enhanced molecular ordering in the BHJ, despite an increase in intermixing between the donor-acceptor domains.

3.4 Photovoltaic Performance and Device stability

Now that it is established that MCP has an effect on the molecular ordering and phase segregation of the BHJ, to elucidate the photovoltaic stability of the BHJ under prolonged thermal annealing, standard ITO/PEDOT:PSS/BHJ/Al solar cell devices were prepared with a BHJ at 1:1 - DPP(TBFu)$_2$:EP-PDI by

weight ratio. All devices were subjected to thermal stress at 110°C with the top electrode on top of the spun coated BHJ over a period of 480 min (8h) to drive the crystallization and phase segregation of the primary components, and the current density-voltage (J-V) characteristics were measured periodically under standard 1 sun illumination upon cooling the devices to room temperature. The power conversion efficiency (PCE) as a function of the thermal treatment time is shown in Figure 3a with respect to the included MCP loading in the BHJ. J-V curves at the time point corresponding to the highest PCE for each MCP loading shown in Figure 3b. Full device performance metrics are also included in appendix 3 in Table S2.

At 0wt% of MCP, the performance observed an increase to achieve its highest PCE of 1.6% PCE after 10 min of annealing (red trace in Figure 3a). This increase in performance from an as-cast state is attributed to the initial stages of crystallization to obtain an optimum BHJ phase segregation, similarly observed in the DPP(TBFu)$_2$:PC$_{61}$BM BHJ devices (See Chapter 2 Figure 2.). Subsequent thermal treatment drives further phase segregation and the performance of the device decreased by 78% to a PCE of 0.36% after 490 min. The addition of 1wt% of MCP into the BHJ resulted in a slightly higher best PCE of 1.7% after 10 min of annealing due to increases in FF and J$_{sc}$ (brown trace in Figure 2a.), while an improvement in PCE to 1.27% was similarly observed for the BHJ with 10wt% of MCP (blue trace in Figure 2a.). The BHJ with 1wt% of MCP showed a higher performance as compared to the BHJ at 0 and 10 wt% of MCP. This is likely due to the enhancement in molecular ordering of DPP(TBFu)$_2$ (See DSC and GIWAXS data in Figure 2a and b) and enhanced intermixing between the donor-acceptor domains (See PL quenching in Figure 2c) in the BHJ, which could facilitate charge transport and exciton separation. Conversely the lower performance of best PCE at 10wt% of MCP is reasonably due to a lower degree of molecular ordering that could likely hamper charge transport in the BHJ.

Interestingly, devices with 1 and 10wt% of MCP showed an initial sharp decrease in PCE to 1.4% and 1.03% respectively after thermal treatment of 70 min, but the performance relatively stabilized upon further annealing to 250 min with only a loss of 0.08% and 0.06% in PCE accordingly. The BHJ with

1wt% of MCP then showed a distinct decrease by 43% to 0.81% PCE, while the performance of BHJ

with 10wt% of MCP remained remarkably stable with only a loss of 7% to 0.96% PCE over the thermal

treatment period of 480 min. The stability in PCE observed here is similar to the CP system of

DPP(TBFu)$_2$:PC$_{61}$BM discussed in chapter 2, where an enhanced stability is induced at a higher amount

of the compatiblizer in the BHJ.
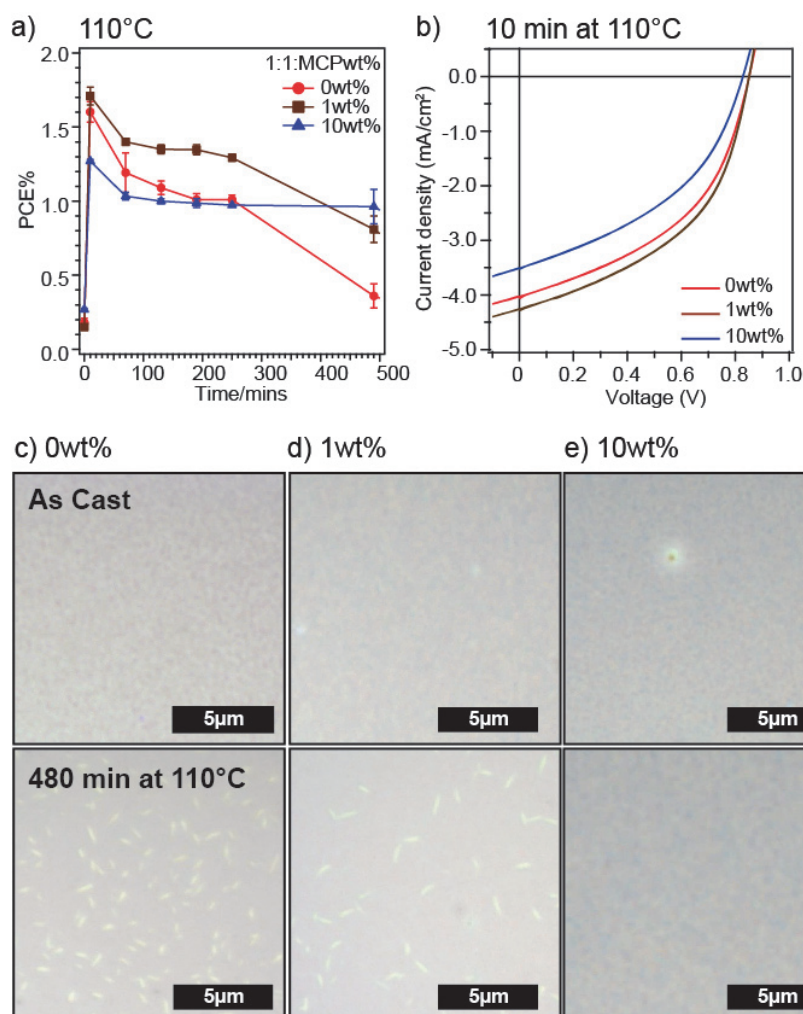
Figure 7. a) Photovoltaic performance with respect to thermal stress at 110°C over a period of 480 min of devices containing 1:1 Blends of DPP(TBFu)$_2$:EP-PDI with 1 and 10wt% of MCP; b) Current density vs voltage curves of devices at after annealing at 110°C for 10 minutes.

Further evidence from the optical micrographs of as cast thin films of the BHJ across all MCP loading

showed a relatively featureless morphology (See Figure 3 c-e top images), but upon annealing at 110°C

for 8 hours (the length of the thermal stability test), thin films with 0wt% of MCP revealed crystallite

formation of about 1μm in size (See Figure 3a bottom image). BHJ thin films with 1 wt% of MCP also observed a similar morphology but with a relatively lower amount of crystallites as compared to thin films at 0wt% of MCP, while the BHJ with 10wt% of MCP showed a relatively similar optical micrographs before and after thermal treatment (See Figure 3c). The observation in the optical micrographs suggest a difference in evolution of the crystallization and phase separation of the BHJ, which correlates well with the OPV stability results where the BHJ with 10wt% of MCP revealed remarkable stability over a period of 480 min at 110°C as compared to the BHJ performance with 0 and 1 wt% of MCP. Moreover, the suppression of BHJ crystallinity and phase segregation coincides well with the DSC and GIXD data shown in Figure 2a and b that suggests a gradual disruption in crystallinity of the components in BHJ with increasing MCP loadings.

3.5 Conclusion

In conclusion, we have demonstrated the compatibilizer approach is able to control the crystallization and phase segregation of a BHJ containing two highly crystalline small molecules DPP(TBFu)$_2$ and EP-PDI. The control over crystallization of the BHJ was reflected in the relative overall depression in enthalpy of endothermic transitions shown in the DSC data, and a decrease scattering intensity of the peaks reflected in the XRD data with increasing MCP loading. Notably, the BHJ with 1 wt% of MCP showed a slight enhancement in molecular order of DPP(TBFu)$_2$ as indicative of a higher intensity of the (020) defection peak, and a higher level of intermixing in the BHJ as observed in the increase in PL quenching. This resulted in a higher best PCE of 1.7% likely due to enhanced charge transport and exciton separation in the BHJ, as compared to devices with 0 and 10wt% of MCP. On the other hand, the lowest best performance at 10wt% of MCP is likely due to a lack of molecular order in the BHJ, as shown from a lower scattering intensity from the GIXD data, despite having the highest level intermixing as reflected from a higher PL quenching. In relation to the stability of the BHJ with respect to the device performance, increasing the amount of MCP in the BHJ slowed down phase segregation, which resulted in the preservation of PCE, particularly with 10wt% of MCP in the BHJ where the device

performance remained relatively stable over the testing period of 480 min, following an initial decrease during the first 70 min. Optical micrographs of the BHJ thin films at 10wt% of MCP also revealed the suppression of crystallite formation before and after prolonged thermal treatment. Overall based on the insights revealed in the compatibilization approach to stabilize a highly crystalline small-molecule BHJ system, the next chapter will build upon this understanding to demonstrate the use of MCP in engineering a melt-compatibilization processing technique for a stable and functional BHJ for OPV.

3.6 References

1.   Namepetra, A.; Kitching, E.; Eftaiha, A. a. F.; Hill, I. G.; Welch, G. C., Understanding the morphology of solution processed fullerene-free small molecule bulk heterojunction blends. *Physical Chemistry Chemical Physics* **2016,** *18* (18), 12476-12485.

2.   (a) Guo, Y.; Li, Y.; Awartani, O.; Zhao, J.; Han, H.; Ade, H.; Zhao, D.; Yan, H., A Vinylene-Bridged Perylenediimide-Based Polymeric Acceptor Enabling Efficient All-Polymer Solar Cells Processed under Ambient Conditions. *Advanced Materials* **2016,** *28* (38), 8483-8489; (b) Liu, S.-Y.; Wu, C.-H.; Li, C.-Z.; Liu, S.-Q.; Wei, K.-H.; Chen, H.-Z.; Jen, A. K. Y., A Tetraperylene Diimides Based 3D Nonfullerene Acceptor for Efficient Organic Photovoltaics. *Advanced Science* **2015,** *2* (4), n/a-n/a; (c) Singh, R.; Aluicio-Sarduy, E.; Kan, Z.; Ye, T.; MacKenzie, R. C. I.; Keivanidis, P. E., Fullerene-free organic solar cells with an efficiency of 3.7% based on a low-cost geometrically planar perylene diimide monomer. *Journal of Materials Chemistry A* **2014,** *2* (35), 14348-14353; (d) Sharenko, A.; Proctor, C. M.; van der Poll, T. S.; Henson, Z. B.; Nguyen, T.-Q.; Bazan, G. C., A High-Performing Solution-Processed Small Molecule:Perylene Diimide Bulk Heterojunction Solar Cell. *Advanced Materials* **2013,** *25* (32), 4403-4406; (e) Kamm, V.; Battagliarin, G.; Howard, I. A.; Pisula, W.; Mavrinskiy, A.; Li, C.; Müllen, K.; Laquai, F., Polythiophene:Perylene Diimide Solar Cells – the Impact of Alkyl-Substitution on the Photovoltaic Performance. *Advanced Energy Materials* **2011,** *1* (2), 297-302.

3.   (a) Jeanbourquin, X. A.; Rahmanudin, A.; Gasperini, A.; Ripaud, E.; Yu, X.; Johnson, M.; Guijarro, N.; Sivula, K., Engineering the self-assembly of diketopyrrolopyrrole-based molecular semiconductors via an aliphatic linker strategy. *Journal of Materials Chemistry A* **2017,** *5* (21), 10526-10536; (b) Rahmanudin, A.; Jeanbourquin, X. A.; Hanni, S.; Sekar, A.; Ripaud, E.; Yao, L.; Sivula, K., Morphology stabilization strategies for small-molecule bulk heterojunction photovoltaics. *Journal of Materials Chemistry A* **2017**.

4.   (a) Keivanidis, P. E.; Howard, I. A.; Friend, R. H., Intermolecular Interactions of Perylene diimides in Photovoltaic Blends of Fluorene Copolymers: Disorder Effects on Photophysical Properties, Film Morphology and Device Efficiency. *Advanced Functional Materials* **2008,** *18* (20), 3189-3202; (b) Dittmer, J. J.; Lazzaroni, R.; Leclère, P.; Moretti, P.; Granström, M.; Petritsch, K.; Marseglia, E. A.; Friend, R. H.; Brédas, J. L.; Rost, H.; Holmes, A. B., Crystal network formation in organic solar cells. *Solar Energy Materials and Solar Cells* **2000,** *61* (1), 53-61.

5.   Liang, Q.; Han, J.; Song, C.; Wang, Z.; Xin, J.; Yu, X.; Xie, Z.; Ma, W.; Liu, J.; Han, Y., Tuning molecule diffusion to control the phase separation of the p-DTS(FBTTh2)2/EP-PDI blend system via thermal annealing. *Journal of Materials Chemistry C* **2017,** *5* (27), 6842-6851.

6.   (a) Sharenko, A.; Gehrig, D.; Laquai, F.; Nguyen, T.-Q., The Effect of Solvent Additive on the Charge Generation and Photovoltaic Performance of a Solution-Processed Small Molecule:Perylene Diimide Bulk Heterojunction Solar Cell. *Chemistry of Materials* **2014,** *26* (14), 4109-4118; (b) Viterisi, A.; Gispert-Guirado, F.; Ryan, J. W.; Palomares, E., Formation of highly crystalline and texturized donor domains in DPP(TBFu)2:PC71BM SM-BHJ devices via solvent vapour annealing: implications for device function. *Journal of Materials Chemistry* **2012,** *22* (30), 15175-15182.

Chapter 4

Melt-processing of Small Molecule Organic Photovoltaics via Bulk Heterojunction Compatibilization

Abstract

Melt-processing of organic semiconductors (OSCs) is potentially an environmentally friendly technique that alleviates the need to use toxic chlorinated solvents. Aside from a handful of examples of melt-processed single-component OSCs in field-effect-transistors, processing of binary component bulk heterojunctions (BHJs) for organic photovoltaics (OPVs) still remain a challenge. Herein, we demonstrate a melt-compatibilization of a strongly-crystalline molecular BHJ system based on a diketorpyrrolopyrrole donor and a perylenediimde acceptor molecule with a molecular compatibilizing additive (MCP). BHJ morphological characterization using atomic force and kelvin probe microscopy, X-ray diffraction and photoluminescence measurements suggests that high crystallinity drives phase segregation in the BHJ, while MCP affords tunabilility of domains size by achieving a homogenous single-phase melt during melt-annealing. An optimum photoactive BHJ at a 1:1 donor:acceptor ratio with 50wt% MCP, achieved an efficiency of approximately 1%. Furthermore, a functional OPV was also obtained from melt-processing of micron-sized solid dispersions of the BHJ with MCP. These results demonstrate that molecular compatbilization is a key prerequisite for further developments towards true solvent-free melt processed BHJ OPV systems.

4.1 Introduction

Organic photovoltaic (OPV) devices, which rely on a bulk-heterojunction (BHJ) between polymeric or small-molecule carbon-based p-type (electron donor) and n-type (electron acceptor) semiconductors, have attracted significant interest given their promise for achieving high performance while also being low-cost and amenable with scalable roll-to-roll manufacturing.[1] While the ongoing development of OPVs has led to impressive power conversion efficiency >10%, typical state-of-the-art devices are fabricated using toxic chlorinated or aromatic solvents,[2] which undermines their sustainable application at a global scale. Processing in environmentally-benign "green" solvents, is a potential alternative,[3] but requires altering the molecular structure of the organic semiconductors (OSCs) to afford solubility, or dispersing the OSCs in colloidal systems, both of which greatly affect the OSC solid-state self-assembly and resulting optoelectronic properties.[4] Alternatively, melt processing, which involves a reversible liquefaction-solidification process and is widely used in industry to produce commodity plastic thin films,[5] could be employed to afford the solvent-free manufacture of OPVs. However, while melt-processing techniques have been recently studied and developed for single-component OSC devices (e.g. field effect transistors),[6] and despite the suggested similarities between solvent quenching and melt quenching techniques from thermodynamic arguments,[7] the processing of BHJ OPV devices from homogeneous liquid melts into high efficiency OPVs has yet to be demonstrated due to the extreme sensitivity of the BHJ morphology on the device performance. Indeed a percolating network of precisely-sized nanometer donor/acceptor domains in the BHJ is required for high OPV efficiency.[8] While the optimum BHJ morphology can be readily tuned using solvent processing techniques,[9] similar morphology control in melt-processed BHJs remains a challenge.

The use of donor-acceptor block-copolymers[10] is a rational route to control the size of donor/acceptor domains under melt-processing conditions given the covalent link between the two components that prevents the macro-scale phase segregation, which is the thermodynamically preferred solid-sate

arrangement of typical BHJ components. Indeed, Lombeck et al. recently reported a donor-acceptor block-copolymer-based system that afforded promising performance in melt-annealed OPVs.[11] However this work also established that the alteration of component molecular structure (through side-chain fluorination) is required for this approach to produce a system wherein the donor and acceptor components remain phase-separated in the melt to ensure that that they form the required nanometer phase segregated BHJ upon solidification. In addition to this drawback, the processing of the requisite nano-phase separated melts poses additional challenges (e.g. due to shear-induced domain alignment[12]) toward obtaining the BHJ optimum morphology.

An ideal melt-processed BHJ OPV system would allow a single phase liquid melt to be converted into a nanostructured BHJ with tunable domain sizes in a robust and reproducible manner. We hypothesized that this could be accomplished with strongly-crystalline molecular donor and acceptor components (to drive phase separation in the solid state) together with a molecular compatiblizing additive (consisting of the molecular donor and acceptor covalently attached with a non-conjugated linker)[13] to afford tunability of the BHJ phase domains. Herein we demonstrate this melt-compatibilization approach based on a molecular BHJ system with two common OSCs; a diketopyrrolopyrrole-based donor and a perylene diimide acceptor, both which are known to strongly crystalize in the solid state. We establish that the use of a molecular compatibilizer is essential to tune the BHJ and obtain functional OPVs via melt annealing. Furthermore, we demonstrate a strategy towards the "green" processing of BHJ thin films via a solid dispersion, melt-processing technique.

4.2 Establishing Melt Processing Conditions

The molecular structures of the electron donor, coded as DPP(TBFu)$_2$,[14] and acceptor (coded as EP-PDI), both chosen based on their established high crystallinity in BHJs,[15] are shown in Figure 1a along with the corresponding molecular compatibilizer (MCP). Detailed synthesis and characterization of the MCP is given in Chapter 3.1. In order to first establish the solid-state phase behavior and melt-processing conditions, differential scanning calorimetry (DSC) was performed on solvent-cast BHJ

blends (1:1 donor:acceptor by weight) with varying wt% of added MCP (see Figure 1b). For the control BHJ (0 wt% MCP) during the first heating scan, two separate endothermic transitions were observed and are attributed to a liquid-crystal mesophase transition[16] in EP-PDI at T_{LC} = 73°C (the melting temperature of EP-PDI is above 350°C[6c]) and the melting[17] of DPP(TBFu)$_2$ at T_m = 231°C (Similarly observed in Chapter 3.1, and see DSC scans for the pure components Appendix 3 Figure S1c). These transitions were both observed to be reversible upon cooling. A loading of MCP of 10 or 25 wt% in the BHJ leads to a decrease in the enthalpy (see Appendix 4 Table S1, for specific component enthalpies) and a depression of transition temperatures as expected for a compatibilizer.[13] However these results suggest that the donor and acceptor retain the ability to recrystallize from the melt in the presence of significant amounts of the MCP. Notably, no obvious transitions were observed with 50 or 75 wt% MCP, suggesting a disruption of crystallinity in both DPP(TBFu)$_2$ and EP-PDI with sufficiently high MCP loading. The pure compatibilizer (100 wt% MCP) also shows no phase transition, suggesting no long range crystalline ordering in this material, consistent with similar systems.[18]
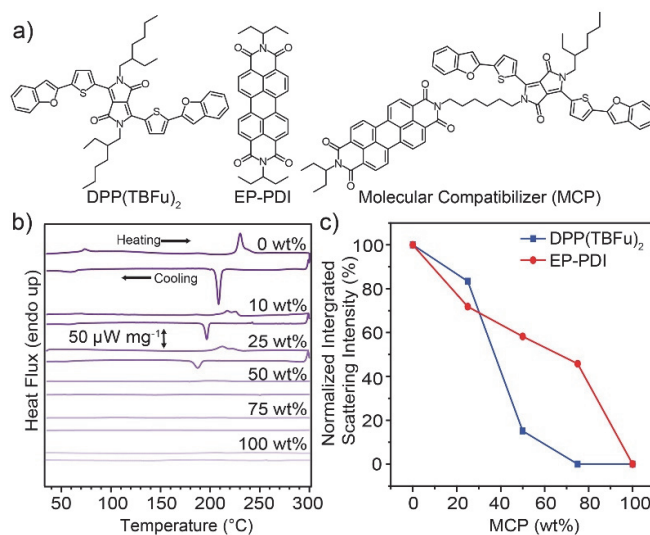
Figure 1. a) Molecular structures of the organic semiconductors used in this study: DPP(TBFu)$_2$, EP-PDI and the molecular compatibilizer (MCP). b) DSC of the first heating/cooling scans (10°C min^{-1}) of 1:1 donor:acceptor BHJs with varying MCP loading (wt%). c) Normalized integrated XRD scattering intensity of the (020) peak of DPP(TBFu)$_2$ and the (200) peak of EP-PDI in 1:1 BHJ films treated at 240°C (15 min) and cooled to rt. The normalization was performed with respect to the control (0 wt%) BHJ. The XRD data was collected from the grazing incidence geometry in the out-of-plane direction (see Appendix 4 Figure S1a, for the XRD patterns).

The trend in the molecular ordering in the presence of the MCPas implied by the DSC, was further investigated by x-ray diffraction (XRD) measurements of BHJ films treated at 240°C (above T_m of the donor) and cooled to ambient temperature. Diffraction peaks for both the DPP(TBFu)$_2$ and EP-PDI (as indexed from previous reports[19]) were observed in the melt-annealed BHJ films (see Appendix 4 Figure S1a), and the relative crystallinity of each component in the BHJs with added MCP was estimated by peak integration. The normalized trends are shown in Figure 1c. For the DPP(TBFu)$_2$ these results agree qualitatively with the DSC data and confirm that the donor retains some crystallinity even after melting/cooling in the presence of the MCP. In addition, the XRD measurements show that the molecular ordering of the donor exists even after melting with 50 wt% MCP, in contrast to the DSC where no clear transition was detected (likely due to peak broadening). This contrast is greater with the EP-PDI, where the XRD data suggest that, while the crystallinity does decrease with added MCP loading, a significant amount of acceptor phase ordering remains present in films with 75 wt% MCP. Given the high melting point of the EP-PDI (> 350°C) this calls into question the nature of the acceptor phase at 240°C in the presence of the (melted) donor and MCP. To clarify this, we performed *in situ* XRD measurements of BHJ films with and without the MCP at 240°C (see Appendix 4 Figure S1b). These results clearly indicate an absence of crystallinity of the EP-PDI at 240°C even without the MCP present, consistent with the donor and acceptor forming a single homogeneous liquid phase at a temperature above the melting temperature of the donor phase, similar to other systems.[7a, 7b] Thus overall, the DSC and XRD results confirm that the DPP(TBFu)$_2$:EP-PDI BHJ blend can be processed from a homogenous melt phase at 240°C into the solid state, while retaining the crystallinity of both components. Moreover, the degree of crystallinity of both phases can be tuned by adding the MCP.

4.3 BHJ Morphology Characterization
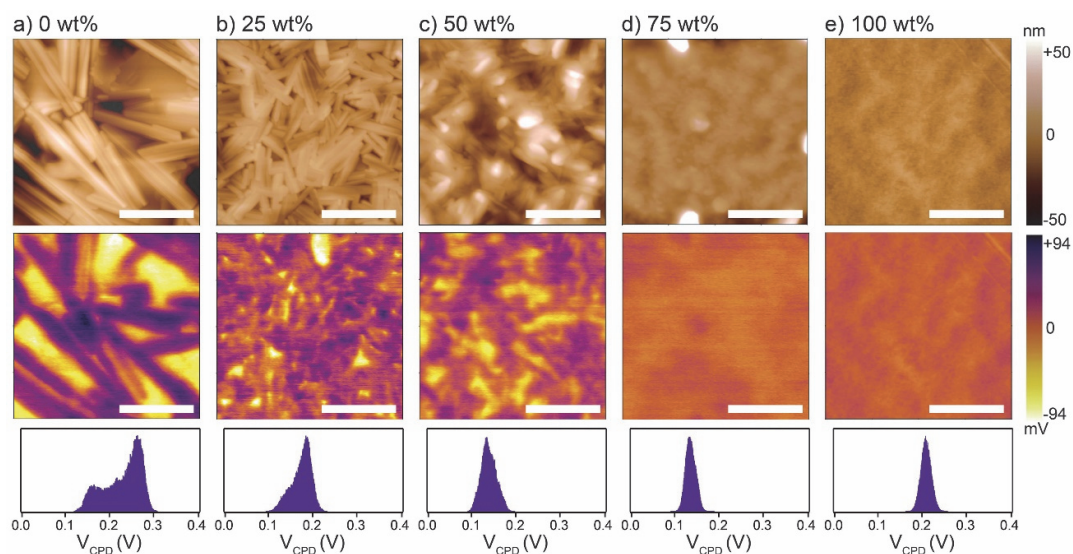
Figure 2. Morphological characterization of melt-annealed (240°C) BHJ thin films of DPP(TBFu)$_2$:EP-PDI (1:1 by weight) with varying amount of MCP (a-d) and pure MCP (e). Height topography (top panel) and KPFM potential images (middle panel) were measured under dark ambient conditions. The scale bars are 400 nm. The bottom panel shows the contact potential difference, V$_{CPD}$, histogram for each KPFM image.

To next investigate the effect of the MCP on the BHJ morphology, melt-annealed (240°C) thin films were examined by atomic force and kelvin probe force microscopy (AFM and KPFM, respectively). Relative height and surface potential difference maps are shown in Figure 2 for 1:1 donor:acceptor BHJs with different MCP loading. The height maps show rod-like crystallite domains hundreds of nanometers in length in the control (0 wt%) BHJ, which are diminished in size with increasing amount of MCP. While some crystalline features are visible in the 50 wt% film, the 75 wt% film appears essentially homogeneous with a morphology similar to the pure MCP (100 wt%) film. The chemical nature of the phase domains was further assessed with the KPFM maps where the absolute values of the surface potential difference (*i.e.* the difference in potential between the Pt tip and the surface) were related to the pure component phases (as established by measurements on pure component thin films, see Appendix 4 Figure S2). Briefly, the donor phase is expected to appear with a lower contact potential difference, V$_{CPD}$, in the BHJ compared to the acceptor phase. Therefore, the KPFM map of the control BHJ (0 wt%) exhibits a clear phase segregation between the platelet-shaped crystals of

73

DPP(TBFu)$_2$ (yellow) and the rod-like crystals of EP-PDI (purple). The extent of the phase segregation is also indicated by the V$_{CPD}$ histogram (bottom panel Figure 2), which shows a bimodal distribution. With increasing MCP loading and the corresponding change in topographical morphology, the KPFM data show a decrease in the size of the donor and acceptor domains and an increase in donor:acceptor mixing in the BHJ as implied by the V$_{CPD}$ histograms, which become increasingly narrow. Importantly, even with 50 wt% MPC after melt-annealing, it appears that some degree of phase segregation still occurs, while at 75 wt% a surface potential homogeneity similar to the pure MCP is observed (we note that the tip radius convolution prevents resolution of phase domains below approximately 20 nm). Therefore, we conclude that the level of donor:acceptor intermixing and the phase domain sizes in melted BHJs can be modulated with varying MCP loading. To further support this claim, photoluminescence (PL) emission of the respective thin films were characterized (see Appendix 4 Figure S3). Upon excitation of the BHJ films at 532nm, a prominent quenching of two peaks attributed to the PL emission of DPP(TBFu)$_2$ (observed at 816 nm) and EP-PDI (610 nm) with increasing amount of MCP is noted. Since PL quenching corresponds to an increased probability for photogenerated excitons to reach the donor-acceptor interface and undergo charge separation (instead of radiative recombination) this trend corresponds well with the morphological changes exhibited in the KPFM analysis.

4.4 Photovoltaic Performance

To investigate the relation between the BHJ phase segregation after melt-annealing and the, photovoltaic performance, devices with an inverted architecture (substrate/ITO/ZnO/BHJ/MO$_3$/Ag) were fabricated and tested under standard 1 Sun illumination. The BHJ was solvent-cast (from chloroform solution) followed by melt-annealing at 240°C (15 min) before deposition of the top blocking layer and electrode (details of device fabrication and testing are given in the Appendix 4). Representative current density-voltage (J-V) curves for devices prepared with different MCP loadings are shown in Figure 3a, while the corresponding performance parameters and external quantum

efficiency (EQE) are given in Appendix 4 Figure S4 and Table S2. A clear trend in photovoltaic performance was observed with MCP loading. The power conversion efficiency (PCE) increased from 0.1% (control 1:1 BHJ with 0 wt% MCP) to a maximum of 0.83% at 50 wt% MCP. At 75 wt% MCP the PCE decreased to 0.74% PCE and was 0.15% PCE for pure MCP (100 wt%). The change in PCE is attributed primarily to changes in short circuit current density, J_{sc}, while only slight changes in open-circuit voltage and fill factor were observed with respect to MCP loading. The EQE as a function of the illumination wavelength exhibited a similar trend to the J_{sc} and did not significantly change shape (see Figure S5b, SI) with respect to the MCP loading suggesting that the change in the device performance can be predominantly attributed to the BHJ morphology.
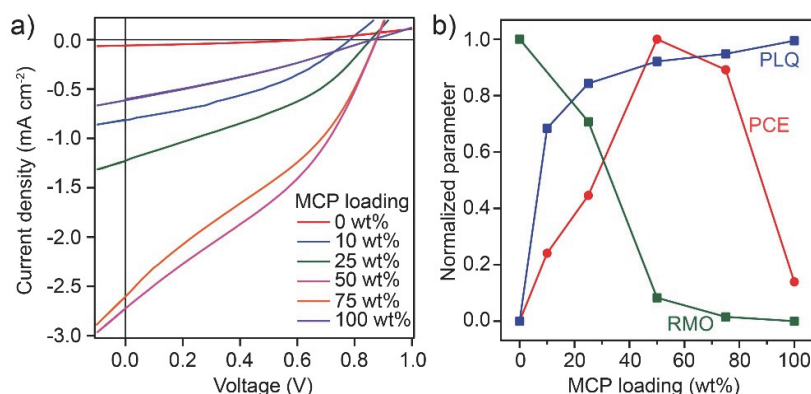
Figure 3. a) Current-density vs voltage curves of melt-annealed photovoltaics devices of DPP(TBFu)$_2$:EP-PDI – 1:1 with varying amounts of MCP. b) Summary on the effect of MCP on the BHJ morphology and the device performance is shown with normalized parameters: the device power conversion efficiency (PCE), the photoluminescence quenching (PLQ, calculated based on the integration of the respective PL emission, see Figure S4, SI) and relative molecular ordering (RMO, estimated from the integration of XRD scattering from both donor and acceptor components, see Figure S2a).

Indeed, the trend in the PCE with respect to the MCP loading (as shown normalized as the red curve in Figure 3b) can be well understood by a trade-off between free charge generation (exciton dissociation) at the donor:acceptor interface and the presence of sufficiently large pure domains to afford the transport of free charges to their respective collecting electrodes. The amount of free charge generation can be estimated by the observed amount of photoluminescence quenching (PLQ) in the BHJ as mentioned before, while the ability to transport free charges in pure domains is related to the relative molecular ordering (RMO) as implied from the previously-discussed XRD results. These two

parameters (PLQ and RMO) are shown normalized in Figure 3b. Thus the optimum melt-annealed BHJ

occurs at 50 wt% loading of the MCP, where the trade-off between RMO and PLQ is best balanced. To

elucidate this behavior further, devices processed from chloroform solution and then thermally

annealed at temperatures below melting conditions were also fabricated (See Appendix 4 Figure S5).

When the BHJ was annealed for 15 min at 180°C, a similar trend to devices melt-annealed at 240°C

was observed with an optimum loading of MCP at 50 wt% and a max PCE of 1.4%. However, when

thermally annealed for 15 min at 110°C the optimum PCE occurred at 0 wt% MCP. The observed

decrease in PCE with increasing MCP in this case is likely due to its role in compatiblizing the BHJ.

During solvent quenching, a more homogeneous donor:acceptor blend is formed with the MCP

present. The 110°C, 15 min annealing conditions are evidently insufficient to drive the crystallization

and phase segregation of the donor and acceptor to form the necessary percolating network. This is

supported by the decrease in fill-factor and J_{sc} in the 110°C annealed devices with increasing MCP

loading. In addition we note that since the results from the 180°C devices show a similar max PCE

compared to the optimum conditions at 110°C and the 240°C melt-annealed films, we can conclude

that the melt-processing of the film does not lead to a significant decrease in the best possible device

performance with the DPP(TBFu)$_2$:EP-PDI system. We note that the slightly lower PCEs observed at

240°C could be due to degradation of the electrode or blocking layer or their interfaces with the BHJ.[20]

Given the encouraging photovoltaic behavior of the chloroform solvent cast, melt-annealed devices in

the presence of the MCP, we sought to investigate the feasibility of using melt-processing towards the

"green" processing of devices. We dispersed 1:1 BHJ mixtures with or without 50 wt% MCP in

isopropanol using a minimal amount of chloroform and sonication to create a colloid of micron-sized

particles which were subsequently drop-cast onto ITO/PEDOT:PSS substrates (see Figure 4 for cross-

sectional SEM images of drop-cast films and optical microscope images in Appendix 4 Figure S6) to

form a rough and non-continuous powder coating of BHJ particles. Upon melting at 240°C for 15 min

(and cooling to rt over 30 min) a drastic difference was observed in the resulting thin films.
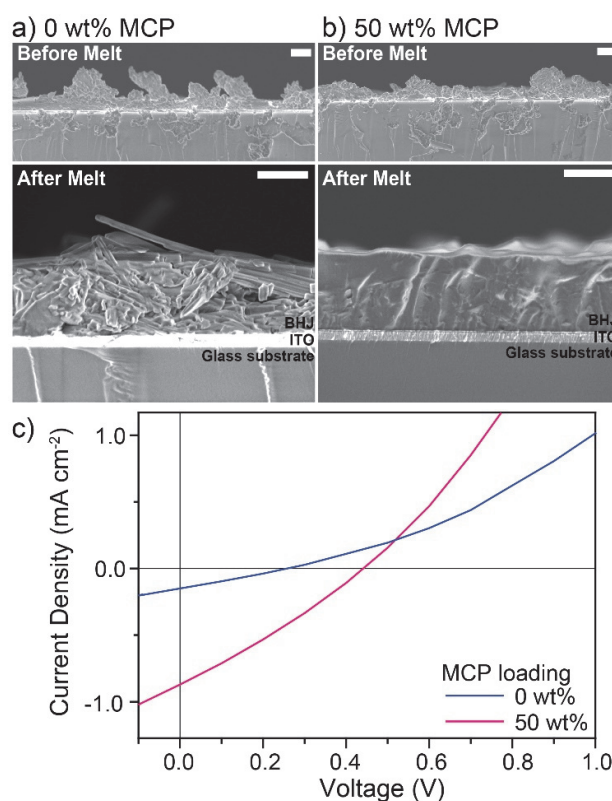
Figure 4. Cross-sectional scanning electron microscopy images of the drop-cast dispersions of 1:1 BHJ of DPP(TBFu)$_2$:EP-PDI with a) 0 wt% and b) 50 wt% of MCP before melt-processing (top) and after melting at 240°C for 15 min (bottom). The scale bars are 1 µm. c) J-V curves of the corresponding solid-state melt-processed photovoltaic devices.

While the control (0 wt%) BHJ exhibited crystal domains microns in length, the BHJ with 50 wt% melted into a remarkably smooth and homogeneous film (Figure 4). The photovoltaic properties of these melt-processed films were then characterized using Ga-In top contact to give the J-V curves shown in Figure 4c (See Appendix 4 Figure S7 for detailed experimental procedure and individual photovoltaic parameters). As expected the control device (containing 0 wt% MCP) showed a significantly lower performance of 0.002% PCE compared to 0.11% PCE when 50 wt% of MCP was included in the BHJ. Although the PCE is significantly lower than the chloroform-cast devices, a relatively thick active layer (approximately 1 µm) was used and further optimization was not performed. Importantly, this demonstration clearly shows that large solid particles of small-molecule BHJs can be melt-processed into a homogenous and functional active layer through compatibilization with our MCP approach. The further optimization of the processing method and the use of higher-performance molecular

77

donor:acceptor combinations[21] with their tailored molecular compatibilizers will likely result in melt-processed molecular photovoltaics with high efficiency and excellent thermal stability.

4.5 Conclusion

In conclusion, we have shown that a molecular compatablizer, which consists of donor and acceptor species covalently-linked with a non-conjugated linker, affords morphology control in melt-annealed BHJs. By employing highly crystalline molecular donor and acceptor species we demonstrated the ability to process a BHJ from a homogeneous single phase melt into a photoactive OPV device with tunable domain sizes in the BHJ by modulating? the loading of the MCP. Tuning the trade-off between donor:acceptor interfacial area and ordered pure domains using the MCP, as supported by AFM, KPFM, XRD and PL measurements, revealed the optimum device performance with a PCE of approximately 1% at 50 wt% loading of MCP in a 1:1 donor:acceptor BHJ. Furthermore, we demonstrated a functional OPV from the processing of micron-sized solid dispersions of BHJ with 50 wt% MCP into a homogeneous thin films via a melt-processing technique. These results show that molecular compatibilization is the key for further developments toward true solvent-free melt-processed BHJ OPV systems.

4.6 References

1.   (a) Kang, H.; Kim, G.; Kim, J.; Kwon, S.; Kim, H.; Lee, K., Bulk-Heterojunction Organic Solar Cells: Five Core Technologies for Their Commercialization. *Advanced Materials* **2016,** *28* (36), 7821-7861; (b) Mazzio, K. A.; Luscombe, C. K., The future of organic photovoltaics. *Chemical Society Reviews* **2015,** *44* (1), 78-90.

2.   Zhao, J.; Li, Y.; Yang, G.; Jiang, K.; Lin, H.; Ade, H.; Ma, W.; Yan, H., Efficient organic solar cells processed from hydrocarbon solvents. *Nature Energy* **2016,** *1*, 15027.

3.   (a) Jessop, P. G., Searching for green solvents. *Green Chemistry* **2011,** *13* (6), 1391-1398; (b) Burgues-Ceballos, I.; Stella, M.; Lacharmoise, P.; Martinez-Ferrero, E., Towards industrialization of polymer solar cells: material processing for upscaling. *Journal of Materials Chemistry A* **2014,** *2* (42), 17711-17722.

4.   (a) McDowell, C.; Bazan, G. C., Organic solar cells processed from green solvents. *Current Opinion in Green and Sustainable Chemistry* **2017,** *5* (Supplement C), 49-54; (b) Burgués-Ceballos, I.; Machui, F.; Min, J.; Ameri, T.; Voigt, M. M.; Luponosov, Y. N.; Ponomarenko, S. A.; Lacharmoise, P. D.; Campoy-Quiles, M.; Brabec, C. J., Solubility Based Identification of Green Solvents for Small Molecule Organic Solar Cells. *Advanced Functional Materials* **2014,** *24* (10), 1449-1457; (c) Cho, J.; Yoon, S.; Min Sim, K.; Jin Jeong, Y.; Eon Park, C.; Kwon, S.-K.; Kim, Y.-H.; Chung, D. S., Universal selection rule for surfactants used in miniemulsion processes for eco-friendly and high performance polymer semiconductors. *Energy & Environmental Science* **2017,** *10* (11), 2324-2333; (d) Zhang, S.; Ye, L.; Zhang, H.; Hou, J., Green-solvent-processable organic solar cells. *Materials Today* **2016,** *19* (9), 533-543.

5.   John M Dealy, J. W., *Melt Rheology and its Applications in the Plastics Industry*. 2 ed.; Springer Netherlands: 2013; p XVI, 282.

6.   (a) Müller, C.; Radano, C. P.; Smith, P.; Stingelin-Stutzmann, N., Crystalline–crystalline poly(3-hexylthiophene)–polyethylene diblock copolymers: Solidification from the melt. *Polymer* **2008,** *49* (18), 3973-3978; (b) Maunoury, J. C.; Howse, J. R.; Turner, M. L., Melt-Processing of Conjugated Liquid Crystals: A Simple Route to Fabricate OFETs. *Advanced Materials* **2007,** *19* (6), 805-809; (c) Baklar, M. A.; Koch, F.; Kumar, A.; Domingo, E. B.; Campoy-Quiles, M.; Feldman, K.; Yu, L.; Wobkenberg, P.; Ball, J.; Wilson, R. M.; McCulloch, I.; Kreouzis, T.; Heeney, M.; Anthopoulos, T.; Smith, P.; Stingelin, N., Solid-State Processing of Organic Semiconductors. *Advanced Materials* **2010,** *22* (35), 3942-3947; (d) Zhao, Y.; Zhao, X.; Roders, M.; Gumyusenge, A.; Ayzner, A. L.; Mei, J., Melt-Processing of Complementary Semiconducting Polymer Blends for High Performance Organic Transistors. *Advanced Materials* **2017,** *29* (6), 1605056-n/a.

7.   (a) Müller, C.; Ferenczi, T. A. M.; Campoy-Quiles, M.; Frost, J. M.; Bradley, D. D. C.; Smith, P.; Stingelin-Stutzmann, N.; Nelson, J., Binary Organic Photovoltaic Blends: A Simple Rationale for Optimum Compositions. *Advanced Materials* **2008,** *20* (18), 3510-3515; (b) Zhao, J.; Swinnen, A.; Van Assche, G.; Manca, J.; Vanderzande, D.; Mele, B. V., Phase Diagram of P3HT/PCBM Blends and Its Implication for the Stability of Morphology. *The Journal of Physical Chemistry B* **2009,** *113* (6), 1587-1591; (c) Wolfer, P.; Schwenn, P. E.; Pandey, A. K.; Fang, Y.; Stingelin, N.; Burn, P. L.; Meredith, P., Identifying the optimum composition in organic solar cells comprising non-fullerene electron acceptors. *Journal of Materials Chemistry A* **2013,** *1* (19), 5989-5995.

8.   (a) Brabec, C. J.; Heeney, M.; McCulloch, I.; Nelson, J., Influence of blend microstructure on bulk heterojunction organic photovoltaic performance. *Chemical Society Reviews* **2011,** *40* (3), 1185-1199; (b) Heeger, A. J., 25th Anniversary Article: Bulk Heterojunction Solar Cells: Understanding the Mechanism of Operation. *Advanced Materials* **2014,** *26* (1), 10-28; (c) Huang, Y.; Kramer, E. J.; Heeger, A. J.; Bazan, G. C., Bulk Heterojunction Solar Cells: Morphology and Performance Relationships. *Chemical Reviews* **2014,** *114* (14), 7006-7043.

9.   Moulé, A. J.; Meerholz, K., Morphology Control in Solution-Processed Bulk-Heterojunction Solar Cell Mixtures. *Advanced Functional Materials* **2009,** *19* (19), 3028-3036.

10.   Lee, Y.; Gomez, E. D., Challenges and Opportunities in the Development of Conjugated Block Copolymers for Photovoltaics. *Macromolecules* **2015,** *48* (20), 7385-7395.

11.   Lombeck, F.; Sepe, A.; Thomann, R.; Friend, R. H.; Sommer, M., Compatibilization of All-Conjugated Polymer Blends for Organic Photovoltaics. *ACS Nano* **2016,** *10* (8), 8087-8096.

12.   Martello, M. T.; Schneiderman, D. K.; Hillmyer, M. A., Synthesis and Melt Processing of Sustainable Poly(ε-decalactone)-block-Poly(lactide) Multiblock Thermoplastic Elastomers. *ACS Sustainable Chemistry & Engineering* **2014,** *2* (11), 2519-2526.

13.   Rahmanudin, A.; Jeanbourquin, X. A.; Hanni, S.; Sekar, A.; Ripaud, E.; Yao, L.; Sivula, K., Morphology stabilization strategies for small-molecule bulk heterojunction photovoltaics. *Journal of Materials Chemistry A* **2017**.

14.   Walker, B.; Tamayo, A. B.; Dang, X.-D.; Zalar, P.; Seo, J. H.; Garcia, A.; Tantiwiwat, M.; Nguyen, T.-Q., Nanoscale Phase Separation and High Photovoltaic Efficiency in Solution-Processed, Small-Molecule Bulk Heterojunction Solar Cells. *Advanced Functional Materials* **2009,** *19* (19), 3063-3069.

15.   (a) Sharenko, A.; Kuik, M.; Toney, M. F.; Nguyen, T.-Q., Crystallization-Induced Phase Separation in Solution-Processed Small Molecule Bulk Heterojunction Organic Solar Cells. *Advanced Functional Materials* **2014,** *24* (23), 3543-3550; (b) Liang, Q.; Han, J.; Song, C.; Wang, Z.; Xin, J.; Yu, X.; Xie, Z.; Ma, W.; Liu, J.; Han, Y., Tuning molecule diffusion to control the phase separation of the p-DTS(FBTTh2)2/EP-PDI blend system via thermal annealing. *Journal of Materials Chemistry C* **2017,** *5* (27), 6842-6851.

16.   Keivanidis, P. E.; Howard, I. A.; Friend, R. H., Intermolecular Interactions of Perylene diimides in Photovoltaic Blends of Fluorene Copolymers: Disorder Effects on Photophysical Properties, Film Morphology and Device Efficiency. *Advanced Functional Materials* **2008,** *18* (20), 3189-3202.

17.   Liu, J.; Zhang, Y.; Phan, H.; Sharenko, A.; Moonsin, P.; Walker, B.; Promarak, V.; Nguyen, T.-Q., Effects of Stereoisomerism on the Crystallization Behavior and Optoelectrical Properties of Conjugated Molecules. *Advanced Materials* **2013,** *25* (27), 3645-3650.

18.   Jeanbourquin, X. A.; Rahmanudin, A.; Gasperini, A.; Ripaud, E.; Yu, X.; Johnson, M.; Guijarro, N.; Sivula, K., Engineering the self-assembly of diketopyrrolopyrrole-based molecular semiconductors via an aliphatic linker strategy. *Journal of Materials Chemistry A* **2017,** *5* (21), 10526-10536.

19.	(a) Sharenko, A.; Gehrig, D.; Laquai, F.; Nguyen, T.-Q., The Effect of Solvent Additive on the Charge Generation and Photovoltaic Performance of a Solution-Processed Small Molecule:Perylene Diimide Bulk Heterojunction Solar Cell. *Chemistry of Materials* **2014,** *26* (14), 4109-4118; (b) Viterisi, A.; Gispert-Guirado, F.; Ryan, J. W.; Palomares, E., Formation of highly crystalline and texturized donor domains in DPP(TBFu)2:PC71BM SM-BHJ devices via solvent vapour annealing: implications for device function. *Journal of Materials Chemistry* **2012,** *22* (30), 15175-15182.

20.	Greenbank, W.; Hirsch, L.; Wantz, G.; Chambon, S., Interfacial thermal degradation in inverted organic solar cells. *Applied Physics Letters* **2015,** *107* (26), 263301.

21.	(a) Yang, L.; Zhang, S.; He, C.; Zhang, J.; Yao, H.; Yang, Y.; Zhang, Y.; Zhao, W.; Hou, J., New Wide Band Gap Donor for Efficient Fullerene-Free All-Small-Molecule Organic Solar Cells. *Journal of the American Chemical Society* **2017,** *139* (5), 1958-1966; (b) Qiu, B.; Xue, L.; Yang, Y.; Bin, H.; Zhang, Y.; Zhang, C.; Xiao, M.; Park, K.; Morrison, W.; Zhang, Z.-G.; Li, Y., All-Small-Molecule Nonfullerene Organic Solar Cells with High Fill Factor and High Efficiency over 10%. *Chemistry of Materials* **2017,** *29* (17), 7543-7553; (c) Bin, H.; Yang, Y.; Zhang, Z.-G.; Ye, L.; Ghasemi, M.; Chen, S.; Zhang, Y.; Zhang, C.; Sun, C.; Xue, L.; Yang, C.; Ade, H.; Li, Y., 9.73% Efficiency Nonfullerene All Organic Small Molecule Solar Cells with Absorption-Complementary Donor and Acceptor. *Journal of the American Chemical Society* **2017,** *139* (14), 5085-5094.

Chapter 5

Heck-Mizoroki reaction of functionalized macromonomers for the formation of fully-conjugated block-copolymers for organic photovoltaics

Abstract

Fully-conjugated block-copolymers (BCPs) have attracted a lot of attention for their use as a single-component bulk heterojunctions (BHJ) in organic photovoltaics (OPVs). However, state-of-the-art BCPs typically employ P3HT as a donor block, due to its ease in forming well-defined narrow molecular weight with precise end capping blocks through the use of catalyst transfer polymerization methods. This limits the efficiencies of BCPs in OPVs, where high efficiency donor and acceptor polymers used in modern BHJ blends are based on complex monomeric moieties that are prepared via step-growth polycondensation. In this study, we present a modular synthetic strategy using a Heck-Mizoroki coupling reaction between two functionalized macromonomers based on high performing copolymers, a donor coded PBDTT-DPP, and PDI-V as an acceptor polymer. These polymers were selected due to complementary energy levels and absorption spectra, and particularly the vinylene comonomer unit in PDI-V, which is a useful functional group for the Heck-Mizoroki reaction. Stille polycondensation with an imbalanced feed ratio afforded control over the halogen and vinylene chain-end functionalities of the two macromonomers, which allowed for the formation of a tri-BCP consisting of PDI-V-*b*-PBDTT-DPP-*b*-PDI-V *via* Heck coupling. Furthermore, tri-BCP achieved a device efficiency of 1.51%, which was significantly higher than its corresponding molar blend ratio where the efficiency was 0.04% after annealing at 150°C for 15 minutes. Therefore, the results demonstrate a promising synthetic strategy *via* a Heck-Mizoroki coupling reaction between functionalized macromonomers for obtaining functional photoactive BHJ based on fully-conjugated BCPs.

5.1 Introduction

As discussed in the introduction chapter 1 (Section 1.4.2), fully-conjugated block copolymers (BCP) consisting of donor-acceptor blocks have garnered significant interest, due to their potential to form thermodynamically stable phase-segregated bulk heterojunction (BHJ) morphologies with ideal microstructures for efficient OPVs.[1] This approach is slightly different from that of the previous chapters, where the (kinetic) stability of a binary donor-acceptor BHJ was addressed. In the case of a single-component BHJ using BCPs, the covalent linkage between the donor and acceptor blocks prevents macroscopic separation, and domain sizes can be tuned (based on the chain length of the blocks) to length scales preferential for exciton diffusion, while maintaining continuous pathways to enable charge extraction for an efficient BHJ network. . However, the main challenge is in the synthetic methodology (See Chapter 1 section 1.4.2) whereby the current state-of-the-art BCPs is dependent on the use of relatively high bandgap P3HT as a donor block because its preparation using catalyst transfer polymerization enables the formation of well-defined, narrow molecular weight, and precise end-capping blocks.[2] However, this limits OPV performance since conventional high efficiency binary donor-acceptor BHJ blends typically uses low-band gap copolymers that rely on step-growth polycondensation that is unsuitable for the formation of BCPs,[3] where it inevitably leads to a mixture of products composed homo polymers, diblock and multi-block copolymers. Although, there are recent developments in catalytic design that have shown the induction of living chain-growth polymerization for electron deficient units[3b, 4], or transforming step-growth to chain growth reactions.[5] Despite the promise of these synthetic methodologies, further understanding and demonstration in obtaining well-defined BCPs for OPVs is still required, and will not be the focus of this study.

A simpler approach uses conventional step-growth polymerization between di-functionalized macromonomers to give multi-block copolymers.[6] The clear advantage of this method is that each block can be prepared separately and purified before the final polymerization, but preparing a pure functionalized macromonomer is a major challenge. Recently, our group demonstrated that using

preparatory size exclusion chromatography facilitated the preparation of pure macromonomers to synthesize an alternating multi-BCP, *via* stille-coupling polymerization with a di-brominated PBTTT block as a donor, and a di-stannylated DPP based polymer as the acceptor (See Scheme 6b in Chapter 1.4.2).[7] However, the purification of pure stannylated DPP macromonomer proved to be difficult due to the stability of the stannylated end-capping group. Furthermore, OPV devices were not demonstrated with the novel multi-BCP, likely due to the less than ideal energetics of the donor:acceptor combination.

In this chapter, a synthetic strategy utilizing palladium-catalysed Heck-Mizoroki coupling reaction between two macromonomers functionalized with bromine and vinylene end-capping groups will be presented (See Scheme 1). Low-band-gap conjugated copolymers are selected: PBDTT-DPP[8] as the donor block and PDI-V[9] as the acceptor block, since their energy levels and absorption spectra are complementary as a donor-acceptor pair in a BHJ for an efficient OPV device. Moreover, both copolymers are known to form highly ordered domains due their relatively planar conjugated backbone,[10] and more importantly this could aid in driving phase segregation during self-assembly into thin films, as it has been shown that incompatibly of the respective blocks in a BCP is crucial to form separate ordered donor-acceptor assemblies for an efficient BHJ network.[11] PDI-V was also specifically chosen due to the vinylene co-monomer unit, which is an active stable functional group for the Heck-Mizoroki coupling reaction that avoids the need to use the unstable stannylated end-capping of the marcomonomer.[12] To achieve control over the chain-end functionalities, standard Stille polycondensation with an imbalanced monomer feed ratio were used to synthesize the respective donor and acceptor macromonomers coded PBDTT-DPP-Br$_2$ and PDI-V-Vinylene. The final Heck-coupling reaction resulted in a BCP consisting of an acceptor-*b*-donor-*b*-acceptor configuration, i.e, PDI-V-*b*-PBDTT-DPP-*b*-PDI-V, coded tri-BCP. The photovoltaic performance of this BHJ system was subsequently characterised and compared with its donor-acceptor blend at a 1:2 molar ratio.

Synthesis of Macromonomers
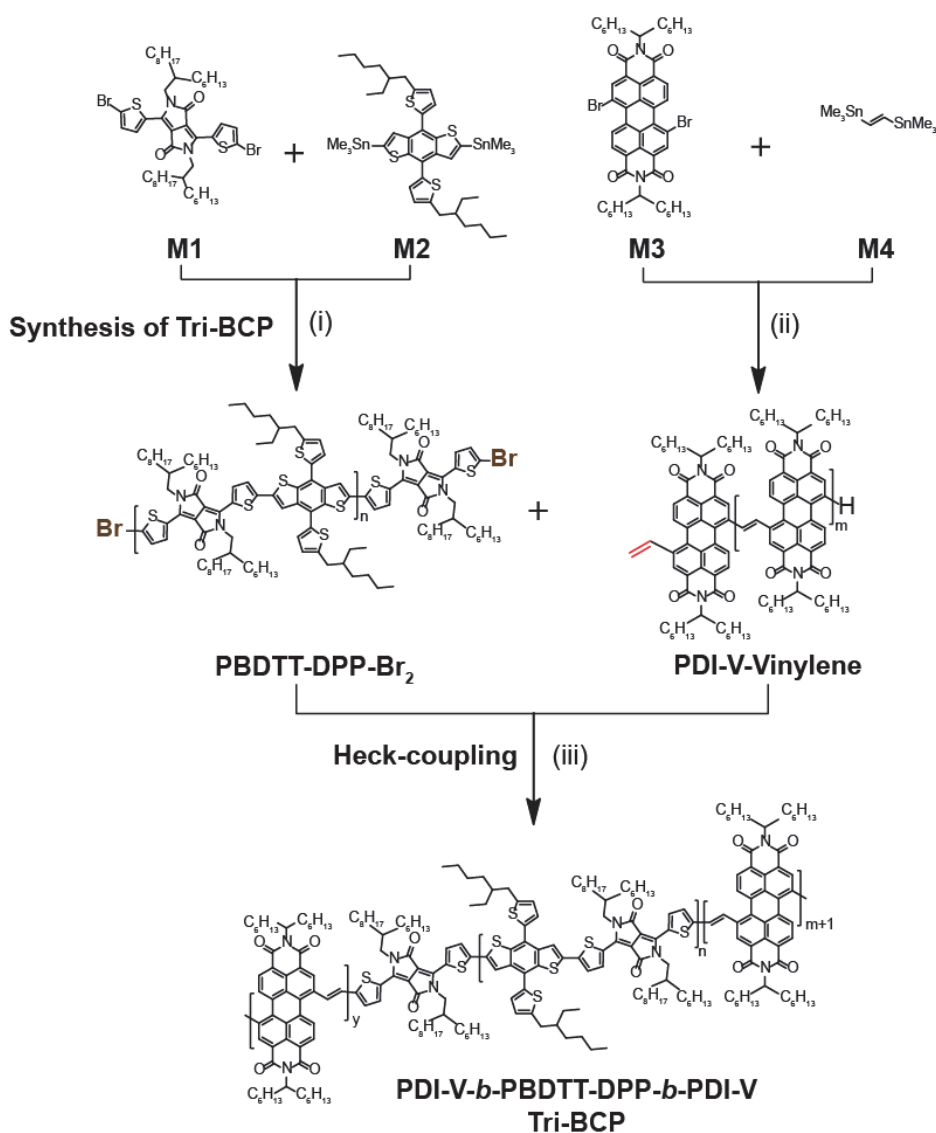
Scheme 1. Synthetic route for the preparation of tri-block-copolymer, PDI-V-*b*-PBDTT-DPP-*b*-PDI-V via Heck-Mizoroki coupling with dibromo end-capped copolymer, PBDTTT-DPP -Br$_2$, and mono-vinylene end-capped copolymer, PDI-V-Vinylene; Reaction conditions: (i) Pd(PPh)$_3$, Toluene:DMF, 110°C; (ii) Pd$_2$(dba)$_3$, P-(o-tol)$_3$,Toluene, 95°C; (iii) Pd(OAc)$_2$, P-(o-tol)$_3$, TEA:DMF:Toluene, 95°C.

5.2 Synthesis of Marcomonomers

A detailed description and characterization of the monomers (M1-M4) used for the preparation of the macromonomers, and the synthesis of PDBTT-DPP -Br$_2$, PDI-V -Vinylene and tri-BCP are in appendix 5 under experimental procedures. The molecular weight and molar mass distribution (dispersity index - Đ) of all polymers were estimated by analytical gel permeation chromatography (GPC) using polystyrene standards, and end group-composition was measured by matrix-assisted laser

desorption/ionization time-of-flight mass spectrometry (MALDI-TOF MS) in the reflection mode, using

trans-2-[3-(4-tert-Butylphenyl)-2-methyl-2-propenyllidene]malononitrile as a matrix. ^{1}H NMR analysis

of the macromonomer and the tri-BCP is used as supporting evidence of the formation of the

respective polymers, and is described in appendix 5. An overall summary of the characterization of the

macromonomers and final tri-BCP are reflected in Table 1 below.

Table 1. Overall summary of the characterization of the macromonomers and the tri-BCP

Macromonomer	Feed ratio	$M_{n,gpc}$ (kg/mol)^b	Repeating unit	$Đ$ ^{b}
PDBTT-DPP -Br$_2$	**M1:M2** 9:8	4.79	*n*=3	1.29
PDI-V -Vinylene	**M3:M4** 8:9	3.78	*m*=5+1	1.21
tri-BCP	1:2.3	16.9	*n*=3, *m+1*=6	1.57

^{A} M$_n$ Calculated based on the integration of the proton labelled in the respective schematics of PBDTT-DPP-Br$_2$ – H$_a$:H$_b$ and PdDI-V-Vinylene – H$_c$:H$_d$.
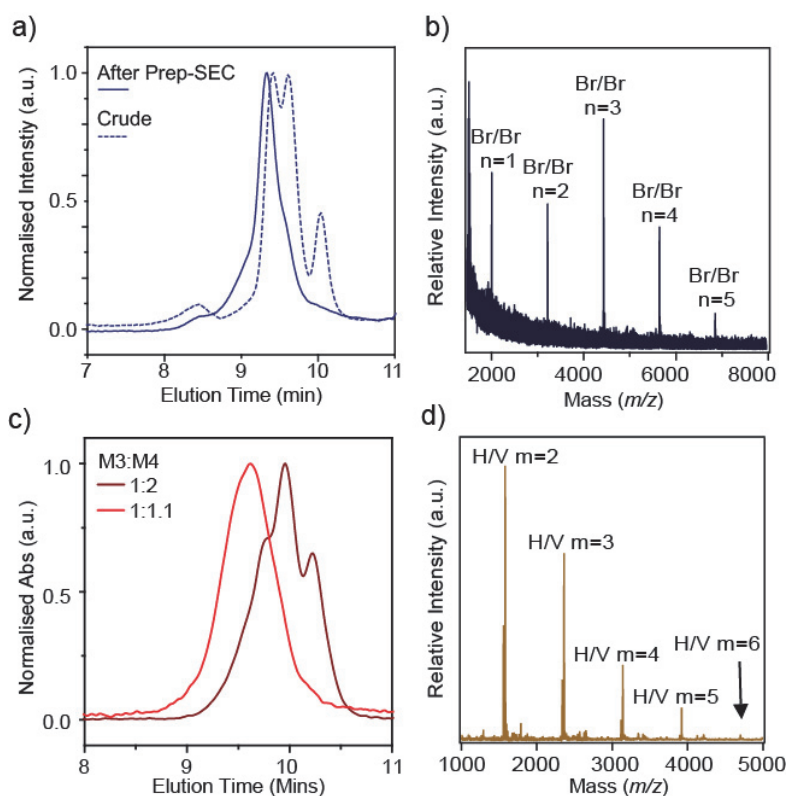^{B} Estimated from the GPC traces based on polystyrene standards.

Figure 2. Characterization of donor macromonomer PBDTT-DPP -Br$_2$: a) GPC traces of the crude sample (dotted line) and after purification via prep-SEC (Solid line); b) MALDI TOF MS spectra of PBDTT-DPP -Br$_2$ after

purification by prep-SEC; Characterization of acceptor macromonomer PDI-V-Vinylene: c) GPC traces at the different feed ratio, 1:2 (brown line) and 1:1.1 (red line); d) MALDI TOF MS spectra of PDI-V-Vinylene.

To prepare the donor block, PBDTT-DPP-Br_2, a slight excess of the brominated monomer, M1, was used at a stoichiometric feed ratio of 9:8 - M1:M2. This afforded a crude sample with a molecular weight of M_n = 3.94 kg mol^{-1}, and a dispersity of Đ=1.51 as estimated from the GPC traces shown in figure 1a (dotted blue line). Further purification using preparatory size exclusion chromatography (prep-SEC), narrowed the poly dispersity to Đ=1.23, and a M_n = 4.2 kg mol^{-1} with a degree of polymerization of n=3 (See table 1). MALDI-TOF MS analysis of purified PBDTT-DPP- Br_2 determined the functionalization of dibromo end-caps in the polymer, but also revealed that the purified sample contained polymer chains with n between 1 and 5 (See Figure 1b). On a side note, the number of repeat units in PBDTTT-DPP - Br_2 is relatively low compared to using a balanced feed ratio of 1:1 – M1:M2 where a significantly larger M_n of 48.9 kg mol^{-1} and a Đ=2.05 was obtained (See appendix 5 Figure S1a).[13] This suggest that a larger molecular weight is attainable provided a further optimization of the feed ratio is performed. In addition, ^{1}H NMR analysis of PBDTT-DPP-Br_2 revealed a satellite peak representing the proton adjacent to the bromine end cap on the terminal thiophene unit of the polymer (See appendix 5 figure S1b).

Before the synthesis of the acceptor block, PDI-V-Vinylene, repetitive recrystallization of M3 was performed to increase the proportion of the 1,7-regio-isomer (See appendix 5 Figure S2 for the chemical structure of the 1,7 and 1,6 regio-isomer of the bromine groups on M3, and the ^{1}H NMR analysis of the regio-isomeric purity of M3). Regio-isomeric purity of M3 is crucial as the 1,6 isomer introduces structural defects along the polymer backbone of PDI-V-vinylene, which is known to affect π- π stacking and charge transport,[14] and possibly disrupts effective Heck-Mizoroki coupling with the donor block. For the preparation of the acceptor block, a slight excess of M4 at a feed ratio of 8:9 - M3:M4 was used, to induce vinylene end-caps in the resulting acceptor block. GPC traces shown in Figure 1c estimated M_n = 3.78 kg mol^{-1} with a relatively narrow Đ=1.21. However, MALDI-TOF MS revealed a vinylene end group only on one side of the polymer chain (See Figure 1d for MS spectra and Scheme1 of the chemical structure of PDI-V-Vinylene). Increasing the feed of M4 to 1:2 - M3:M4,

did not afford di-vinylene end caps as indicated from its MS spectra (Appendix 5 Figure S3a), but it severely affected the degree of polymerization, where M_n = 1.82 kg/mol^{-1} as estimated by its GPC trace (See Figure 1c). It is important to note that the stannylated vinylene end caps in the acceptor block should be expected based on our pervious report of di-functionalized macromonomers,[7] but predictably it did not remain stable during the work-up and purification using the prep-SEC. Interestingly, a bromine end cap on the terminal PDI monomer unit was not observed, which is likely due to Pd insertion into the PDI-Br moiety during oxidative addition that leads to dehalogenation during quenching of the reaction with HCl.[15] ^{1}H NMR analysis of PDI-V-vinylene revealed the a broad satellite peak adjacent to the main peak related to the vinylene co-monomer along the polymer backbone, which likely relates to the end capping vinylene group, but accurate deconvolution for the integration of peaks were difficult (See appendix 5 Figure S3c). Nonetheless, MALDI-TOF MS analysis has provide sufficient determination for the presence of the vinylene end capping group.

Based on the end capping group functionality obtained on the individual macromonomers, Heck-Mizoroki coupling obtained a tri-BCP of PDI-*V*-*b*-PBDTT-DPP-*b*-PDI-V, using a 1:2.3 feed ratio of PDBTT-DPP-Br$_2$:PDI-V-Vinylene. The stoichiometric ratio of the marcomonomers were calculated based on the molecular weight estimated from the GPC traces (See Table 1.), and a slight excess of PDI-V-Vinylene was used to ensure complete reaction at both terminal bromine ends in PDBTTT-DPP-Br$_2$.

As shown from the GPC traces, a significant increase in molecular weight was observed in the crude sample from the two starting compounds (See Figure 2a.). Subsequent purification by prep-SEC yielded an estimated M_n = 16.9 kg mol^{-1} and a $Đ$=1.51, which is slightly larger from the expected M_n = 13.82 kg/mol^{-1} for a tri-BCP with repeating units of *n*=3 and *m+1*=6 (See Table 1). This may be attributed to the presence of individual donor-acceptor blocks with varying molecular weights as indicated from the MALDI-TOF MS analysis (See Figure 1b and d), where the presence of multiple repeating units of both marcomonomers were observed. Regardless, it does indicate that a higher molecular weight polymer is obtained after the reaction. In addition, the GPC trace of tri-BCP has a slight overlap of about 10%

with the GPC traces of the two starting macromonomers, which could be present in the purified sample (See Figure 2a).

Further characterization *via* ^{1}H NMR revealed the presence of proton environments attributed to the aromatic region of the donor, PDBTT-DPP-*b* and acceptor, PDI-V-*b* blocks (See Figure 2b for the zoomed ^{1}H NMR spectrum and see Figure 2c for the assignment of the protons on the chemical structure of tri-BCP). Similarly, three main sets of peaks related to the distinctive α-CH (H_h @ 5.24 ppm) on PDI-V-*b*, and α-CH$_2$ protons (H_i @ 4.027ppm and H_j @ 2.98 ppm) of the aliphatic chains from the respective blocks were observed Integration of the aliphatic peaks (H_h, H_i and H_j does correspond to the formation of a tri-BCP (See appendix 5 Figure S4 for a comparison between the ^{1}H NMR spectrum of the macromonomers and tri-BCP), but taking into consideration that there is a slight overlap in the GPC trace of the tri-BCP with the starting marcomonomers, further experimental evidence is required ensure the formation of a tri-BCP (this will be discussed in the section 5.4)
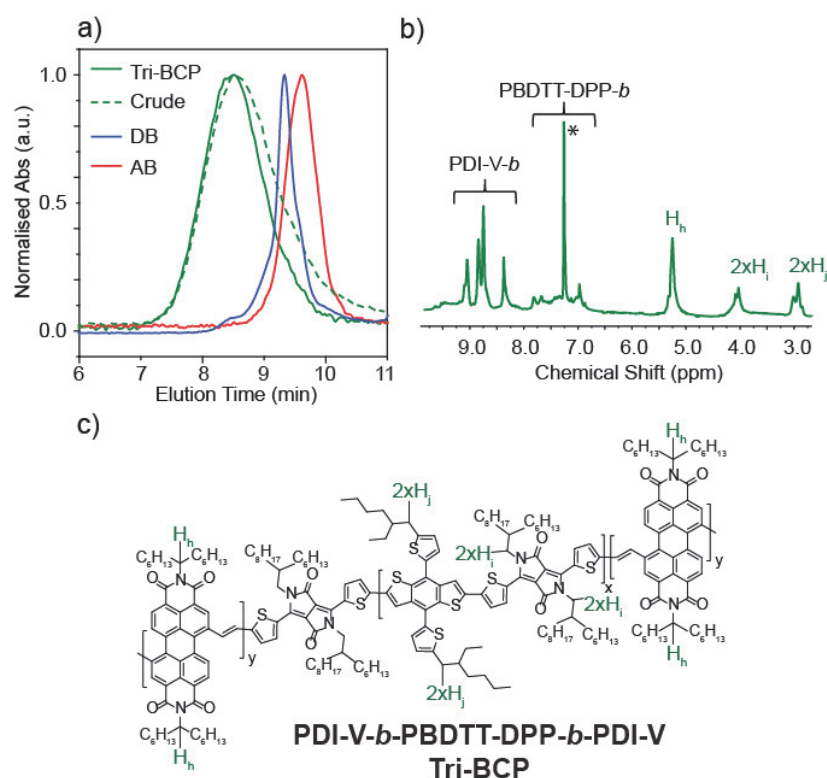

Figure 3. Characterization of Tri-block-copolymer, PDI-V-b-PBDTT-DPP-b-PDI-V (Tri-BCP): a) GPC traces consisting of Tri-BCP (green solid line), crude sample (green dotted line), donor copolymer block, PDBTT-DPP-Br$_2$, (blue

solid) and acceptor copolymer block, PDI-V-Vinylene (red solid);b) ^{1}H NMR spectrum of tri-BCP to indicate the proton assignments on tri-BCP of the aromatic region and the respective protons on the aliphatic chains of the donor and acceptor blocks where * indicates deuterated-chloroform solvent peak (See Appendix 5 Figure S4 for the full ^{1}H NMR Spectra), and c) The chemical structure of tri-BCP.

Thin film optical absorption spectrum of tri-BCP consisted of two characteristic absorption peaks at λ_{max} at 748nm and 638nm that can be related to the contribution of the donor PBDTT-DPP-b,[8] and acceptor PDI-V-b[9] blocks respectively (See Figure 3a and appendix 5 Figure S5 for optical absorption spectra in solution). Furthermore, a lower peak intensity at 748nm is expected as it implies a lower molecular weight fraction of the PBDTTT-DPP block in the tri-BCP, which is similar to the absorption spectra of the molar blend of 1:2 - PDBTT-DPP-Br$_2$:PDI-V-Vinylene. Photoluminescence (PL) emission spectra of tri-BCP thin film indicate a significant quenching of its emission peak at 709nm by 95% relative to the emission of acceptor block, PDI-V-Vinylene, upon excitation at 633nm (See Figure 4b). This is similarly observed in the blend film but with a 90% PL quenching of the emission peak at 709nm.is the quenching of the PL emission is indicative of a higher probability of excitons generated (mainly in the acceptor) to undergo charge separation, likely to due to proximity of the covalently linked adjacent donor PDBTT-DPP block in the BHJ thin film morphology. On a side note, no significant emission from the donor block was observed probably due to a lower absorption intensity at excitation wavelength of 633nm.
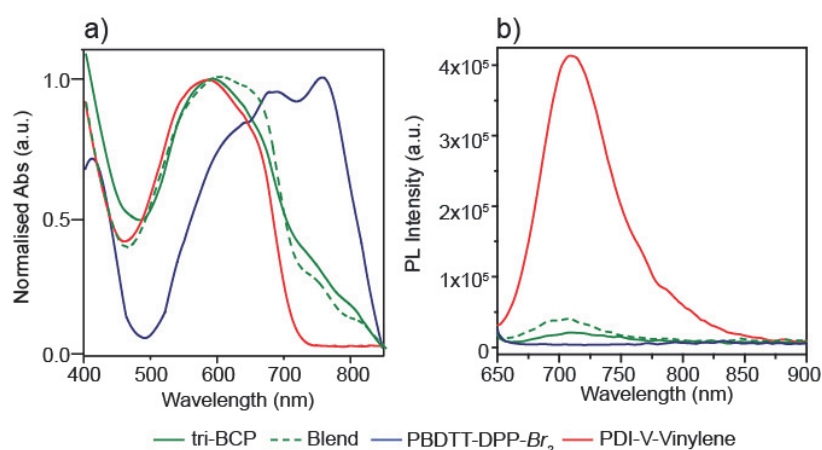

Figure 4. Thin film characterization of tri-BCP (Green line), Blend of the donor and acceptor blocks (Green dotted line), PBDTTT-DPP-Br$_2$ (Blue line) and PDI-V-Vinylene (Red line): a) Optical absorption spectra and b)

Photoluminescence emission spectra after excitation at 633nm (See Appendix experimental procedures for thin film preparation method).

5.3 Photovoltaic Performance

To investigate the photovoltaic performance of the tri-BCP and its corresponding donor-acceptor molar blend of at a ratio of 1:2 - PBDTT-DPP:PDI-V, spin-coated BHJs devices with an inverted architecture of glass/ITO/ZnO/Active-Layer/MO$_3$/Ag were fabricated and tested under standard 1 sun illumination under Argon (Detailed device fabrication method is described in the appendix experimental procedures section). Current-density-voltage (*J-V)* curves of annealed devices (150°C for 15 minutes) are shown in Figure 5a, while the overall summary of the photovoltaics parameters are presented in Table 2. The performance of as-cast devices were relatively similar with a PCE of 0.01% for tri-BCP and 0.04% for the blend (See Appendix 5 Figure S6 for the respective J-V curves). However, upon thermal annealing, the performance between the two BHJ systems were significantly different with improvements in the overall photovoltaic parameters were observed for tri-BCP, achieving a reasonable PCE of 1.51%, while the blend observed a decrease in PCE to 0.02%. Although, it is important to note that the molar blend ratio of 1:2 - PBDTT-DPP:PDI-V may not be the optimized ratio of an efficient OPV BHJ.

Table 2. Overall summary of photovoltaic parameter of tri-BCP and its blend at 1:2 molar ratio

BHJ	Annealing Conditions (°C)	Jsc (mA/cm^{-2})	Voc (V)	Fill Factor (%)	PCE (%)
tri-BCP	As cast	0.13	0.34	35	0.01
	150°C	6.17	0.72	40	1.51
Molar Blend[a] PDBTT-DPP-*b*:	As cast	0.20	0.58	33	0.04
PDI-V-*b* 1:2	150°C	0.16	0.36	36	0.02

[a] Molar blend ratio is calculated based on the estimated ratio of the PBDTT-DPP-*b* and PDI-V-*b* blocks present in the tri-BCP estimated using GPC analysis.
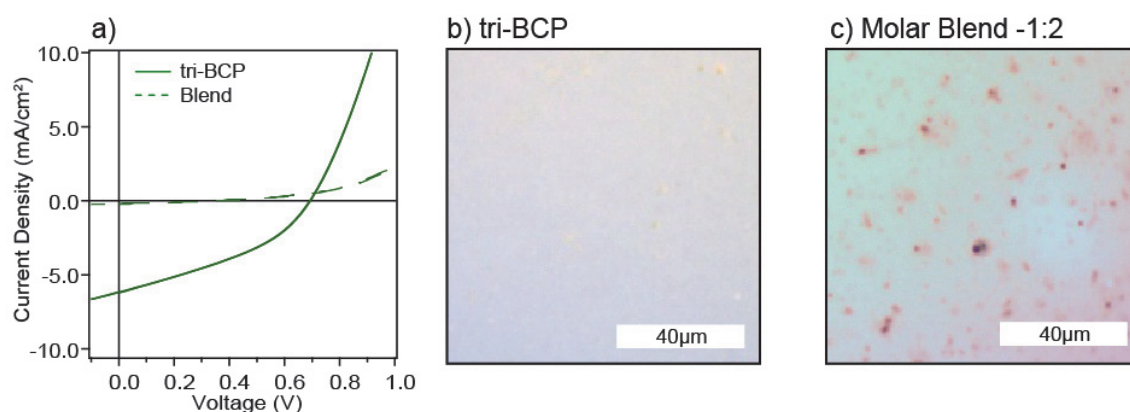
Figure 5. a) Current density vs Voltage curves of the devices containing tri-BCP and the its respective blend after thermal annealing at 150°C for 15 minutes under argon atmosphere; Optical micrographs of thin films after annealing at 150°C for 15 minutes under Argon: b) Molar Blend (1:2) and c) tri-BCP.

Optical microscope images of the BHJ thin films revealed the formation of large aggregates in the blend film after annealing, while the film containing tri-BCP did not show any obvious aggregate formation (See Figure 4b-c). This suggests an incompatibility of the low molecular weight donor and acceptor copolymer blend, which self-assembles into large domains sizes that prevents the formation of a preferred phase segregation of an efficient BHJ after thermal annealing. However, when the respective blocks are covalently linked into a fully-conjugated BCP, the thermodynamics of the phase separation may have been altered, resulting in a BHJ that consists of donor-acceptor domain sizes limited to the size of the individual blocks in the tri-BCP. Hence, the higher performance observed for the tri-BCP could be attributed to the formation of a preferred nano-phase separated BHJ, as compared to the large macroscopic phase segregation that occurs in the molar blend of the donor and acceptor components.

5.4 Future Work and further improvements

Admittedly, a thorough morphological characterization such as resonant soft X-ray scattering (as shown in the P3HT-*b*-PFTBT BCP by Gomez and co-workers in chapter 1 section1.4.2 figure 6a)or atomic force and kelvin probe microscopy of both BHJ system could provide a reasonable visualization of the BHJ phase segregation that is obtained between the molar blend and tri-BCP.Nonetheless, a reasonable PCE was obtained with tri-BCP, despite containing a polydispersity of donor-acceptor

blocks with varying lengths due to the impurities of starting macromonomers with different repeating units during the Heck-Mizoroki coupling reaction.This suggests that further purification of the starting macromonomers and the resulting tri-BCP could improve the performance further by attaining a more homogenous donor-acceptor domains sizes in the BHJ network, which could enhance exciton separation and percolation pathways. Another possible reason for the modest performance, is that the OPV performance of the corresponding donor or acceptor macromonomer, PBDTT-DPP:PC$_{71}$BM[8] and PTB7-Th:PDI-V[9] show PCEs over 7%, where the molecular weights are significantly larger than the size of the blocks used in tri-BCP (PBDTT-DPP - 48.3 kg/mol^{-1} and PDI-V - 14 kg/mol^{-1}). Therefore, optimization of the feed ratio would be required to obtain higher molecular weights while still attaining precise end-capping functionalities for a Heck-Mizoroki coupling reaction. Achieving this would allow tuning of domain sizes and identify an optimum nano-phase segregation of the BHJ for efficient device performance.

Furthermore, supporting synthetic experiments should be performed to support the formation of tri-BCP, despite the GPC trace indicating the formation of a higher molecular weight polymer, since we cannot rule out the possibility of homo-coupling occurring between the respective marcomonomers under the Heck-Mizoroki coupling catalytic conditions.[16] Therefore, control reactions to justify the lack of homo-coupling between the respective macromonomers, PBDTT-DPP-Br$_2$ and PDI-V-Vinylene should be performed in the future.

5.4 Conclusion

This brief demonstration shows that a fully-conjugated BCP is attainable by using Heck-Mizoroki coupling between two functionalized macromonomers. Precise end-capping functionalities determined by MALDI-TOF MS revealed that di-bromo and mono-vinylene groups were obtained in the PBDTT-DPP-Br$_2$ donor and PDI-V-vinlyene acceptor macromonomers respectively. This resulted in a tri-BCP formation of PDI-V-*b*-PBDTT-DPP-*b*-PDI-V PDBTT-DPP as shown in the ^{1}HNMR and GPC analysis. However, a relatively large poly dispersity of *Đ*=1.51 was observed from its GPC trace, that is

attributed to the presence of tri-BCP with varying repeating units of the individual donor and acceptor blocks. This is likely due to the starting macromonomer containing polymers with multiple repeating units as shown in the MALDI-TOF MS analysis, despite it having a narrow poly dispersity ($Đ<1.3$). Despite, the non-homogeneity of the tri-BCP, its photovoltaic performance showed a promising PCE of 1.51%, which was significantly larger than its corresponding molar blend of donor and acceptor macromonomers at a ratio of 1:2 that obtained a PCE of 0.02% after thermal annealing at 150°C for 15 minutes. Morphological characterization using optical microscopy of the annealed thin films revealed the formation of large aggregates in the molar blend, while tri-BCP did not have an obvious aggregate formation. Hence, this suggests that in a blend the separate individual blocks are non-compatible, which results in large macroscopic phase segregation after thermal annealing. Conversely, the covalent linkage between the donor-acceptor block in tri-BCP limits the phase segregation of the BHJ to the chain length of the individual blocks, thus maintaining a preferred nano-phase segregated BHJ network with efficient photovoltaic properties. Notably, further morphological characterization is needed to compare the formation of the respective BHJ morphology. Nonetheless, other possible improvements can still be made to improve device efficiencies: 1) Further purification of the starting macromonomer is needed to ensure a well-defined starting block before the final Heck-Mizoroki coupling reaction, so that the resulting BCP would contain well-defined donor-acceptor domain sizes that is preferred for higher device performance; 2)The molecular weight obtained of the respective donor and acceptor blocks were relatively low as compared to its parent polymer, and optimization of feed ratios of the individual blocks is required to enhance molecular weight, while still maintaining precise end capping groups for the Heck-Mizoroki coupling reaction. In summary, the main objective of this study is to demonstrate the applicability of aHeck-Mizoroki - reaction between two functionalized macromonomers as a promising synthetic methodology to obtain fully-conjugated BCPs for OPVs.

5.4 References

1.   Lee, Y.; Gomez, E. D., Challenges and Opportunities in the Development of Conjugated Block Copolymers for Photovoltaics. *Macromolecules* **2015,** *48* (20), 7385-7395.

2.   (a) Wang, S.; Yang, Q.; Tao, Y.; Guo, Y.; Yang, J.; Liu, Y.; Zhao, L.; Xie, Z.; Huang, W., Fully conjugated block copolymers for single-component solar cells: synthesis, purification, and characterization. *New Journal of Chemistry* **2016,** *40* (2), 1825-1833; (b) Nakabayashi, K.; Mori, H., All-Polymer Solar Cells Based on Fully Conjugated Block Copolymers Composed of Poly(3-hexylthiophene) and Poly(naphthalene bisimide) Segments. *Macromolecules* **2012,** *45* (24), 9618-9625; (c) Guo, C.; Lin, Y.-H.; Witman, M. D.; Smith, K. A.; Wang, C.; Hexemer, A.; Strzalka, J.; Gomez, E. D.; Verduzco, R., Conjugated Block Copolymer Photovoltaics with near 3% Efficiency through Microphase Separation. *Nano Letters* **2013,** *13* (6), 2957-2963.

3.   (a) Po, R.; Bianchi, G.; Carbonera, C.; Pellegrino, A., "All That Glisters Is Not Gold": An Analysis of the Synthetic Complexity of Efficient Polymer Donors for Polymer Solar Cells. *Macromolecules* **2015,** *48* (3), 453-461; (b) Grisorio, R.; Suranna, G. P., Intramolecular catalyst transfer polymerisation of conjugated monomers: from lessons learned to future challenges. *Polymer Chemistry* **2015,** *6* (45), 7781-7795.

4.   Senkovskyy, V.; Tkachov, R.; Komber, H.; Sommer, M.; Heuken, M.; Voit, B.; Huck, W. T. S.; Kataev, V.; Petr, A.; Kiriy, A., Chain-Growth Polymerization of Unusual Anion-Radical Monomers Based on Naphthalene Diimide: A New Route to Well-Defined n-Type Conjugated Copolymers. *Journal of the American Chemical Society* **2011,** *133* (49), 19966-19970.

5.   Yokozawa, T.; Ohta, Y., Transformation of Step-Growth Polymerization into Living Chain-Growth Polymerization. *Chemical Reviews* **2016,** *116* (4), 1950-1968.

6.   (a) Mok, J. W.; Kipp, D.; Hasbun, L. R.; Dolocan, A.; Strzalka, J.; Ganesan, V.; Verduzco, R., Parallel bulk heterojunction photovoltaics based on all-conjugated block copolymer additives. *Journal of Materials Chemistry A* **2016,** *4* (38), 14804-14813; (b) Gao, D.; Gibson, G. L.; Hollinger, J.; Li, P.; Seferos, D. S., 'Blocky' donor-acceptor polymers containing selenophene, benzodithiophene and thienothiophene for improved molecular ordering. *Polymer Chemistry* **2015,** *6* (17), 3353-3360.

7.   Gasperini, A.; Johnson, M.; Jeanbourquin, X.; Yao, L.; Rahmanudin, A.; Guijarro, N.; Sivula, K., Semiconducting alternating multi-block copolymers via a di-functionalized macromonomer approach. *Polymer Chemistry* **2017,** *8* (5), 824-827.

8.   Dou, L.; You, J.; Yang, J.; Chen, C.-C.; He, Y.; Murase, S.; Moriarty, T.; Emery, K.; Li, G.; Yang, Y., Tandem polymer solar cells featuring a spectrally matched low-bandgap polymer. *Nat Photon* **2012,** *6* (3), 180-185.

9.   Guo, Y.; Li, Y.; Awartani, O.; Zhao, J.; Han, H.; Ade, H.; Zhao, D.; Yan, H., A Vinylene-Bridged Perylenediimide-Based Polymeric Acceptor Enabling Efficient All-Polymer Solar Cells Processed under Ambient Conditions. *Advanced Materials* **2016,** *28* (38), 8483-8489.

10.   (a) Ma, Y.; Wu, Y.; Zhao, Y.; Fu, H.; Yao, J., Synthesis and photophysics of monodisperse co-oligomers consisting of alternating thiophene and perylene bisimide. *Physical Chemistry Chemical*

Physics **2011,** *13* (6), 2036-2043; (b) Wen, S.; Chen, W.; Fan, M.; Duan, L.; Qiu, M.; Sun, M.; Han, L.; Yang, R., A diketopyrrolopyrrole-based low bandgap polymer with enhanced photovoltaic performances through backbone twisting. *Journal of Materials Chemistry A* **2016,** *4* (46), 18174-18180.

11.   Lombeck, F.; Komber, H.; Sepe, A.; Friend, R. H.; Sommer, M., Enhancing Phase Separation and Photovoltaic Performance of All-Conjugated Donor–Acceptor Block Copolymers with Semifluorinated Alkyl Side Chains. *Macromolecules* **2015,** *48* (21), 7851-7860.

12.   Gu, C.; Li, Y.; Xiao, L.; Fu, H.; Wang, D.; Cheng, L.; Liu, L., Tunable Heck–Mizoroki Reaction of Dibromonaphthalene Diimide with Aryl Ethylenes: Design, Synthesis, and Characterization of Coplanar NDI-Based Conjugated Molecules. *The Journal of Organic Chemistry* **2017,** *82* (23), 12806-12812.

13.   Dou, L.; Gao, J.; Richard, E.; You, J.; Chen, C.-C.; Cha, K. C.; He, Y.; Li, G.; Yang, Y., Systematic Investigation of Benzodithiophene- and Diketopyrrolopyrrole-Based Low-Bandgap Polymers Designed for Single Junction and Tandem Polymer Solar Cells. *Journal of the American Chemical Society* **2012,** *134* (24), 10071-10079.

14.   Zhou, Y.; Yan, Q.; Zheng, Y.-Q.; Wang, J.-Y.; Zhao, D.; Pei, J., New polymer acceptors for organic solar cells: the effect of regio-regularity and device configuration. *Journal of Materials Chemistry A* **2013,** *1* (22), 6609-6613.

15.   (a) Goto, E.; Ando, S.; Ueda, M.; Higashihara, T., Nonstoichiometric Stille Coupling Polycondensation for Synthesizing Naphthalene-Diimide-Based π-Conjugated Polymers. *ACS Macro Letters* **2015,** *4* (9), 1004-1007; (b) Matsidik, R.; Komber, H.; Luzio, A.; Caironi, M.; Sommer, M., Defect-free Naphthalene Diimide Bithiophene Copolymers with Controlled Molar Mass and High Performance via Direct Arylation Polycondensation. *Journal of the American Chemical Society* **2015,** *137* (20), 6705-6711.

16.   (a) Dudnik, A. S.; Aldrich, T. J.; Eastham, N. D.; Chang, R. P. H.; Facchetti, A.; Marks, T. J., Tin-Free Direct C–H Arylation Polymerization for High Photovoltaic Efficiency Conjugated Copolymers. *Journal of the American Chemical Society* **2016**; (b) Lombeck, F.; Komber, H.; Gorelsky, S. I.; Sommer, M., Identifying Homocouplings as Critical Side Reactions in Direct Arylation Polycondensation. *ACS Macro Letters* **2014,** *3* (8), 819-823.

CHAPTER 6

Summary and Future Outlook

Thus far, the thesis has generally covered a molecular engineering approach to address the self-assembly of a donor-acceptor bulk heterojunction (BHJ) and the relation to its optoelectronic properties. In the first section of this chapter, a summary of the main chapter will be given, before concluding with a broader perspective on the outcome of this thesis.

6.1 Summary of main chapters

As discussed in the introduction (Chapter 1), the self-assembly of π-conjugated semiconductors has significant effects on the resulting device performance of the organic electronic device. It was highlighted that the key parameter that drives self-assembly is the supramolecular π-π stacking interactions between the conjugated backbone of the organic semiconductor (OSC). Various molecular engineering approaches such as backbone modulation, which alters the chemical structure of the π-conjugated system intrinsically affects self-assembly properties, but it fundamentally changes the electronic properties of the π-conjugated system. Side-chain engineering on the other hand, has shown promise in controlling self-assembly without affecting the electronic properties of the OSC, by enhancing procesability, but the underlying attribute that drives self-assembly is still the supramolecular π-π stacking interactions. As such, due to the vast library of OSCs that have been synthesized, a general versatile strategy is needed to control the morphology of the OSCs.

It was underlined that the molecular engineering strategy of introducing conjugation break spacers (flexible linkers) between the π-conjugated segments in the OSC, showed great promise in controlling supramolecular self-assembly without altering the semiconducting core of the OSC. This was exemplified using prototypical semiconductors such as PBTTT and DPP(TBFu)$_2$ by the work of Sivula and co-workers(See chapter 1 section 1.3.1). Notably, the prominent work using a similar method by Zhao *et.al* (See Chapter 1 section 1.3.2) and Schroeder *et.al* (See Chapter 1 section 1.3.2 and 1.3.3) have reinforced the strategy by demonstrating the tuning of physical properties of the OSC for unique processing techniques such as melt and solution shearing methods. However, these examples largely addresses the control over self-assembly of a single π-conjugated component in the active layer, either

as an additive to its parent (non-flexibly linked) semiconductor, or as a semiconductor itself. This leads to the subsequent challenge that is addressed in the main chapters of this thesis, which is to use the flexible linker approach to control the self-assembly of a multi-component active layer commonly found in donor-acceptor BHJs used in organic photovoltaics.

As extensively described in the main chapters, the performance of OPV devices is extremely sensitive to the BHJ morphology, where a precise nanometer donor-acceptor domain size is required to balance both interfacial area (for exciton separation) and pure ordered domains (for percolation pathways of separated charges) as illustrated in chapter 1 figure 4. While the optimum BHJ morphology can be readily tuned using solvent processing techniques, the resulting morphology is still in a kinetically trapped metastable state that is en-route towards a thermodynamic equilibrium of large phase segregated domains, non-ideal for device performance.

In chapter 2, this was addressed by applying BHJ morphology stabilization strategies commonly used in polymer:fullerene BHJs such as crosslinking of the BHJ network, and a compatibilization approach for a prototypical small molecule BHJ OPV device, DPP(TBFu)$_2$:PC$_{61}$BM. Only a handful of reports have addressed the BHJ stability in small molecule BHJs, even though the greater crystallinity of molecular semiconductors poses a reasonably greater challenge as compared to its polymer counterpart, where it is more susceptible to phase segregation under thermal stress.

To demonstrate this, two novel molecular additives were synthesized and designed to afford compatibilization, where the compatibilizer (CP) consists of the donor and acceptor components that are flexibly linked with an aliphatic spacer, and to in-situ link (ISL) the components in the BHJ, the donor molecule was functionalized with a terminal azide on its aliphatic chain (N$_3$-ISL). The results presented provided a clear indication that both additives were able to slow down phase segregation of the BHJ and preserve device performances under thermal stress. However, a difference was observed in the optimum performance obtained between the two additives. The presence of non-specified linked

species observed in the mass spectral analysis (chapter 2 section 2.3) caused by both thermal and UV induced nitrene insertion reactions, led to an increase in BHJ charge trapping as detected in the photoluminescence and impedance spectroscopy measurements (chapter 2 section 2.6). This resulted in a generally lower device performance of the BHJs in the presence N_3-ISL, as compared to the CP additive. Notably, 10wt% of CP slowed down the crystallization and phase segregation of the BHJ from as cast, resulting in a gradual increase in performance which saturated at 2% PCE after 120 min with no decrease after 300min (the length of the test). Furthermore, melt-annealed films with CP demonstrated control over phase segregation suggesting a potential for melt processing of the BHJ. Overall, the comparison between the approaches indicates that compatibilization is a preferred strategy to stabilize the BHJ morphology.

Consequently, chapter 3 presented the versatility of the compatibilization approach on a challenging highly crystalline small molecule BHJ using a diketopyrrolopyrrole donor molecule with a perylenediimide acceptor. As expected the molecular compatibilizer (MCP) based on this system was able to slow down the BHJ phase segregation under thermal stress (at 110°C for 480 min), while preserving device performance, which reinforced the usefulness of the compatibilization approach. Taking leverage from this, chapter 5 demonstrated for the unique ability of the MCP to tune the phase-domain size of the BHJ that is processed from a homogeneous single-phase melt. Atomic force and kelvin probe microscopy, X-ray diffraction and photoluminescence measurements revealed control over interfacial area and ordered pure domains in the BHJ by modulating the amount of MCP under melt-processing conditions. This resulted in an optimum photoactive BHJ with an OPV efficiency of approximately 1% at 50wt% MCP with a 1:1- donor:acceptor ratio of melt –annealed spin coated films. Furthermore, it was also demonstrated that a homogenous photoactive BHJ thin film is achievable from melt processing of micron-sized solid dispersions containing MCP. In conclusion, the overall results presented in chapter 2 to 4 ultimately reflects a novel demonstration of a BHJ compatibilization strategy that represents a powerful tool to precisely control phase segregation and

self-assembly of donor and acceptor domains that is quenched from a single-phase homogenous melt, which opens up vast new possibilities for solvent free "green" processing of OPVs.

In chapter 5, the approached used to address BHJ morphological stabilization is slightly different from that of previous chapters, where the (kinetic) stability of a binary donor-acceptor BHJ was addressed. Instead of using a secondary compatibilizing additive, a fully-conjugated block copolymer (BCP) consisting of donor–acceptor blocks was used to demonstrate its applicability for a single-component BHJ for OPVs. However, the main challenge is in the synthetic methodology (See Chapter 1 section 1.4.2) whereby the current state-of-the-art BCPs is dependent on the use of relatively high bandgap P3HT as a donor block, due to the ease of catalyst transfer polymerization methods to prepare well-defined, narrow molecular weight blocks. This limits OPV performance since conventional high efficiency binary donor-acceptor BHJ blends typically uses low-band gap copolymers that rely on step-growth polycondensation unsuitable for the formation of BCPs, where it inevitably leads to a mixture of products composed homo polymers, diblock and multi-block copolymers.

To overcome this limitation, a modular synthetic strategy using Heck coupling between two functionalized marcromonomers based on two high performing low-band gap copolymers, PDBTT-DPP as a donor, and PDI-V as an acceptor was demonstrated. Stille polycondensation with an imbalanced feed ratio afforded control over the halogen and vinylene chain-end functionalities of the two macromonomers. This allowed for the formation of a tri-BCP consisting of PDI-V-*b*-PBDTT-DPP-*b*-PDI-V *via* Heck coupling. Furthermore, tri-BCP achieved a device efficiency of 1.51%, which was significantly higher than its corresponding molar blend ratio where the efficiency was 0.04% after annealing at 150°C for 15 minutes. This brief study shows promise that a photoactive fully-conjugated BCP is attainable using a heck coupling reaction between functionalized macromonomers.

6.2 Future Outlook

Based on the outcome of the research presented in this thesis, the flexible linker strategy shows a promising approach to control morphology of OCSs. The introduction of the aliphatic spacers between conjugated segments have shown that it does not negatively affect charge transport, but induces unique self-assembly motif of the OSC. Particularly, the example by Mei and co-workers (See Chapter 1 Section 1.3.2) on the melt processing of the DPP base polymer for field-effect transistors, and the processing of a multi-component BHJ from a homogenous single-phase melt using a novel molecular compatibilizer approach for a photoactive OPV device described in chapter 4. Melt-processing has a significant clear advantage over the standard solvent deposition techniques, which typically utilizes toxic chlorinate solvents for the formation of thin films of OSCs. Alleviating the need for solvents would encourage a "greener" and sustainable processing method particularly for large scale fabrication of organic electronic devices. Moreover, there is already an extensive library of studies on understanding the self-assembly of OSCs from solvent quenching, whereas only a limited number of studies have described the film formation of OSCs from a melted state. Therefore, we hope that by presenting examples of melt processing methods of OSCs, it would encourage further development towards solvent free processing of these materials, which could benefit its commercialization In addition, the work by Bao and co-workers on using functionalized flexible linkers for self-healing OSC polymers[1], demonstrates a further unique self-assembly function of this approach considering the potential application in bioelectronics (i.e electronic skin).[2] Nonetheless, the continued inter-disciplinary effort from chemists, physiscts, biologists and material scientists would lead to further development of new materials, devices and applciations. Therefore, organic electronics would remain an excting area of research with plenty of fundametnal challenges to address and a wealth of opportunites to discover novel phenomenas and fucntionalites.

6.3 References

1. Oh, J. Y.; Rondeau-Gagné, S.; Chiu, Y.-C.; Chortos, A.; Lissel, F.; Wang, G.-J. N.; Schroeder, B. C.; Kurosawa, T.; Lopez, J.; Katsumata, T.; Xu, J.; Zhu, C.; Gu, X.; Bae, W.-G.; Kim, Y.; Jin, L.; Chung, J. W.; Tok, J. B. H.; Bao, Z., Intrinsically stretchable and healable semiconducting polymer for organic transistors. *Nature* **2016,** *539*, 411.

2. Someya, T.; Bao, Z.; Malliaras, G. G., The rise of plastic bioelectronics. *Nature* **2016,** *540* (7633), 379-385.

Appendix 2

Supplementary Figures in Chapter 2

Contents

Figure S1. UV-Vis absorption.

UV-Vis absorption of respective neat components dissolved in Chloroform at 0.2 mg/mL (Left) and after casting into thin films (Right).
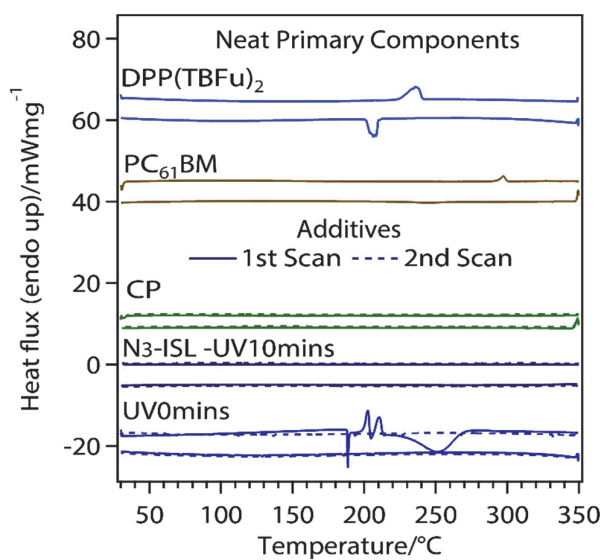
Figure S2. DSC thermograms.

DSC thermograms of DPP(TBFu)$_2$ (2nd Cycle), PC$_{61}$BM (2nd Cycle), CP (1st & 2nd Cycle), and N$_3$- ISL (1st & 2nd Cycle).
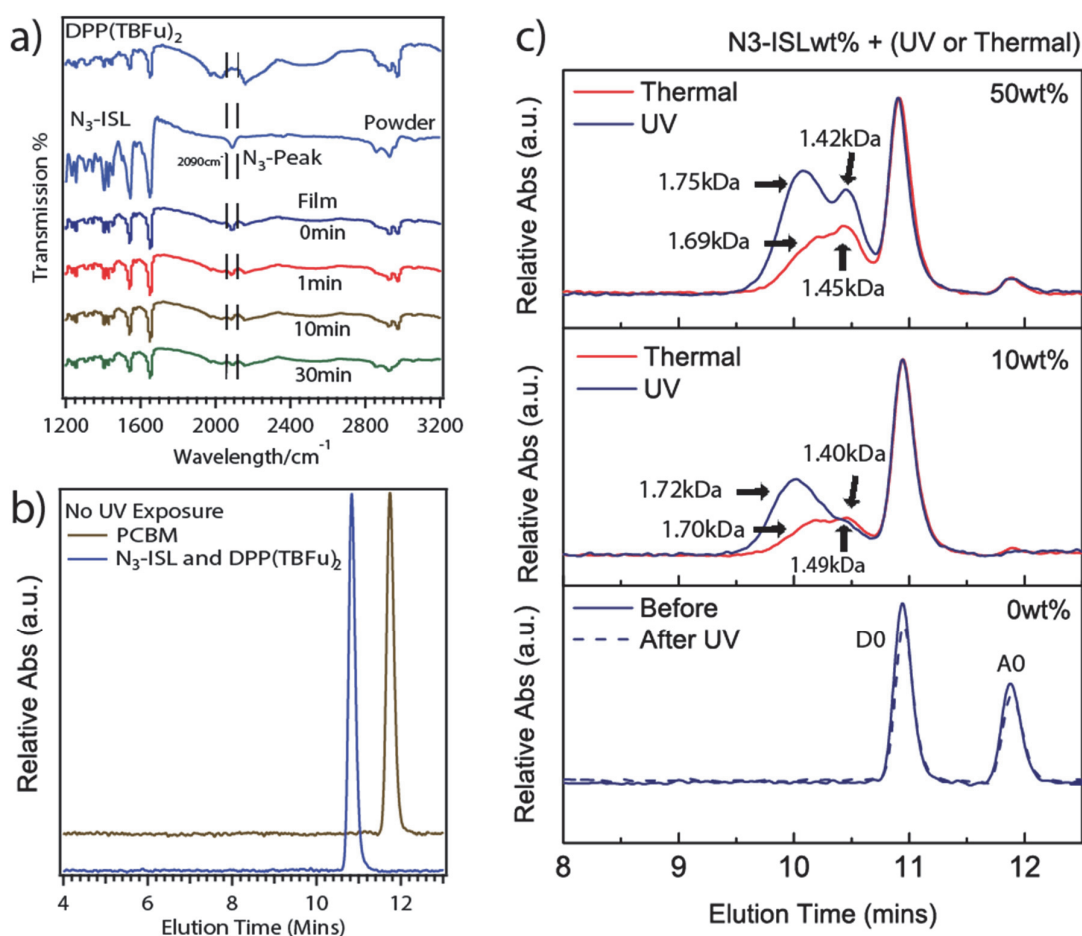
Figure S3. FTIR Spectrum and Size-exclusion chromatography (SEC) traces of thin films.

a) FTIR Spectrum of N_3-ISL at various UV-Exposure Time. The presence of azides on N_3-ISL are easily observable from its characteristic peak at 2090 cm^{-1}. As a reference, no azide peak was visible on DPP(TBFu)$_2$. The results clearly shows that as the UV-exposure time is increased, the intensity of the azide peak gradually decreases, indicating the conversion of the azide into the reactive nitrene for the photo-crosslinking reaction. Size-exclusion chromatography (SEC) traces of thin films; b) Reference neat components without UV or thermal stimuli; c) Blends of DPP(TBFu)$_2$:PCBM (6:4) with 0wt%, 10wt% and 50wt% of N_3-ISL with the corresponding UV(254nm for 10mins) or thermal (110°C for 60mins) stimuli. Broad peaks were observed between 9.5 min to 10.5 min elution times after UV and thermal treatment of samples with N_3-ISL indicating evidence of higher molecular weight species(arrows indicate estimated average molecular weights of the respective peaks which is within the range of the corresponding the azide linked species and PCBM dimer (A3) (See SI Fig S5.), whereas no obvious shoulder peak was observed for the blend samples without N3-ISL. Qualitatively, it is clear that at 50wt% of N3-ISL, a larger fraction of higher molecular weight peaks were observed as compared to 10wt% of N3-ISL. Additionally, UV treatment resulted in a proportionally larger amount of higher molecular weight species than the thermal treatment. Interestingly, the absorption of the PCBM peak significantly decreased upon UV and Thermal stimuli, which may suggests that PCBM is more reactive towards the external stimuli as compared to DPP(TBFu)$_2$. However, this may not be precisely quantifiable as it is difficult to quantify the efficiency of the linking reaction according to the intensity

of the absorption peaks from the GPC traces due to the differences in absorption coefficient the respective components during the SEC measurements (See experimental procedures section for details on sample preparation and measurement conditions).
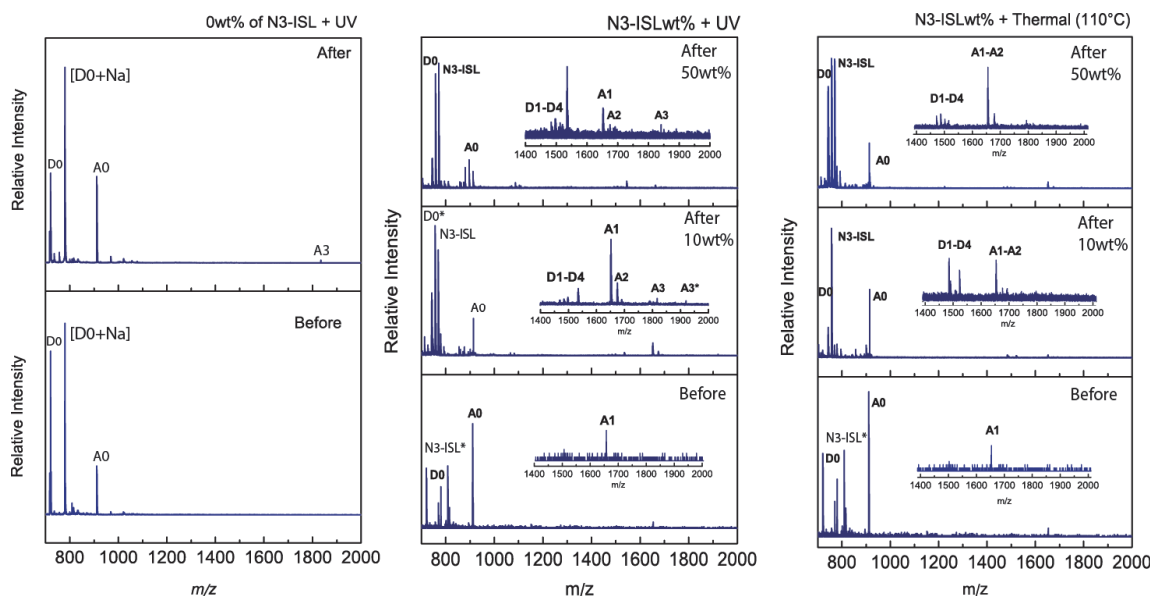

Figure S4. MALDI-TOF MS analysis.

(a) represents the control 6:4 blend of DPP(TBFu)$_2$ donor and PCBM acceptor before (bottom) and after (top) 10 min of UV treatment showing the showing the presence of the dimerized PCBM species (A3, see Figure S5). Panel (b-c) is from the control blend before UV(b) and thermal (c) treatment with 50wt% of the N$_3$-ISL loading and after UV exposure (b) and thermal treatment at 110°C for 1 hour with 10wt% and 50wt% of N$_3$-ISL(Insets are zoomed-in to the m/z range to indicate the linked species (D1-D4 and A1-A3) present in the blend. Asterisk (*) indicates the additional molecular weight of one matrix molecule or Na$^+$ .Peaks are labelled according to the species outlined in Figure S5. It is evident that PCBM dimer (A3) is only formed upon UV exposure but not thermal treatment, whereas the azide linked species D1-D4 and A1-A2 are formed *via* both external stimuli. On a side note, A1 is detected in the blend before the respective UV or thermal treatment, likely due to the nitrene insertion reaction occurring in the solution at 50°C in chloroform before film deposition.
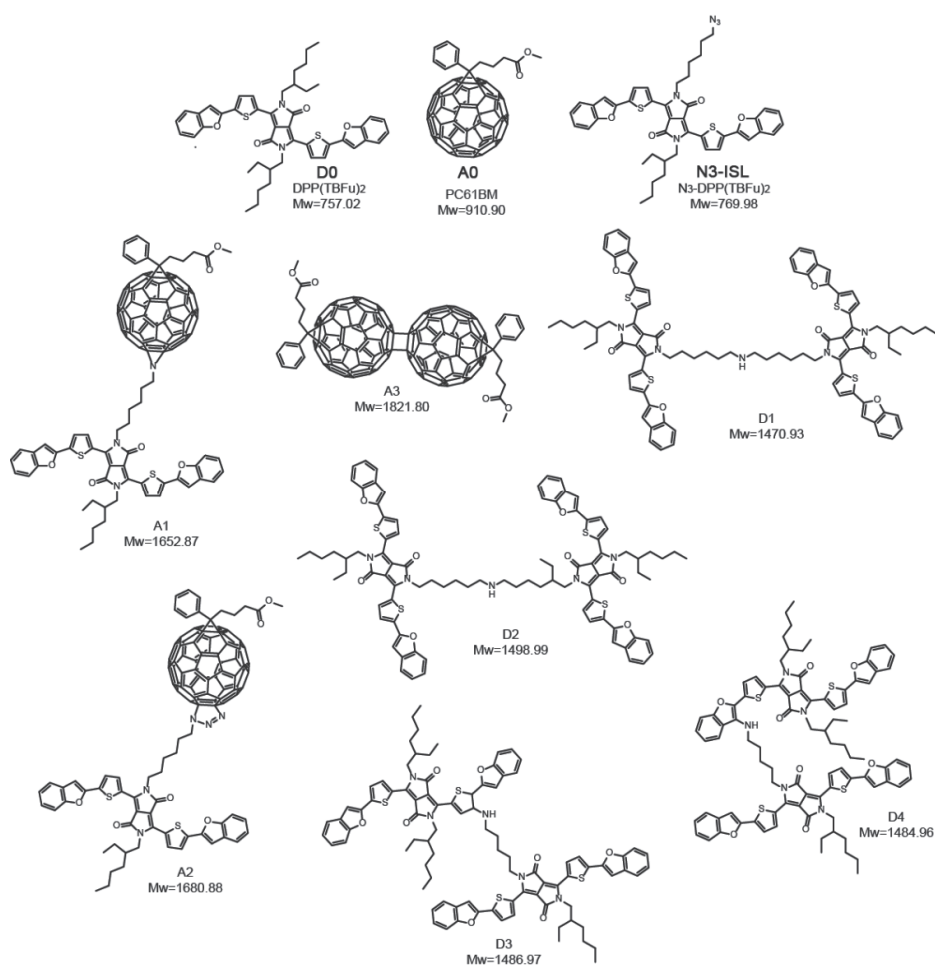
Figure S5. Predicted azide-linked species.

Predicted azide-linked species present in the BHJ under either UV or thermal activation. Each species is labeled with a designator A0, A1….D0, D1 etc. which correspond to the peaks observed in Figure S4.

Summary of the overall device data of the optimum(Opt), and after 50h of thermal stability test at 110°C in Argon with and without the respective additives

Additive (%)	V_{oc} (V)		J_{sc} (mA cm^{-2})		FF (%)		PCE (%)			
	Opt	After 50h	Max.	After 50h	Opt	After 50h	Opt[a]	Gain in PCE[b] (%)	After 50h	Loss in PCE[b] (%)
0	0.91	0.78	7.99	5.09	42.0	42.3	3.01	-	1.58	-47.5
0(UV10)[d]	0.93	0.88	7.25	6.06	42.0	40.8	3.00	-0.33	2.09	-34.6
CP										
1	0.89	0.80	8.54	7.18	44.5	42.5	3.50	+14	2.39	-30.8
5	0.86	0.85	8.53	7.29	44.3	43.5	3.34	+10.9	2.45	-18.2
10	0.84	0.86	4.23	7.46	36.7	45.3	2.00[c]	-34	2.05	+0.02
N$_3$-ISL (UV10)[d]										
1	0.91	0.86	7.02	6.18	47.0	43.8	2.85	-5.3	2.37	-16.8
5	0.76	0.80	3.24	3.54	36.0	37.5	1.06	-65.5	0.99	-6.36
10	0.65	0.66	1.56	1.62	32.2	31.7	0.415	-86.3	0.40	-0.05
N$_3$-ISl (UV0)										
1	0.91	0.85	7.10	5.39	46.7	42.3	2.93	-0.03	1.99	-32.1
5	0.90	0.86	6.10	5.43	39.7	43.3	2.2	-26.9	1.98	-20.0
10	0.91	0.86	4.65	3.84	38.7	37.5	1.61	-46.5	1.33	-19.3

[a] Photovoltaics data were taken from an average of 6 batches of devices.

[b] The gain in PCE were calculated using the optimum PCE of the control device as reference.

[c] Loss in PCE was calculated from the optimum PCE of the individual device.

[d] Devices were exposed to 10 minutes of UV exposure (254nm) before aluminum deposition.
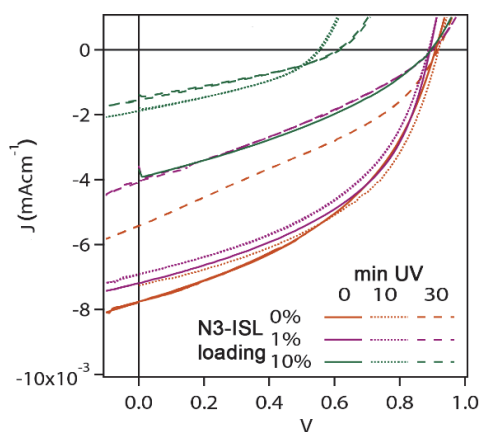
Figure S6. J-V curves.

J-V curves of DPP(TBFu)$_2$:PC$_{61}$BM 6:4 with varying amount of the N3ISL linker (0, 1 and 10 wt%) under various UV exposure times (0, 10, and 30 min as the solid, dotted and dashed lines, respectively). Devices were thermally treated for 10 min at 110°C.

TABLE S2. Calculated endothermic enthalpy

Calculated endothermic enthalpy of melting of 6:4 - DPP(TBFu)$_2$:PC$_{61}$BM blend with varying additive loading

ADDITIVE LOADING %	Enthalpy of melting (j/g)[a]	
	CP	N$_3$-ISL
0	21.4	-
10	7.61	12.5
25	2.38	7.26
50	-	5.46

[a] enthalpy of melting was calculated based on the specific mass of DPP(TBFu)$_2$ in the blend of 6:4 - DPP(TBFu)$_2$:pc$_{61}$bm with varying loading of the additive from the DSC thermograms
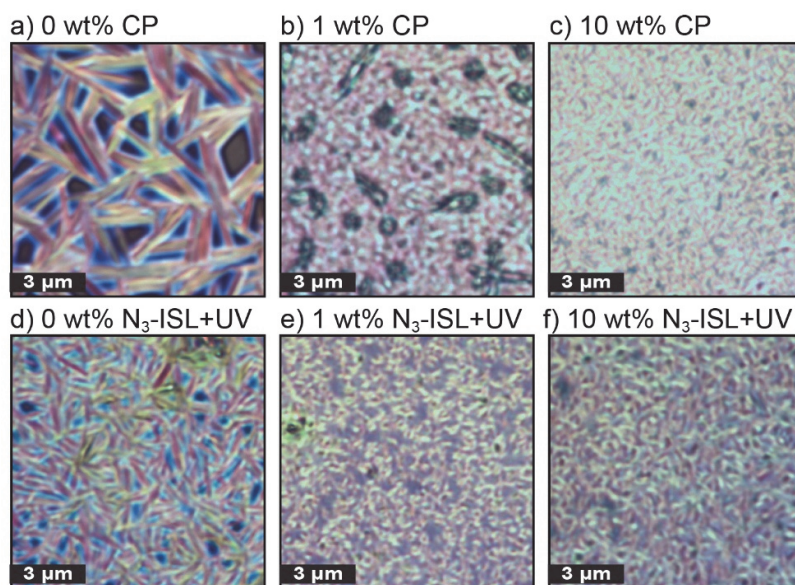
Figure S7. Optical micrographs

Optical microscopy of the BHJ films after heating to 240 °C (above the melting temperature) for 5 min. The amount of the respective additive is indicated for each panel.
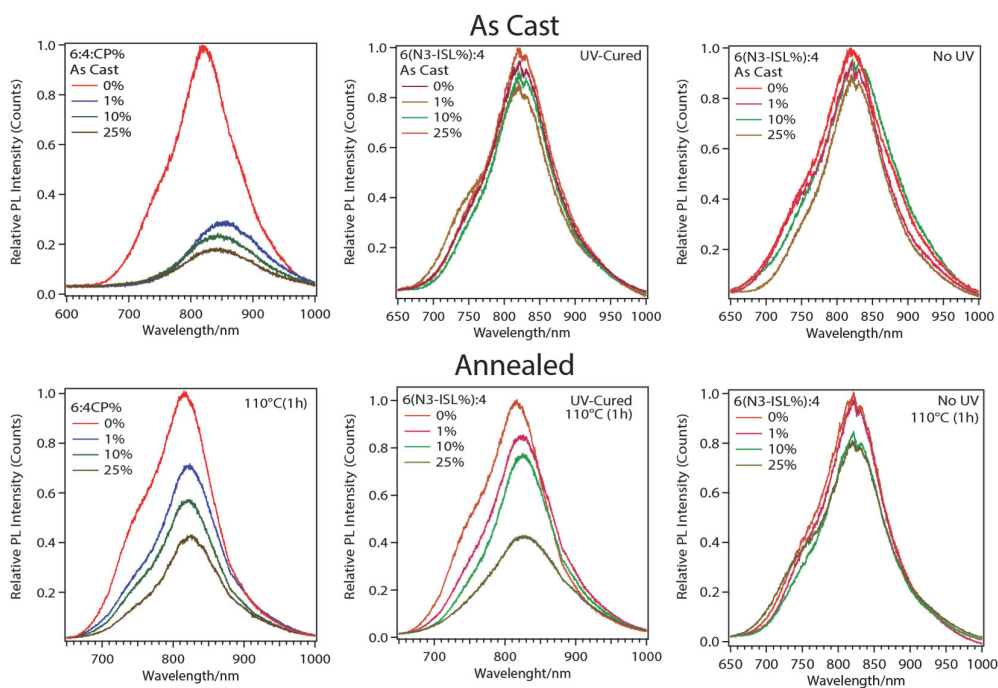
Figure S8. Photoluminescence emission spectra

Photoluminescence emission spectra of the 6:4 blends of DPP(TBFu)$_2$:PC$_{61}$BM with the respective additives at As cast (top three panels) and after thermal treatment of 110°C for 1 h (bottoms three panels). The normalized integrated PL emission is summarized in Figure 4b of the main text.
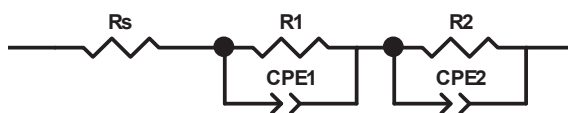
Figure S9. Equivalent circuit used for impedance Spectroscopy
Equivalent circuit used to fit the IS response in Figure 4c of the main text. The second RC element was only used for devices containing the azide linker.

Thin film preparation for morphological and electrochemical characterization:

The photoactive layers of each respective material were prepared by first dissolving each stock solution separately for 24hrs in the respective solvents at 50°C in chloroform at a concentration of 20mg/ml. The blended solutions were then stirred for 2hrs, and then filtered with a 0.2μm pore diameter PTFE filter, and left to stir for another hour before deposition on glass/ITO/PEDOT:PSS substrates via spin coating at 3000rpm. Thermal annealing were performed under Argon atmosphere at 110°C at various time intervals, and were allowed to cool down to room temperature under argon atmosphere before conducting any morphological and electrochemical analysis. The film thickness were kept between 140nm-152nm as determined by a Dektak 150 prolifometer.

Atomic force microscopy characterization:
Surface topography of all blend films were studied by atomic force microscopy (AFM) using an Asylum Research Cypher in AC mode using Atomic Force AC240TS tips directly on measured transistors surface under ambient conditions.

Optical Microscope:
Optical microscope images were obtained with a NIKON Eclipse E600.

UV-Vis and PL Characterization:
 Absorption spectra of the thin films were acquired with a UV–vis-NIR UV-3600 (Shimadzu) spectrophotometer, and the optical band gap (E_g^{opt}) was determined from the absorption edge of the thin film sample. Photoluminescence Spectra was carried out on a LabRAM HR Raman spectrometer at a laser excitation at 532 nm. An average of 15 measurements were conducted across the thin film to ensure accuracy of the data.

Thermal Characterisation:
 Differential scanning calorimeter (DSC) thermograms were measured with a PerkinElmer DSC8000 calibrated with indium and zinc, using a scanning rate of 10 °C/min. The respective Melting (T_m), and Crystallization (T_c) temperatures were characterized by their peak temperatures, and their endothermic and exothermic enthalpies were calculated from the surface area underneath both melting endotherms and crystallizing exotherms using the specific mass ratio in the stated blend composition of the primary components and the two additives. Samples were drop-casted evenly onto a SiO_2 substrate with a slow evaporation of the solvent (Chloroform) at 30 °C under argon atmosphere

before transferring the powder into an aluminium pan. Samples with N_3-ISL were UV cured for 10 minutes after drying on the SiO_2 substrate.

Solar-Cell Fabrication and Testing:

Solar cells were fabricated with a 35 nm layer of PEDOT:PSS (Ossilla M 121 Al 4083) deposited and annealed (110 °C) on a glass substrate patterned with 300 nm of ITO. The BHJ active layer was spin-cast at 3000 rpm from a solution of a blend of DPP(TBFu)$_2$:PC$_{61}$BM with the respective loading of the additive CP and N_3-ISL in chloroform at a total solid concentration of 20g/mL^{-1}. The active layers were determined to be ≈143nm thick using a Bruker Dektak XT profilometer. An 80 nm thick aluminium cathode was deposited (area 16 mm^2) by thermal evaporation (Kurt J. Lesker Mini-SPECTROS). Electronic characterization was performed under simulated AM1.5G irradiation from a 300 W Xe arc lamp set to 100 mW cm 2 with a calibrated Si photodiode (ThorLabs). Current– voltage curves were obtained with a Keithley 2400 source measure unit. Thermal stability measurements were performed with the device annealed under Argon atmosphere at 110°C at various time intervals, and were allowed to cool down to room temperature under argon atmosphere before measuring its photovoltaic performance. Impedance spectroscopy was carried out using a SP-200 potentiostat at frequencies ranging from 1 MHz up to 1 Hz. Each semicircle in the impedance response were fitted with a resistance in parallel to constant phase element (model shown in Figure S9). Device fabrication was performed under an argon atmosphere and testing was performed in a nitrogen filled glovebox.

Photocrosslinking (UV) reaction:

Photo-crosslinking reaction were performed using a low intensity hand-held (8W) UV lamp, set to emit 254nm light, with the bulb positioned approximately 1cm from the substrates at the specified time intervals under argon conditions.

FTIR:

The FTIR measurements were conducted on Nicolet 6700 from ThermoFisher Scientific. N_3-ISL was dissolved in chloroform at a concentration of 20mg/ml and left to stir at 50°C for 1h. Before drop casting 10µL on SiO_2 substrates under Argon atmosphere, and left to dry at room temperature before conducting the measurements at ambient conditions.

GPC and Mass Spectrum analysis:

The GPC measurements were made on a Shimazu CT-20A with a detector Shimazu SPD- 20A. Matrix-Assisted-Laser-Desorption/Ionization Time of Flight (MALDI-TOF) MS spectrum was recorded on a Bruker MALDI-TOF AutoFlex speed instrument using *trans*-2-[3-(4-*tert*-Butylphenyl)-2-methyl-2-propenylidene] malononitrile and 2,5-Dihydroxybenzoic acid as matrix using Tetrahydrofuran as a solvent. The samples were spin-coated onto SiO_2 substrates according to the solar cells thin film fabrication without deposition of PEDOT:PSS and the respective electrodes. The active layer were then treated with UV(254nm) or thermal annealing at 110°C at the respective time intervals under Argon atmosphere, and subsequently dissolved in 1ml of THF to perform the respective GPC and MALDI-MS measurements.

Synthetic Methods for CP and N₃-ISL:

All reagents were of commercial reagent grade (Sigma-Aldrich, Acros and Fluorochem) and were used without further purification. Toluene, Chloroform, Tetrahydrofuran (Fisher Chemical, HPLC grade) and chlorobenzene (Alfa Aesar, HPLC grade) were purified and dried on a Pure Solv-MD Solvent Purification System (Innovative Technology, Amesbury, United States) apparatus. Normal phase silica gel chromatography was performed with an Acros Organic silicon dioxide (pore size 60 Å, 40–50 μm technical grades). The (1H) and (13C) NMR spectra were recorded at room temperature using per-deuterated solvents as internal standards on a NMR Bruker Advance III-400 spectrometer (Bruker, Rheinstetten, Germany). Chemical shifts are given in parts per million (ppm) referenced to residual 1H or 13C signals in $CDCl_2$ (1H: 7.26, 13C: 77.16) and dichloromethane-d_2 (2H: 5.32, 13C:53.84). EI-MS spectrum was recorded on an EI/CI-1200L GC-MS (Varian) instrument. Atomatic-Pressure-Photoinonization-Source(APPI) MS spectrum was recorded on an ESI/APCI LC-MS Autopurification System with a ZQ Mass detector (Waters, Milford, United States) instrument using a positive mode. Matrix-Assisted-Laser-Desorption/Ionization Time of Flight (MALDI-TOF) MS spectrum was recorded on a Bruker MALDI-TOF AutoFlex speed instrument using alpha-cyano-4-hydroxycinnamic acid, and 2,5-Dihydroxybenzoic acid as matrix. Final products synthesized used in the active layers were purified using a Biotage Isolera™ Spektra Accelerated Chromatographic Isolation System™ with a Biotage ZIP® Sphere cartridges (60μm spherical silica) before device fabrication.

Synthetic Route for CP and N3-ISL
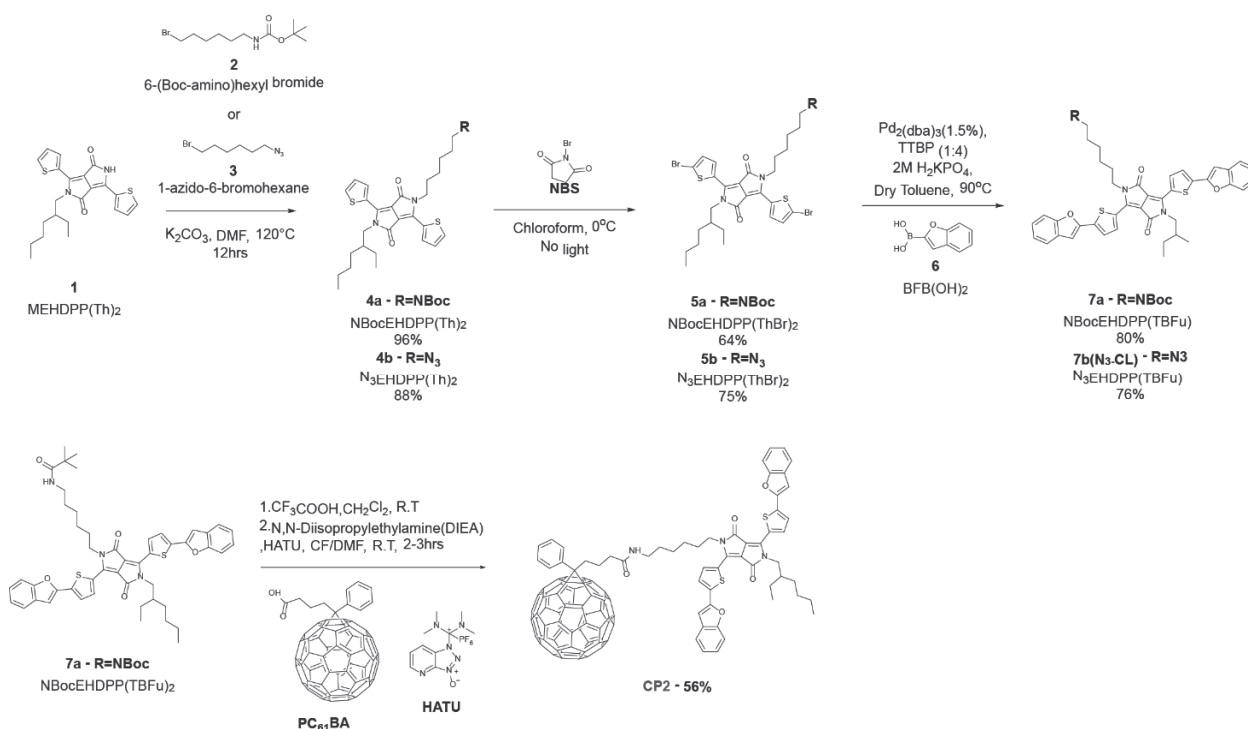
Figure S10. Overall synthetic route for CP and N₃-ISL

Synthetic Procedures

DPP(TBFu)$_2$ [S1] and [6,6]-phenyl-C61-butyric acid (PCBA) [S2] was synthesized according to literature procedure, while PC$_{61}$BM was purchased from Ossila. Synthesis of 2,5-Dihydro-3,6-di-2-thienyl-pyrrolo[3,4-c]pyrrole-1,4-dione (DPP(Th)$_2$) [S3] and subsequent mono-alkylation [S4] of the DPP(Th)$_2$ with 3-(bromomethyl)heptane to obtain MEHDPP(Th)$_2$ (1) and 1-azido-6-bromohexane (3) [S5] are based on literature procedures. 6-(Boc-amino)hexyl bromide (2) and 2-Benzofuranylboronic acid (6) was purchased from Sigma Aldrich.

NBocEHDPP(Th)$_2$ (4a) and N$_3$EHDPP(Th)$_2$ (4b)

MEHDPP(Th)$_2$ (1) (0.492g, 1.19 mmol) and anhydrous potassium carbonate (0.329 g, 2.39 mmol) were stirred in anhydrous (DMF) (50 mL) under nitrogen at 130 °C for 1 h. 6-(Boc-amino)hexyl bromide (2) (0.401g, 1.43 mmol) was then added dropwise and the reaction mixture stirred at 130 °C for a further 20 h. The reaction mixture was allowed to cool to room temperature, 1N HCl(aq)was added and left to stir for 1hr before pouring into ice water (1 L) . The suspension was then left to stir for 3 hours, and the precipitate was filtered and, dried under vacuum to give the crude product, and later separated via chromatography using an elution solvent of CHCl$_2$:Hexane (2:1) to obtain NBocEHDPP (4a) (0.729 g, 96%) as a dark red solid;

^{1}H NMR (400 MHz, Chloroform-d) δ 8.92 (dd, J = 28.2, 3.9 Hz, 1H), 7.65 (t, J = 4.2 Hz, 1H), 7.36 − 7.21 (m, 1H), 4.57 (d, J = 7.6 Hz, 1H), 4.19 − 3.93 (m, 2H), 3.12 (q, J = 6.7 Hz, 1H), 1.97 − 1.69 (m, 2H), 1.59 − 1.13 (m, 10H), 0.88 (q, J = 7.1 Hz, 4H); δ $_C$ (101 MHz, CDCl$_3$) 10.50, 14.05, 23.08, 23.51, 26.37, 26.50, 28.34, 28.45, 29.87, 30.21, 39.08, 40.46, 42.02, 45.85, 107.60, 107.98, 128.40, 128.68, 129.70, 129.83, 130.63, 130.69, 135.21, 135.41, 139.97, 140.45, 161.35, 161.75. MS (APPI): m/z [M+K]$^+$= 650.32493.

For N$_3$EHDPP(Th)$_2$ (4b), procedure is similar to 4a but using 1-azido-6-bromohexane (1.2eq) to obtain a yield of 88%. ^{1}H NMR (400 MHz, Chloroform-d) δ 8.93 (dd, J = 29.6, 3.8 Hz, 2H), 7.66 (d, J = 5.0 Hz, 2H), 7.37 − 7.24 (m, 2H), 4.11 (t, J = 7.8 Hz, 2H), 4.05 (dd, J = 7.6, 5.8 Hz, 2H), 3.29 (t, J = 6.8 Hz, 2H), 1.95 − 1.84 (m, 1H), 1.80 (t, J = 7.6 Hz, 2H), 1.71 − 1.58 (m, 4H), 1.47 (dq, J = 6.8, 3.7 Hz, 4H), 1.43 − 1.19 (m, 6H), 0.89 (q, J = 7.2 Hz, 6H); MS (ESI-TOF): m/z [M]$^+$= 538.23.

NBocEHDPP(ThBr)$_2$ (5a) and N$_3$EHDPP(ThBr)$_2$ (5b)

N-bromosuccinimide (NBS) (0.230g, 1.29mmol) was added to a solution of NBocEHDPP(Th)$_2$(4a) 0.396g, 0.647mmol) in chloroform at 0°C in which the flask was wrapped in aluminium foil to exclude light. After 24 hrs, the reaction mixture was poured into Hexane and left to stir in an ice bath. The mixture was filtered and the solid was washed with methanol (2 × 200 mL) then dried under vacuum. The crude product was recrystallized from Hexane/chloroform to give NBocEHDPP(ThBr)$_2$ (5a) as a dark purple solid (0.320g, 64%).

^{1}H NMR (400 MHz, Methylene Chloride-d_2) δ 8.68 (dd, J = 23.0, 4.2 Hz, 2H), 7.31 (dd, J = 7.3, 4.2 Hz,2H), 4.62 (s, 1H), 4.02 (t, J = 7.8 Hz, 2H), 3.96 (t, J = 7.7 Hz, 2H), 3.11 (q, J = 6.6 Hz, 2H), 1.85 (d, J = 7.2 Hz, 1H), 1.74 (d, J = 7.5 Hz, 2H), 1.62 − 1.22 (m, 16H), 0.91 (td, J = 7.2, 2.3 Hz, 18H); δ $_C$ (101 MHz, CDCl$_3$)

161.42, 139.43, 135.49, 135.33, 131.73, 131.47, 119.15, 119.11, 108.07, 107.73, 46.01, 42.09, 40.46, 39.12, 38.16, 31.25, 30.33, 30.17, 29.98, 29.95, 29.71, 28.44, 28.31, 26.51, 26.38, 23.53, 23.05, 22.99, 22.71, 14.14, 14.04, 10.48. MS (APPI): m/z [M+Na]$^+$= 792.094. For N$_3$EHDPP(ThBr)$_2$ (**5b**),the procedure is similar to **5a** to obtain a yield of 75%. ^{1}H NMR (400 MHz, Chloroform-d) δ 8.72 (d, J = 4.2 Hz, 1H), 8.66 (d, J = 4.2 Hz, 1H), 7.36 – 7.20 (m, 2H), 4.02 (q, J = 6.7, 5.7 Hz, 2H), 3.99 – 3.91 (m, 2H), 3.30 (t, J = 6.8 Hz, 2H), 1.85 (d, J = 6.0 Hz, 1H), 1.78 (t, J = 7.6 Hz, 2H), 1.64 (q, J = 6.9 Hz, 2H), 1.58 (s, 8H), 1.53 – 1.43 (m, 4H), 1.43 – 1.20 (m, 9H), 0.99 – 0.83 (m, 6H); MS (ESI-TOF): m/z [M]$^+$= 696.05.

NBocEHDPP(TBFu)$_2$ (7a) and N$_3$-ISL (7b)

NBocEHDPP(ThBr)$_2$ (**5a**) (0.114g, 0.148mmol), Benzofuran-2-boronic acid (**6**) (0.059g, 0.370mmol), tris(dibenzylideneacetone)dipalladium(0)(0.1eq), and tri-tert-butylphosphonium tetrafluoroborate (0.4eq) was mixed with anhydrous toluene and 2.0 M potassium phosphate (aq) in a 50mL Schleck Tube and the resulting mixture was degassed for 10 min. The reaction mixture was then stirred and heated to 90°C under argon overnight. The reaction mixture was allowed to cool down to room temperature, after which it was poured into 300mL of methanol and then stirred for 30 min. The precipitated solid was then collected by vacuum filtration and washed with several portions of distilled water, methanol, isopropanol, and petroleum ether. The crude product was purified by flash chromatography using chloroform as eluent, and the solvent was removed in vacuo to obtain a Greenish-Gold solid of NBocEHDPP(TBFu)$_2$ (**7a**) (0.101g, 80%).

 ^{1}H NMR (400 MHz, Chloroform-d) δ 9.04 (dd, J = 24.9, 4.2 Hz, 0H), 7.64 (q, J = 5.5 Hz, 1H), 7.56 (t, J = 7.9 Hz, 1H), 7.37 (t, J = 7.7 Hz, 1H), 7.29 (d, J = 1.6 Hz, 3H), 7.12 (d, J = 12.1 Hz, 0H), 4.57 (s, 0H), 4.19 (t, J = 7.9 Hz, 1H), 4.13 (t, J = 6.9 Hz, 0H), 3.16 (s, 1H), 1.98 (s, 0H), 1.86 (s, 1H), 1.51 (d, J = 48.2 Hz, 10H), 0.94 (dt, J = 13.2, 7.0 Hz, 2H). δ $_C$ (101 MHz, CD$_2$Cl2) 0.75, 10.28, 13.85, 23.10, 23.58, 26.37, 26.48, 28.12, 28.51, 29.68, 29.96, 30.28, 39.31, 103.59, 103.72, 111.13, 111.15, 121.25, 123.55, 125.38, 125.58, 128.90, 129.77, 136.24, 137.83, 150.08, 154.99, 161.08, 161.47. MS (MALDI-TOF): m/z [M]$^+$= 843.33. For N$_3$-ISL (**7b**) or **N$_3$-CL**, the procedure similar to **7a** to obtain a yield of 76%. ^{1}H NMR (400 MHz, Chloroform-d) δ 9.08 (d, J = 4.2 Hz, 1H), 9.01 (d, J = 4.3 Hz, 1H), 7.68 – 7.59 (m, 4H), 7.56 (dd, J = 8.2, 5.3 Hz, 2H), 7.37 (t, J = 7.8 Hz, 2H), 7.29 (m, 2H), 7.12 (s, 1H), 7.10 (s, 1H), 4.19 (q, J = 7.2 Hz, 2H), 4.11 (dt, J = 14.7, 7.1 Hz, 2H), 3.32 (t, J = 6.8 Hz, 2H), 1.97 (s, 2H), 1.87 (d, J = 7.3 Hz, 1H), 1.68 (p, J = 6.8 Hz, 2H), 1.58 (m, 8H), 1.49 – 1.25 (m, 8H), 1.05 – 0.81 (m, 6H); δ $_C$ (101 MHz, CDCl$_3$) 161.63, 161.22, 138.09, 138.01, 136.68, 136.46, 129.51, 128.84, 125.69, 125.44, 125.40, 123.58, 123.55, 121.22, 111.28, 103.84, 51.38, 46.08, 42.12, 39.28, 30.34, 29.95, 28.78, 28.52, 26.48, 26.41, 23.65, 10.58, 5.97; MS (MALDI-TOF): m/z [M]$^+$= 769.95.

CP

Firstly, NBocEHDPP(TBFu)$_2$ (**7a**) (175 mg, 0.17 mmol) was dissolved in dichloromethane (8mL), and 1.5 mL of TFA was added and stirred at room temperature. The reaction as measured using thin layer chromatography until all of the starting material has reacted, which is approximately 2 hours later. 8mL of saturated Na2CO3 aqueous and water were respectively used to quench the reaction. The Organic phase was then separated from the aqueous phase ,collected and dried with Na$_2$SO$_4$. The organic solvent was then removed to afford NH$_2$EHDPP(TBFu)$_2$ as a dark Green Solid. This was then precipitated using a mixture of hexane:CH$_2$Cl$_2$,and used for the next step without any further

purification. NH$_2$EHDPP(TBFu)$_2$ (27.0 mg, 36.29 μmol) was then dissolved in DMF (500 μl). A separate solution of PCBA (14.62mg, 16.3μmol) in CHCl$_3$ (900 μl), was stirred and sonicated at room temperature for 15 min, and then HATU (6.82 mg, 17.93 μmol) and DIEA (7.58mg, 10.22μl, 58.68 μmol) were sequentially added. After 10 min stirring at room temperature, this was added to the solution of NH$_2$EHDPP(TBFu)2. The reaction as measured using thin layer chromatography until all of the starting material has reacted. At the end of the reaction, the resulting mixture was concentrated under reduced pressure. The residue was dissolved in CHCl$_3$ (2 ml), washed with HCl (5%) and NaHCO$_3$ (sat.), dried over Na$_2$SO$_4$, and concentrated under reduced pressure. The resulting crude was washed with methanol/hexane and purified by flash chromatography using CH$_2$Cl$_2$ as eluent giving a dark green solid of **CP** (56.6%, 15mg). ^{1}H NMR (400 MHz, Chloroform-*d*) δ 9.08 (d, *J* = 4.2 Hz, 1H), 8.96 (d, *J* = 4.2 Hz, 1H), 7.95 – 7.84 (m, 2H), 7.64 (dd, *J* = 9.5, 4.0 Hz, 4H), 7.56 (m, 2H), 7.51 (t, *J* = 7.4 Hz, 2H), 7.45 (br,1H), 7.37 (t, *J* = 7.7 Hz, 2H), 7.29 (br, 1H), 7.15 (s, 1H), 7.10 (s, 1H), 5.88 (s, 1H), 4.13 (dq, *J* = 16.2, 7.4 Hz, 4H), 3.33 (d, *J* = 6.1 Hz, 2H), 2.94 – 2.82 (m, 2H), 2.41 (t, *J* = 7.5 Hz, 2H), 2.30 – 2.15 (m, 2H), 1.57-1.2(br,17H),1.02 – 0.80 (m, 6H). δ $_C$ (101 MHz, CD$_2$Cl2) 154.35, 154.35, 148.21, 147.17, 145.16, 144.43, 143.80, 143.63, 143.29, 143.07, 143.01, 142.27, 141.42, 141.38, 140.23, 137.32, 136.86, 136.13, 131.50, 130.37, 128.76, 128.24, 127.87, 57.90, 53.26, 50.28, 40.78, 35.47, 34.15, 33.96, 31.05, 29.19, 28.54, 27.11, 26.41, 24.81, 22.16, 20.27, 19.95, 18.96, 18.29, 17.98, 13.92, 13.72, 11.02. MS (MALDI-TOF): *m/z* [M]$^+$=1624.0.
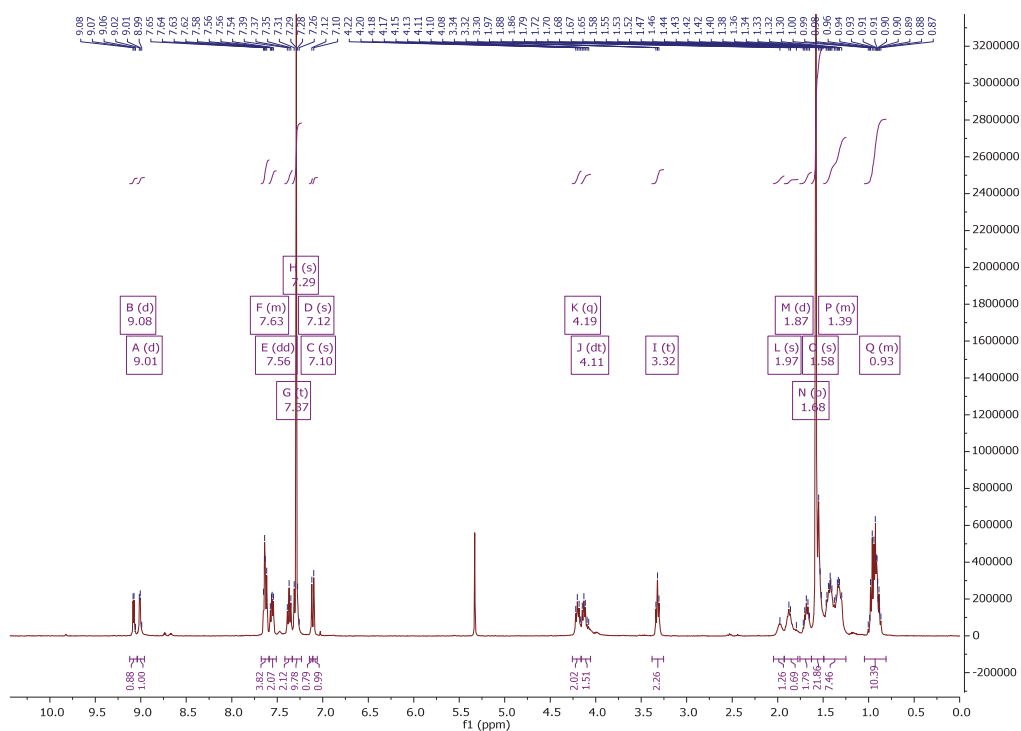
Figure S11. ^{1}H NMR of N$_3$-ISL
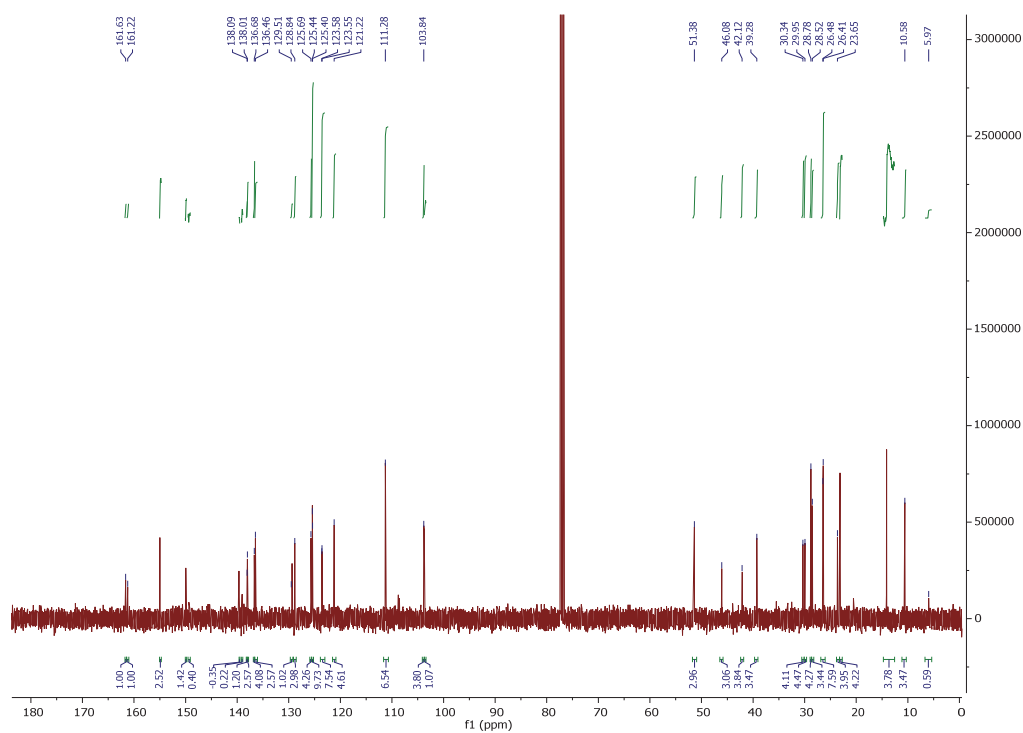
Figure S12. ^{13}C NMR of N_3-ISL
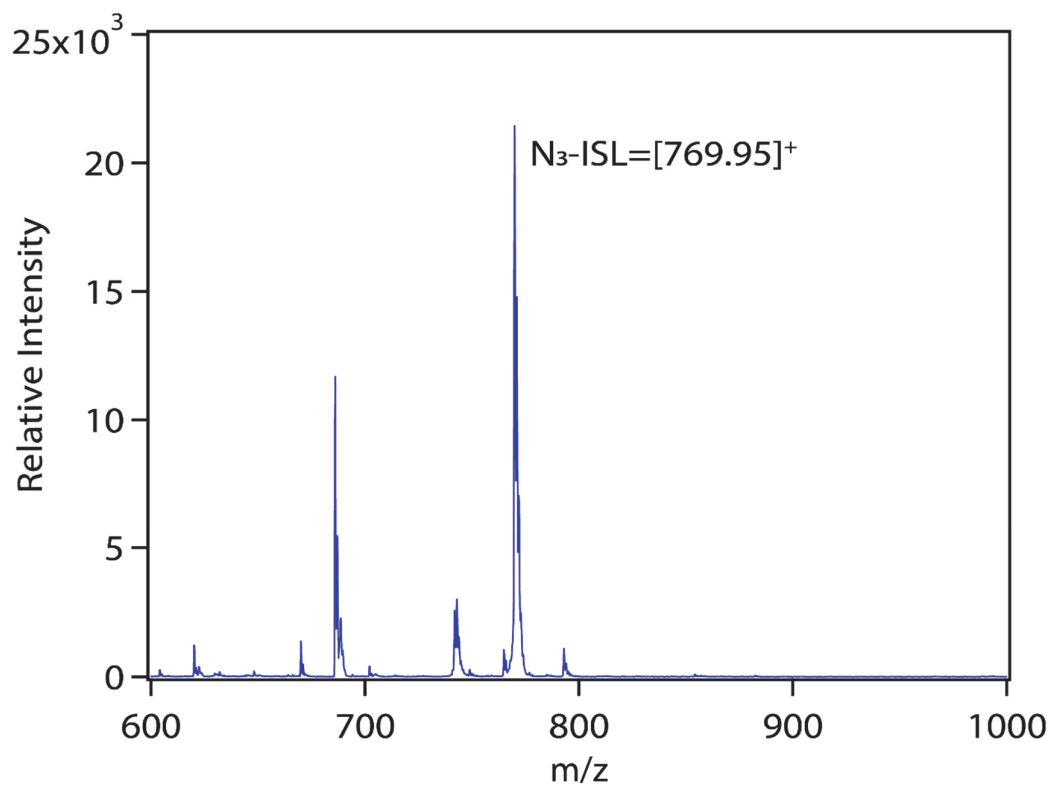
Figure S13. MALDI-TOF Mass Spectra of of N$_3$-ISL
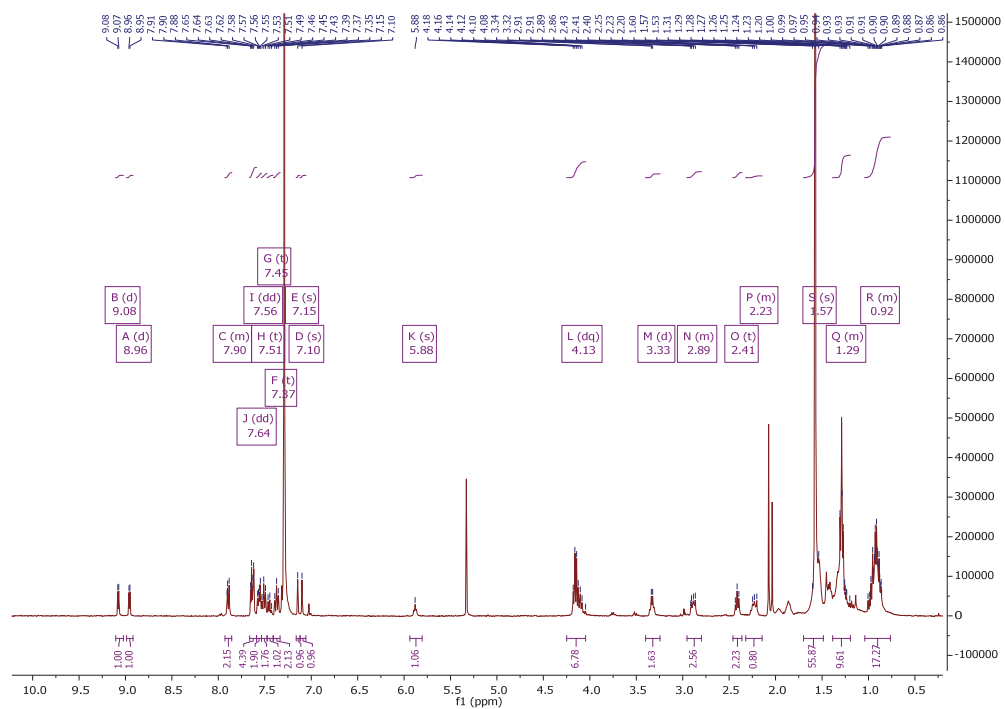
Figure S14. ^{1}H NMR of CP.
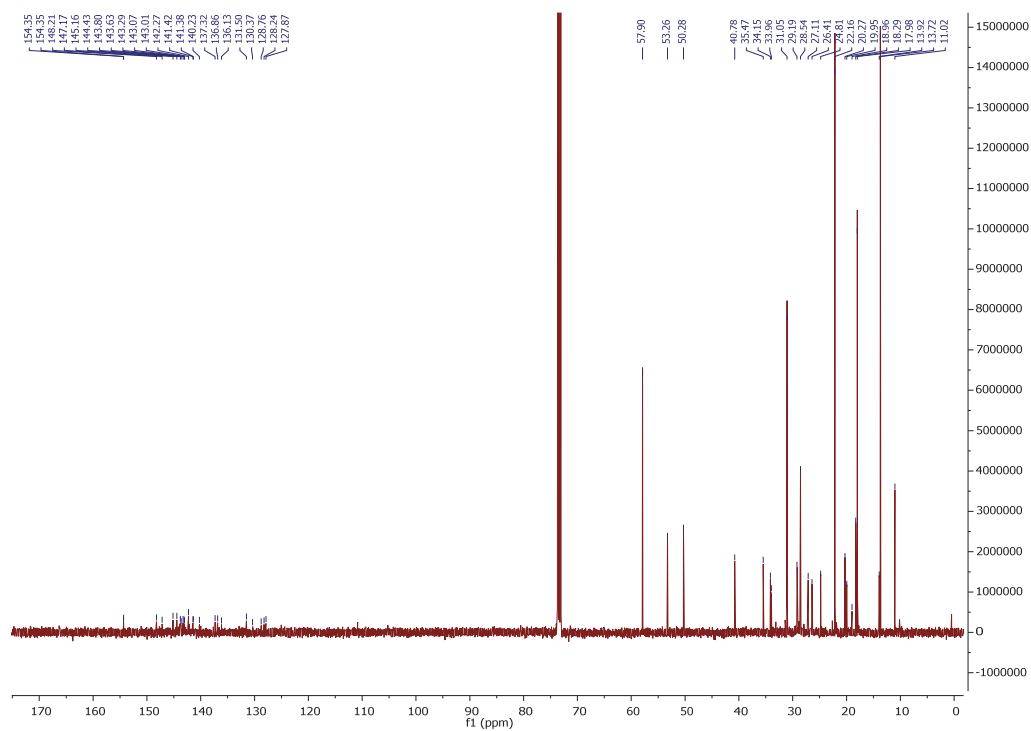
Figure S15. ^{13}C NMR of CP.
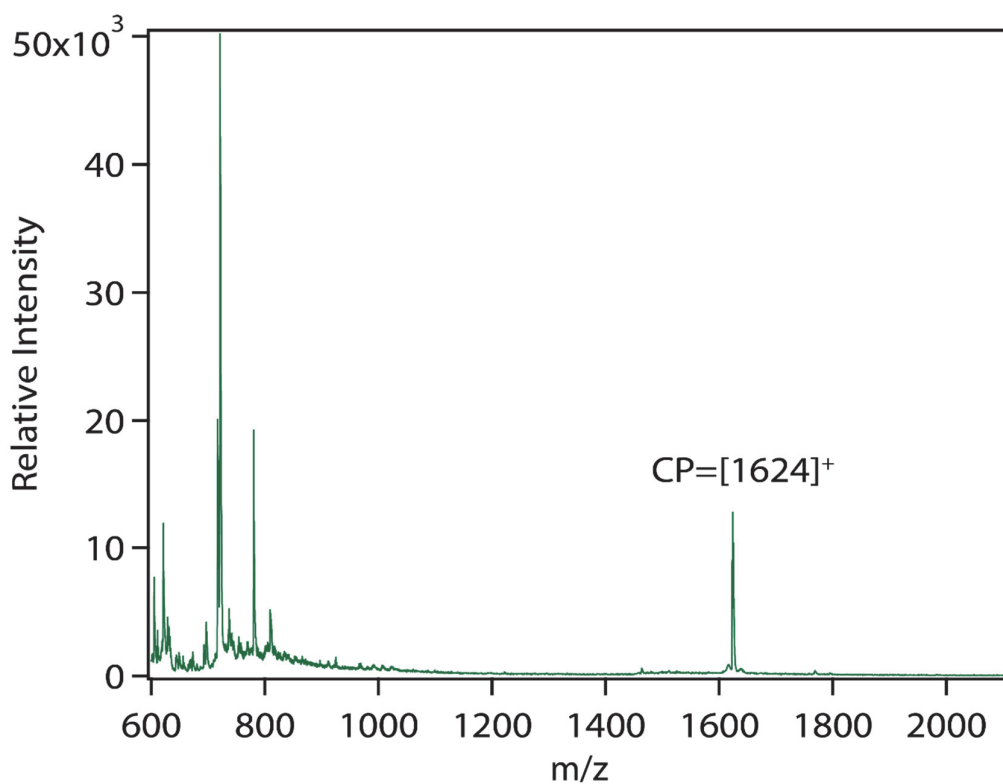
Figure S16. MALDI-TOF Mass Spectra of CP.

Supporting References

S1.   B. Walker, A. B. Tamayo, X.-D. Dang, P. Zalar, J. H. Seo, A. Garcia, M. Tantiwiwat and T.-Q. Nguyen, *Advanced Functional Materials*, 2009, **19**, 3063-3069.

S2.   Q. Wei, T. Nishizawa, K. Tajima and K. Hashimoto, *Advanced Materials*, 2008, **20**, 2211-2216.

S3.   G.-Y. Chen, C.-M. Chiang, D. Kekuda, S.-C. Lan, C.-W. Chu and K.-H. Wei, *Journal of Polymer Science Part A: Polymer Chemistry*, 2010, **48**, 1669-1675.

S4.   S. Izawa, K. Hashimoto and K. Tajima, *Chemical Communications*, 2011, **47**, 6365-6367.

S5.   J. Ramos-Soriano, U. Niss, J. Angulo, M. Angulo, A. J. Moreno-Vargas, A. T. Carmona, S. Ohlson and I. Robina, *Chemistry – A European Journal*, 2013, **19**, 17989-18003.

Appendix 3
Supplementary Figures in Chapter 3

Contents

Figure S1. ^{1}H-NMR, UV-Vis absorption, DSC Thermograms and GIXD

a) Aromatic region of the ^{1}H NMR of DPP(TBFu)$_2$-C$_6$H$_{12}$-EP-PDI (CP). Peaks were determined via 2D COSY (See Figure S14); **b)** Optical Absorption of the individual components dissolved in chloroform at 0.02mL/mg; **c)** DSC Thermograms of the 1[st](Dotted Line) and 2[nd](Solid Line) Heating and cooling scans of DPP(TBFu)$_2$(Blue), EP-PDI (Red) and MCP (Purple); **d)** Grazing Incidence X-ray Diffraction in the out-of-plane direction from the thin films of MCP (See Experimental procedure for thin film preparation).

Table S1. Endothermic transition enthalpy values

Calculated endothermic enthalpy of melting of a 1:1 blend of DPP(TBFu)$_2$:EP-PDI with varying MCP.

MCP (%)	Endothermic Enthalpy (J/g)		Endothermic Temperature Onset (°C)	
	DPP(TBFu)$_2$	EP-PDI	DPP(TBFu)$_2$	EP-PDI
0	20.574	2.78598	212.14	64.92
1	20.88702	2.60162	208.91	62.11
10	9.07397	0.85203	197.65	55.245

[e] *Enthalpy of melting was calculated based on the specific mass of each component in the blend*
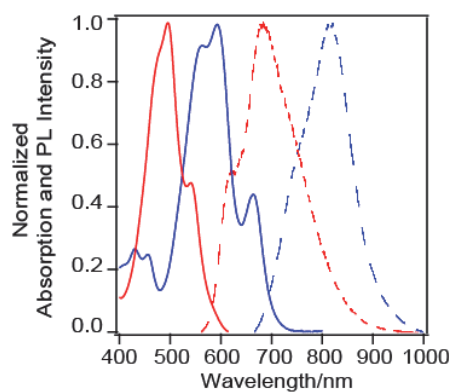
Figure S2. UV-Vis and PL Spectra

As cast thin films of DPP(TBFu)$_2$ (Blue) and EP-PDI (Red) where Solid lines indicate UV-Vis absorption Spectra and dotted lines indicate its PL emission. See experimental procedure for detailed Thin Film preparation.

Table S2. Summary of the Overall device data
Device metrics for devices at DPP(TBFu)$_2$:EP-PDI - 1:1 at various time intervals

Time (min)	10	70	130	190	250	490
CP	Average PCE (%)					
0%	1.60±0.07	1.192±0.13	1.09±0.046	1.01±0.04	1.01±0.03	0.36±0.081
1%	1.71±0.06	1.40±0.016	1.35±0.030	1.34±0.033	1.29±0.013	0.81±0.81
10%	1.27±0.01	1.03±0.025	1.00±0.016	0.99±0.29	0.97±0.05	0.960±12
	Average J$_{sc}$ (mAcm^{-2})					
0%	-0.0040 ±8.59×10^{-5}	-0.00336 ±2.37×10^{-4}	-0.00337 ±9.23×10^{-5}	-0.00321 ±5.91×10^{-5}	-0.00329 ±8.83×10^{-5}	-0.00142 ±2.4×10^{-4}
1%	-0.00417 ±8.59×10^{-5}	-0.00394 ±5.30×10^{-5}	-0.00386 ±4.91×10^{-5}	-0.00381 ±1.33×10^{-5}	-0.00369 ±3.99×10^{-5}	-0.00274 ±2.45×10^{-4}
10%	-0.00350 ±7.25×10^{-6}	-0.00302 ±3.08×10^{-5}	-0.00317 ±4.96×10^{-5}	-0.00307 ±6.62×10^{-5}	-0.00311 ±2.92×10^{-5}	-0.00279 ±3.1×10^{-4}
	Average V$_{oc}$ (V)					
0%	0.880±0.015	0.852±0.009	0.840±0.013	0.805±0.015	0.82±0.02	0.815±0.0087
1%	0.880±0.0	0.853±0.009	0.830±0.009	0.813±0.004	0.827±0.009	0.800±0.0
10%	0.860±0.0	0.833±0.009	0.820±0.0	0.796±0.004	0.813±0.009	0.832±0.024
	Average Fill Factor					
0%	0.456±0.01	0.432±0.017	0.428±0.015	0.400±0.02	0.410±0.02	0.35±0.019
1%	0.475±0.005	0.457±0.004	0.450±0.01	0.443±0.009	0.447±0.009	0.400±0.01
10%	0.43±0.0	0.427±0.004	0.427±0.004	0.420±0.008	0.427±0.004	0.430±0.018

The results were calculated based on an average of 6 pixels from 2 devices which were annealed at 110°C at the stated time intervals.

General Experimental Procedure

Thin film preparation for morphological and electrochemical characterization

Preparation of BHJ Blend solution and Spin-Coated Thin films:
The photoactive layers of each respective material were prepared by first dissolving each stock solution separately for 12hrs at 50°C in chloroform (CF) at a concentration of 20mg/ml. The individual solutions

were then blended with varying MCP loading and left to stir for at least 2hrs before filtering with a 1.0μm pore diameter PTFE filter, and left to stir for another hour before deposition onto the respective substrates. Pre-patterned ITO was cleaned by sequential sonication in water, isopropanol and acetone for 30 min each, and dried by argon. A 35 nm layer of PEDOT:PSS (Ossila M 121 Al 4083) was then spin coated onto of the ITO surface and annealed at 130°C for 25 min and cooled down to room temperature before depositing the BHJ active layer *via* spin-coating onto the substrate at 3000rpm for 60 seconds to obtain a thickness of approximately ≈140nm as measured from a Bruker Dektak XT profilometer. The substrates were then annealed at the respective temperatures 110°C under argon before and allowed to cool down to room temperature before further morphological characterization

Morphological and Photo-electrochemical Characterization

UV-Vis and PL Characterization:
Absorption spectra of the thin films were acquired with a UV–vis-NIR UV-3600 (Shimadzu) spectrophotometer, and the optical band gap (E_g^{opt}) was determined from the absorption edge of the thin film sample. Photoluminescence Spectra was carried out on a Fluorolog-3 spectrofluorometer (Horiba) equipped with a Xe lamp with an excitation light source at 532 nm. The sample was placed at 45° from the lamp to the detector.

Thermal Characterisation:
Differential scanning calorimeter (DSC) thermograms were measured with a PerkinElmer DSC8000 calibrated with indium and zinc, using a scanning rate of 10 °C/min. The respective Melting (T_m), and Crystallization (T_c) temperatures were characterized by their peak temperatures, and their endothermic and exothermic enthalpies were calculated from the surface area underneath both melting endotherms and crystallizing exotherms using the specific mass ratio in the stated blend composition of the primary components and MCP. Samples were drop-casted evenly onto a SiO_2 substrate with a slow evaporation of the solvent (chloroform) at 30 °C under argon atmosphere before transferring the solid powder into an aluminium pan.

X-ray Diffraction Characterization:
XRD was measured with a D8 Discovery (Bruker) diffractometer using CuKα radiation and Ni β-filter with a scan rate of 0.05°/min and a step width of 0.01°. For the GIWAXS measurements, an incident wavelength of 1.54Å and angle of 0.2° was used

Optical Microscope:
Optical microscope images were obtained with a NIKON Eclipse E600.

Solar-Cell Fabrication and Testing
Upon spin coating of the respective BHJ active layer the substrates were transferred into the deposition chamber to thermally evaporate 4 nm of MoO_3 and 100 nm Ag at ~10^{-6} mbar through a shadow mask with an active area of 16 mm^2. An 80 nm thick aluminium cathode was deposited (area 16 mm^2) by thermal evaporation (Kurt J. Lesker Mini-SPECTROS). Electronic characterization was performed under simulated AM1.5G irradiation from a 300 W Xe arc lamp set to 100 mW cm 2 with a calibrated Si photodiode (ThorLabs). Current– voltage curves were obtained with a Keithley 2400 source measure unit. Thermal stability measurements were performed with the device annealed under

Argon atmosphere at 110°C at various time intervals, and were allowed to cool down to room temperature under argon atmosphere before measuring its photovoltaic performance.

Synthetic Procedures

Synthetic methods and characterization:
All reagents were of commercial reagent grade (Sigma-Aldrich, Acros and Fluorochem) and were used without further purification. Toluene, Chloroform, Tetrahydrofuran (Fisher Chemical, HPLC grade) and chlorobenzene (Alfa Aesar, HPLC grade) were purified and dried on a Pure Solv-MD Solvent Purification System (Innovative Technology, Amesbury, United States) apparatus. Normal phase silica gel chromatography was performed with an Acros Organic silicon dioxide (pore size 60 Å, 40–50 μm technical grades). The (1H) and (13C) NMR spectra were recorded at room temperature using per-deuterated solvents as internal standards on a NMR Bruker Advance III-400 spectrometer (Bruker, Rheinstetten, Germany). Chemical shifts are given in parts per million (ppm) referenced to residual 1H or 13C signals in $CDCl_2$ (1H: 7.26, 13C: 77.16) and dichloromethane-d_2 (2H: 5.32, 13C:53.84). Atomatic-Pressure-Photoinonization-Source(APPI) MS spectrum was recorded on an ESI/APCI LC-MS Autopurification System with a ZQ Mass detector (Waters, Milford, United States) instrument using a positive mode. Matrix-Assisted-Laser-Desorption/Ionization Time of Flight (MALDI-TOF) MS spectrum was recorded on aBruker MALDI-TOF AutoFlex speed instrument using alpha-cyano-4-hydroxycinnamic acid as the matrix. DPP(TBFu)$_2$ was synthesized according to literature procedure while *N,N'*-Bis(3-pentyl)perylene-3,4,9,10-bis(dicarboximide) (EP-PDI) was purchased from Sigma Aldrich. Both materials were purified using a Biotage Isolera™ Spektra Accelerated Chromatographic Isolation System™ with a Biotage ZIP® Sphere cartridges (60μm spherical silica) before device fabrication.

Synthetic Procedures:
DPP(TBFu)$_2$ was synthesized according to literature procedures[3] while EP-PDI was purchased commercially from Sigma-Aldrich. Synthesis of 2-(6-aminohexyl) -3,6- (5-(benzofuran-2-yl) thiophen-2-yl)-5-(2-ethylhexyl)-2,5- dihydropyrrolo [3,4-c] pyrrole-1,4-dione (**NH₂EHDPP(TBFu)₂**) is based on our previous report on the synthesis of a similar molecular compatibilizer and as shown in Chapter 1 Figure1 b [4]. Detailed synthetic steps are described below:
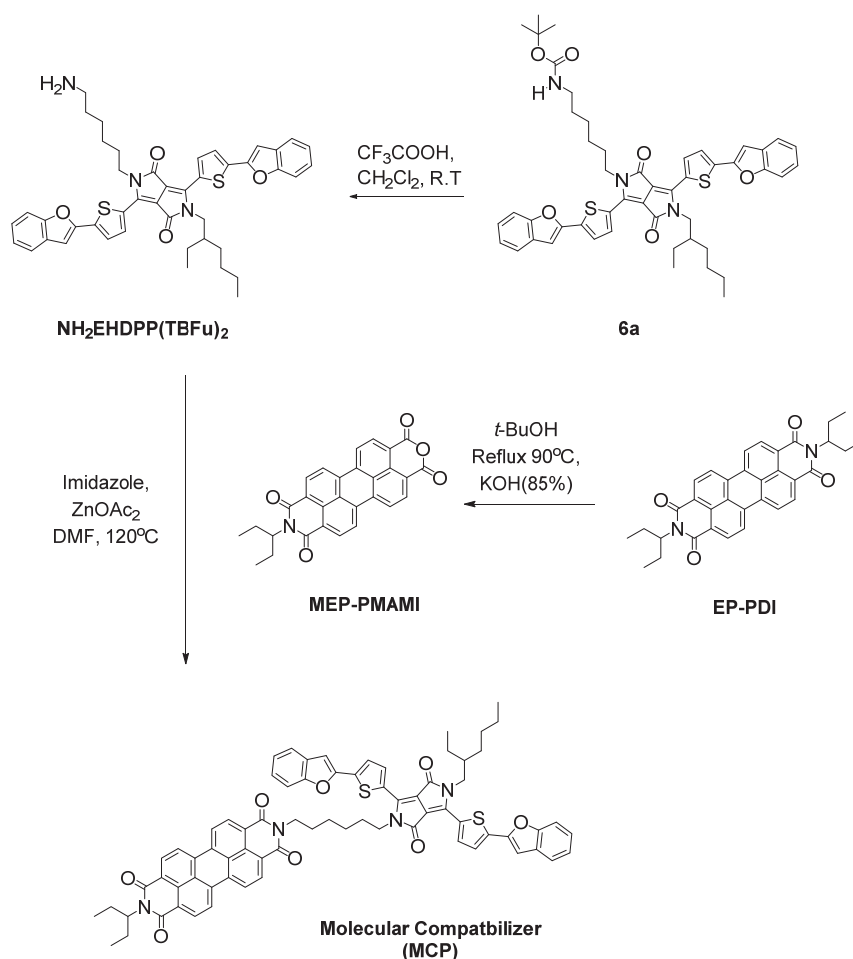
Figure S3. Full Synthetic route of the molecular compatibilizer

9-(pentan-3-yl)-1H-isochromeno[6',5',4':10,5,6]anthra[2,1,9-def]isoquinoline-1,3,8,10(9H)-tetraone (MEP-PMAMI):

To a mixture of EP-PDI (6.22 g, 6.0 mmol) and *t*-BuOH (150 mL) was added 85% KOH powder (1.98 g, 30.0 mmol). The resulting mixture was refluxed for 90 °C and the conversion was monitored via TLC (CHCl3/AcOH 10:1 *v/v*). After complete disappearance of the starting material (2h), the mixture was poured slowly with stirring into Glacial Acetic acid (150 mL) and stirred for 2 h. Then 2N HCl (60 mL) was added and stirring was continued for additional 30 min untila dispersion of the precipitate is seen. This was collected by filtration, washed with water until the aqueous solution is neutral. The crude product was further purified by column chromatography on silica gel with CHCl3/AcOH (10:1) to remove any starting material to obtain a dark brown solid (3.06 g, 71.4 %). ^{1}H NMR (400 MHz, Chloroform-*d*) δ 8.86 – 8.65 (m, 8H), 5.17 – 5.00 (m, 1H), 2.30 (ddd, *J* = 13.9, 9.3, 7.1 Hz, 2H), 1.98 (dt, *J* = 13.9, 6.7 Hz, 2H), 0.96 (t, *J* = 7.5 Hz,6). MS (APPI): *m/z* [M]$^+$= 461.47.

MCP:

MEP-PMAMI (0.066g, 1.43 mmol), NH$_2$EHDPP(TBFu)$_2$ (0.16 g, 1.43 mmol), and Zn(OAc)$_2$ (0.019mg, 1.07mmol) were suspended in a solution of imidazole (5g) and DMF (10 mL). The mixture was heated overnight at 120°C before being cooled to room temperature. Ethanol/Methanol (200 mL) followed by the addition of aqueous citric acid (10%, 200 mL) was added into the mixture to precipitate the product which was removed by filtration. The crude solid was subjected to column chromatography using CHCl$_3$ as eluent and subsequently precipitated in a mixture of methanol/Hexane/CH$_2$Cl$_2$ to obtain a dark purple solid (0.079g, 40%). ^{1}H NMR (400 MHz, Chloroform-*d*) δ 8.97 (dd, *J* = 15.8, 4.1 Hz, 2H), 8.60 (d, *J* = 7.9 Hz, 2H), 8.52 (d, *J* = 7.9 Hz, 2H), 8.45 (d, *J* = 8.1 Hz, 2H), 8.40 (d, *J* = 8.1 Hz, 2H), 7.51 (qd, *J* = 16.8, 15.8, 7.8 Hz, 4H), 7.41 – 7.15 (m, 6H), 7.00 (s, 2H), 5.09 (t, *J* = 8.0 Hz, 1H), 4.18 (dt, *J* = 27.4, 7.6 Hz, 4H), 4.05 (q, *J* = 11.4, 7.3 Hz, 2H), 2.30 (dp, *J* = 15.9, 7.8 Hz, 2H), 1.94 (ddt, *J* = 44.1, 15.7, 7.5 Hz,4H), 1.60 (d, *J* = 10.7 Hz, 8H), 1.36 (ddd, *J* = 33.0, 14.6, 8.1 Hz, 8H), 0.95 (dt, *J* = 25.7, 7.4 Hz, 12H); δ $_C$ (101 MHz, CDCl$_3$) 10.56, 11.43, 14.13, 23.13, 25.04, 26.59, 26.73, 27.94, 28.51, 29.95, 30.32, 35.71, 39.25, 40.40, 42.26, 46.00, 57.77, 103.62, 111.23, 121.11, 121.18, 122.80, 122.92, 123.05, 123.44, 123.54, 125.28, 125.37, 125.61, 126.16, 128.77, 128.81, 129.16, 129.42, 129.51, 131.17, 134.21, 134.40, 136.39, 136.52, 137.88, 137.91, 154.93, 163.24; MS (MALDI-TOF): *m/z* [M]$^+$= 1186.8.
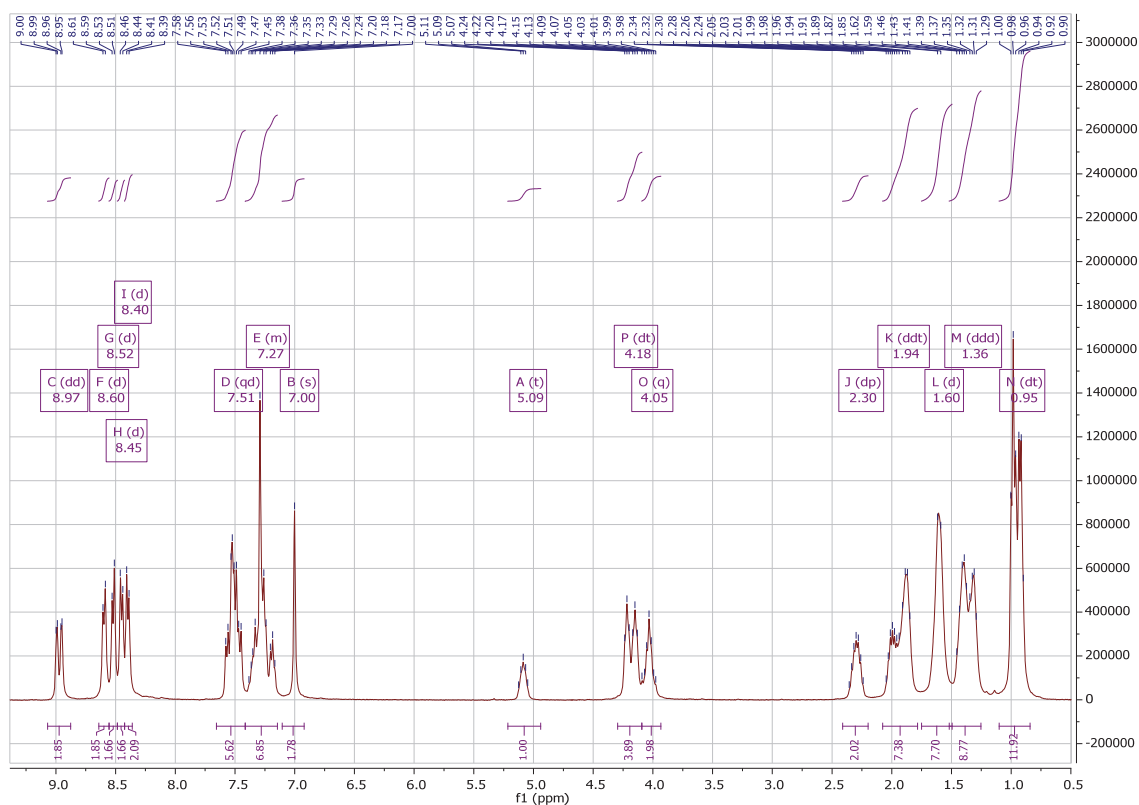
Figure S4.^{1}H NMR of MCP
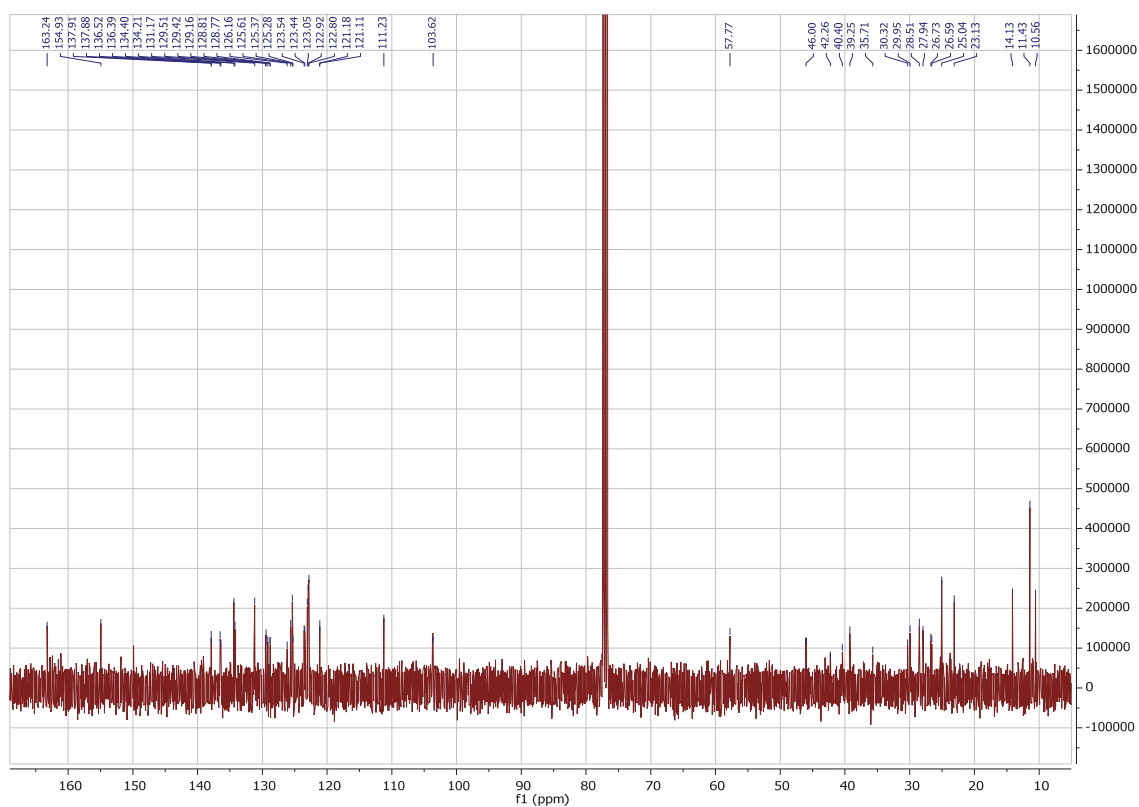
Figure S5. ^{1}C NMR of MCP
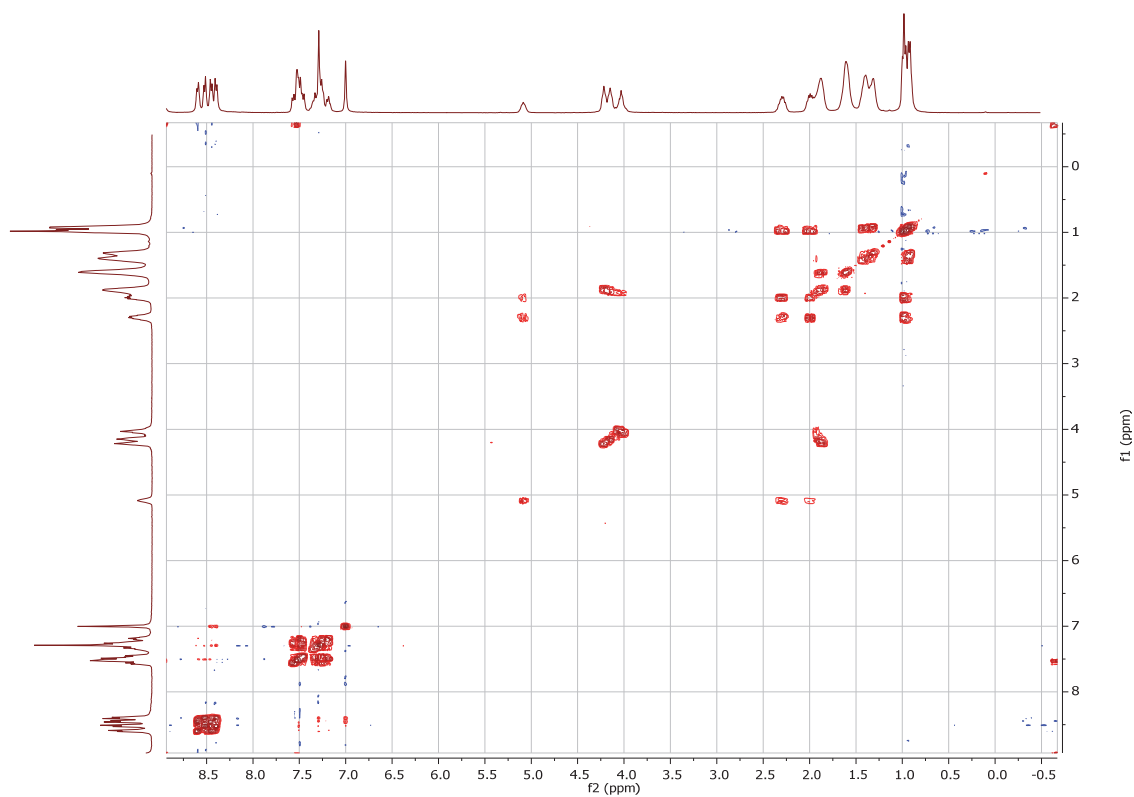
Figure S6. 2D Correlation Spectroscopy (COSY) NMR of the MCP
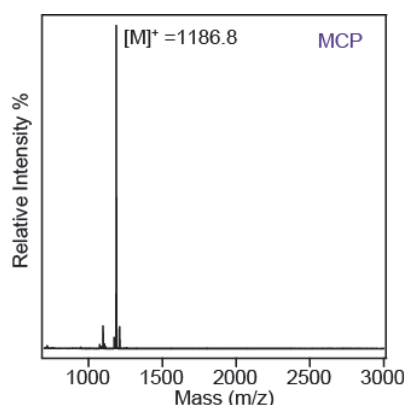
Figure S7.MALDI TOF MS of MCP

Reference

1.	(a) Jeanbourquin, X. A.; Rahmanudin, A.; Gasperini, A.; Ripaud, E.; Yu, X.; Johnson, M.; Guijarro, N.; Sivula, K., Engineering the self-assembly of diketopyrrolopyrrole-based molecular semiconductors via an aliphatic linker strategy. *Journal of Materials Chemistry A* **2017,** *5* (21), 10526-10536; (b) Viterisi, A.; Gispert-Guirado, F.; Ryan, J. W.; Palomares, E., Formation of highly crystalline and texturized donor domains in DPP(TBFu)2:PC71BM SM-BHJ devices via solvent vapour annealing: implications for device function. *Journal of Materials Chemistry* **2012,** *22* (30), 15175-15182.

2.	(a) Li, M.; Liang, Q.; Zhao, Q.; Zhou, K.; Yu, X.; Xie, Z.; Liu, J.; Han, Y., A bi-continuous network structure of p-DTS(FBTTh2)2/EP-PDI via selective solvent vapor annealing. *Journal of Materials Chemistry C* **2016,** *4* (42), 10095-10104; (b) Li, M.; Liu, J.; Cao, X.; Zhou, K.; Zhao, Q.; Yu, X.; Xing, R.; Han, Y., Achieving balanced intermixed and pure crystalline phases in PDI-based non-fullerene organic solar cells via selective solvent additives. *Physical Chemistry Chemical Physics* **2014,** *16* (48), 26917-26928; (c) Chen, L.; Peng, S.; Chen, Y., Cooperative Assembly of Pyrene-Functionalized Donor/Acceptor Blend for Ordered Nanomorphology by Intermolecular Noncovalent π–π Interactions. *ACS Applied Materials & Interfaces* **2014,** *6* (11), 8115-8123; (d) Namepetra, A.; Kitching, E.; Eftaiha, A. a. F.; Hill, I. G.; Welch, G. C., Understanding the morphology of solution processed fullerene-free small molecule bulk heterojunction blends. *Physical Chemistry Chemical Physics* **2016,** *18* (18), 12476-12485.

3.	Walker, B.; Tamayo, A. B.; Dang, X.-D.; Zalar, P.; Seo, J. H.; Garcia, A.; Tantiwiwat, M.; Nguyen, T.-Q., Nanoscale Phase Separation and High Photovoltaic Efficiency in Solution-Processed, Small-Molecule Bulk Heterojunction Solar Cells. *Advanced Functional Materials* **2009,** *19* (19), 3063-3069.

4.	Rahmanudin, A.; Jeanbourquin, X. A.; Hanni, S.; Sekar, A.; Ripaud, E.; Yao, L.; Sivula, K., Morphology stabilization strategies for small-molecule bulk heterojunction photovoltaics. *Journal of Materials Chemistry A* **2017**.

Appendix 4

Supplementary Figures in chapter 4

Contents

Table S1. Calculated endothermic and exothermic (specific) enthalpies of 1:1 BHJs of DPP(TBFu)$_2$:EP-PDI with varying MCPwt%.

See experimental procedure for detailed sample preparation and measurement conditions.

MCP (%)	Enthalpy (J/g)[a]				Temperature (°C)[b]			
	Endothermic		Exothermic		Endothermic		Exothermic	
	DPP(TBFu)$_2$	EP-PDI	DPP(TBFu)$_2$	EP-PDI	DPP(TBFu)$_2$	EP-PDI	DPP(TBFu)$_2$	EP-PDI
0	20.574	2.78598	20.216	3.58572	230.5	73.3	208.4	59.4
10	9.07397	0.85203	7.60968	1.20463	217.6	70.2	196.2	57.7
25	7.0624	0.20603	6.29926	0.52583	212.1	69.6	187.4	52.6
50	5.85775	0	-	-	202.4	-	-	-
75	-	-	-	-	-	-	-	-

[a] The endothermic and exothermic enthalpies were calculated based on the integration of each phase transition using the exact mass ratio of the component in the blend at a 1:1 - DPP(TBFu)$_2$:EP-PDI ratio with varying MCPwt% from the DSC thermograms.
[b] The respective endothermic and exothermic temperatures were characterized by their peak Temperature.
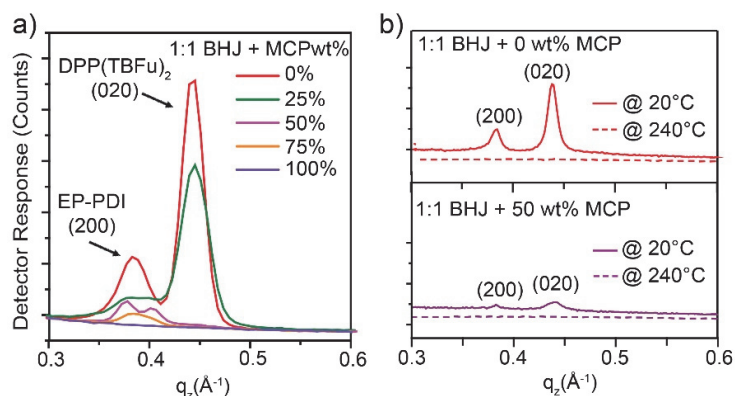

Figure S1. X-ray diffraction results.

Panel (a) shows the out-of-plane grazing-incidence wide-angle x-ray scattering patterns of 1:1 BHJs with added MCP in thin films that have been treated at 240°C for 15 min and cooled over 30 min to room temperature. Panel (b) shows *in-situ* x-ray scattering patterns (Bragg-Brentano geometry) of BHJ thin films at 20°C (solid-line) and at 240°C (dash-line) with 0 wt% (top) and 50 wt% (bottom) of MCP.
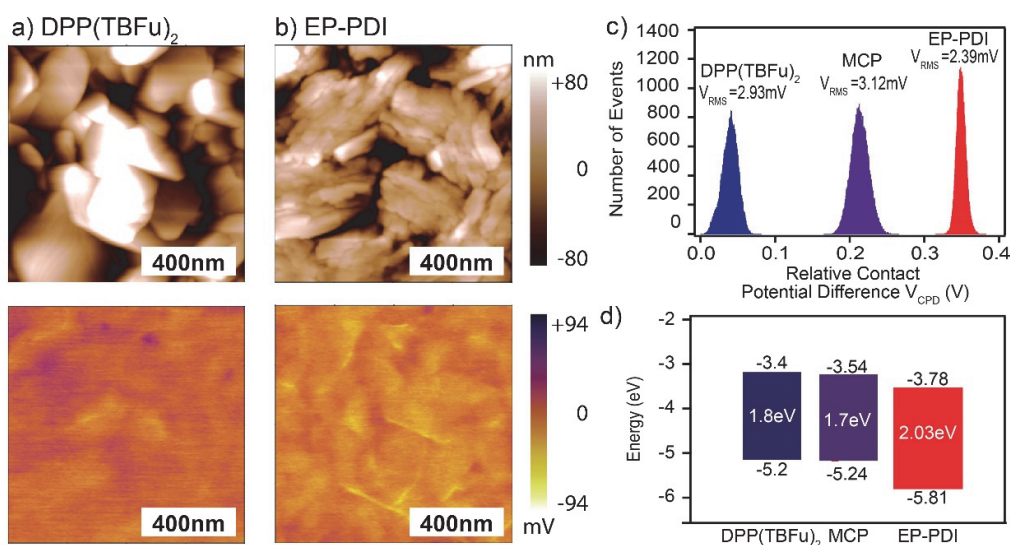
Figure S2. AFM and KPFM analysis:
Height-topography and potential Images of individual components a)DPP(TBFu)$_2$,b) MCP, Panel (c) shows the relative Contact Potential difference (V$_{CPD}$) histograms of the individual components d) Estimated HOMO-LUMO levels measured by the UV-Vis absorption (See Figure S9a) and cyclic voltammetry (See Figure S9b).
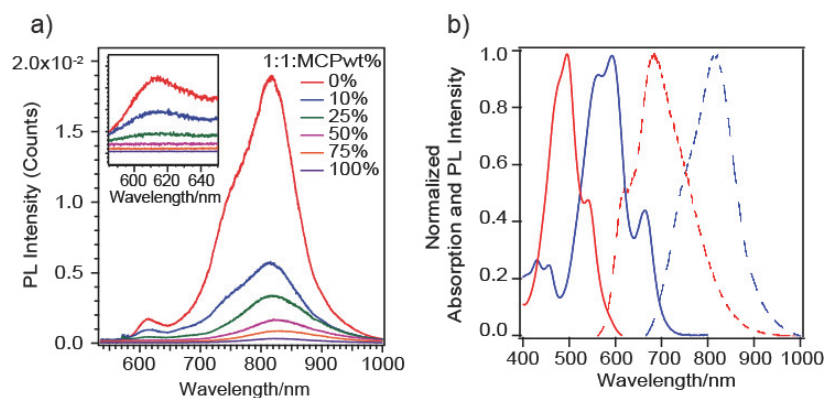

Figure S3. Photoluminescence emission spectra
a) Photoluminescence emission spectra after excitation at 532nm of melt-annealed BHJ thin films of DPP(TBFu)$_2$:EP-PDI – 1:1 with varying amount of MCP w (Inset shows zoomed spectra between 580-650nm to indicate the emission peak for EP-PDI); b) shows the data for the pure components: DPP(TBFu)$_2$ (Blue) and EP-PDI (Red) (Solid lines indicate UV-Vis absorption spectra and dotted lines indicate its PL emission).
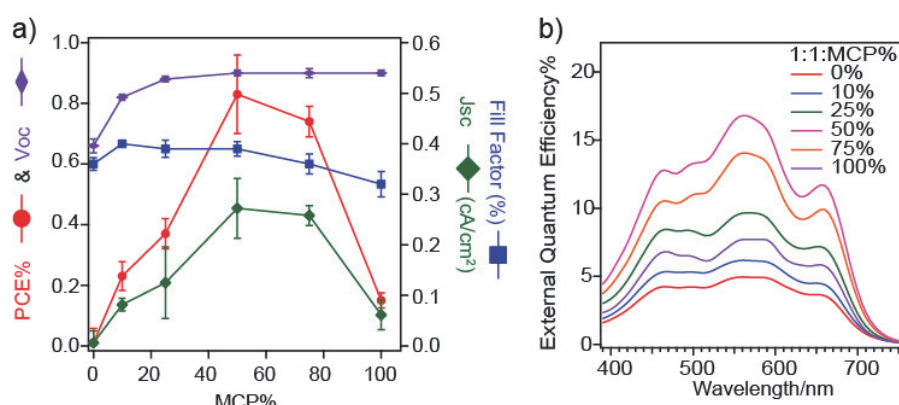
Figure S4. Summary of photovoltaic parameters of the melt-annealed devices:
a) Graphical representation of PCE% (Red), Open Circuit Voltage (Purple), Short-circuit Current (Green) and Fill Factor (Blue).

Table S2. The values of the respective device performance parameters averaged from 5 devices fabricated at each condition.

MCP (%)	Voc (V)	Jsc[b] (mA/cm^2)	FF (%)	PCE (%)
0	0.66±0.023	0.23±0.024	0.36±.0013	0.010±0.047
10	0.82±0.0098	0.815±0.13	0.4 0±0.0047	0.23 ±0.050
25	0.88±.00094	1.24±0.071	0.39±0.017	0.37 ±0.017
50	0.9±0.0094	2.72±0.059	0.39±0.059	0.83 ±0.014
75	0.9±0.015	2.58±0.020	0.36±0.0196	0.74 ±0.020
100	0.9±0.0095	0.614±0.029	0.32±0.029	0.116 ±0.25

[a] Error bars were calculated based on an average of 5 batches of Photovoltaic devices .
[b] Values presented in the graph were converted from mA/cm^2 to cA/cm^2.
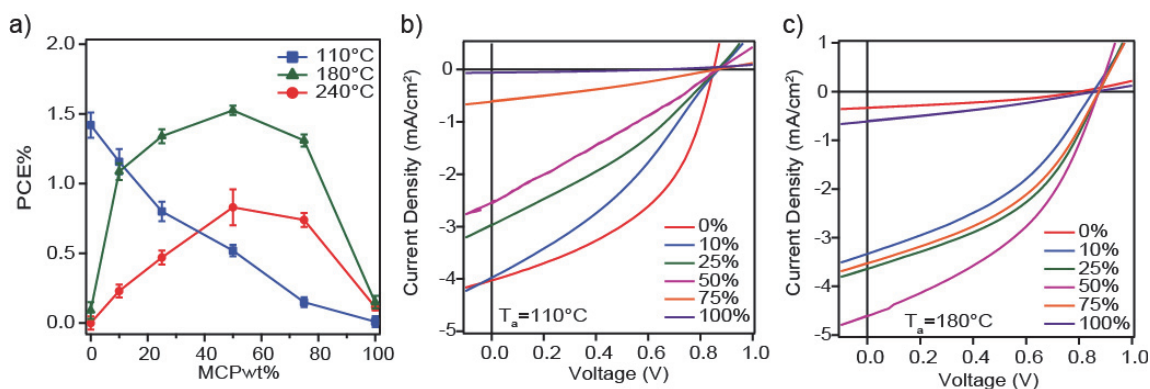

Figure S5. Photovoltaic performance of devices with 1:1 ratio of DPP(TBFu)$_2$:EP-PDI with varying amounts of MCPwt% at different annealing Temperatures (BHJ cast from chloroform):
a) PCE vs MCPwt% (Red - 240°C, Green – 180°C and blue – 110°C); Current vs Voltage Curves for devices at b) T$_a$=110°C b) and c) T$_a$=180°C. (See experimental procedure for detailed thin film preparation and device Fabrication method.)
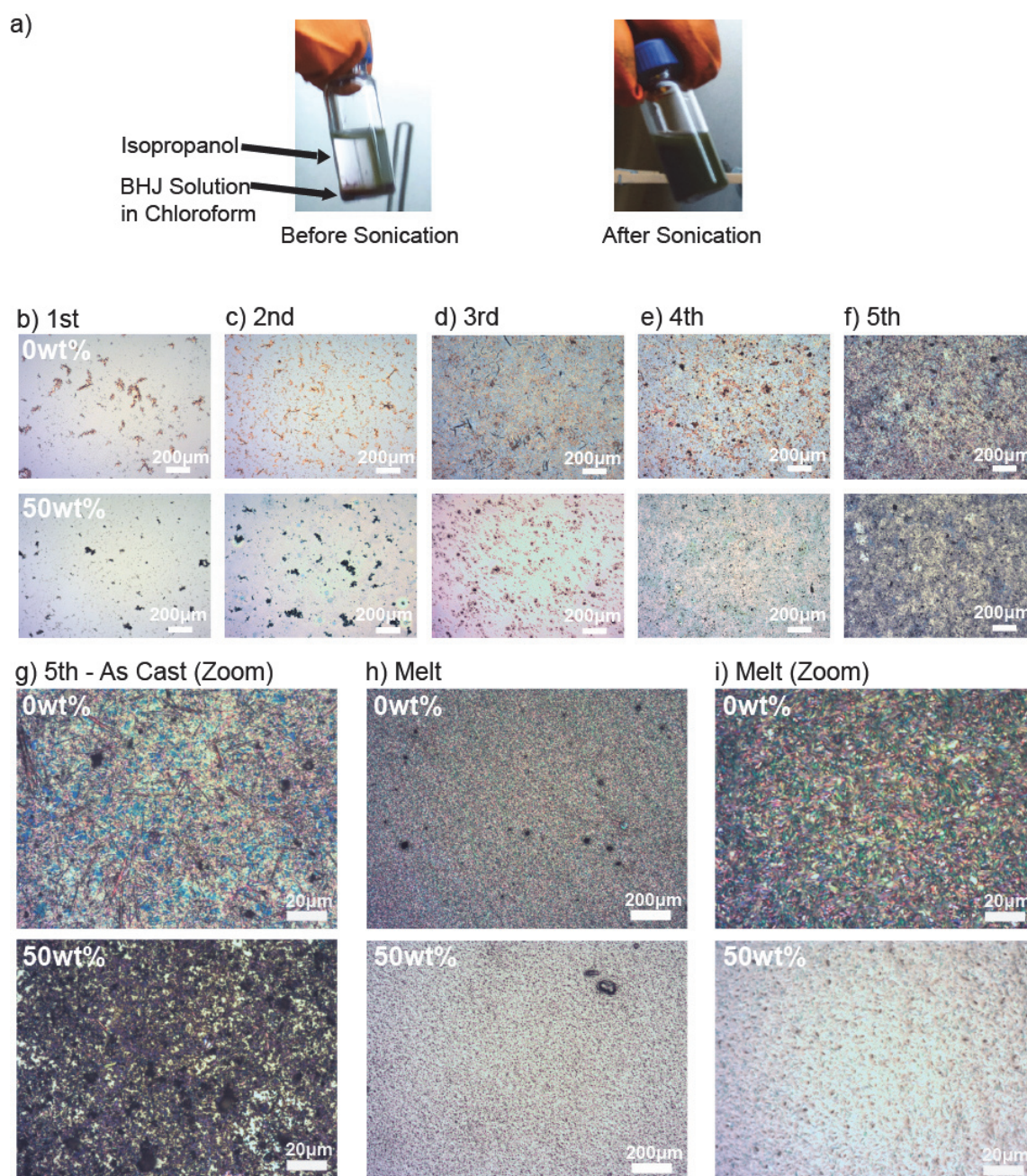
144

Figure S6. Solid-dispersion Melt Processing device fabrication procedure:
a) Picture of BHJ solid dispersion in IPA before and after sonication for 30mins; b-f) Optical Microscope images of the sequential drop-casting of the BHJ solid dispersion with 0 and 50wt% MCP; g) Zoomed of image; h-i) OM images after melting of the BHJ solid dispersions at 240°C for 15minutes and cooling for 30 minutes. See experimental procedure for detailed BHJ solution and thin film preparation.
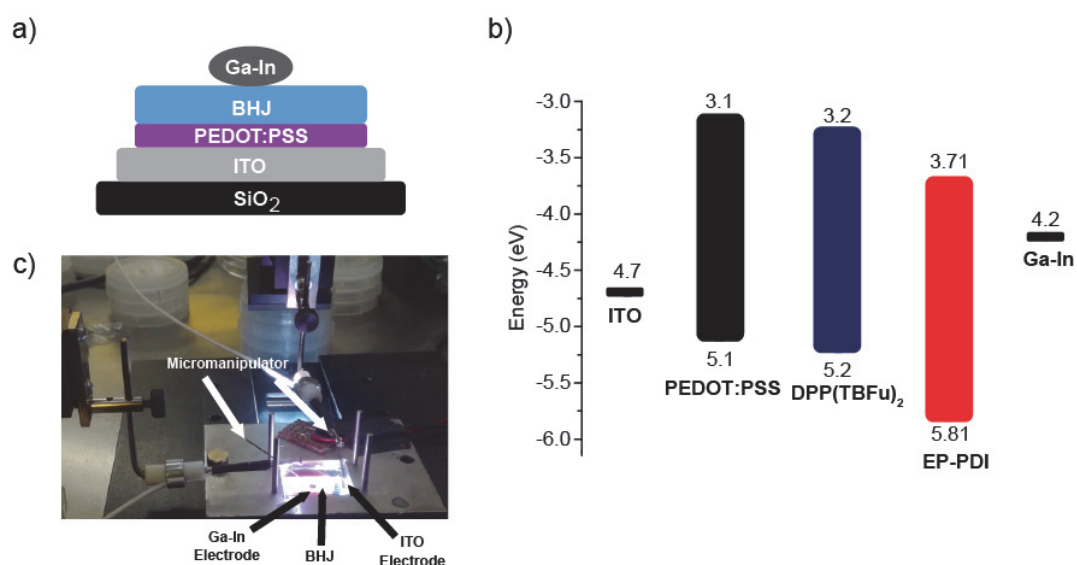
Figure S7. Solid-State Melt Processed Photovoltaic device fabrication Schematics.

a) Schematic of the device architecture; b) Energy Level diagram of the device configuration; c) Picture of the photovoltaic measurement set-up using two micromanipulator contacts on ITO and Ga-In electrodes. Device fabrication was based on reference literature procedures using Ga-In eutectic electrodes[1] and see experimental procedures for detailed explanation.

Table S3. Photovoltaic parameters measured from the two dispersion cast/melt processed devices.

MCPwt%	Jsc (mA/cm²)*	Voc (V)	FF	PCE%
0%	0.0571	0.256	0.19	0.0023
50%	0.874	0.448	0.272	0.11

*Approximate active area = 1.392cm² - The diameter of the Ga-In drop was measured using a caliper.
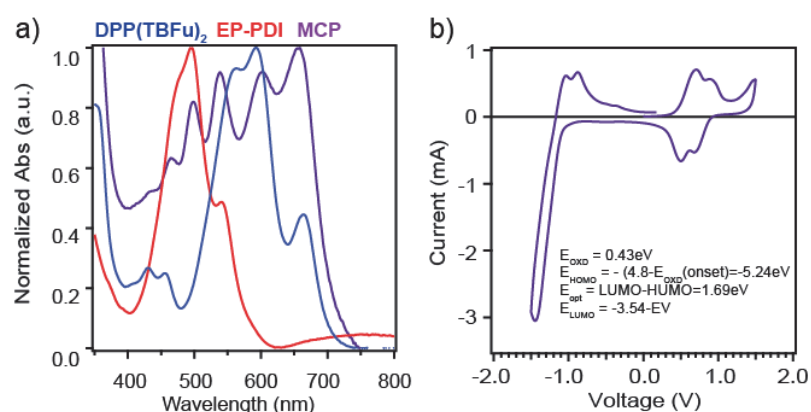
Figure S8. a) UV-vis absorption of the primary components and MCP and b) the Cyclic voltammetry of MCP

General Experimental Procedure

Thin film preparation for morphological and electrochemical characterization

Preparation of BHJ Blend solution and Spin-Coated Thin films:
The photoactive layers of each respective material were prepared by first dissolving each stock solution separately for 12hrs at 50°C in chloroform (CF) at a concentration of 20mg/ml. The individual solutions were then blended with varying MCP loading and left to stir for at least 2hrs before filtering with a 1.0μm pore diameter PTFE filter, and left to stir for another hour before deposition onto the respective substrates. Pre-patterned ITO was cleaned by sequential sonication in water, isopropanol and acetone for 30 min each, and dried by argon. ZnO (20 nm) was utilized for the electron transport layer in the inverted solar cells. The ZnO precursor solution, which contains 0.5 M zinc acetate dehydrate and 0.5 M monoethanolamine in 2-methoxyethanol, was stirred under 60 °C for 12hrs. The ZnO electron transport layer was deposited on the clean ITO substrates *via* spin-coating with the spin rate of 5000 rpm. After exposing a section of the ITO electrical contact, the substrates were annealed at 200 °C in air for 30 min to obtain a thin layer of ZnO film on ITO. The BHJ active layer were then prepared *via* spin-coating onto the substrate at 3000rpm for 60 seconds to obtain a thickness of approximately ≈140nm as measured from a Bruker Dektak XT profilometer. The substrates were then annealed at the respective temperatures (110°C, 180°C and 240°C) for 15mins under argon before and allowed to cool down to room temperature in approximately 35minutes before further morphological characterization and electrode deposition.

Preparation of solid-dispersed BHJ Blends solution and thin film preparation:
The BHJ blend solution at a 1:1 ratio of DPP(TBFu)$_2$:EP-PDI with 0 and 50 MCPwt% at 10mg/mL in chloroform(CF) was first added into an empty vial. Isopropanol (IPA) was subsequently added slowly to obtain a volume ratio of 8:2-IPA:CF as a biphasic solution (See Figure S7a.). This solution was then sonicated for 30minutes in order to obtain a homogenous solid dispersion of the BHJ blend in IPA. The dispersion was then sequentially drop-casted, while allowing for the solvent to dry-up before repeating the procedure (4x80μL) in order to obtain a relatively homogenous distribution of solid aggregates on a PEDOT:PSS/ITO/Glass substrate. This was then melt processed at 240°C for 15minutes under Argon atmosphere to obtain approximately ≈1μm thick active layer as seen in the CR-SEM images (See Figure 4a-b.) before further morphological characterization and electrode deposition. Patterned and cleaned ITO substrates as described above were used to spin coat a 35 nm layer of PEDOT:PSS (Ossilla M 121 Al 4083).

Morphological and Photo-electrochemical Characterization

Atomic force microscopy characterization
Surface topography of all blend films were studied by atomic force microscopy (AFM) using an Asylum Research Cypher in AC mode using Atomic Force AC240TS tips directly on measured transistors surface under ambient conditions.

Kelvin Probe Force Microscopy Characterization
Surface potential measurements were performed with a Cypher atomic force microscope (Asylum Research) using Pt:Ir-coated tips (AC240TM, Olympus) under dark ambient conditions. The work function of the tip was calibrated using reference samples of Pt, Mo, and Cu.

UV-Vis and PL Characterization
Absorption spectra of the thin films were acquired with a UV–vis-NIR UV-3600 (Shimadzu) spectrophotometer, and the optical band gap (E_g^{opt}) was determined from the absorption edge of the thin film sample. Photoluminescence Spectra was carried out on a Fluorolog-3 spectrofluorometer (Horiba) equipped with a Xe lamp with an excitation light source at 532 nm. The sample was placed at a 45° from the lamp to the detector.

Thermal Characterisation
Differential scanning calorimeter (DSC) thermograms were measured with a PerkinElmer DSC8000 calibrated with indium and zinc, using a scanning rate of 10 °C/min. The respective Melting (T_m), and Crystallization (T_c) temperatures were characterized by their peak temperatures, and their endothermic and exothermic enthalpies were calculated from the surface area underneath both melting endotherms and crystallizing exotherms using the specific mass ratio in the stated blend composition of the primary components and MCP. Samples were drop-casted evenly onto a SiO_2 substrate with a slow evaporation of the solvent (chloroform) at 30 °C under argon atmosphere before transferring the solid powder into an aluminium pan.

X-ray Diffraction Characterization
XRD was measured with a D8 Discovery (Bruker) diffractometer using CuKα radiation and Ni β-filter with a scan rate of 0.05°/min and a step width of 0.01°. For the GIWAXS measurements, an incident wavelength of 1.54Å and angle of 0.2° was used. *In-situ* thermal X-ray scattering experiments were performed under ambient conditions where samples were first measured in a Bragg-Brentano geometry at room temperature before placing the sample on a heated cell at 240°C±5.0°C for 2 minutes before conducting a 15 minute scan.

Cyclic voltammetry measurements
The electrochemical CV was conducted on a computer controlled SP-200 potentiostat (Biologic Technologies) in a three electrode configuration with a glassy carbon disk, Pt wire and Ag/Ag$^+$ electrode as the working electrode, counter electrode, and reference electrode, respectively in a 0.1 M tetrabutylammonium hexafluorophosphate (Bu$_4$NPF$_6$) acetonitrile solution as supporting electrolyte, at a scan rate of 50mV s^{-1}. Thin Films of individual primary compoenet were drop casted on a bare Pt foil from a 2.0mgmL^{-1} chloroform solution. The potential of Ag/AgCl reference electrode was internally calibrated by using Fc/Fc$^+$ redox couple. The electrochemical energy levels were estimated by using the empirical formula: E_{HOMO}= -(4.80+ $E_{onset, ox}$) and E_{LUMO}= -(4.80 +$E_{onset, red}$). A platinum bead was used as a working electrode, a platinum wire was used as an auxiliary electrode, and a silver wire was used as a pseudo-reference. Ferrocene/Ferrocenium was used as an internal standard, and potentials were recorded versus FeCp$_2^+$ /FeCp$_2^0$.

Solar-Cell Fabrication and Testing

Spin-Coated Melt-Annealed Devices

Upon spin coating of the respective BHJ active layer and annealing at the respective temperatures (110°C, 180°C and 240°C) for 15mins under argon, the substrates were transferred into the deposition chamber to thermally evaporate 4 nm of MoO_3 and 100 nm Ag at ~10^{-6} mbar through a shadow mask with an active area of 16 mm^2. Current density-voltage (*J-V*) characteristics of the devices were tested under simulated AM1.5G irradiation from a 300 W Xe arc lamp set to 100 mW cm^{-2} with a calibrated Si photodiode. For Single carrier devices, the BHJ active layer was first annealed at 240°C under argon before the deposition of a 100nm thick Al electrode *via* thermal evaporation at ~10^{-6} mbar through a shadow mask with an active area of 0.16 mm^2. Electronic characterization was measured by Keithley 2400 source measure unit. The external quantum efficiency (EQE) of the devices was characterized by illumination from a Tunable PowerArc illuminator (Optical Building Blocks Corporation). A calibrated Si photodiode was employed to measure the incident photon number at each wavelength.

Solid-dispersed Melt Processed Devices

Upon melt processing of the respective BHJ active layer. A Ga-In Eutectic mixture was drop casted on the active layer and used as an electrode. A micromanipulator was used to form an electrical contact with the respective electrodes to measure the current-voltage (*I-V*) characteristics of the photovoltaic device under a nitrogen atmosphere using a custom-built probe station and a Keithley 2612A dual-channel source measure unit under simulated AM1.5G irradiation from a 300 W Xe arc lamp set to 100 mW cm^{-2} with a calibrated Si photodiode.

References

1.   Chiechi, R. C.; Weiss, E. A.; Dickey, M. D.; Whitesides, G. M., *Eutectic Gallium–Indium (EGaIn): A Moldable Liquid Metal for Electrical Characterization of Self-Assembled Monolayers. Angewandte Chemie International Edition* **2008,** *47 (1), 142-144.*

Appendix 5

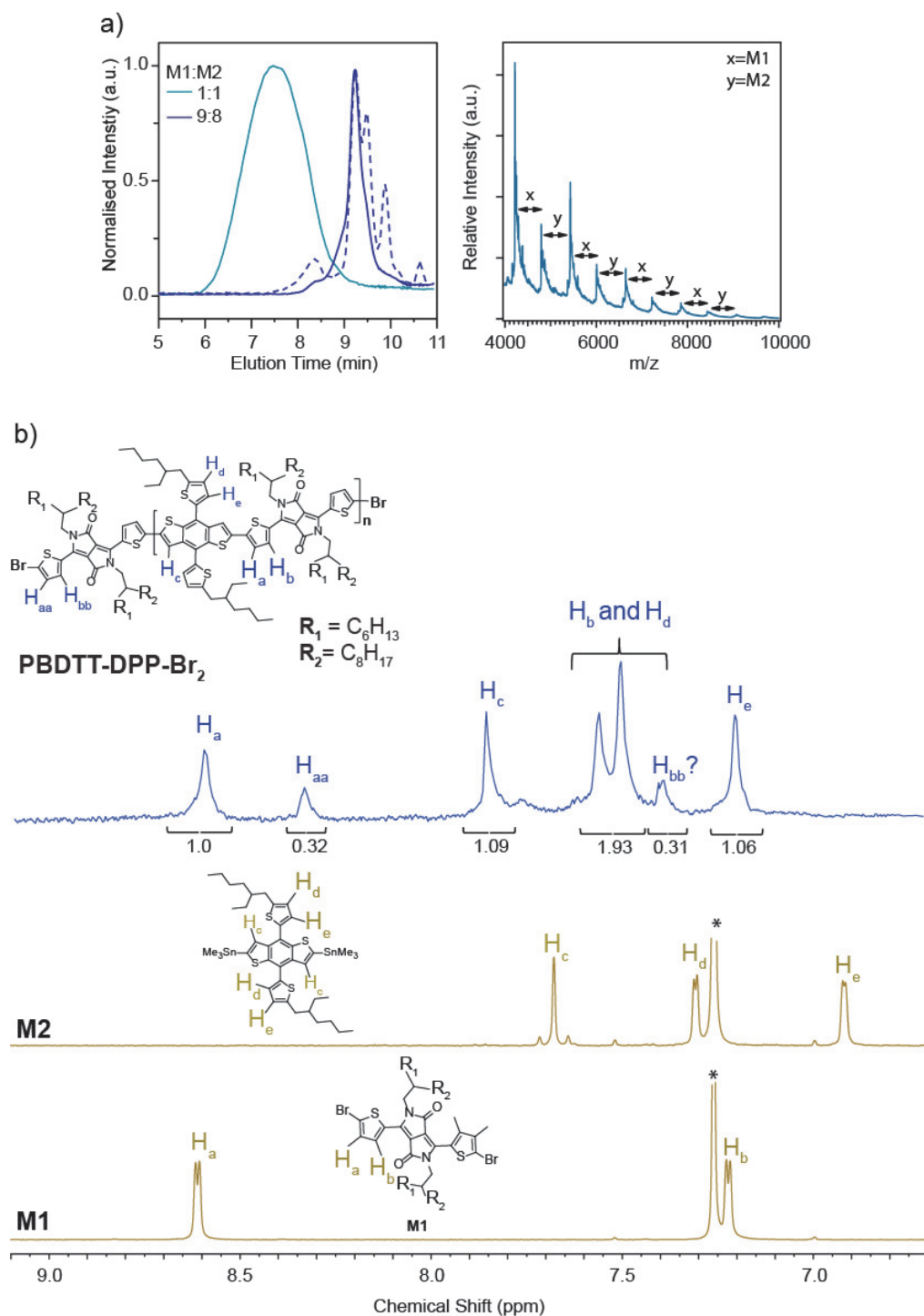## Supplementary Figures in Chapter 5

Contents

Figure S1. Donor Macromonomer PBDTT-DPP-Br$_2$
a) GPC traces (Left figure) of feed ratios of M1:2 at 1:1 (light blue line) , and 9:8 (solid line for purified and dotted line for crude) and MALDI-TOF MS analysis (Righ figure);b) Zoomed ^{1}H NMR spectrum of PBDTT-DPP-Br$_2$ stacked with the corresponding monomer M2 and M1 to indicate the relation of the respective protons or the aromatic region in the marcomonomer. Full ^{1}H NMR spectrum of PBDTT-

DPP-Br$_2$ is shown in the experimental procedure figure S7 (*indicates deuterated chloroform peak for M1 and M2, while deuterated tetracholroethane was used for PBDTT-DPP-Br$_2$ not shown in the NMR spectrum – 6.0ppm).
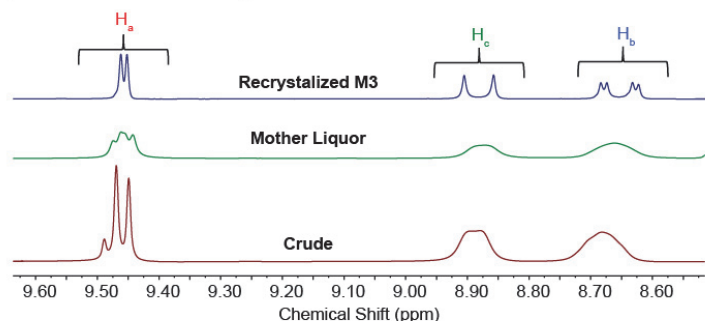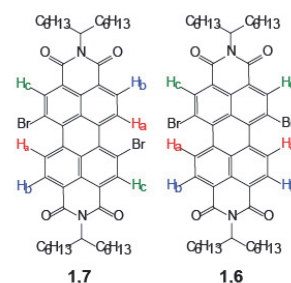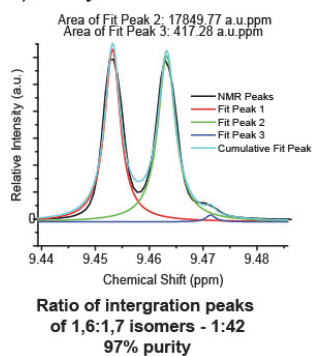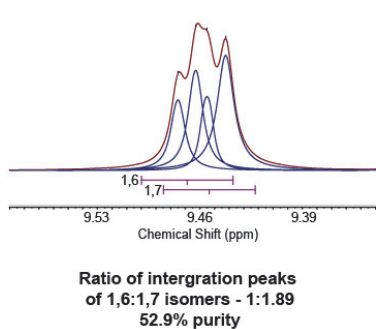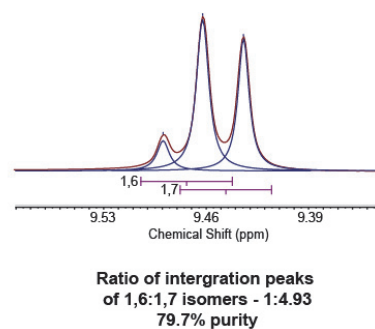
Figure S2. ^{1}H NMR analysis of the monomer M3

a) ^{1}H NMR spectrum of the aromatic region of the crude, recrystallized and mother liquor samples of M3; b) Schematic of the 1,6 and 1,7 regio-isomers of M3; c) Calculation of the integration peaks of proton environment, H$_a$, to determine the purity of the 1,7 isomer (Deconvolution assuming a Lorentzian behaviour of the peaks for recrystallization of M3 had to be performed in origin since the integration of the 1,6 peak was not detected in MestReNova, unlike the mother liquor and crude samples).
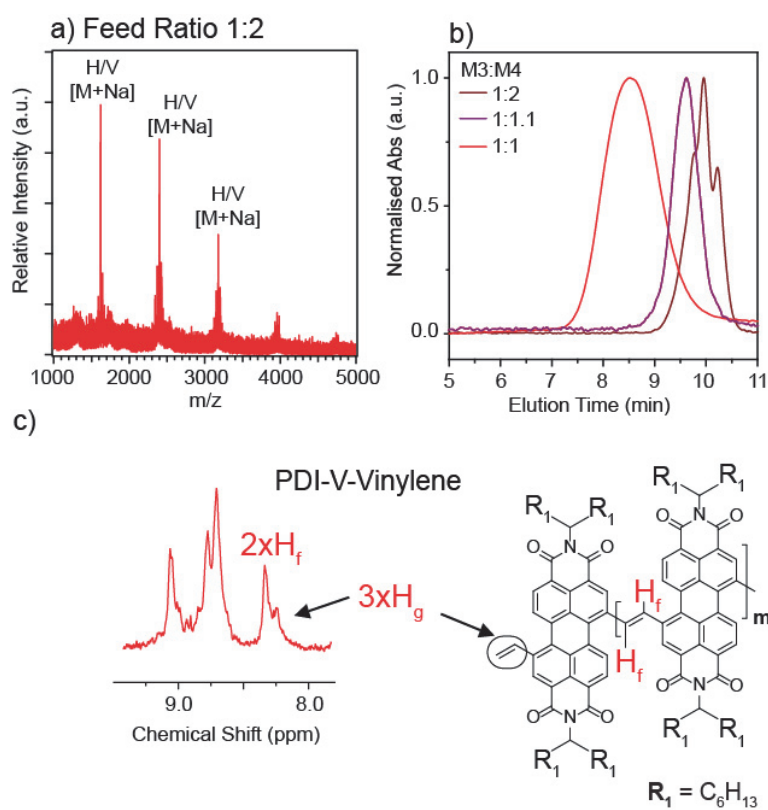
Figure S3. Acceptor Macromonomer, PDI-V-Vinylene

a) MALDI-TOF MS of PDI-V-Vinylene at the feed ratio of M3:M4 – 1:2; b) GPC traces of feed ratio of M3:M4 at 1:2 (brown line), 1:1.1 (marron line), and 1:1 (red line); c) Full ^{1}H NMR spectrum of PDI-V-Vinylene is shown in the experimental procedure figure S8.
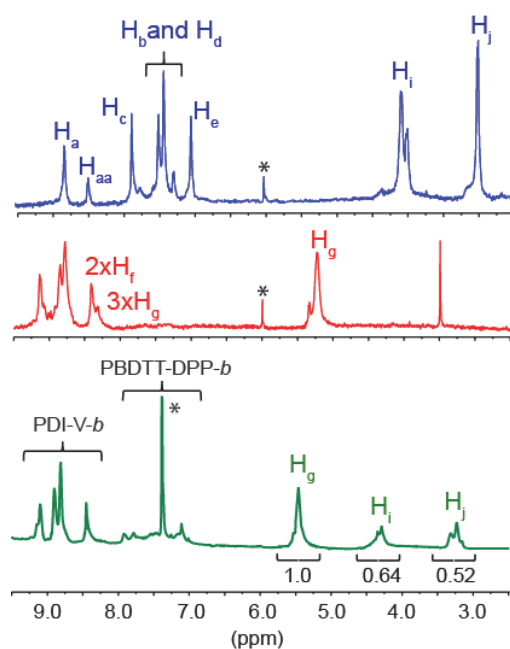
Figure S4. ^{1}H NMR spectrum of the macromonomers and tri-BCP zoomed to the chemical shift to indicate the aromatic region and the distinctive aliphatic protons (H_g, H_i and H_j). (* indicates deuterated chloroform peak for PBDTT-DPP-Br$_2$ and PDI-V-Vinylene and deuterated tetracholoroethane for tri-BCP, and Full ^{1}H NMR spectrum of tri-BCP is shown in the experimental procedure figure S9)
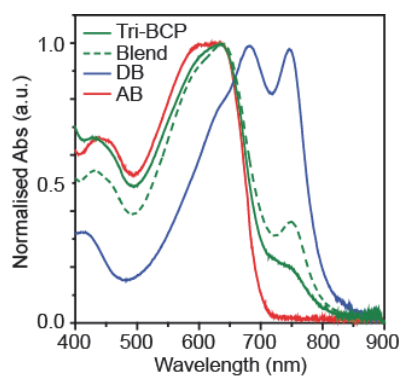
Figure S5. Optical Absorption Spectra of macromonoerms, tri-BCP and its molar blend (1:2)

Optical Absorption Spectra of tri-BCP (Green line), Blend at 1:2 molar ratio (dotted green line), Donor block (DB), PDBTT-DPP-Br$_2$ (Blue line), and accetor block, PDI-V-Vinylene (Red Line) in solution in Chloroform at a concentration of 0.002mL/mg.

Figure S6. *J-V* curve of the as cast devices of tri-BCP and the Blend at a molar ratio of 1:2 – PBDTT-DPP-Br$_2$:PDI-V-Vinylene

Experimental Procedures
Synthetic procedures

Gel Permeation Chromatography (GPC) and Prepatory- Size exclusion Chromatography (prep-SEC):
Polymers were analysed & fractionalized using Shimadzu Prominence LC-20AP (Preparative Liquid Chromatography) in chlorobenzene solvent at 80ºC with the UV-Vis detectors at 663nm and 552 nm. Preparative size exclusion chromatography was performed by firstly dissolving 100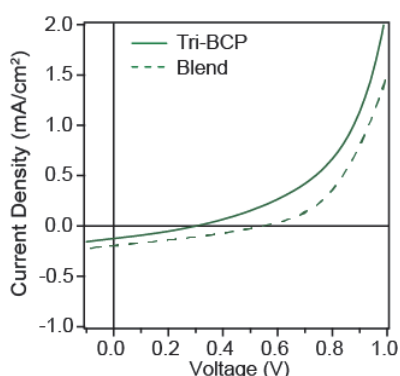 mg of product dissolved in 10 ml of chlorobenzene (80°C) and injecting the solution in a size exclusion preparative column (PSS SDV preparative linear M, 40mm×250mm) at 80°C using chlorobenzene as mobile phase at a constant elution flow of 6 mL/min. Fraction collection was carried out every 20 seconds (0.33 mL). Single fractions (and crude polymerizations) were analysed through an analytical size exclusion PSS SDV analytical linear M column (8mm×250mm, 80°C, CB mobile phase, 1mL/min).

Matrix assisted laser desorption/ionization time-of-flight Mass spectrometry (MALDI-TOF MS)
Separate solution of the matrix (trans-2-[3-(4-tert-Butylphenyl)-2-methyl-2-propenyllidene] malononitrile) at 5mg/mL in THF, and the respective polymer at 5mg/mL in Chloroform were mixed at a ratio of 2:1 – Matrix:Polymer, where a volume of 1µL of the mixture was dropped on the target and allowed to dry at room temperature before measurements. Mass spectra was acquired in the positive-ion reflector mode at the respective detection range.

^{1}H Nuclear Magnetic Resonance (^{1}H NMR)
For monomer characterization: The (^{1}H) & (^{13}C) NMR spectra were recorded at room temperature using per-deuterated solvents as internal standards on a 400 MHz NMR Bruker AVANCE III-400 spectrometer (Bruker, Rheinstetten, Germany) unless explicitly mentioned. Macromonomer and BCP Charactization were performed on a 800 MHz NMR Bruker AVANCEII-800 spectrometer (Bruker, Rheinstetten, Germany). Chemical shifts are given in parts per million (ppm) referenced to residual ^{1}H or ^{13}C signals in deuterated chloroform- *d*, and tetrachloroethane-*d$_2$*.

Synthetic methods:
All reagents were of commercial reagent grade (Sigma-Aldrich, Acros & Fluorochem) & were used without further purification. Toluene, Chloroform, Tetrahydrofuran (Fisher Chemical, HPLC grade) & chlorobenzene (Alfa Aesar, HPLC grade) were purified & dried on a Pure Solv-MD Solvent Purification System (Innovative Technology, Amesbury, United States) apparatus. Normal phase silica gel chromatography was performed with an Acros Organic silicon dioxide (pore size 60 Å, 40–50 µm

technical grades). EI-MS spectrum was recorded on an EI/CI-1200L GC-MS (Varian) instrument & APPI-MS spectrum was recorded on an ESI/APCI LC-MS Autopurification System with a ZQ Mass detector (Waters, Milford, United States) instrument using a positive mode.

Macromonomer Synthesis Procedures

Synthesis of PBDTT-DPP-Br$_2$

In an over-dried schlenck tube, the monomers M1 and M2 was added at the specified molar ratios, and the reagents were dried under vacuum and flushed with argon (3x). The tube was then transferred into an argon glove box, to add Pd(PPh$_3$)$_4$ at a 10% molar equivalence. This mixture was then dissolved in Toluene:DMF at a volume ratio of 10:1 ratio with a concentration of concentration 0.76 mg/mL of the total mass of the starting monomers. After removal from the glove box, the solution was degassed with an argon-vacuum evacuation cycle (3x), and subsequently heated at 95°C for 12 hours. To stop the reaction, the mixture was cooled to room temperature and a solution of potassium fluoride 2M was added and left to stir for an hour before precipitation in excess methanol. The solid precipitate was then filtered over celite, and washed with three rounds of methanol and hexane. The crude mixture was then dissolved in chloroform and subjected to GPC analysis before performing prep-SEC, and an average reaction yield 46% was obtained. After purification, the polymer was characterized *via* ^{1}H NMR, MALDI TOF MS and GPC as described in the main text.

Synthesis of PDI-V-Vinylene

In an over-dried schlenck tube, the monomer M3 and M4 was added at the specified molar ratios, and the tube was transferred into an argon glove box. Pd$_2$dba$_3$ and P(otol)$_3$ at 5% and 20% molar equivalence (ratio of 1:4) was added into the tube, and the solid mixture was dissolved in toluene at a concentration of 37.5 mg/mL of the total mass of the monomers. After removal from the glove box, the solution was degassed with an argon-vacuum evacuation cycle (3x), and subsequently heated at 95°C for 12 hours. To stop the reaction, the mixture was cooled to room temperature and a solution of HCl 2M was added and left to stir for an hour before precipitation in excess methanol. The solid precipitate was then filtered over celite, and washed with three rounds of methanol and hexane. The crude mixture was then dissolved in chloroform and subjected to GPC analysis before performing prep-SEC, and an average reaction yield 96% was obtained. After purification, the polymer was characterized *via* ^{1}H NMR, MALDI TOF MS and GPC as described in the main text.

BCP Synthesis Procedure

The respective marcomonomers were added into a 10ml Schlenk Flask at a stoichiometric ratio of 1:2.3 - PBDTT-DPP-Br$_2$:PDI-V-Vinylene, and dissolved in a mixture of Tol:DMF:TEA – 0.3 : 0.3: 0.25 at a concentration of 20mg/mL with respective to the total weight ratio of the macromonomers. Pd(OAc)$_2$ (5% mol) and P-(*o*-tol)$_3$ (20%mol) was then added into the reaction solution. The flask was subsequently degassed and purged with Argon (3 cycles), and was left at 90°C for 12hours. After cooling the crude reaction to room temperature, methanol was added into flask to precipitate crude polymer. This was then filtered through celite and washed with methanol and hexane sequentially, and finally dissolved in Chloroform which was evaporated and precipitated in methanol to collect a solid crude product. The crude was then purified *via* prep-SEC to obtain the purified sample of tri-BCP. After purification, the polymer was characterized *via* ^{1}H NMR, and analytical GPC as described in the main text.
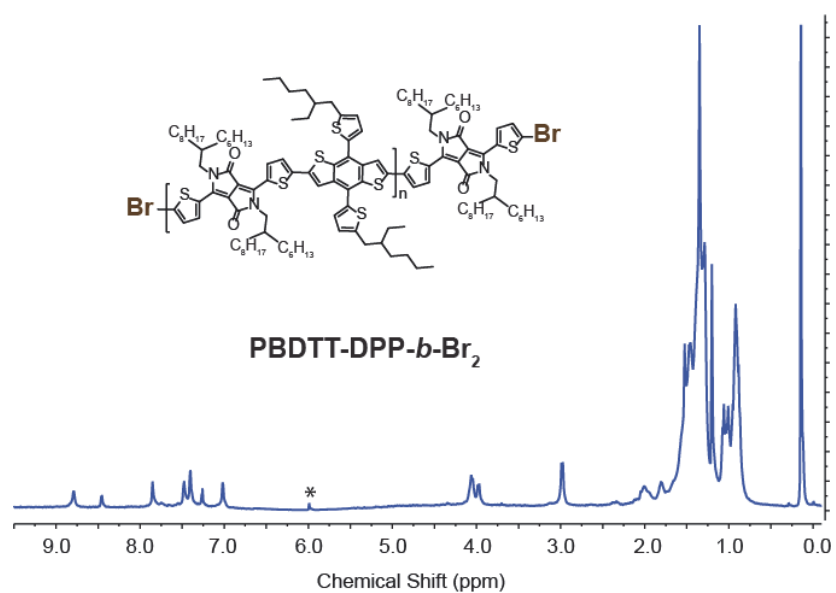
Figure S7. ^{1}H NMR Spectrum of PBDTT-DPP-Br$_2$ (* indicates deuterated tetracholoroethane peak)
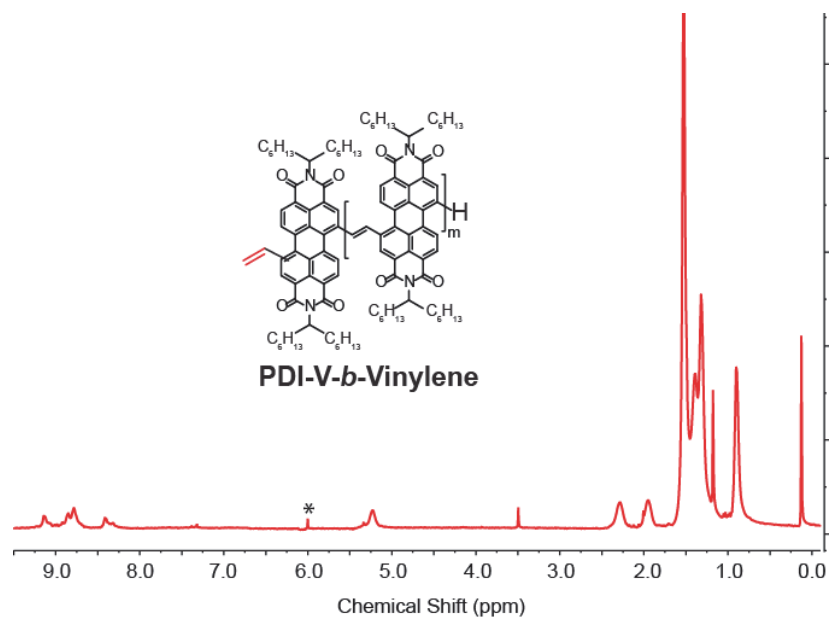

Figure S8. ^{1}H NMR Spectrum of PDI-V-Vinylene (* indicates deuterated tetracholoroethane peak)
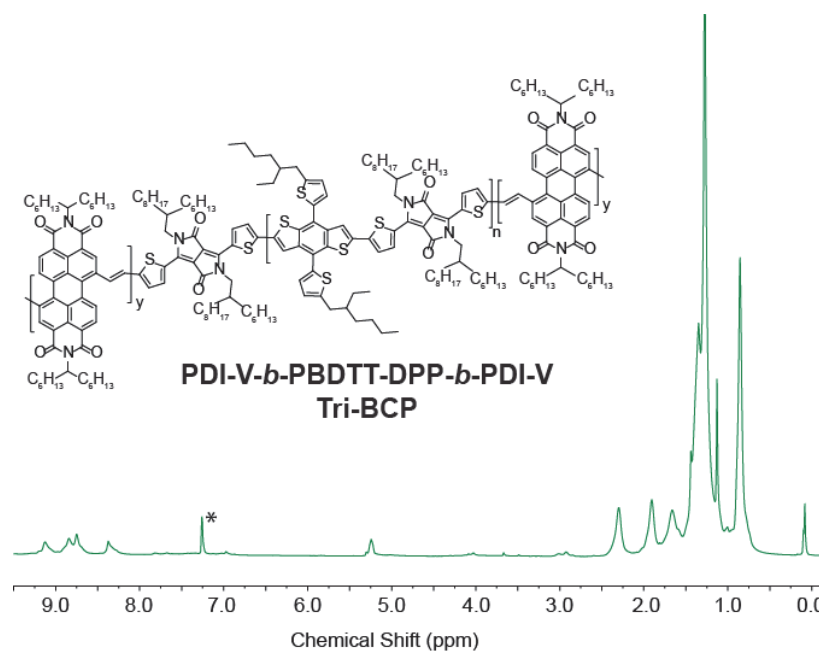
159

Figure S9. ^{1}H NMR Spectrum of tri-BCP (* indicates deuterated chloroform peak)

Monomer Synthesis Procedures and Characterization

2-butyl octanol, 7-tridecanone, perylene-3 4-dicarboxylic anhydride, & M4 were purchased commercially from Sigma Aldrich. DPP-Th$_2$ & M2 were synthesized according to procedures in previous literature [1], [2].

Synthesis of 2-butyl Octyl Bromide
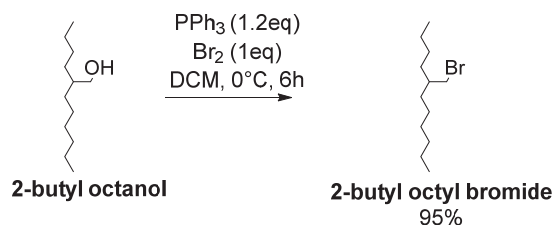
PPh$_3$ (5.07 gm, 19.32 mmol, 1.2 eq.) was dissolved in DCM with a concentration of 6 mL DCM for every gram of PPh$_3$. Argon gas was bubbled through the solution to remove dissolved gases & the solution was cooled to 0°C. Bromine (828 μL, 16.1 mmol, 1 eq.) was added dropwise using syringe into the solution & was allowed to stir for 30 minutes, after which 2-butyl octanol (3.6 mL, 16.1 mmol, 1 eq.) was added dropwise over a period of 1 hour. After allowing the reaction mixture to gradually reach room temperature (~8 hours), DCM was removed using a rotavapor, petrolether/hexane was added and the resulting suspension ultrasonicated for 5 minutes. The precipitate was filtered out and the mother liquor was concentrated and passed through a plug column of silica using an elution mixture of hexane:petrolether. A colorless oil of 2-butyl Octyl Bromide with a yield of 95% was obtained.

EI-MS (positive mode): 248.09 m/z. ^{1}H NMR (400 MHz, Chloroform-*d*) δ 3.39 (d, *J* = 4.6 Hz, 2H), 2.04 – 1.92 (m, 1H), 1.61 – 1.49 (m, 1H), 1.38 – 1.28 (m, 4H), 1.28 (s, 10H), 0.89 (q, *J* = 6.6 Hz, 6H). ^{13}C NMR (101 MHz, CDCl$_3$) δ 39.79, 39.09, 32.96, 32.63, 32.21, 29.87, 29.14, 26.91, 23.22, 23.03, 14.36, 14.33.

Synthesis of 2,5-bis(2-butyloctyl)-3,6-di(thiophen-2-yl)-2,5-dihydropyrrolo[3,4-c]pyrrole-1,4-dione (BODPP-Th$_2$)

DPP-Th$_2$

2-butyl octyl bromide

K$_2$CO$_3$ (5eq)
DMF, 130°C, 24 h
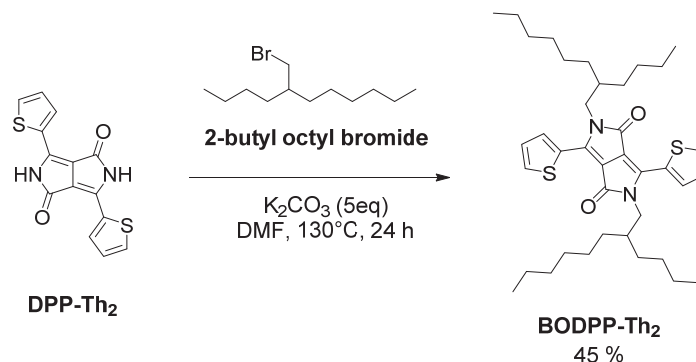
BODPP-Th$_2$
45 %

DPP-Th$_2$ (1.0 g, 3.33 mmol, 1 eq.) & anhydrous potassium carbonate (2.3 gm, 16.65 mmol, 5 eq.) were dissolved into DMF (25 mL) in a two-neck round flask & heated to 130°C under argon protection. BOB (2.07 gm, 8.32 mmol, 2.5 eq.) dissolved in ~5 mL DMF was added dropwise. After the reaction was stirred for 24 hours at 130°C, the solution was cooled to room temperature & acetic acid was added to neutralize the base & protonate the unreacted DPP. Solution was stirred for ~1 hour & filtered. The filter cake was washed with water & methanol several times. After being dried in a vacuum, the crude product was purified by silica gel chromatography using DCM: Hexane (3:1) as eluent to get an orange red solution which on drying turns to maroon red powder product (precipitate in methanol & filter out to dry; 45% yield).

^{1}H NMR (400 MHz, Chloroform-*d*) δ 8.85 (d, *J* = 3.8 Hz, 2H), 7.62 (d, *J* = 4.8 Hz, 2H), 7.28 (s,2H), 4.02 (d, *J* = 7.7 Hz, 4H), 1.94 – 1.86 (m, 2H), 1.53 (d, *J* = 12.0 Hz, 4H), 1.29 (d, *J* = 5.9 Hz, 12H), 1.20 (s, 15H), 0.84 (dt, *J* = 9.9, 4.9 Hz, 12H). ^{13}C NMR (101 MHz, CDCl$_3$) δ 161.93, 140.59, 135.31, 130.62, 129.99, 128.54, 108.12, 46.35, 37.86, 31.90, 31.32, 31.05, 29.82, 28.56, 26.33, 23.20, 22.78, 14.23, 14.16; ESI+ MS: 637.39 m/z.

Synthesis of M1

BODPP-Th₂ → **M1** (65 %)

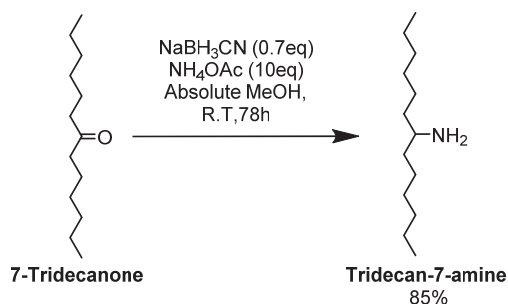Reagents: NBS (1.2eq), CHCl₃, 0°C, dark
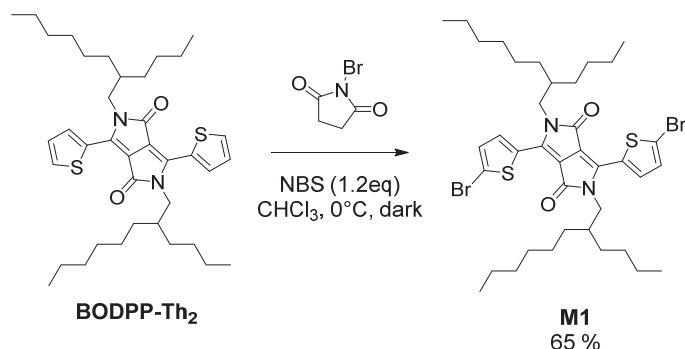
DDPP (500 mg, 785 µmol, 1 eq.) dissolved in chloroform at 0°C was stirred for ~1 hour. NBS (294 mg, 1.65 mmol, 2.1 eq.) in chloroform was added dropwise to this system in dark conditions & left overnight to gradually warm to room temperature. Solvent was removed by rotavapor (in vacuum at low heating temperatures) & solid was allowed to precipitate in methanol after ultrasonication. Resulting crude precipitate was subjected to silica column chromatography using DCM: Hexane (2:1) eluent. Resulting red-purple solid obtained is the product (62% yield).

^{1}H NMR (400 MHz, Chloroform-d) δ 8.61 (d, J = 4.2 Hz, 2H), 7.22 (d, J = 4.3 Hz, 2H), 3.93 (d, J = 7.7 Hz, 4H), 1.27 (dd, J = 12.9, 5.1 Hz, 23H), 1.22 (d, J = 7.2 Hz, 16H), 0.85 (dt, J = 7.4, 3.7 Hz, 12H). ^{13}C NMR (101 MHz, CDCl₃) δ 161.57, 139.56, 135.44, 131.59, 131.32, 119.11, 108.19, 59.68, 53.56, 46.47, 38.30, 37.89, 32.09, 31.91, 31.39, 31.29, 31.01, 29.86, 29.80, 29.52, 28.53, 26.29, 23.18, 22.85, 22.78, 14.27, 14.23, 14.16; TOF ES+ MS: 792.198 m/z.

Synthesis of Tridecan-7-amine

7-Tridecanone → **Tridecan-7-amine** (85%)

Reagents: NaBH₃CN (0.7eq), NH₄OAc (10eq), Absolute MeOH, R.T, 78h

2.50 g (12.6 mmol; 1 eq.) 7-tridecanone, 10.0 g (129 mmol; 10.5 eq.) NH₄OAc, & 0.56 g (8.9 mmol; 0.75 eq.) NaBH₃CN were dissolved in 30 mL absolute MeOH & stirred at room temperature for ~3 days, until starting material was gone by TLC (Rf = 0.8 in CHCl3, KMnO₄ stained TLC plate). The mixture was quenched by added concentrated HCl dropwise (~3 mL), then concentrated with a rotary evaorator. The resulting white solid was taken up in 200 mL H₂O, taken to pH~10 with solid KOH, & extracted with 300 mL & then 150 mL of CHCl₃. The CHCl₃ fractions were combined & concentrated to give 2.18 g (85%) of pale yellow oil.

^{1}H NMR (400 MHz, Chloroform-d) δ 5.60 (s, 2H), 2.86 (p, J = 6.1 Hz, 1H), 1.51 – 1.41 (m, 3H), 1.38 – 1.25 (m, 3H), 1.22 (h, J = 6.7 Hz, 14H), 0.85 – 0.76 (m, 6H). ^{13}C NMR (101 MHz, CDCl$_3$) δ 50.58, 37.49, 31.30, 28.92, 25.54, 22.02, 13.36; TOF ES+ MS: 200.237 m/z.

Synthesis of (C$_6$H$_{13}$)$_2$PDI

Perylene-3,4,9,10-tetracarboxylic dianhydride
(PDA)

Tridecan-7-amine

Imidazole,
180°C, 4h

(C$_6$H$_{13}$)$_2$PDI
90%
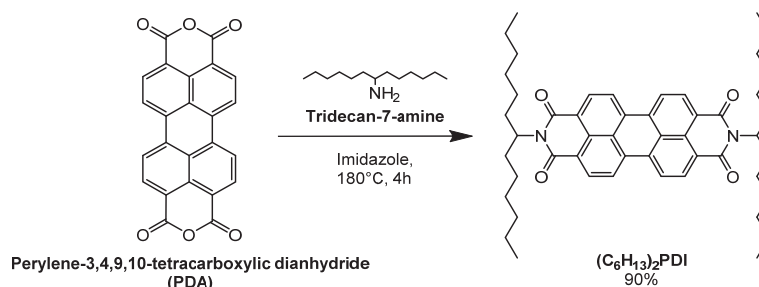
1.00 gm (97% pure; 2.47 mmol; 1 eq.) of perylene-3 4-dicarboxylic anhydride (PDA) was added to a schlenk tube containing excess (10x mass) of imidazole (solid) & 351 mg (0.75 eq.; 1.92 mmol) of Zn(OAc)$_2$. The reaction vessel was evacuated & argon flushed thrice before adding the 1.4 gm of the pale oil amine (TAM; 2.75 eq.; 7.02 mmol) & heated to 160-180ºC overnight. After cooling down, the crude was precipitated in EtOH:H$_2$O (water in a 1:1 (v/v) with 2N HCl. Crude was filtered & washed with methanol before drying. Column chromatography on the crude in DCM:hexane (1:1) isolates the PDI small molecule (90% yield, 1.73 gm).

^{1}H NMR (400 MHz, Chloroform-d) δ 8.93 – 8.36 (m, 8H), 5.19 (tt, J = 9.4, 5.8 Hz, 2H), 2.24 (qd, J = 9.7, 4.9 Hz, 4H), 1.86 (dq, J = 14.1, 5.4, 4.9 Hz, 4H), 1.44 – 1.06 (m, 33H), 0.82 (t, J = 6.7 Hz, 11H). ^{13}C NMR (101 MHz, CDCl$_3$) δ 134.58, 131.96, 131.25, 129.66, 123.08, 77.34, 77.02, 76.70, 54.78, 35.58, 32.40, 31.77, 29.23, 26.94, 22.60, 14.06, 1.03; MS MALDI-TOF (reflective neutral mode): 753.497 m/z.

Synthesis of M3

Br$_2$ (80eq)
CHCl$_3$,78hrs

Br

Br

1,7-M3

Br

Br

1,6-M3
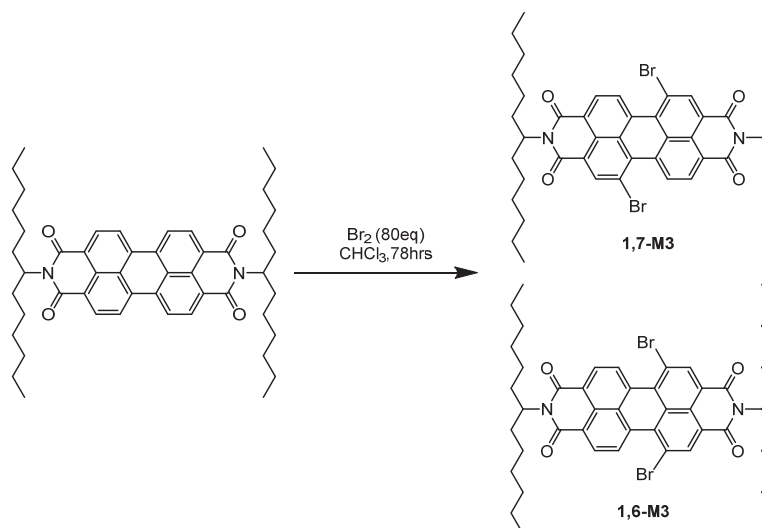
(C$_6$H$_{13}$)$_2$PDI (1.00 gm; 1.32 mmol; 1 eq.) was taken in a schlenk flask & dissolved in chloroform (10 mg/mL concentration) & argon gas was bubbled through for 10 minutes to remove dissolved gases. Excess liquid bromine (5.5 mL; 80+ eq.) was injected into the system & the flask was heated to reflux conditions for 3+ days. After cooling down the solution, compressed air was bubbled to remove

bromine (channeled into reducing agent). The crude was adsorbed onto dry silica to perform dry loaded column chromatography. Broadly 3 fractions could be isolated & the fraction with the highest R_f value is the needed M3+isomers. Repeated columns were performed to isolate out the monobrominated PDI. (Refer main report on isolating/enriching M3 from regioisomers).

NMR (of 95+% enriched M3 at 50ºC): ^{1}H NMR (800 MHz, Chloroform-*d*) δ 9.67 (d, *J* = 7.8 Hz, 1H), 9.08 (s, 1H), 9.00 – 8.76 (m, 1H), 5.34 (tt, *J* = 9.9, 5.9 Hz, 1H), 2.41 (dtd, *J* = 14.6, 9.6, 5.1 Hz, 3H), 2.03 (ddt, *J* = 15.0, 10.8, 5.2 Hz, 3H), 1.45 (dddd, *J* = 58.4, 21.4, 14.5, 6.8 Hz, 21H), 1.01 (t, *J* = 7.0 Hz, 6H); MS APCI (positive mode): 913.296 m/z.

Thin Film Preparation and Characterization

Solution preparation of macromonomers, tri-BCP and its molar blend
Each respective material were prepared by first dissolving each stock solution separately for 12hrs at 50°C in chloroform (CF) at a concentration of 20mg/ml, before filtering with a 1.0µm pore diameter PTFE filter, and left to stir for another hour before deposition onto the respective substrates. For the blend solution, each component were fixed mixed and left to stir for at least 2hrs before filtering.

Spin coated thin film preparation
Pre-patterned ITO on glass was cleaned by sequential sonication in water, isopropanol and acetone for 30 min each, and dried by argon. ZnO (20 nm) was utilized for the electron transport layer in the inverted solar cells. The ZnO precursor solution, which contains 0.5 M zinc acetate dehydrate and 0.5 M monoethanolamine in 2-methoxyethanol, was stirred under 60 ^{o}C for overnight. The ZnO electron transport layer was deposited on the clean ITO substrates via spin-coating with the spin rate of 5000 rpm. After exposing a section of the ITO electrical contact, the substrates were annealed at 200 ^{o}C in air for 30 min to obtain a thin layer of ZnO film on ITO. The respective solution prepared were then prepared via spin-coating onto the substrate at 1500rpm for 60 seconds to obtain a thickness of approximately ≈120nm s measured from a Bruker Dektak XT profilometer.

UV-Vis and PL Characterization:
Absorption spectra of the solution and thin films were acquired with a UV–vis-NIR UV-3600 (Shimadzu) spectrophotometer, and the optical band gap (E_g^{opt}) was determined from the absorption edge of the thin film sample. Photoluminescence Spectra of the thin films was carried out on a Fluorolog-3 spectrofluorometer (Horiba) equipped with a Xe lamp with an excitation light source at 532 nm. The sample was placed at a 45° from the lamp to the detector.

Optical Microscope
Optical microscope images were obtained with a NIKON Eclipse E600.

Solar-Cell Fabrication and Testing
Upon spin coating of the respective BHJ active layer on ZnO/ITO/Glass, the substrates were then transferred into the deposition chamber to thermally evaporate 4 nm of MoO_3 and 100 nm Ag at ~10^{-6} mbar through a shadow mask with an active area of 16 mm^2. An 80 nm thick aluminium cathode was deposited (area 16 mm^2) by thermal evaporation (Kurt J. Lesker Mini-SPECTROS). Electronic characterization was performed under simulated AM1.5G irradiation from a 300 W Xe arc lamp set to 100 mW cm 2 with a calibrated Si photodiode (ThorLabs) at room temperature. Current– voltage curves were obtained with a Keithley 2400 source measure unit. Thermal annealing at 150°C for 15

Curriculum Vitae

Aiman Rahmanudin

Nationality : Singaporean

Date of Birth : 06/06/1988

Address: Ecole polytechnique fédérale de Lausanne, Institut des sciences et ingénierie chimiques

EPFL SB ISIC LIMNO, CH H4 565, Station 6, CH-1015 Lausanne, Switzerland

Email: aiman.rahmanudin@epfl.ch/aimanrahmanudin@gmail.com

Google Scholar ID: Aiman Rahmanudin

Website: www.linkedin.com/in/aimanrahmanudin

Education

PhD in Chemistry and Chemical Engineering

École Polytechnique Fédérale de Lausanne (Lausanne, Switzerland)

Advised by Professor Kevin Sivula

> Thesis Title: Molecular engineering of organic semiconductors for morphology control in optoelectronic devices

PhD Defence

2nd March 2018

Master degree (MChem) in Chemistry with Business Management

University of Manchester (Manchester, United Kingdom)

Advised by Professor Michael Turner

> *Overall Upper 2nd Class Honours (2.1)*
>
> *Masters grade (1st Class – 4th Year 2012-2013)*
>
> *Bachelor Overall grade (Upper 2nd Class – 2009-2012)*

September 2009 to June 2013

General Certificate of Education Advanced Level

Innova Junior College (Singapore)

January 2005 To December 2007

Employment History

Doctoral Assistant

École Polytechnique Fédérale de Lausanne

Laboratory for Molecular Engineering of Optoelectronic Nanomaterials (LIMNO)

Advised by Professor Kevin Sivula

Research Summary

To understand the relationship between solid-state self-assembly of π-conjugated semiconductors and its effect on optoelectronic performance in order to develop novel morphology stabilization strategies and processing techniques *via* a molecular engineering approach.

Teaching Experience

Chemical Engineering Lab & Project Practical Work Teaching Assistant for 3rd year and Masters Level courses at EPFL

Supervision of Junior Researchers

Master's Thesis project Supervisor in Chemical Engineering & biotechnology for Simon Hänni and Arvindh Sekar (currently a PhD student in our group). *I planned and supervised the research projects on the synthesis of molecular and polymer semiconductors, and device fabrication & characterization of organic photovoltaic devices.*

January 2014 To March 2018

Technical Skills

Advanced knowledge and experience on the synthesis of small-molecule and polymeric π-conjugated systems and various characterization Techniques:

- Multinuclear NMR (solution and solid-state)
- UV-VIS-NIR. FT-IR, Raman, fluorescence Spectrometry, Cyclic voltammetry and Differential Scanning Calorimetry

Size-Exclusion Chromatography and Mass Spectrometry (GPC and MALDI-TOF analysis)

Morphological characterization of Organic Semiconductor Thin films

- Atomic Force Microscopy and Kelvin Probe Force microscopy
- Nano-Mechanical Mapping
- Optical Microscopy
- Photoluminescence Spectroscopy
- X-ray Diffraction

Electronic Device Fabrication and Characterization

- Formulation of inks for solution processed thin-films
- Processing of thin films - spin coating, spray casting, doctor blading, melt processing
- Fabrication of organic solar cells, organic field effect transistors and single-carrier diodes
- Vacuum deposition of metal electrodes via sputtering and thermal evaporation
- *Current density – voltage* characterization
- Impedance Spectroscopy

Research Assistant

University College London

Clean Materials Technology Group

Advised by <u>Professor. Jawwad A. Darr</u>

June-August 2013

Research Summary: Investigation into the electrochemical performance of Graphene modified Carbon-coated $LiFePO_4$ nano-structured cathode material for Lithium-Ion Batteries.

Technical Skills: Material Characterization analysis (XRD, BET Surface Area, Raman Spectroscopy), Electrode preparation and printing using doctor blade technique, CR 3025 Coin cell fabrication , Electrochemical characterization for batteries (Cyclic Voltammetry, Charge/Discharge Cycling performance of cells etc.)

Research Assistant

University of Manchester

Organic Materials Innovation Centre

Advised by <u>Professor. Michael L. Turner</u>

**July 2012
to
June 2013**

Research Summary: Developing a novel synthetic route of fused-ring heterocyclic organic semiconductors based on carbazoles derivatives for Organic-Field-Effect-Transistors (OFETs). Here, I optimized a C-H activation cyclization *via* Buchwald-Hartwig amination using a series of Palladium Catalytic systems and reaction method (batch and microwave reactors) for the formation of oligomeric ladder-type molecular semiconductors.

Other Work Experience

Technical Application Assistant

M&I Materials ltd , Manchester, United Kingdom

July –September 2012

Military Servicemen - Rank 2nd Sergeant (Platoon Sergeant)

Singapore Armed Forces - 3rd Singapore Infantry Regiment

**January 2007
to
December 2008**

Primary school Teacher	**March – August**
MENDAKI Qxcel Pte Ltd, Singapore	**2009**

Conferences

9th International Conference on Materials for Advanced Technologies, *Singapore*
Presenting author for an oral presentation
Title: Developing Bulk Heterojunction Morphology stabilization strategies for Organic Photovoltaics

18-23
June 2017

Hybrid & Organic Photovoltaics 2017, Lausanne, Switzerland
Presenting author for a Poster presentation
Title: Developing Bulk Heterojunction Morphology stabilization strategies for Organic Photovoltaics

21-24
September 2017

1st Organic Semiconductors Conference 2016, Dubrovnik , Croatia
Presenting author for a Poster presentation
Title: Developing Bulk Heterojunction Morphology stabilization strategies for Organic Photovoltaics

22-25
September 2016

Organic(Opto)Electronics International Summer School, Boutheon, France

2-6
June 2014

Awards

Swiss Academy of Sciences (SCNAT) Chemistry Photo Competition – Runner-up
(https://naturalsciences.ch/organisations/chemistry/photo_2017

Membership

Swiss Chemical Society, Material Research Society of Singapore

Other Relevant Skills

Languages: English & Malay (Fluent in both spoken and written), basic elementary French
IT: Extensive knowledge of standard office software, Adobe Photoshop and Illustrator, ChemDraw, Origin Pro, IGOR.

References

Assistant Professor
Kevin Sivula
kevin.sivula@epfl.ch
http://limno.epfl.ch
Tel: +41 (0) 21 69 37979
École Polytechnique Fédérale de Lausanne Station 6, Bâtiment CH H4 565, CH-1015,
Lausanne, Switzerland

Senior Researcher
Dr. Giuseppe Sforazzini
giuseppa.sforazzini@epfl.ch
http://lmom.epfl.ch
Tel: +41 (0) 21 69 37867
École Polytechnique Fédérale de Lausanne,
MXG 037, Station 12 1015
Lausanne, Switzerland

Professor of Materials Chemistry
Michael Turner
michael.turner @manchester.ac.uk
http://www.functionalmaterials.manchester.ac.uk/
Tel: +44 (0) 161 275-4625
Chemistry Building-1.24, School of Chemistry The University of Manchester M13 9PL
Manchester, United Kingdom

Scientist
Dr. Florian Le Formal
florian.leformal@epfl.ch
http://limno.epfl.ch
Tel :+41 (0) 21 69 33827
École Polytechnique Fédérale de Lausanne Station 6, Bâtiment CH H5 525, CH-1015,
Lausanne, Switzerland

Research Output List

Publications in peer-reviewed scientific Journals

1. **Rahmanudin, A.**, Jeanbourquin, X. A., Hänni, S., Sekar, A., Ripaud, E., Yao, L., & Sivula, K. (**2017**). Morphology stabilization strategies for small-molecule bulk heterojunction photovoltaics. *Journal of Materials Chemistry A*, *5*(33), 17517-17524. DOI: 10.1039/C7TA05405J.

2. **Rahmanudin, A.**, & Sivula, K. (**2017**). Molecular Strategies for Morphology Control in Semiconducting Polymers for Optoelectronics. *CHIMIA International Journal for Chemistry*, *71*(6), 369-375. *DOI:* 10.2533/chimia.2017.369.

3. **Rahmanudin, A.**, L.Yao, Jeanbourquin, X. A., Liu. Y., Sekar. A., & Sivula, K., (**2018**). Melt-processing of small molecule organic photovoltaics via bulk heterojunction compatibilization. *Green Chemistry. DOI:* 10.1039/c8gc00335a.

4. Yao, L., **Rahmanudin, A.**, Jeanbourquin, X. A., X Yu, X., Johnson, Guijarro, N., Sekar, A., Sivula, K. (**2018**). Advanced Functional Materials, 1706303. DOI: 10.1002/adfm201806303

5. Jeanbourquin, X. A., **Rahmanudin, A.**, Gasperini, A., Ripaud, E., Yu, X., Johnson, M., & Sivula, K. (**2017**). Engineering the self-assembly of diketopyrrolopyrrole-based molecular semiconductors via an aliphatic linker strategy. *Journal of Materials Chemistry A*, *5*(21), 10526-10536. *DOI:* 10.1039/C7TA00896A.

6. Yu, X., **Rahmanudin, A.**, Jeanbourquin, X. A., Tsokkou, D., Guijarro, N., Banerji, N., & Sivula, K. (**2017**). Hybrid Heterojunctions of Solution-Processed Semiconducting 2D Transition Metal Dichalcogenides. *ACS Energy Letters*, *2*(2), 524-531. **DOI:** 10.1021/acsenergylett.6b00707.

7. Jeanbourquin, X. A., **Rahmanudin, A.**, Yu, X., Johnson, M., Guijarro, N., Yao, L., & Sivula, K. (**2017**). Amorphous Ternary Charge-Cascade Molecules for Bulk Heterojunction Photovoltaics. *ACS applied materials & interfaces*, *9*(33), 27825-27831. DOI: 10.1021/acsami.7b04983;

8. Gasperini, A., Jeanbourquin, X. A., **Rahmanudin, A.**, Yu, X., & Sivula, K. (**2015**). Enhancing the Thermal Stability of Solution-Processed Small-Molecule Semiconductor Thin Films Using a Flexible Linker Approach. *Advanced Materials*, *27*(37), 5541-5546. DOI:10.1002/adma.201501826

9. Gasperini, A., Johnson, M., Jeanbourquin, X., Yao, L., **Rahmanudin, A.**, Guijarro, N., & Sivula, K. (**2017**). Semiconducting alternating multi-block copolymers via a di-functionalized macromonomer approach. *Polymer Chemistry*, *8*(5), 824-827. DOI: 10.1039/C6PY01921H;

Unpublished work

10. **Rahmanudin, A.**, L.Yao., Sekar, A., and Sivula, K., (**2018**). *Heck-Mizoroki Reaction of Functionalized Macromonomers for the Formation of Fully-Conjugated Block Copolymers for Organic Photovoltaics. American Chemical Society - Marco Letters* **(Manuscript Submitted).**

11. **Rahmanudin, A**., Yao, L., & Sivula, K. (**2018**). Conjugation break spacers and flexible linkers as tools to engineer the properties of semiconducting polymers. *Polymer Journal – Invited Focus Review* **(Manuscript Submitted and under review).**